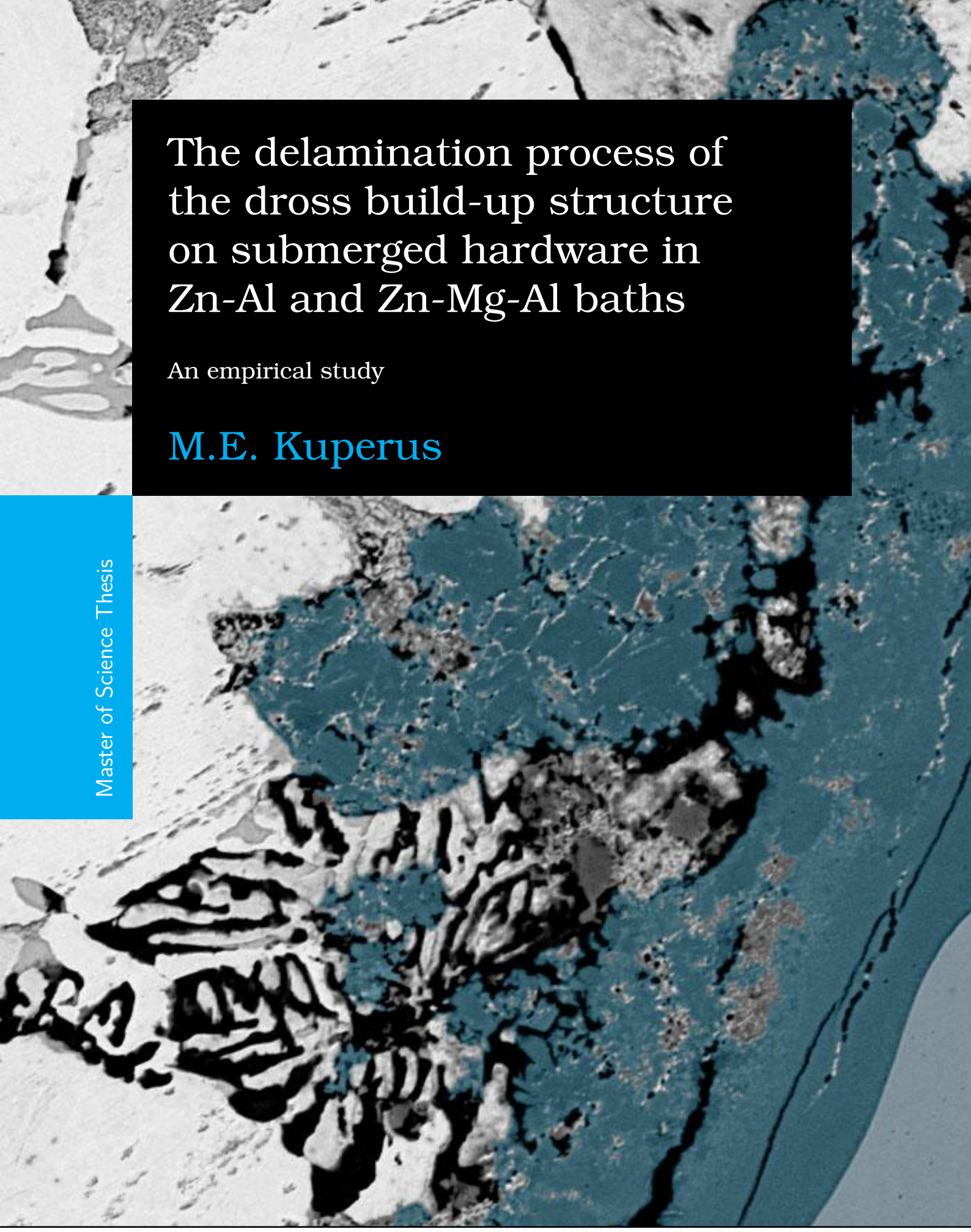

The delamination process of the dross build-up structure on submerged hardware in Zn-Al and Zn-Mg-Al baths

An empirical study

M.E. Kuperus

Master of Science Thesis

TU Delft Delft University of Technology

Materials Science and Engineering

The delamination process of the dross build-up structure on submerged hardware in Zn-Al and Zn-Mg-Al baths

An empirical study

Master of Science Thesis

M.E. KUPERUS

For the degree of Master of Science in Materials Science and Engineering at Delft University of Technology

to be defended publicly on August 30, 2018 at 14.00h.

Student number:	4005384
Project Duration:	14 November 2016 - 22 September 2017
Supervisors:	dr.ir. S.E. Offerman - TU Delft
	dr.ir. M. Bright - Tata Steel
Readers:	dr.ir. J.M.C. Mol - TU Delft
	C. Ioannidou M.Sc - TU Delft

The work in this thesis was supported by Tata Steel Europe. Their cooperation is hereby gratefully acknowledged.

Abstract

Hot-dip galvanizing is a well-known process to increase the corrosion resistance of steel. As a by-product dross is formed in the Zn-bath. The dross particles are composed of Fe, Al and Zn in the form of $Fe_2Al_5Zn_x$ and interact with the hardware that is submerged in the Zn-bath and eventually accumulate on the surface of the hardware. This accumulation of dross on the hardware is known as dross build-up.

Dross is formed in the Zn-bath as a result of the dissolution of Fe from the steel strip. This Fe reacts with Al present in the liquid Zn forming the $Fe_2Al_5Zn_x$ dross particles. Once the hardware is submerged in the liquid Zn a thin compact Fe_2Al_5-layer is formed on top of the surface of the hardware, known as the diffusion layer. This diffusion layer acts as a barrier for Fe towards the Zn-bath and Zn towards the hardware surface. Once the diffusion layer is formed dross particles precipitate on top of this diffusion layer followed by a slow growth of the intermetallic dross particles. The diffusion layer and accumulated intermetallic dross particles are known as the dross build-up. The thickness of this dross build-up depends on immersion time, bath temperature and bath chemistry and varies typically between 90 µm up to several millimetres.

The dross build-up is thought to be a critical factor in the bath hardware lifetime. The surface quality of the bath hardware directly influences the quality of products produced on the galvanizing line. More dross in the Zn-bath could lead to more defects in the coating, which could lead to failure when the steel strips are processed further, or giving the coating on the steel strip a bad appearance. Because of the dross build-up on the hardware, the bath hardware is changed every 4-6 weeks. By controlling the dross in the Zn-bath, the service lifetime of the hardware could possibly be extended. When the service lifetime of the hardware is extended the maintenance downtime and costs of the galvanizing lines are reduced.

Recently, Tata Steel introduced a new type of Zn-coating: MagiZinc (MZ). This type of Zn-coating differs from the conventional Zn-coating: Conventional Zn-coating (GI) consists of Zn with 0,30 wt% Al whereas MagiZinc consists of Zn with 1,60 wt% Al and 1,60 wt% Mg. This difference in composition has an influence on the dross build-up formed on the hardware. At Tata Steel, there is some evidence that the dross build-up layer on the bath hardware created in the conventional Zn-bath is diminishing when the hardware is submerged in the MagiZinc-bath.
This thesis project aims to identify the characteristics of this cleaning behaviour in MagiZinc of the dross build-up that is formed on bath hardware when submerged in conventional Zn.

For this thesis project two main experiments were performed. For each main experiment four individual samples were placed in the Zn-bath, where each sample corresponds to a different stage of the experiment. Each sample was analysed to give a better understanding about the dross build-up characteristics during a typical hardware campaign after transitioning from GI to MZ and vice versa. The samples are made of the same stainless steel as the bath hardware (316L SS). The microstructure and composition of the dross build-up were characterised by Scanning Electron Microscopy (SEM) with Energy Dispersive X-ray Spectroscopy (EDX).

Based on the results obtained from experiments in this study it can be concluded that the delamination process of the intermetallic dross particles is a combination of intergranular diffusion of Zn and crack formation as a result of thermal shock.

By changing the baths from conventional Zn to MagiZinc the composition of the bath changes. As a result the thermodynamic stability of the intermetallic $Fe_2Al_5Zn_x$ dross particles change with respect to the liquid Zn-phase in such a way that the intermetallic dross particles partly dissolve in the liquid MagiZinc. As a result, the intermetallic dross particle/liquid Zn interface changes from a faceted to a curved interface. As a consequence of this change in structure intergranular diffusion can take place between the intermetallic dross particles. By the intergranular diffusion of Zn the cohesion of the grain boundaries of the intermetallic dross particles is reduced. This reduction in cohesion is probably the start of the delamination of the intermetallic dross particles, breaking into smaller pieces at the grain boundaries when enriched with Zn.

The diffusion layer remains largely unaffected in the delamination process due to the better adhesion to the hardware surface compared with the adhesion of the intermetallic dross particles to the diffusion layer. The better adhesion of the diffusion layer to the hardware surface is the result of diffusion of Cr and Ni from the 316L SS substrate into the liquid Zn at time of immersion. The area from where Cr and Ni are dissolved, Al is diffusing into the 316L SS substrate forming the diffusion layer. Simultaneously the intermetallic dross particles form at the hardware surface. This layer is mainly formed from Fe and Al from the bath, not from the 316L SS substrate.
Due to this limited bonding between the intermetallic dross particles and the diffusion layer the intermetallic dross particles are more prone to crack formation due to thermal shock.
By changing the Zn-bath from conventional Zn to MagiZinc and vice versa the hardware and thus also the dross build-up rapidly cools down to room temperature. This thermal shock creates stresses within the intermetallic dross particle-layer. Due to a difference in thermal expansion between the 316L stainless steel matrix and the intermetallic dross particle-layer large cracks form in the intermetallic dross particle-layer. When the hardware is immersed again in liquid Zn the cracks still exist and these cracks accelerate the delamination process of the dross build-up structure. This observed mechanism is independent from the type of Zn-bath that the hardware is immersed in. The process also takes place when the hardware is taken out a conventional Zn-bath and placed back into a conventional Zn-bath.

Acknowledgements

This thesis work is based on my research project at Tata steel in IJmuiden and is written for the degree of the master program Materials Science and Engineering at Delft University of Technology. I would like to give a short thanks to some of the individuals that helped me in various ways in completing this thesis.

First of all, I would like to express my appreciation to Erik Offerman for his supervision, discussions and advice throughout this time. Likewise, I would like to thank Mark Bright for being my daily supervisor, whose guidance and feedback helped me during the entire time of this project.

Furthermore I would like to thank everybody at Tata Steel for their kindness, support and assistance. A special thanks goes to Jenneke Bakker for being great company and providing me with very helpful feedback and motivation during the time I worked on this thesis.
I am also very grateful to Koen Lammers and Maxim Aarnts for everything they have contributed to this work, by performing the various measurements together with the interesting discussions on the interpretation of the results.

Without having support of some great friends and family, I would not have been able to finish my masters. Although they did not exactly understand what I was doing, they gave me their full support whilst performing this thesis project.

And last but not least, Frank; thank you for your remarkable patience and support. I am so happy to be with you.

Marianne Kuperus
Delft, Oktober 2017

Table of Contents

List of Figures

List of Tables

Nomenclature

Symbols

α	Thermal expansion coefficient [m m^{-1} °C]
Γ	Fe_3Zn_{10}-phase with 23,5-28 wt% Fe
γ_{GB}	Grain boundary energy
γ_{SL}	Solid/Liquid interphase energy
δ	$FeZn_{10}$-phase with 7-11,5 wt% Fe
ζ	$FeZn_{13}$-phase with 5-6 wt% Fe
η	Fe_2Al_5-phase with 30-40 wt% Fe
σ	Surface stress
θ	Contact angle
D	Diffusion coefficient [m^2 s^{-1}]
D_0	Pre-exponential factor for diffusion [m^2 s^{-1}]
E	Young's Modulus [MPa]
H	Enthalpy [J mol^{-1}]
G	Gibss Free Energy [J mol^{-1}]
L	Liquid phase
Q_D	Activation energy for diffusion [kJ mol^{-1}]
R	Gas Constant for diffusion [8,314 J K^{-1} mol^{-1}]
S	Entropy [J K^{-1} mol^{-1}]
T	Temperature [K]

Acronyms

3mE	Mechanical, Maritime and Materials Engineering
BCC	Body Centered Cubic crystal structure
DVL	Dompelverzinklijn. In English: HDG
EBSD	Electon Backscatter Diffraction
EDX	Energy-dispersive X-ray spectroscopy
EPMA	Electon Probe Micro Analysis
FCC	Face Centered Cubis crystal structure

GI	Conventional zinc (0,3wt% Al Zn-alloy)
HCP	Hexagonal close-packed crystal structure
HDG	Hot-dip galvanizing line
MSE	Materials Science and Engineering
MZ	MagiZinc (1,6wt% Al + 1,6wt% Mg Zn-alloy)
SEM	Scanning Electron Microscopy
SS	Stainless steel
TEM	Transmission Electron Microscopy
TU	Delft University of Technology

Elements

Al	Aluminium
C	Carbon
Cr	Chromium
Fe	Iron
Mg	Magnesium
Mn	Manganese
Mo	Molybdenum
Ni	Nickel
O	Oxygen
P	Phosphorus
S	Sulphur
Si	Silicon
Zn	Zinc

Chapter 1

Introduction

This chapter gives an introduction to the general topic of this thesis. Section 1-1 gives an introduction of Tata Steel Europe and details of the principles of the galvanizing process. Also the different types of zinc coatings are briefly explained. Section 1-2 discusses briefly what dross is and the effect of the dross build-up is on the production of galvanized products for Tata Steel. The scope and outline of the thesis are given in Section 1-3 and 1-4, respectively.

1-1 Galvanizing of steel at Tata Steel

1-1-1 Properties of Iron and Steel

Iron (Fe) is one of the most present metals on the surface of the earth and constitutes up to 35% of its mass [1]. The applications of Fe are numerous, because of its relatively easy accessibility and extractability in combination of good mechanical properties and low costs. These characteristics makes Fe a suitable option for various applications in the automotive industry and mechanical structures.

Steel is an alloy of iron (Fe) and carbon (C), with addition of other elements, most common are chromium (Cr) and nickel (Ni). In the process of steel making there are changes happening on a micro-level in the steel. Various grades of steels are formed by the addition of several alloying elements, where Fe and C are the major constituents. The objective of these alloying elements is to improve certain properties of the steel in favour of its application.
The mechanical properties of steel are also influenced by heat treatment processes. The wide range of alloy compositions, mechanical properties and product forms makes steel one of the most versatile materials currently available. Therefore, steel is used in applications ranging from small applications like packaging cans and paper clips to structural applications like the construction and automotive industries.

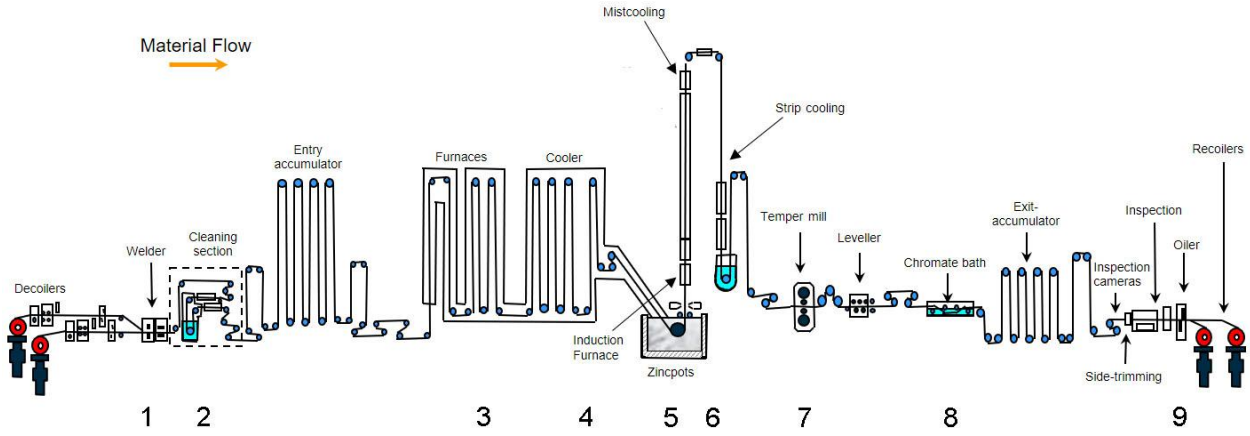

Figure 1-1: Schematic overview of a continuous galvanizing line [4].

1-1-2 Tata Steel Europe

Tata Steel Europe, formerly known as Koninklijke Hoogovens and Corus and purchased by Tata Steel in 2010, is the second largest steel producer in Europe. The company has manufacturing operations in Western Europe, with plants in the UK, Netherlands, Germany, France and Belgium.
In the Netherlands the main site of Tata Steel is situated in IJmuiden. This site is an integrated blast furnace-based steelmaking site, producing slab, hot and cold rolled coils and coated strip products such as galvanized coil and packaging steels. The steel produced in IJmuiden is mainly processed in the automotive, construction and packaging industries. The site area is 750 hectares, making it the largest contiguous business area in the Netherlands [2].

1-1-3 Galvanizing of Steel

Tata Steel IJmuiden has three hot-dip galvanizing lines in operation, at Tata Steel these lines are commonly known as DVL (in dutch: DompelVerzinkLijn). This thesis project focuses on the second hot-dip galvanizing line: DVL 2. The reason for focusing on this galvanizing line is that this line has in general more bath switches compared to the other two lines. Furthermore the Zn-bath in DVL 2 is easy accessible for experiments.
Galvanizing is the generic term for any of several techniques for applying thin coatings of zinc (Zn) to steel products in order to protect the ferrous base metal from corrosion and to maximize performance life for many applications [3]. There are two ways for galvanizing: batch galvanizing and continuous hot dip galvanizing. The latter is used by most steel producers, because of the capability of high tonnage throughputs with a higher quality of the coating (uniformity and paintability of the coating).

Continuous hot dip galvanizing involves continuous submersion of steel strip in a molten zinc bath resulting in coating of the steel strip. In Figure 1-1 a typical hot-dip galvanizing process used at Tata Steel in IJmuiden is shown. The process of continuous hot dip galvanizing involves the following steps:
First, the steel strips are welded end to end in order to form a continuous steel strip. This

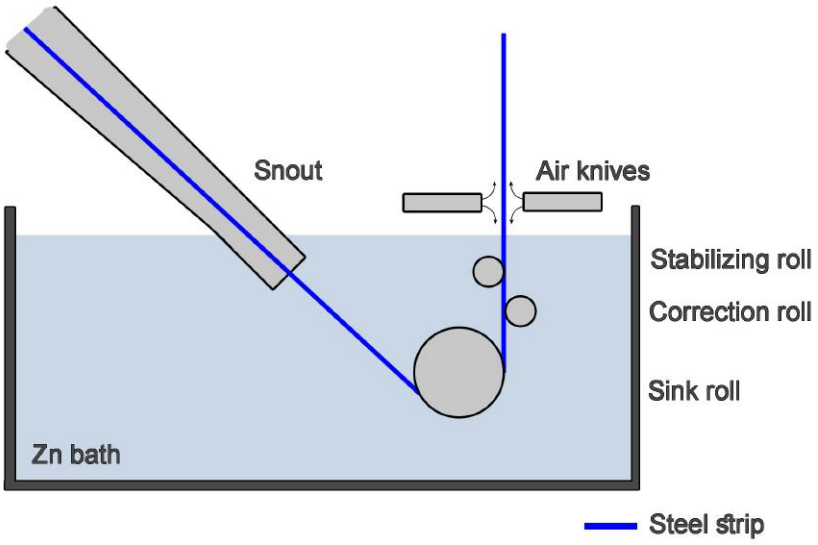

Figure 1-2: Cross section of hot-dip galvanizing bath

step is situated at point 1 in Figure 1-1. Next, the steel strip is cleaned to remove the dirt and oxides. At point 3 in Figure 1-1 the strip is annealed in a N_2/H_2 atmosphere to achieve the desired microstructure and mechanical properties. The N_2/H_2 environment is chosen to reduce the oxides, to obtain good reactive wetting of the surface in the zinc bath. In step 4 the steel strip is cooled to a temperature of about 460°C, to have the same temperature as the liquid Zn-bath. At the fifth step the steel strip is dipped into the molten Zn-bath to form a coating on the steel strip. This stage is the focus point of this thesis project. At the end of the bath the excessive Zn is removed to obtain the desired thickness of the coating.
At step 6 in Figure 1-1 the steel and coating are cooled by forced convection. The coating solidifies. Steps 7 to 9 are finishing steps, e.g. temper rolling (7), oiling (9), inspection and coiling [3].

1-1-4 Bath Hardware

In the Zn-bath area (step 5 in Figure 1-1) there are several components guiding the steel strip through the Zn-bath. The components are the snout, the rolls and air knives as seen in Figure 1-2.
The snout guides the steel strip from the surface of the annealing step into the liquid Zn towards the rolls without exposure to the air. In the Zn-bath there are three rolls hanging in the Zn-bath supported by arms that allow for positioning. The arms are attached to a rig positioned outside the bath. The sink roll is a turning point for the steel strip and the correction roll and stabilizing roll give the steel strip a good positioning for the air knives. Wiping with air knives forces part of the liquid Zn to run back into the bath and thereby controls the final coating thickness.[4, 5].
The final thickness of the Zn-coating varies between 5 µm and 65 µm. Most layers for automotive steels are around 10 µm. The total time of immersion of the steel strip in the Zn-bath is about 2 to 5 seconds, depending on the line speed [4].

The performance of the galvanising bath hardware can have a marked effect on both the

Element	% Present
Fe	Balance
C	<0,03%
Cr	16-18,5%
Ni	10-14%
Mn	<2,0%
Mo	2-3%
Si	<1%
P	<0,045%
S	<0,03%

Table 1-1: General composition of 316L SS, the material that is used for the bath hardware in the DVL2 [6]

amount of downtime experienced by a line and the quality of the coated strip. The hardware submerged in the liquid Zn-alloy are subject to the harsh operating conditions within the bath. These conditions are characterised by high temperatures (460°C) and corrosive attack by the liquid Zn-alloy. The bath hardware therefore needs to resistant to corrosion, cracking, thermal shock and elevated temperatures. Also economic factors which must be considered: the material must be readily available and components manufactured at a cost appropriate to the galvanizer.

The bath hardware is typically made of stainless steel (SS). Austenitic stainless steels are most used for constructions at elevated temperatures, because of its high thermal expansion coefficient and low heat conductivity. The two most common stainless steel grades used in constructions are 304 and 316L. The key difference between 304 and 316L is the addition of Mo and a higher Ni content [6, 7].
Tata Steel IJmuiden uses the 316L for the hardware components in the Zn-bath in DVL2. Grade 316L is an austenitic stainless steel with molybdenum-bearing grade. The chemical composition of 316L SS is shown in Table 1-1.

The Mo and higher content of Ni gives 316 better overall corrosion resistant properties, particularly higher resistance to pitting and crevice corrosion compared to grade 304. Furthermore, 316L imparts hot strength characteristics (high creep strength at elevated temperatures). The L in grade 316L stands for the low carbon version of grade 316. Because of this low carbon content this grade is less prone to grain boundary carbide precipitation (sensitisation) [8]. Owing to the good corrosion resistant properties and the good performance at elevated temperatures, the 316L SS is commonly used as material for the bath hardware. The 316L SS has a good combination of resistance to molten Zn-Al galvanizing alloy attack, compatible mechanical properties and reasonable cost [6][8].

1-1-5 Conventional Zinc and MagiZinc

Tata Steel IJmuiden uses two types of zinc coatings for commercial products: 1.) the conventional galvanized coating and 2.) the MagiZinc coating. These two types of coatings are of importance in this thesis project.

The conventional galvanized coating is a ZnAl-coating commonly known as GI. This coating consists mainly of Zn with the addition of aluminium (Al) (0,20wt%) and some Fe (0,01wt%) because of dissolution of Fe from the strip. This type of coating has been used for decades in the steel making industry and still is a popular choice for providing sacrificial protection to steel components [9].
Over the last decades weight reduction became more important in the automotive industry in order to reduce fuel consumption and carbon dioxide emission. In 2005 the MagiZinc coating was introduced by Tata Steel, often abbreviated as MZ. This coating is a ZnMgAl-coating, containing zinc, aluminium (1,6wt%) and magnesium (1,6wt%). In this coating also a similar amount of Fe is found. The MagiZinc-coating was found to have better corrosion resistant properties, as the alloying additions rendered it a better passivation ability compared to GI. The MZ-coating ensures lower consumption of valuable resources as it provides the same or better corrosion protection by only half as much coating thickness compared to GI.

Nowadays the total throughput of galvanized steel that flows thourgh the three DVLs is 1450 kT a year. About half is produced as GI, the other half is produced as MZ.

1-1-6 Changing Baths

In the galvanizing lines at Tata Steel IJmuiden the two different type Zn-coatings (GI and MZ) are used in the same line. Therefore each DVL has one GI-bath and one MZ-bath. If one bath is in the process, the other bath is stationed under the galvanizing line. When the other bath is needed for the production, the baths will switch.

In Figure 1-3 the process of switching baths is shown. First after the line has stopped, the first bath is lowered (Figure 1-3.a to Figure 1-3.c) and placed (Figure 1-3.d and Figure 1-3.e). Here the bath is heated in order to prevent solidification of the bath [4].
Once stationed, the second bath is moved and placed in position in the line (Figure 1-3.f to Figure 1-3.i). The line is now ready to start. This change in baths takes less than 2 hours.

1-2 Problem Statement

1-2-1 Dross and Dross Build-up

During the galvanizing process, the steel strip is continuously passing through the Zn-bath. Hereby Fe constantly dissolves from the steel strip. The amount of the dissolved Fe is always more than the amount taken out the Zn-bath by the coating. This excess in Fe results in Fe saturation of the bath and leads to the formation of dross. Any Fe in excess of the solubility limit is converted into dross particles near the bath/steel interface. Thereafter, dross particles continue to precipitate during operation of the galvanizing line. Dross normally consists of Zn-Fe-Al intermetallic compounds.

The dross particles will also react with the submerged hardware and precipitate on the surface of the hardware. Once attached on the bath hardware the dross particles will also grow. The reaction of the dross with the bath hardware is known as dross build-up. The thickness of this dross build-up can grow up to several millimetres.

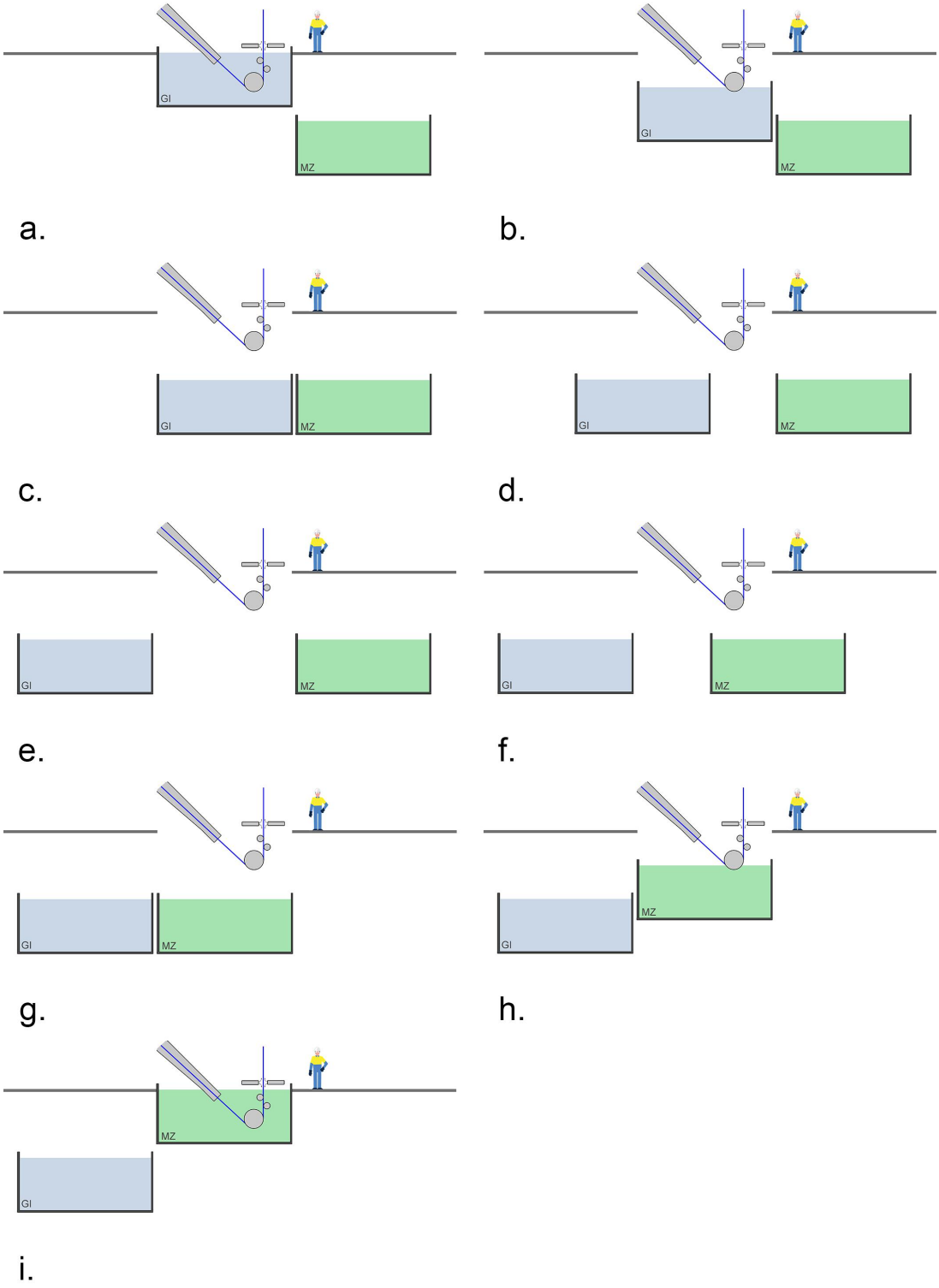

Figure 1-3: A schematic representation of the change of Zn-baths

In operation the clean bath hardware is often submerged first in GI-baths. After a certain time (depending on the production schedule) the baths are switched and the MZ-bath is in production. The dross build-up formed in the GI-bath is cleaned in the MZ-bath.

1-2-2 Effect of Dross Build-up on the Galvanizing process

Understanding the growth behaviour of the dross-build-up in GI and the cleaning of the dross build-up in MZ is thought to be a critical factor in improving the bath hardware lifetime.

The quality of the bath hardware directly influences the volume and quality of products produced on the galvanizing line. More dross in the Zn-bath could lead to more defects in the coating, which could lead to failure when the steel strips are processed further, or giving the coating on the strip a bad appearance. Due to dross build-up the lifetime of the bath hardware is currently 4 to 5 weeks. The lifetime of bath hardware is also known as a hardware campaign. Replacing the bath hardware that is corroded with dross build-up for new clean bath hardware takes about 4 to 6 hours.

The failure (or scheduled maintenance) is the primary cause of downtime in the galvanizing lines and is a major maintenance cost item. Changing the bath hardware often accounts 20% of the total maintenance budget for the galvanizing lines. The total costs for changing the bath hardware add up to several million euros a year. Extending the operating lifetime of the bath hardware will reduce the maintenance downtime, which will reduce the yearly maintenance costs. Therefore, the problem is that the maintenance downtime of the three galvanizing lines at Tata Steel in IJmuiden is too high due to bath hardware failure. The operating bath hardware lifetime is currently too low resulting in high maintenance costs, lost production volumes and poor coating quality which can lead to a decreased customer satisfaction.

1-3 Scope and Objective

Reducing the dross build-up on the hardware components in the Zn-bath is one way to improve the lifetime of the bath hardware. When the service lifetime of the hardware is extended, the maintenance downtime and costs of the galvanizing lines at Tata Steel IJmuiden are reduced. An increase in the understanding in the dross build-up behaviour on the bath hardware in both Zn-baths can lead to an optimal schedule in changing baths (GI and MZ) that prevents large build-up on the bath hardware. Less dross build-up on the bath hardware could extend the lifetime of the bath hardware.
This approach differs from previous research done in the Zn-bath area since this thesis project is the first (large) project at Tata Steel on the dross build-up and the effect of the transition between the two types of baths (GI and MZ). Therefore, this research will mainly be focused on the root cause(s) of the cleaning behaviour of the dross build-up on the hardware (that formed in GI) when submerged in MZ.

Until the start of this thesis project much work has been done to improve the quality of the coating on the steel strip, in order to launch and sell a better product. Less research has been done on the dross build-up behaviour on bath hardware in the Zn-bath itself. No previous research has been done when the bath hardware switches from GI-bath to the MZ-bath, and

what the effect of switching the baths will be on the dross build-up. At Tata Steel there is some evidence that the dross build-up layer on the bath hardware created in the GI-bath is diminishing when the hardware is submerged in the MZ-bath. However, a study about this behaviour with quantitative results was not performed.
This thesis project will be the first project on dross build-up behaviour in the transition between GI and MZ. Is it possible to identify the cleaning behaviour of the dross build-up on the submerged bath hardware?

The research goal of this project is to identify the cleaning behaviour in MZ of the dross build-up that is formed in GI on submerged bath hardware. In order to obtain the research goal requires knowledge and understanding of the contribution of each parameter that influences the growth and cleaning of the dross build-up. The parameters contributing to the dross build-up are bath temperature, bath composition and operational parameters such as line speed. The parameters that contribute to the cleaning of the hardware in MZ are unknown.

1-4 Outline of the Thesis

After this introduction, Chapter 2 deals with the basic theories of the two different coating types as well the dross and dross build-up. Furthermore, the growth and delamination mechanism of dross build-up are discussed.
Chapter 3 is a report written for Tata Steel as a first analysis for this thesis project. The goal of this report is to understand the dross build-up behaviour on the bath hardware when transitioning from GI to MZ.
Chapter 4 introduces the experimental procedure for this thesis project. The materials, the set-up for testing, sample preparation and analytical techniques used in this study are described.
In Chapter 5 the results obtained from the experiments are presented. In Chapter 6 these results are discussed. Furthermore some recommendations related to possible future work are given in this chapter.
Finally, Chapter 7 draws some conclusions on the basis of the results presented in the previous chapters.

Chapter 2

Theoretical Background

Steel strips containing scratches, excessive roughness or incorporated dross particles are unacceptable for automotive industry. The formation of hard intermetallic dross particles in the Zn-bath and on the bath rolls arise from complex interactions between liquid Zn and the steel strip and bath hardware and can lead to poor product quality. To produce steels strips with good product quality can only be controlled by frequently replacing bath hardware components.

The aim of this chapter is to describe the mechanisms underlying the formation of Zn alloy coatings on steel strip by a continuous process and the formation of the dross and dross build-up structure on the bath hardware.

First, in Section 2-1-1 the coating formation process for GI is explained. In this section is the galvanizing process explained when no Al is added to the bath and when there is Al available in the bath. Section 2-1-2 focuses on the galvanizing process in MZ.
In section 2-1-3 the term 'dross' is explained and what the difference is between dross and dross build-up. Furthermore the formation of dross build-up in GI is explained. Since the mechanism behind the cleaning behaviour in MZ is unknown, this part is not explained. Therefore, in Section 2-2-3 the mechanisms that possibly contribute to the delamination of the dross build-up are explained.

2-1 Baths and Dross

2-1-1 Conventional Zinc (GI)

To maximise performance life for many applications, the steel must be made corrosion resistant by galvanizing with a Zn (or Zn alloy) coating. In order to apply a metallurgically bonded zinc coating to a roll surface, the steel must be submerged into a bath of liquid Zn.

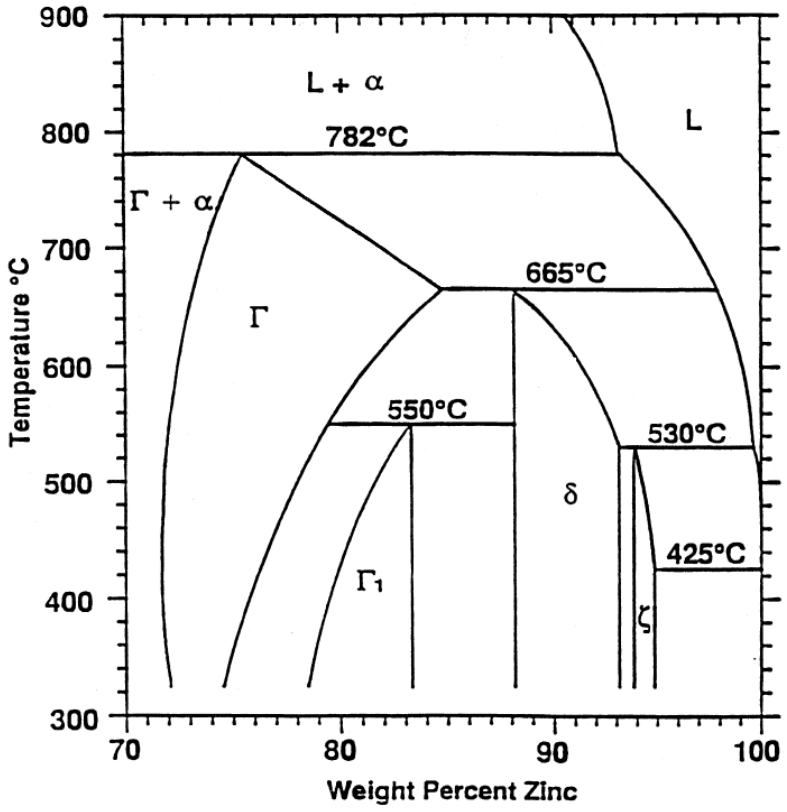

Figure 2-1: The Zn-rich corner of the Fe-Zn phase diagram [3].

Dissolution of Fe

During immersion of the steel strip into the pure liquid Zn-bath, part of the Fe of the strip dissolves into the bath. Part of this dissolved Fe contributes to the formation of intermetallic dross particles. The other part of the dissolved Fe reacts with Zn to form an intermetallic diffusion layer in the surface of the steel strip [10].
The steel strip can dissolve until locally the concentration of Fe reaches a level where the solubility of Fe in the liquid Zn is equal to that in the steel strip. That Fe concentration is the maximum that can be dissolved.

Coating Formation

When the steel is submerged in the liquid Zn-bath, several reactions occur depending upon the bath composition. An understanding of the phase transformations that take place at the liquid Zn/steel interface is necessary in order to predict and control the microstructure of galvanized coatings [9, 10].

The Fe surface atoms of the steel strip diffuse into the pure liquid Zn. As a result a diffusion layer of Fe-Zn is formed at the surface of the steel strip about 10 µm in the steel strip. This layer is known as a diffusion layer. The main function of this layer is to provide a good bond between the steel and the Zn coating [10].

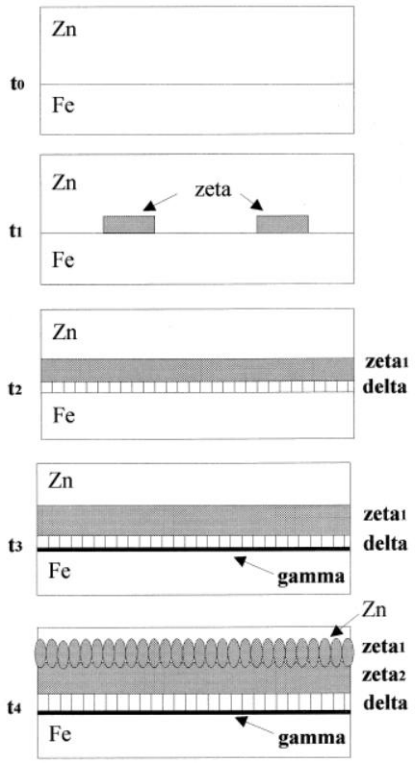

Figure 2-2: Coating formation on steel strip, without addition of Al in the Zn bath [3]. Typically the thickness is about $25\,\mu m$.

Figure 2-1 shows the Zn-rich corner of the Fe-Zn phase diagram. At most steel producers the Zn-bath temperature is held at temperatures between 440°C-480°C. The primary phases that are formed between these temperatures are ζ, δ and Γ. Each of which is explained below [3]:

- The ζ phase consists of $FeZn_{13}$ and contains 5-6 wt% Fe. The crystal structure is monoclinic
- The δ phase consists of $FeZn_{10}$ and contains 7-11,5 wt% Fe. The crystal structure is HCP
- The Γ phase consists of Fe_3Zn_{10} and 23,5-28 wt% Fe. This phase has a BCC crystal structure

Figure 2-2 shows the formation of the Zn coating. This coating layer is formed as follows [3]: When steel is dipped into Zn, first the ζ phase is formed followed by the δ phase layer (t_1 and t_2). After some time period the Γ phase is formed in between the δ and the Fe phase (t_3). These three phases together form the coating layer. In time only the ζ continues to grow (t_4).

The situation explained above is a coating submerged in pure Zn. The problem with this diffusion layer of pure Zn without the addition of Al is that it is relatively hard and brittle. This brittleness becomes a problem when the strip is processed further because cracking of the coating can occur. The coating will flake and/or powder under the pressure of the processing [3]. To avoid this behaviour, steel strip producers add aluminium (Al) to the liquid Zn-bath.

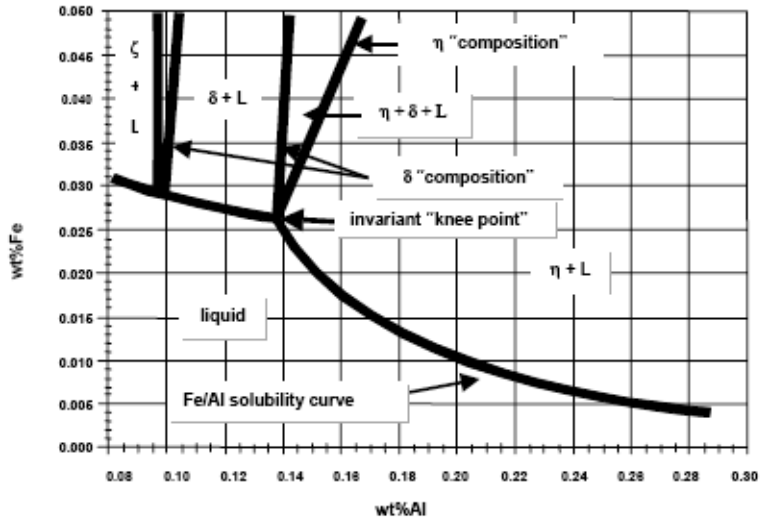

Figure 2-3: The phase diagram of the Zn-rich corner of Zn-Al-Fe system at 460°C [15].

Addition of Al to the Bath

Al is the most important alloying element added to the liquid Zn in continuous galvanizing processes. Al is added to the Zn-bath in order to modify and to control the reaction between Fe and Zn and thereby the various properties of the Zn-coating.
The role of Al can be explained by the thermochemical properties of the ternary Fe-Al-Zn system [11, 12, 13, 14].

Al exist in two forms in the Zn-bath. Some Al is dissolved in the liquid Zn and some Al is present in intermetallic dross particles. The Al in liquid solution is generally referred to as effective Al [11]. The amount of the effective Al is the amount that is able to react with the Fe of the steel strip in order to form the diffusion layer of the coating on the strip [9]. A method to determine the effective Al is based on the solubility of Fe in liquid Zn-alloy. Fe solubility limits in the liquid Zn-alloy are a function of the Al-content [9, 11].

The definition of solubility is the maximum quantity of solute that can dissolve in a certain quantity of solvent or quantity of solution at a specified temperature. In this case the solubility is the maximum quantity of Al that can dissolve in a certain quantity of Zn-bath with the addition of Fe at 460°C.
The solubility of Al varies with the level of Fe dissolved in the bath. In case less Fe is dissolved in the bath the solubility of Al in the liquid Zn in increased [12]. Increasing amount of dissolved Fe, increases the effective Al that the liquid Zn can hold without forming top dross particles in the bath. This behaviour is made clear in the Zn rich corner of the Zn-Al-Fe phase diagram, shown in Figure 2-3.
This Figure shows that Zn at 460°C with an addition of 0,01wt% Fe the Zn can hold about 0,20 wt% Al in solution, without forming intermetallic dross particles. The area below the curve is the under-saturated solubility range where Fe and Al remain in solution. Below the solubility curve no intermetallic particles will form. The area above the curve is the super-saturated range where precipitation occurs [14].

When the amount of Al is higher than the effective Al found in the phase diagram, the

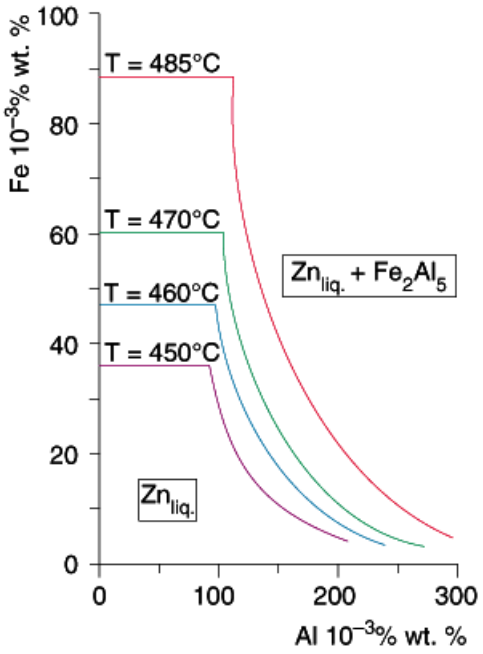

Figure 2-4: The solubility curve for temperatures in the range 450°C - 485°C.

remainder of the Al in the zinc bath is able to react with the dissolved Fe as described in Formula 2-1-1 [11, 16]:

$$Al_{total}\% = Al_{eff}\% + Al_{dross}\% \tag{2-1}$$

The effective Al in the bath is partly dependent upon line geometry and conditions (the bath temperature, line speed and steel strip composition). These parameters can also influence the reaction between Fe and Zn [11].
The Zn bath in the hot dip galvanizing process at Tata Steel typically consists of molten Zn and Al content between 0,18 - 0,25wt%. When the composition lies above the solubility curve, dross particles form. When the composition lies below the solubility curve, all Al is used to form the diffusion layer in the strip and therefore dross particles will not be formed [9]. The diffusion layer has a $Fe_2Al_5Zn_x$ having a composition of about 45 wt% Al, 35 wt% Fe and 20 wt% Zn [9].

The bath temperature has an influence on the effective Al. Fossen et al. [13] showed that an increased bath temperature resulted in a higher effective Al-content. An increase of 5°C leads to a increase in 0,02 wt% effective Al. The effect of temperature is shown in the solubility curve in Figure 2-4. As the Figure indicates, the solubility limit increases with rising temperature [13, 17, 18].
The solubilities are calculated and plotted for different temperatures in the range 440°C - 480°C via equation 2-1-1, founded by Biele [19]:

$$log([Fe]^{1,72} * [Al]^{4,43}) = 14.18 * (\frac{12536}{T}) \tag{2-2}$$

where [Fe] is the concentration of Fe in wt%, [Al] is the concentration of Al in wt% and T the temperature in Kelvin.

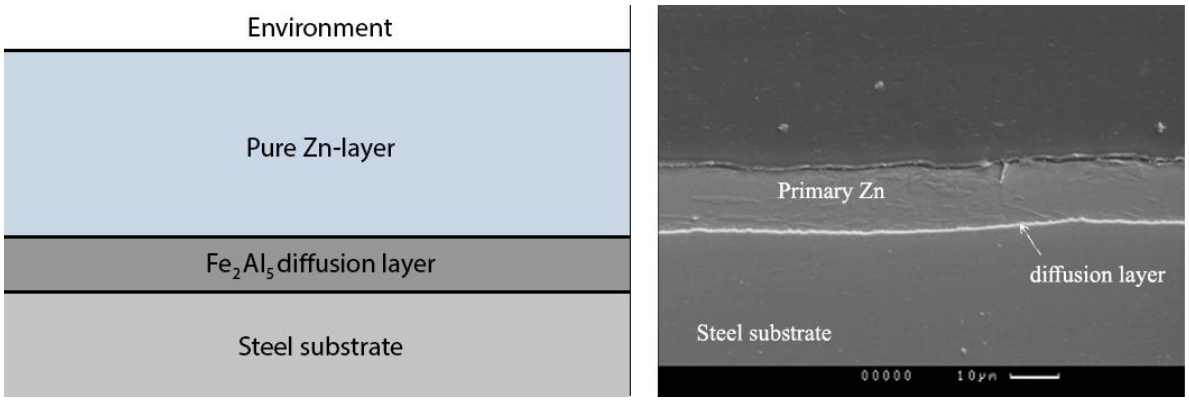

Figure 2-5: On the left a schematic representation is shown of the layers formed in the galvanized coating. On the right a backscattered electron image of the GI-coating is displayed. The coating on steel strip displayed is the coating when aluminium is added to the Zn-bath [4].

Because of the addition of Al the solubility of Fe in the liquid Zn decreases. In the vicinity of the roll surface there is a higher concentration of Fe than in the bulk of the liquid Zn as a result of the dissolution of Fe from the substrate. This higher concentration is forming a local supersaturation of Fe in that area. This local supersaturation leads to the nucleation of Fe-Al intermetallic compounds on the roll surface.
Since Al has a greater attraction to Fe than Zn a more stable intermetallic diffusion layer is formed first between the Al and Fe, instead of Zn and Fe. With the addition of Al, the diffusion rate of the Zn into the roll surface gets lowered because it is dependent on the transport characteristics through the diffusion layer created by the Al-Fe compound Fe_2Al_5 [9][10]. This diffusion layer will avoid uncontrolled formation of the brittle Fe-Zn intermetallic layer.

As a result of the addition of Al in the liquid Zn, the intermetallic Fe_2Al_5 diffusion layer lowers the diffusion rate of the Zn. The addition of Al results in a thinner Zn-coating layer on the roll surface, giving the coating a higher ductility [15]. The thickness of this Fe_2Al_5 diffusion layer is small, usually between 100-500 nm.

Several mechanisms occur at the same time when the strip is submerged in the Zn bath: Once the steel strip enters the bath, the strip gets wetted by the liquid Zn. With this wetting the dissolution of Fe starts, simultaneously the formation of the intermetallic diffusion layer starts. At the point when there is only a small diffusion layer formed, the Zn layer on top of this diffusion layer starts to form. The resulting coating is shown in Figure 2-5. The reactions occurring for each mechanism are very fast; All the mechanisms described above take place in less than a second [3].

In order to form a stable intermetallic Fe_2Al_5 diffusion layer a minimum amount of Al of about 0,15 wt% is needed in the Zn bath. The exact amount that is needed for the formation of the diffusion layer is determined by the solubility curve of Al in the liquid Zn [3].

2-1-2 MagiZinc (MZ)

Up until now this report was about the conventional zinc coating and bath (GI). However, for this thesis project next to the standard conventional galvanizing bath (GI) another type

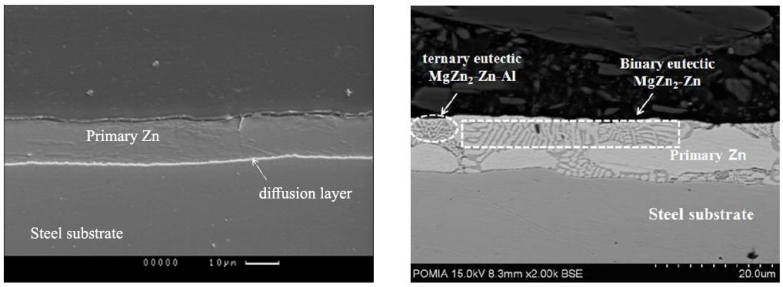

Figure 2-6: On the left a cross section of a GI-coating is displayed. On the right the cross section of a typical MZ-coating is displayed. The various phases in the coatings are designated.

of galvanizing bath is important: MagiZinc bath (MZ).

The need for thinner Zn-coatings with improved performance and coating resistance has led Tata Steel to develop MagiZinc, a thin hot-dip galvanised coating alloyed with Al and magnesium (Mg).

Next to the standard galvanizing (GI) bath that typically contains 0,18 wt% - 0.25 wt% Al, the MagiZinc (MZ) bath with Mg and Al contents varying between 1.4 wt% and 1.8 wt% (usually 1,6 wt%). MagiZinc is one of several commercial Zn-Mg-Al hot dip coatings that together contain between 1 and 3,5 wt% of Mg and Al. Due to the presence of Mg, the coating will form faster and is more compact compared to GI. In general the addition of Mg greatly enhances the corrosion resistance of the Zn-coating [20].

The structure of a MZ coating differs strongly from conventional GI coating, as can be seen in Figure 2-6. The GI coating has a small diffusion layer, followed by pure Zn, whereas MZ coating has a complex microstructure that is characterised by large zinc grains surrounded by Zn-Mg-Al ternary eutectic phases[21]. The microstructures of ZnAlMg-coatings consist of various amounts of Zn-phase, a Zn-Al eutectic, a Zn-Al-$MgZn_2$ ternary eutectic and some separate $MgZn_2$. Similar to GI a Fe-Al diffusion layer is formed in the steel surface.

In the MZ coating two types of eutectic phases can be distinguished [20, 22]:

1. Zn-Mg-Al eutectic
    - Globular phases: a white zinc phase with grey stripes and/or dots containing Zn-Mg-Al. Differences in grey scale correspond to the subtle differences in Zn-Mg-Al composition. The ternary eutectic is composed of Zn, $MgZn_2$ and/or Mg_2Zn_{11}
2. Zn-Al eutectic
    - The black phases contain Zn and Al. This phase is an Al-rich phase: the Al wt% is relatively high, about 20-40 wt%. There is no significant amount of Mg detected in this phase. This phase is also found at the boundaries of the Zn-Mg-Al eutectic phase.

The phases identified in MZ, with the corresponding composition are displayed in Table 2-1.

Contrary to GI-coatings, solidification of MZ takes place step by step with the formation of zinc dendrites, binary eutectic and finally ternary eutectic structures. The formation of a

Phase	Composition
Primary Zn phase	99 wt% Zn, <1 wt% Al
$MgZn_2$ Laves phase	84 wt% Zn, 16 wt% Mg
Zn-Al phase rich in Zn	60-80 wt% Zn, 20-40 wt% Al
Zn-Al binary eutectic	94 wt% Zn, 6 wt% Al
Zn-$MgZn_2$-Al ternary eutectic	93 wt% Zn, 3 wt% Mg, 4 wt% Al

Table 2-1: Various phases present in MZ with the corresponding composition.

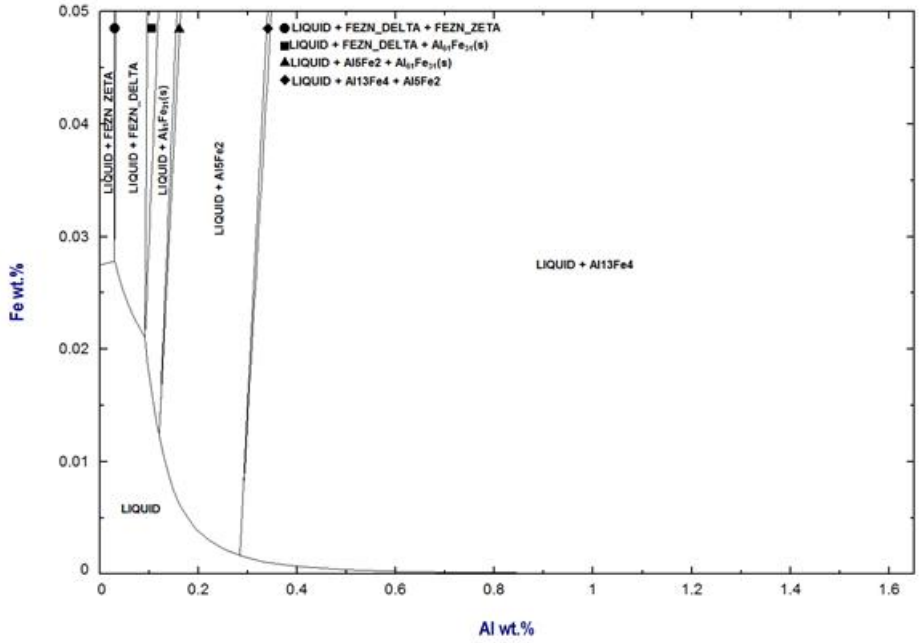

Figure 2-7: The Fe-Al phase diagram with 1,5 wt% Mg and at the temperature of 450° [27].

MagiZinc coating is divided into four steps [23]:
First, the diffusion layer is formed, similar to that of in GI, due to the reactive Al with the steel. Once the diffusion layer is formed, the pure Zn-grains are forming. Next, the $MgZn_2$-phase starts to form too, resulting in Zn and $MgZn_2$ as a binary lamellar eutectic. As a last step, the liquid Zn reaches its ternary eutectic composition and the solidification is instantaneous. Next to more Zn and $MgZn_2$, some Al-phase forms too, resulting in a ternary eutectic phase [24].

In general the addition of Mg greatly enhances the corrosion resistance of the Zn-coating [20]. Furthermore MZ offers a higher hardness than the conventional GI Zn coating. The hardness of Zn-Mg and Zn-Mg-Al coatings is normally higher than that of pure Zn coating. MZ has a higher hardness due to the formation of the binary eutectic structure $MgZn_2$, which has a hexagonal structure [25]. This structure type reduces the abrasion significantly (powder and flakes) and it remains bonded to the steel even after extreme bending of the steel [20, 26].

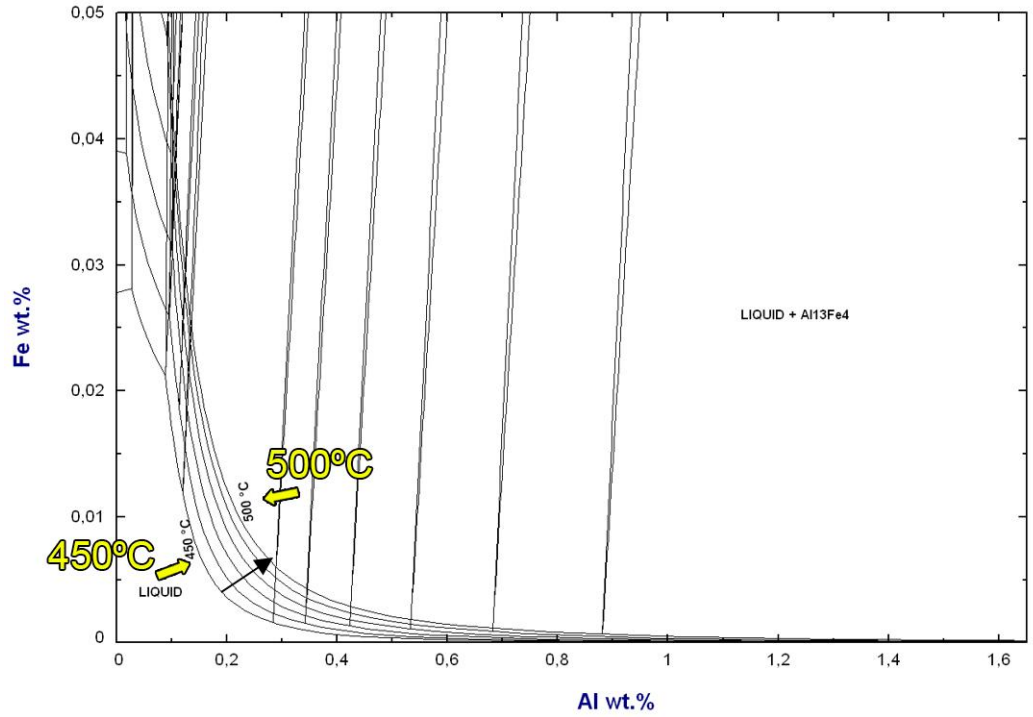

Figure 2-8: The Fe-Al phase diagram with the addition of 1,5 wt% Mg is displayed for different temperatures. This figure does not differ from Figure 2-9, therefore it can be concluded Mg has little influence on the solubility lines of the phase diagram [27].

Solubility Al and Mg in MZ

The solubility of Al and Mg in the Zn HCP-phase is extremely low. The result is that upon addition of only small amounts of Mg and Al already heterogeneous microstructures appear. When the concentration of both Mg and Al exceeds 1 wt% a ternary eutectic phase appears. The HCP Zn-phase is stable up to additions of at least 2 wt% Mg and 5 wt% Al. For higher amounts of Al a binary Zn-Al eutectic structure forms. The Al phase, which is an Al rich FCC Zn-phase is only present as eutectic, either as a binary Zn-Al eutectic or as a ternary Zn-$MgZn_2$-Al eutectic [22].
In Figure 2-8 the solubility curve for 1,5 wt% Mg is shown. In this Figure it can be seen that the solubility of Fe in the liquid phase increases with increase in temperature. Furthermore, this solubility is compared to the solubility curve in GI (Figure 2-3). As can be seen in Figure 2-8 and 2-9 Mg has little influence on the solubility lines.

The formation of intermetallic dross particles is not reduced in the MZ-bath, due to the Fe pick-up and the Al present in the bath.

2-1-3 Dross and Dross Build-up

One of the type of defects in Zn-coatings is the formation of fine pimples at further processing of the steel strips caused by ultrafine particles within the Zn-coating. These particles are composed of Fe, Al and Zn and originate from the precipitation of Fe in the liquid Zn. The

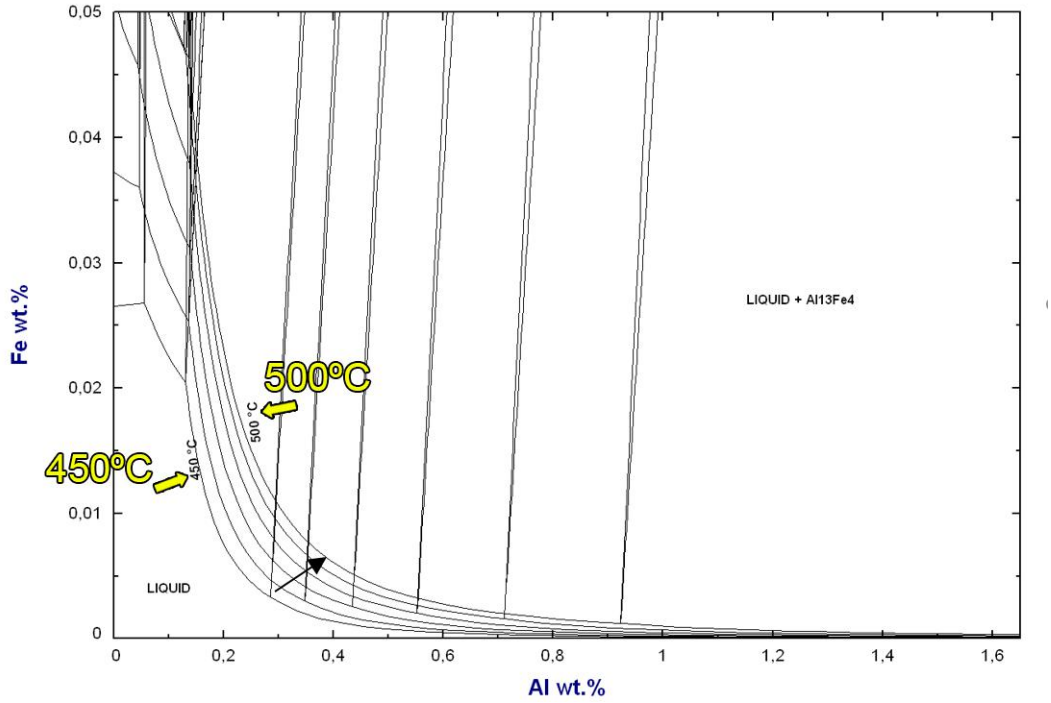

Figure 2-9: The Fe-Al phase diagram without the addition of 1,5 wt% Mg is displayed for different temperatures. This figure does not differ from Figure 2-8, therefore it can be concluded Mg has little influence on the solubility lines of the phase diagram [27].

ultrafine particles are known as dross or intermetallic dross particles [28, 29].

Dross is formed in the Zn-bath as a by-product of the galvanization process when the total Al in the bath is higher than the effective Al in the bath (supersaturation).
Dross formation is unavoidable due to the addition of Al, the dissolution of Fe from the steel strip and temperature non-uniformity [3, 10, 28]. As stated in Section 2-1-1, Al is added to the Zn-bath to guarantee an adequate coating adherence. Furthermore there is a constant input of Fe during the galvanizing process by the dissolution of Fe.

Dross in the Zn-bath can be categorised as oxides (ZnO and/or AlO) and intermetallic compounds (Zn-Fe and Fe-Al). The latter forms in the Zn-bath when Fe and Al are present in the liquid Zn with concentration above their solubility limit, as explained in Section 2-1-1 [19, 28]. In Figure 2-10 the different types of dross are shown. As can be seen that the oxides float mainly at the bath surface in the wiping area as a result of the air knives.

Because of the excess of Fe the intermetallic compounds can form in the Zn-bath. These intermetallic compounds can precipitate as two possible phases. One phase takes the form of an Fe-Al. Being less dense than the liquid Zn, this dross phase came together to the surface of the bath [29, 30, 31]. This phase is known as top dross. The other phase takes the form of an Fe-Zn which settles to the bottom of the Zn-bath, known as bottom dross [19]. The elements that have bonded in the phases above are no longer available for the galvanizing process [19].

If there is Al present in the Zn-bath the formation of the Fe-Zn (bottom dross) is inhibited. If the Al-content in the bath is higher than 0,135 wt% the formation of Fe-Zn compounds is

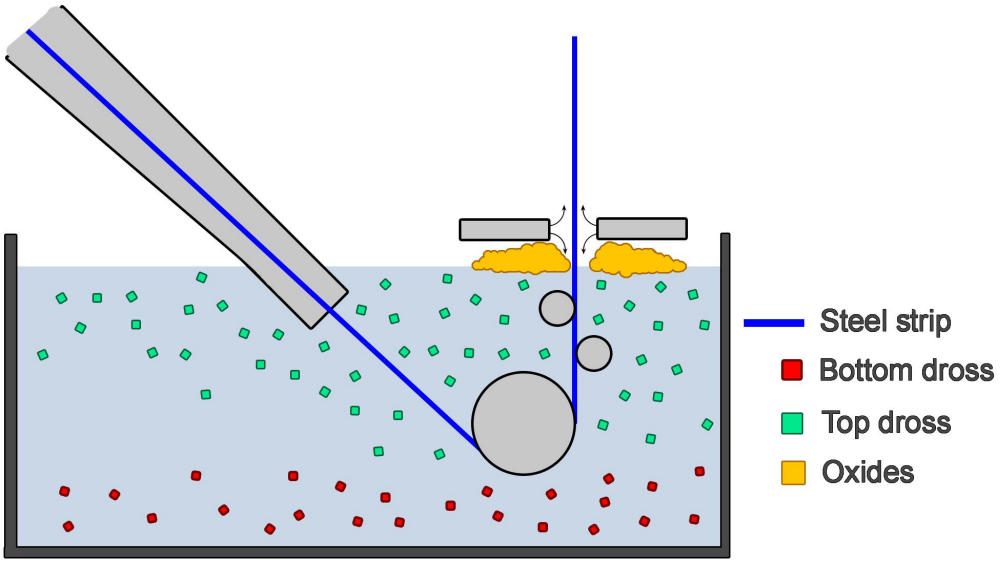

Figure 2-10: The cross section of a hot-dip Zn-bath with the different dross types with their locations they exist in the bath: Bottom dross (red), top dross (green) and oxides (yellow) [30].

completely inhibited [29]. The different types can be indicated in the solubility curve, as shown in Figure 2-3. In the hot-dip galvanizing lines at Tata Steel IJmuiden the Al concentration is greater than 0,20 wt% and therefore only top dross is found in the Zn-baths.

Top dross can be defined as crystallites of intermetallic compounds generated in the liquid Zn-Al alloy through the following chemical reaction [32, 33]:

$$2Fe + 5Al + xZn = Fe_2Al_5Zn_x \tag{2-3}$$

These dross particles have the same flow behaviour as loose particles and liquid Zn. The average size of dross particles floating in the bath is between 10-30 µm [28]. A single Fe_2Al_5-particle has no effect on the Zn coating (e.g. surface defects) and does not cause any hardware failure [9, 32].

The temperature of the bath needs to be considered as an indirect control variable. With increasing the bath temperature, the dissolution of Fe from the strip increases. More Fe dissolution leads to more dross generation in the Zn bath [10][34]. Biele [19] stated that with a rise of 30°C in bath temperature there is a three-fold increase of Fe solubility and thus in Fe-content.

Dross Build-up Formation in GI

In the DVL 2 in IJmuiden all three rolls in the Zn bath are made of 316L stainless steels. This type of stainless steel is generally used as roll material, because of their corrosion resistance against the liquid Zn. Because of the addition of molybdenum (Mo) in the composition 316L SS is the most suitable stainless steel available for this process. However, the material is not fully protected against the liquid Zn. A reaction with the liquid Zn and degradation will still occur. This reaction with the Zn-alloy is known as the dross build-up[33, 34].
This dross build-up effect can cause improper functioning of the hardware, or degrade the

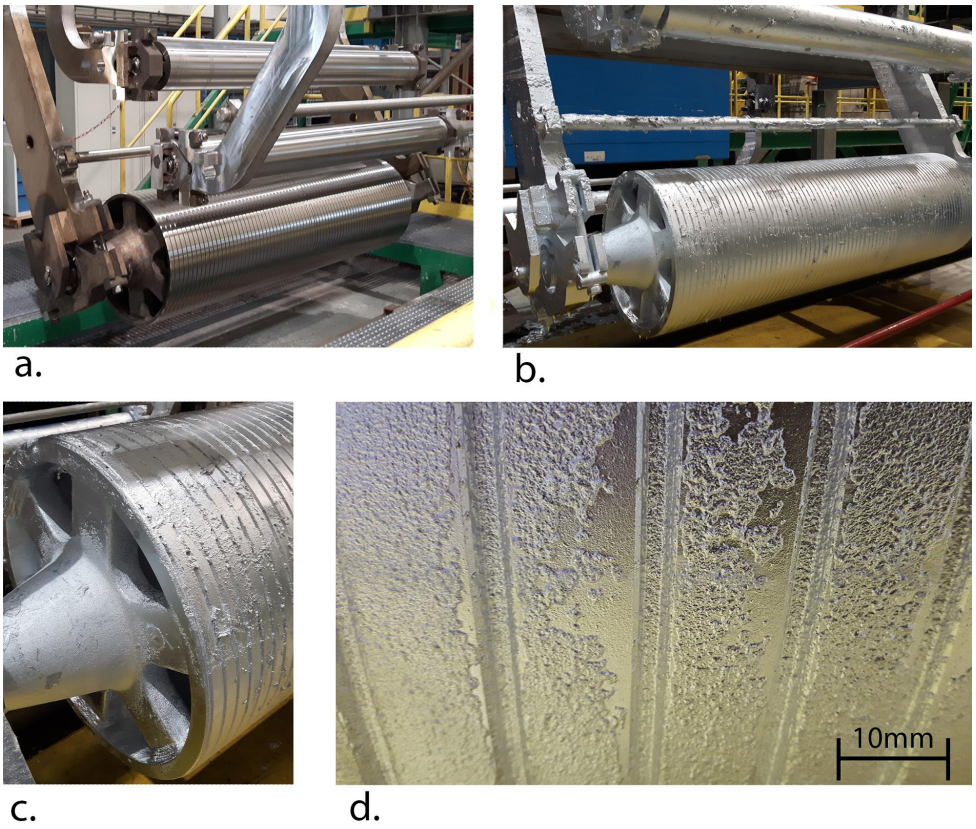

Figure 2-11: In a.) clean bath hardware is shown, b.) shows the bath hardware covered with dross build-up structure that is formed in 4,5 weeks. c.) and d.) show a magnification of the dross build-up on the rolls.

surface quality of the galvanized steel strip because of the very high hardness of the dross particles [33, 34].

Figure 2-11 shows the dross build-up structure that is created on the hardware that was in service for 4,5 weeks. A completely solid layer of dross build-up is visible at the roll surface. Whereas dross particles in the liquid Zn cannot be distinguished, the solidified dross build-up is visible with the naked eye.
The microstructure of the dross build-up structure consists of two layers: 1.) an Al-rich diffusion layer with the roll surface and 2.) a layer of intermetallic dross particles. These layers are shown in Figure 2-12.

Two factors contribute to the dross build-up on the hardware in the Zn bath, namely 1.) growth of a diffusion layer formed in the roll surface of the hardware, and 2.) Collision of the floating dross particles and growth of these particles[33, 34].

The formation of the diffusion layer in the hardware surface is similar to that of the coating formation on the steel strip as explained in section 2-1-1. However, the steel strip goes through the bath within a few seconds, whereas the average service lifetime of the hardware components submerged in GI is three to four weeks in DVL 2 at Tata Steel IJmuiden [4].

A schematic representation of the dross build-up formation is illustrated in Figure 2-13. As

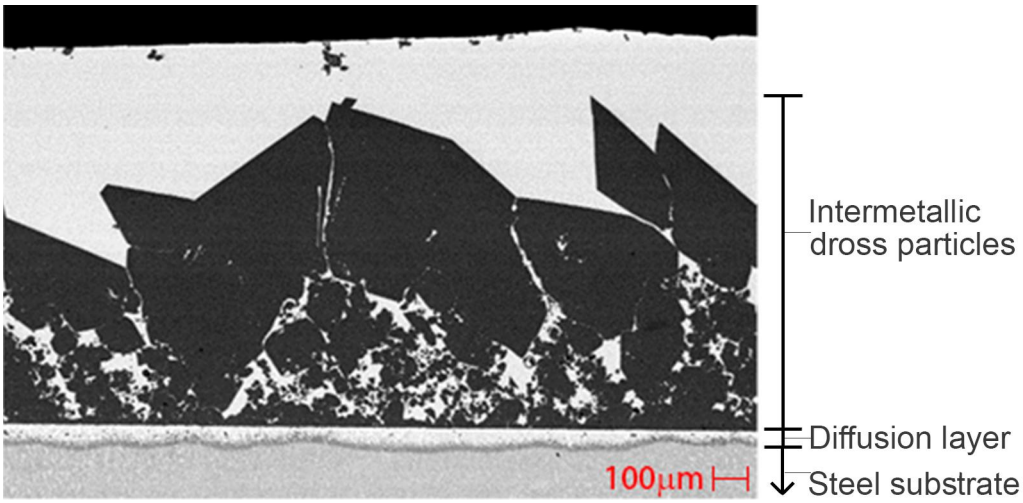

Figure 2-12: A typical dross build-up structure is shown. The intermetallic dross particles and the diffusion layer are indicated.

soon as the steel hardware is in contact with the liquid Zn-alloy, the diffusion layer starts growing into the steel hardware. The diffusion layer forms in two stages. First, the Zn bath needs to approach a metastable equilibrium with the roll surface because of the supersaturation of Fe in the vicinity of the substrate, since there is also some Fe dissolution from the steel hardware. Once this equilibrium is approached, Al diffuses into the steel where Fe-Al compounds nucleates as small equiaxed crystals, followed by lateral growth of the diffusion layer at the steel/Zn interface. This layer is enriched with Al which diffuses into this layer. Al reacts with Fe from the hardware, forming a Fe_2Al_5-phase. [31, 33, 34, 35]. The diffusion layer is a compact layer, consisting of small closed packed crystals of Fe_2Al_5-phase, that have a diameter of hundreds of nanometres [33, 36, 37].

The addition of Al in the Zn bath for a better adhesion of the coating helps to protect the rolls against Zn attack by the formation of a diffusion layer of Fe_2Al_5 on the roll surface [10]. However, this diffusion layer serves as a precursor to the dross build-up. The intermetallic dross particles are always built on top of a diffusion layer, rather than originating directly from a reaction with the roll surface. The formation of this diffusion layer provided a thermodynamically favourable base for the attachment and further build-up of suspended dross particles on the sample surfaces [9, 34].
When the diffusion layer is formed at the roll surface, the intermetallic dross particles deposit on this diffusion layer. When the intermetallic dross particles are deposited on the formed diffusion layer, they isolate from each other by the surrounding liquid Zn. With time the intermetallic dross particles grow by the supply of Al from the bath and Fe from the bath and substrate.
As the particles grow, they build-up on each other. A semi solid dross build-up layer is formed. By contact with the steel strip or by flow in the bath some dross particles occasionally break off and possibly adhere to the steel strip surface. The layer of intermetallic dross particles is a coarser, less compact layer compared to the diffusion layer, consisting of intermetallic dross particles. The crystals of the particles in this layer are in the order of tens of micrometres in diameter. Correspondingly the dross build-up structure can become more compact, depending on the local equilibrium conditions.

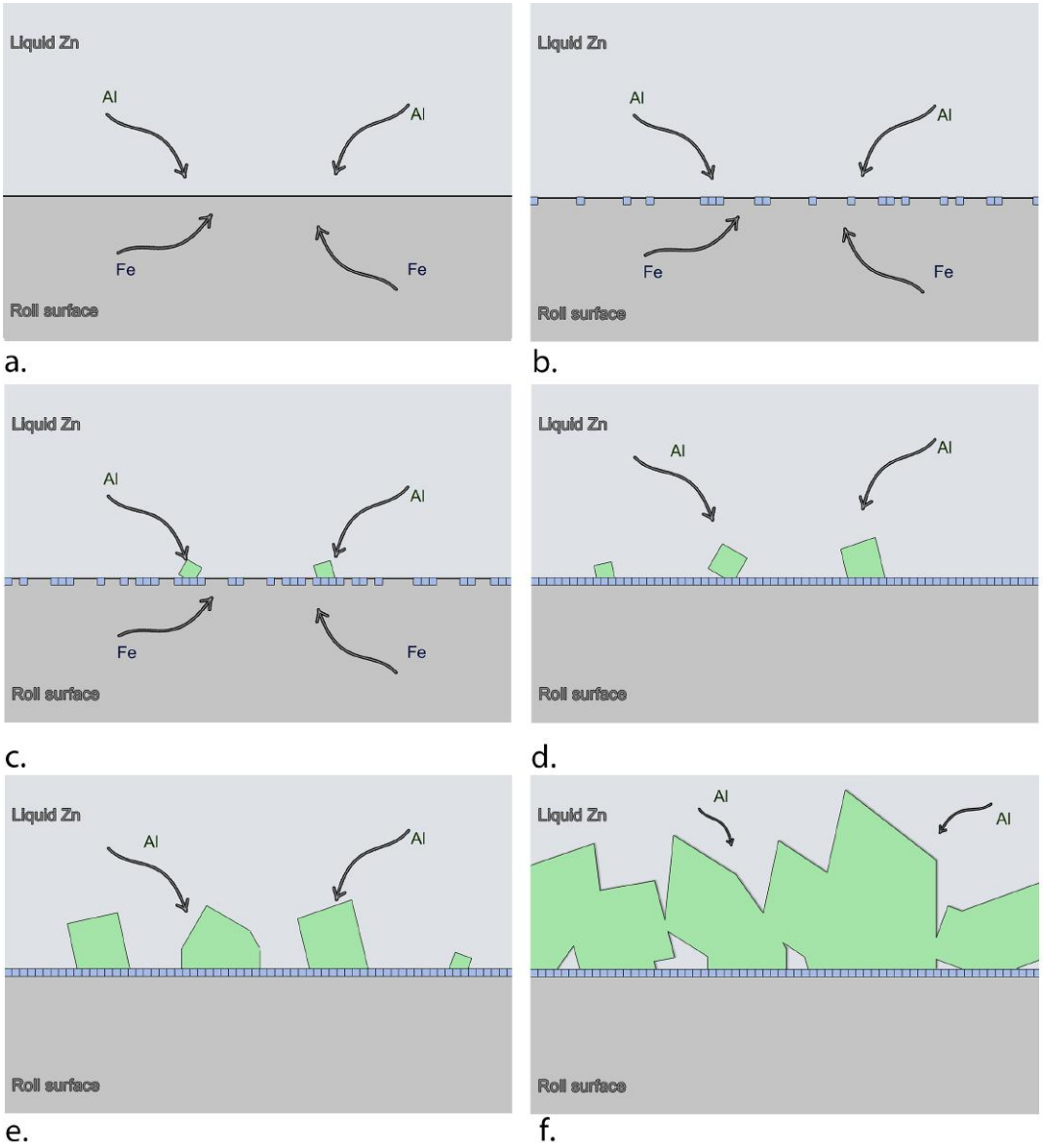

Figure 2-13: A schematic representation of the dross build-up formation is displayed [33]. As soon the hardware is submerged, Al is reacting with Fe from the steel substrate, forming the diffusion layer (as seen a.) and b.)). On top of the diffusion layer intermetallic dross particles are deposited (c.)). With time these intermetallic dross particles grow by the supply of Al and some Fe from the bath.

The formation of the diffusion layer reaching the metastable equilibrium and nucleation of compounds takes less than a second [36]. Including the lateral growth of this diffusion layer to fully cover the surface, the whole diffusion layer formation takes a few seconds. The deposition and growth of the intermetallic dross particles will continue in the remaining immersion time. Furthermore, there is an overlap between the two steps. The intermetallic dross particles do already form once there is a small layer of the diffusion layer formed.

After the substrate is fully covered by the diffusion layer, the system is limited in Fe since the dissolution of Fe from the hardware has almost stopped. Though there is still some transport of Fe from the roll surface through the diffusion layer, nevertheless this is a very small amount compared to the Fe dissolution from the strip. This Fe from the roll surface will react with the Al originating from the bath that is diffused in the intermetallic dross particles towards the diffusion layer/liquid Zn interface to react with Fe. This phenomenon indicates that the layer continues to grow during submersion [33, 36, 38].

The Al uptake in the build-up structure increases by increasing the immersion time via diffusion controlled growth of the layer. With this uptake of Al the morphology of the intermetallic dross particles changes from a fine, compact crystalline layer to a coarser, non-compact crystalline layer. This change in morphology occurs only in the intermetallic dross particle layer. By increasing the Al content in the bath, the Al-uptake of the build-up layer increases [33, 38].

2-2 Cleaning Behaviour

When submerged in MZ the structure formed in GI (displayed in Figure 2-12) is changed to a curved structure, shown in Figure 2-14. Several factors are involved in the cleaning behaviour of the dross build-up structure when submerged in MZ.

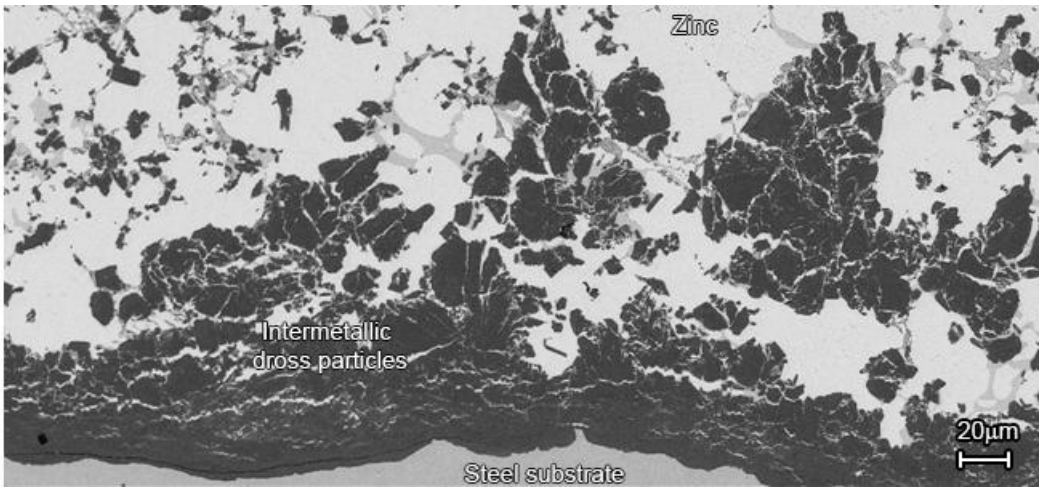

Figure 2-14: The dross build-up structure is shown that is submerged first in GI followed by MZ. Compared to the intermetallic dross particles in Figure 2-13 in this figure the intermetallic dross particles have a curved structure and are split up in smaller dross particles. Furthermore the structure is not compact anymore. The intermetallic dross particles are somewhat pushed to the Zn-bath.

2-2-1 Faceted Interface of GI and Non-Faceted Interface in MZ

The dross build-up structure formed in GI is shown in Figure 2-12. In this Figure it can be seen that the intermetallic dross particles have an average size of 40 µm. Furthermore the interface with the solidified Zn is very flat. This flat interface is an atomically flat close-packed interface with a narrow transition zone (1 atom layer thickness) and commonly known as a faceted interface [39].
A faceted interface is very stable. The stability of an interface is described by the surface energy, is also known as the interfacial energy (γ), which is a fundamental property for the conditions of the interface [40].

Introduced by Gibbs, the surface energy and the surface stress (σ), are the two essential macroscopic parameters that characterise the thermodynamic properties of crystalline surfaces [41]. When the solid $Fe_2Al_5Zn_x$-phase and liquid Zn are in equilibrium, the high enthalpy of the Zn is balanced by a high entropy so that both phases have the same free energy [39, 40]. If this balance is disturbed, this disturbance gives rise to an excess free energy, known as the interface energy or surface energy (γ) [39, 40]. The surface energy can be defined as the excess energy at the surface of a material compared to the bulk.

When the hardware with dross build-up structure is submerged in MZ-bath the faceted interfaces become roughened. A non-faceted, curved interface appears.
When the solid $Fe_2Al_5Zn_x$-phase (intermetallic dross particles) and liquid GI Zn-phase are in equilibrium, the high enthalpy of the liquid Zn is balanced by a high entropy so that both phases have the same free energy [39]. Subsequently, between the interfaces there is a low surface tension.
When submerged in MZ this balance is disturbed, thereby giving rise to the surface tension. This increase in surface tension results in a curved interface. The disturbance in balance is the results of the free energy between the liquid MZ-phase and the intermetallic dross particles.

When the $Fe_2Al_5Zn_x$-phase dissolves in the liquid MZ-phase, ΔH is negative and ΔS is positive, resulting in a large negative Gibbs free energy. The negative value for the Gibbs free energy gives a higher solubility [39].
As can be read in Section 2-1-1 the solubility is the maximum quantity of solute that can dissolve in a certain quantity of solvent or quantity of solution at a specified temperature. Thus, a higher solubility raises the maximum quantity of the intermetallic dross particles ($Fe_2Al_5Zn_x$-phase) that is able to dissolve in the liquid MZ.

2-2-2 Thermal Stresses

At changing the baths the samples are air cooled. Subsequently the liquid Zn solidifies and a solid dross build-up structure is formed. At solidification strains are generated by this temperature change because of the difference in thermal expansion coefficients between the stainless steel and the dross build-up structure which causes thermal expansion mismatch. This mismatch generates strains. If the strain is large enough a greater mismatch is formed and cracking will occur.
Thermal stress arise from the thermal expansion mismatch between two materials (the dross build-up structure and roll surface) [18]. The thermal stress results from a temperature change

during cooling when changing baths:

$$\sigma = \frac{E}{1-\upsilon}(\alpha_1 - \alpha_2)\Delta T \tag{2-4}$$

where σ the stress in the intermetallic dross particle-layer, E the Young's modulus, υ the Poisson's ratio, α the thermal expansion coefficient and ΔT the change in temperature.

2-2-3 Grain Boundary Decohesion

Segregation plays an important role in the changes of the behaviour of the intermetallic dross particles when submerged in MZ.
The intergranular decohesion of the intermetallic dross particles in MZ is caused by liquid Zn diffusing along the grain boundaries into the intermetallic dross particles. By diffusing into the grain boundaries the liquid Zn reduces the cohesion of the grain boundaries. This reduction in cohesion eventually leads to the destruction of the intermetallic dross particles [42].

Grain Boundaries

Grain boundaries are one of the most important factor for determining the properties of an alloy, governing properties such as tensile strength, conductivity, fracture toughness and fatigue resistance. With these properties, the grain boundaries can weaken or strengthen the metallic alloy[43].
A grain boundary is the interface between two grains of the same phase which differ in crystallographic orientations. The grain boundary itself has a different composition than the bulk grains, because the enrichment of impurity atoms in the grain boundary [44, 45, 46].
A grain boundary is crystallographic defined by five degrees of freedom (DOFs). Three independent parameters are required to describe the misorientation between grains, the other two independent parameters describe the orientation of the grain boundary plane [43, 47].

Grain boundaries provide high diffusivity paths in the intermetallic dross particles, because the mobility of atoms along such defects is usually much higher than in the lattice [42, 48]

Intergranular Diffusion of Zn

Intergranular diffusion of Zn is a complex process involving several processes such as direct volume diffusion of Zn from the liquid Zn, diffusion of Zn along the grain boundaries, partial leakage of Zn from the grain boundaries to the intermetallic dross particles and the subsequent volume diffusion around the grain boundaries. Depending on the relative importance of these processes different diffusion regimes can occur. In each particular regime one or two processes control the overall diffusion rate, whereas other processes become not important. Each regime dominates in a combination of a certain temperature range, time, grain size and other relevant parameters [18, 42].

Intergranular diffusion of Zn is the movement of Zn atoms along the grain boundaries activated by a driving force. This driving force is mainly the difference in chemical potentials between

Zn and the intermetallic dross particles. Furthermore, the orientation of the grain boundaries plays a role in the intergranular diffusion rate of Zn. A minimum of intergranular diffusion is shown close to $\theta = 37$ °, where θ is the angle that the Zn-phase makes in the Fe_2Al_5-Fe_2Al_5 grain boundary, also known as the contact angle [39, 42, 43].

Intergranular diffusion of Zn is related to the ability of the liquid Zn to wet the solid intermetallic dross particles.
The term wetting is defined as: *The phenomenon involving a solid and a liquid in such intimate contact that the adhesive force between the two phases is greater than the cohesive force within the liquid* [49]. The penetration of Zn in the grain boundaries of the intermetallic dross particles may be thought of a special case of wetting. The liquid Zn results in an incoherent boundary between two phases.

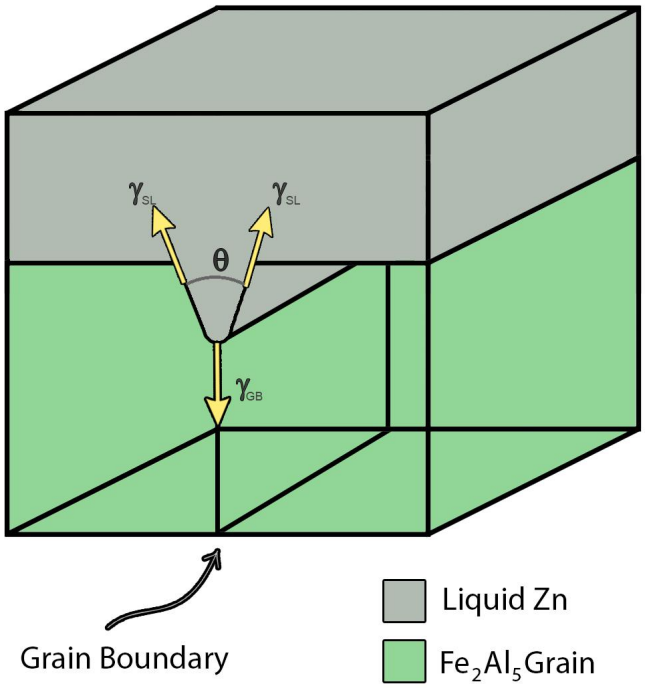

Figure 2-15: A schematic representation of grain boundary wetting, with the energies involved. The grey phase is the liquid Zn, the green phases are the Fe_2Al_5-grains [50].

The surface energies play an important role at wetting. Figure 2-15 displays schematically the structure that is formed in the case where the liquid Zn is located at the junction of three Fe_2Al_5-grains [51].

Since the temperature of the Zn-bath is above the melting point of Zn, the Zn-phase adjusted to the shape between the two Fe_2Al_5-grains, in order to minimize the surface energies in the system. The angle that the Zn-phase makes in the Fe_2Al_5-Fe_2Al_5 grain boundary is the contact angle, denoted with θ [42, 50].
Because at the wetting process only two different phases coexist, the contact angle θ depends only on the two different surface energies: the grain boundary energy (γ_{GB}) and the solid/liquid interphase energy (γ_{SL}). The force balance in the grain boundary with the presence of

the Zn-phase can be written as:[39, 42, 43, 50].

$$\gamma_{GB} = \gamma_{SL} * cos(\frac{\theta}{2}) \tag{2-5}$$

The lower the contact angle θ, the higher the chance wetting occurs. If $2\gamma_{\mathrm{SL}}<\gamma_{\mathrm{GB}}$ the contact angle becomes 0° and complete wetting of Zn of the grain boundaries of the intermetallic dross particles occurs [43, 50]. The grain boundaries are then fully accessible for the liquid Zn to diffuse into.

Chapter 3

The effect of transition from GI to MZ on dross build-up

As preliminary analysis, the build-up on a stainless steel block with dimensions 60x35x25 mm that was attached on the arm of a roll from the Zn-bath was studied.
The block was immersed in the galvanizing line for a total of 33,5 days in the GI and MZ bath (32 days in GI and 1,5 days in MZ). From this block some images were taken of the build-up structure with the optical and scanning electron microscope. Moreover, an element mapping is made of the build-up structure. However, the resulting images were not analysed by researchers of Tata Steel IJmuiden before the start of this thesis project.

The study is presented in a paper, which is displayed in this chapter, starting in Section 3. This paper was published internally at Tata Steel.
The results of this publication [52] launched a pilot trial aimed at reducing the dross build-up structure on the bath hardware. A set of new hardware was placed in the production line and has been maintained only in MZ-bath. At the time of writing this thesis project the results and conclusions of this pilot are not yet known.

The study of this stainless steel block is important for this research project, since it is submerged in GI as well in MZ. The morphology of the dross build-up structure that is immersed in both baths. Though the immersion times are different than in the experiments for this research project (explained in Chapter 4), this analysis gives a good insight what the dross build-up structure could look like during the sampling for this research project.

Paper: Effect of transition from GI to MZ on dross build-up

Summary

A small block made of stainless steel (316L), attached on the pot hardware, was submerged in the zinc bath for a period of 34 days. In this time period there has been a transition in

baths from GI to MZ. The build-up created in GI seems to diminish when the hardware is switched to MZ. In the build-up structure found on the block delamination of Fe_2Al_5 particles is seen on all sides. Though, between the build-ups on the side surfaces and the top surface a difference can be seen in structure. The top surface has a larger thickness than the side surfaces. Furthermore the average size of Fe_2Al_5 particles in top surface is larger than that of the Fe_2Al_5 particles in de side surfaces.

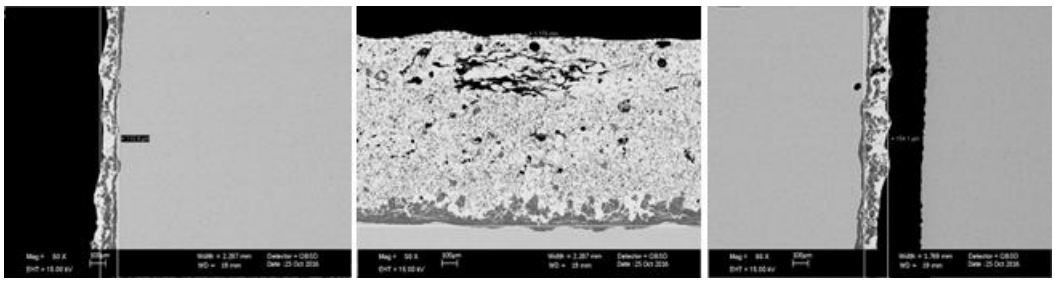

Figure 3-1: Thickness of the build-up on the block a.) Left surface, b.) Top surface, c.) Right surface

Introduction

A block attached on the sink roll arm was submerged in the GI bath as well in a MZ bath of the DVL3. The goal of this analysis is to give more insight on the effect of a transition in baths on the dross build-up on the pot hardware. This report shows the structure and phases detected in the build-up, and what the conditions were in the zinc baths. The result of the build-up on the block is shown in Figure 3-1.

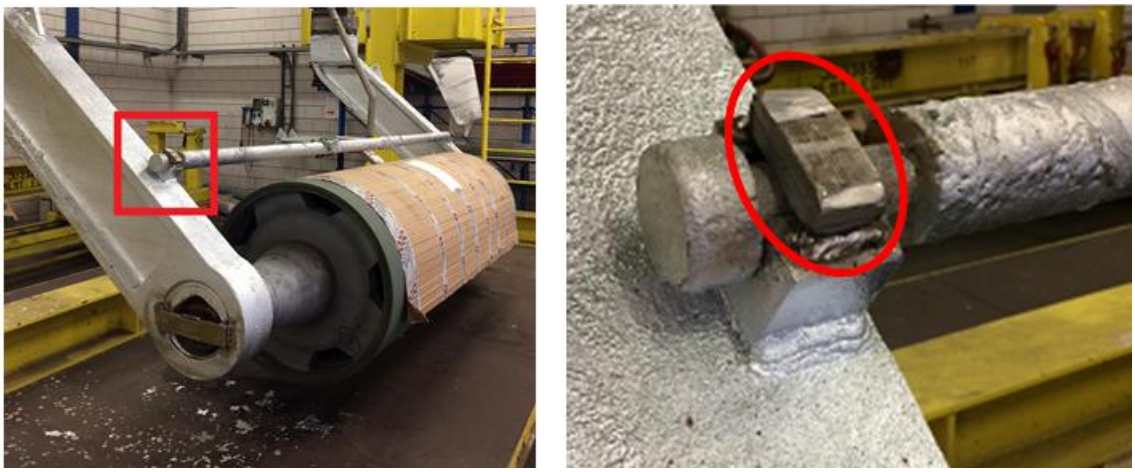

Figure 3-2: Location of the block on the sink roll arm

Sample

The sample submerged in the zinc bath is a small block made of 316L stainless steel with dimensions 60x35x25mm. Main function of this block was to connect the rod with the sink

roll arms (see Figure 3-2). The block was submerged in the zinc bath from 27 august 2016 (1:20h) until 28 September 2016 (20:44h). In this period it was submerged in GI for 32 days and the block was submerged for 1,5 day in MZ.

Process Data

At 27 august 1:20h a campaign with GI started and continued until 27 sept 7:36h. A total of 32 days and 6 hours. In this time period, the temperature was stable. There were two types of periods in temperature in the GI: FF (full finish) and GP (general production). The temperature in FF has an average of 459,6°C, with a range of 4,5°C (maximum is 461,5°C, minimum is 457°C). The average temperature for GP is 454,6°C, with a range of 7,6C (maximum is 457,5°C, minimum is 449,9°C) (see Figure 3-3).

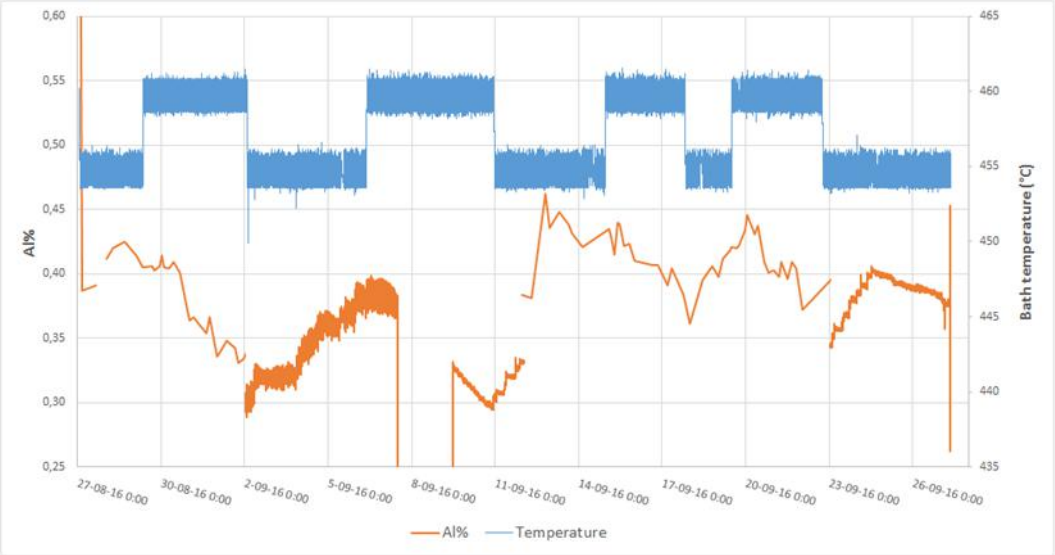

Figure 3-3: Pot composition (Al%) and temperature during DVL3 hardware campaign. The two temperature periods FF and GP can be seen. Al% is decreasing in FF and increasing in GP

The Al% during this GI-campaign is shown in Figure 3-3. In this figure it can be seen that the Al% increases in the GP-period, and decreases in the FF period. The Al% varies between 0,462% and 0,288%.

During the GI-campaign the process stopped 18 times, most of them less than 2 hours. Only two times were longer than 12 hours, respectively 17,5 hours (14sep 3:49h) and 13 hours (15sep 22:36h). However these line stops seem to have no effect on the Al% (Figure 3-4). The block was immersed in MZ from 27 sept 12:40h to 28 sept 20:44h. A total of 32h. Al% and Mg% were approximately 1,6% and 1,6%. Average temperature in the MZ-bath is 459,6°C with a range of 3,1°C (maximum is 461,4°C, minimum is 458,3°C).

Top surface: Phases and structure

The microstructure of the dross build-up on the top surface of the block can be seen in the Figure 3-5 and Figure 3-6. The total thickness of the build-up is about 1,17mm. In this

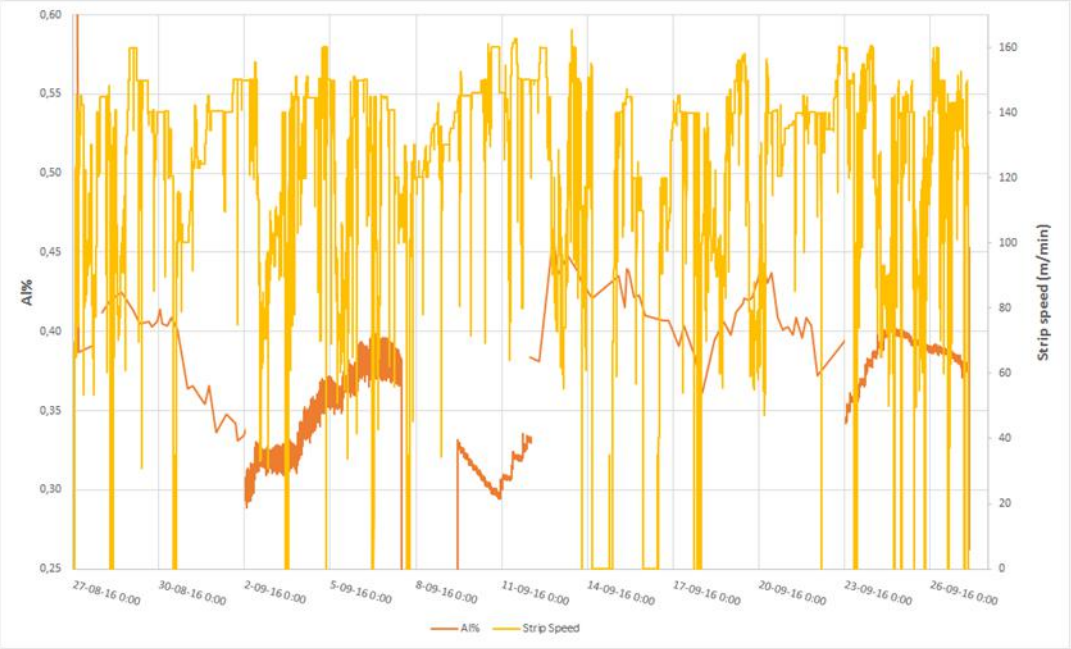

Figure 3-4: DVL3 process speed during the hardware campaign. The process stopped several times, which seems to have no effect on the Al%

build-up several layers of different structures are visible. Phases found were Mg-Zn-phases, Mg-Zn-Al-phases, Fe-Al-Zn-phases and pure Zinc.

At the 316L steel substrate, a dense layer of Fe_2Al_5 particles is visible, surrounded by pure zinc. In these Fe_2Al_5 particles it appears that the beginning of delamination can be seen. This layer of Fe_2Al_5 is about 200 µm thick.

Above the dense Fe_2Al_5-layer a layer of pure zinc with a 150 µm thickness is visible. Within the zinc a low concentration of small Fe_2Al_5 particles are seen, evenly distributed through the pure zinc. Also some small $MgZn_2/Mg_2Zn_{11}$ particles are visible.

The thicker the layer gets, the more small Fe_2Al_5 particles and Mg-Zn-phases are present and less pure zinc. These Fe_2Al_5 particles are smaller than the layer of Fe_2Al_5 particles on the substrate metal. The Mg-Zn-phases are the binary $MgZn_2$ and a ternary Zn-Mg-Al structure The upper 300 µm contains large ribbon-shaped voids combined with large pure Zn-grains with smaller ZnAl-particles and $MgZn_2/Mg_2Zn_{11}$. At the upper surface a higher concentration of small Fe_2Al_5 particles are visible, surrounded by large Zn-grains and $MgZn_2/Mg_2Zn_{11}$. Also some small particles with a Zn-Al-Mg-phase are detected.

Mg is found until about 200 µm from the stainless steel substrate. Thus within the 32h of the MZ-campaign the Mg has penetrated through nearly the entire thickness of the build-up layer on the top surface. Between 200 µm and 450 µm (measured from the substrate) only binary $MgZn_2/Mg_2Zn_{11}$ are found, from 450 µm on also a ternary Zn-Mg-Al is found. Pure magnesium is not detected.

Overall the Zn-grains are large compared to other phases, only in the middle (550 µm-800 µm) the Zn-grains are of similar size as the other phases.

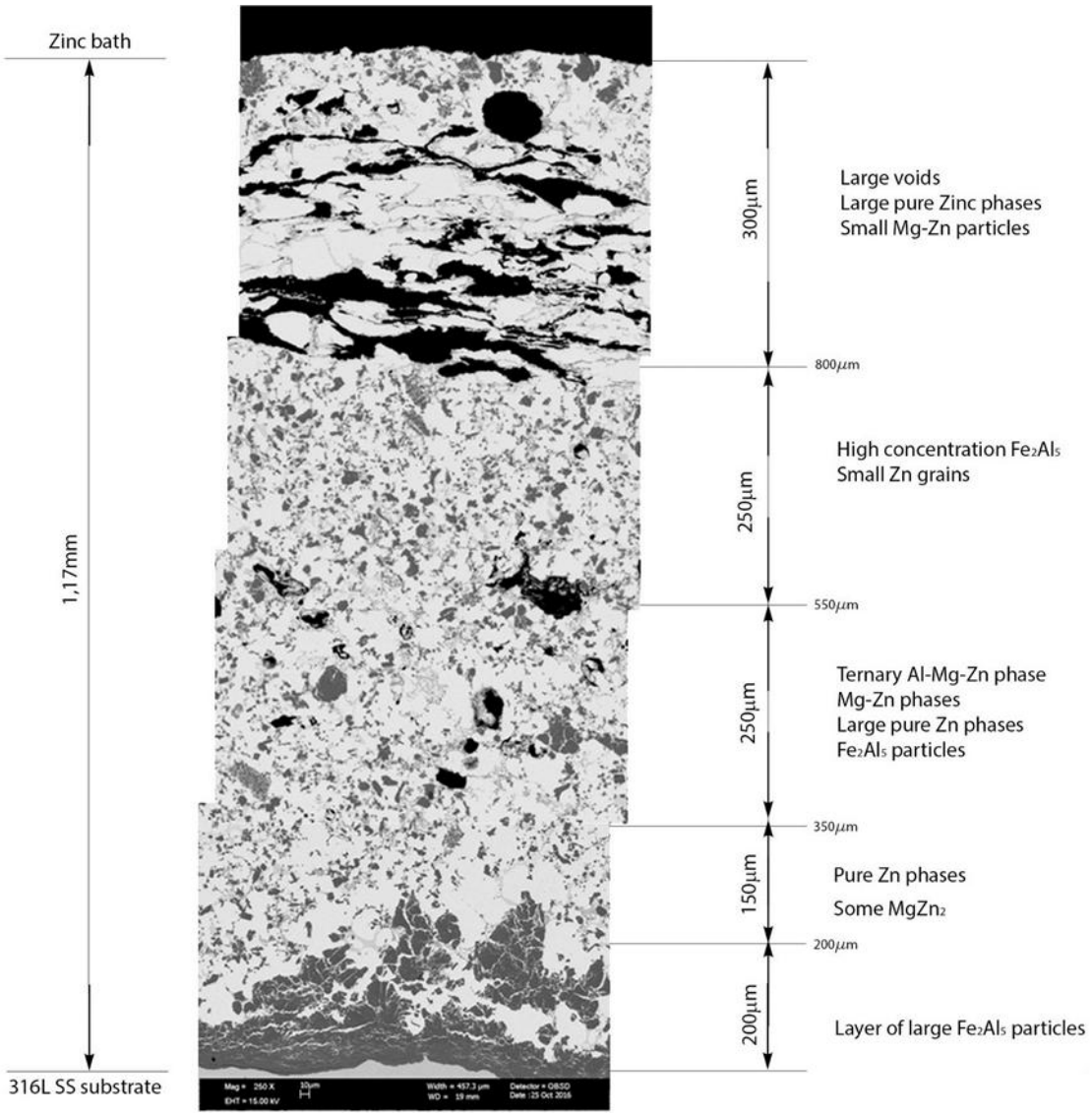

Figure 3-5: Cross section of build-up on top surface of the block. The various layers are explained

The first voids can be seen at around 400 µm from the substrate with some large voids at 550 µm from the substrate (see Figure 3-6). A high concentration of large voids start at about 800 µm over the whole length, surrounded by large Zn-grains.

Side surfaces: Phases and structure

Similarly for the side surfaces a dense layer of Fe_2Al_5 particles is visible on the 316L SS substrate, having a thickness of about 40 µm-80 µm. Large delamination of Fe_2Al_5 throughout the whole build-up layer can be seen (see Figure 3-7 and 3-8).

Between the large pure zinc grains and Fe_2Al_5 particles, compounds of small $MgZn_2$/ Mg_2Zn_{11} particles are seen. When the layer of Fe_2Al_5 particles stops, a typical MagiZinc structure between large Zn-grains is clearly visible in both side surfaces; small zinc-particles surrounded

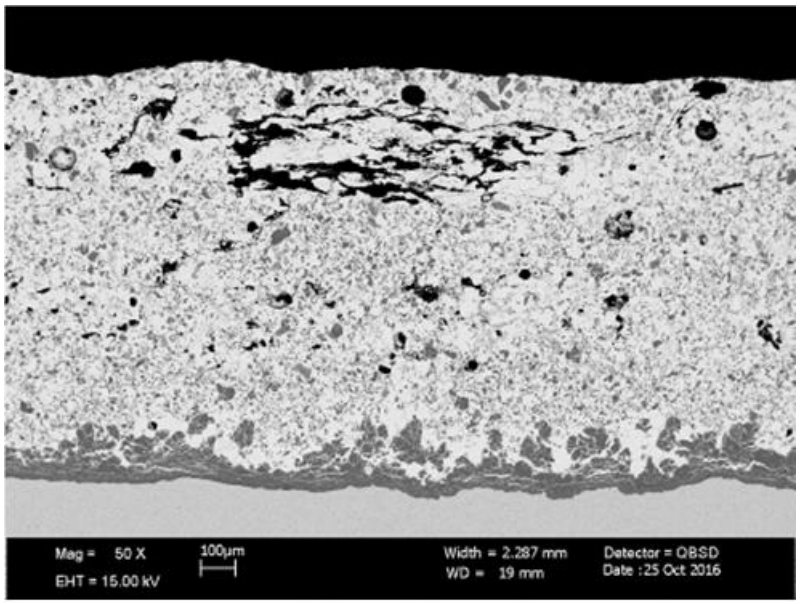

Figure 3-6: Cross section build-up top surface

by eutectic phases (a white zinc phase with grey stripes and/or dots containing Zn-Mg-Al) (see Figure 3-12).

Phases explained

An EDX-analysis was carried out in order to determine the different elements in the build-up. In all the surfaces the dark particles are indeed Fe_2Al_5, as can be seen in the EDX spectra (Figure 3-9.004, Figure 3-10.011 and Figure 3-11.033). The light grey area is a binary Mg-Zn-structure (EDX spectra Figure 3-9.005, Figure 3-10.012 and Figure 3-11.032). Probably this area is Mg_2Zn_{11}, derived from the height of the spectrum of Mg and from the phase diagram (see Figure 3-15). The particles shown in Figure 3-10.009 have a Zn-Al structure (magnification of the structure shown in Figure 3-14). In the SEM-image of Figure 3-10.013 a large light-grey area with very small dark particles is visible. From the EDX spectrum of Figure 3-10.013 can be seen that this area is a ternary Zn-Mg-Al structure. This structure is seen often from 550 µm away from the substrate to the top surface. Figure 3-9.006 and Figure 3-10.010 show also a ternary Zn-Mg-Al structure. In these EDX spectra can be seen that 3-9.006 has a higher Al% than Figure 3-10.010 and 3-10.013, 3-10.010 has a higher Al% than Figure 3-10.013. It seems that the closer at the upper surface measured, the more aluminium is in the ternary Zn-Mg-Al structure.

Differences top and sides

The top surface is thicker than the side surfaces: 1170 µm compared to 113.9 µm and 154.1 µm (Figure 3-1). The side surfaces have a higher concentration Fe_2Al_5 particles compared to the top surfaces. Yet the sizes of the Fe_2Al_5 particles are smaller in the sides than in the top surface. The largest particles in the top surface are about 30x40 µm, whereas in the largest

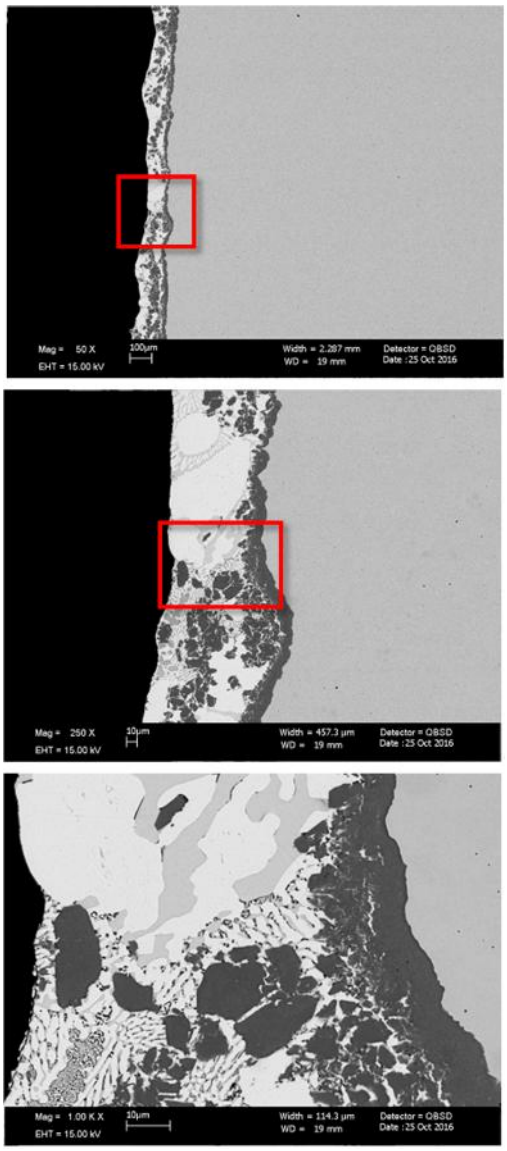

Figure 3-7: Cross section of build-up on left surface of the block. a.) 50x magnification, b.) 250x magnification, c.) 1.000x magnification

Fe_2Al_5 in the side surfaces are 15x20 µm. Also the dense Fe_2Al_5 layer on the stainless steel substrate is smaller on the sides than on the top surface: about 15 µm compared to 60 µm on the top surface. In the side surfaces the Fe_2Al_5 particles are distributed over the whole thickness with about the same size. In the top surface the bigger particles are concentrated near the substrate and some at the outer surface of the build-up layer.

No voids can be seen in the sides surfaces, only in the top surface. A possible explanation could be that the upper part of the build-up of the top is skimming, captured on the top of the sample when the rolls were taken out. If it is the case that extra build-up is because of skimming, it could be the reason why the top surface has a higher thickness than the side surfaces. A typical MagiZinc structure is clearly visible between the large Zn-grains in both side surfaces (Figure 3-12). At the top surface between the Zn this structure is not observable.

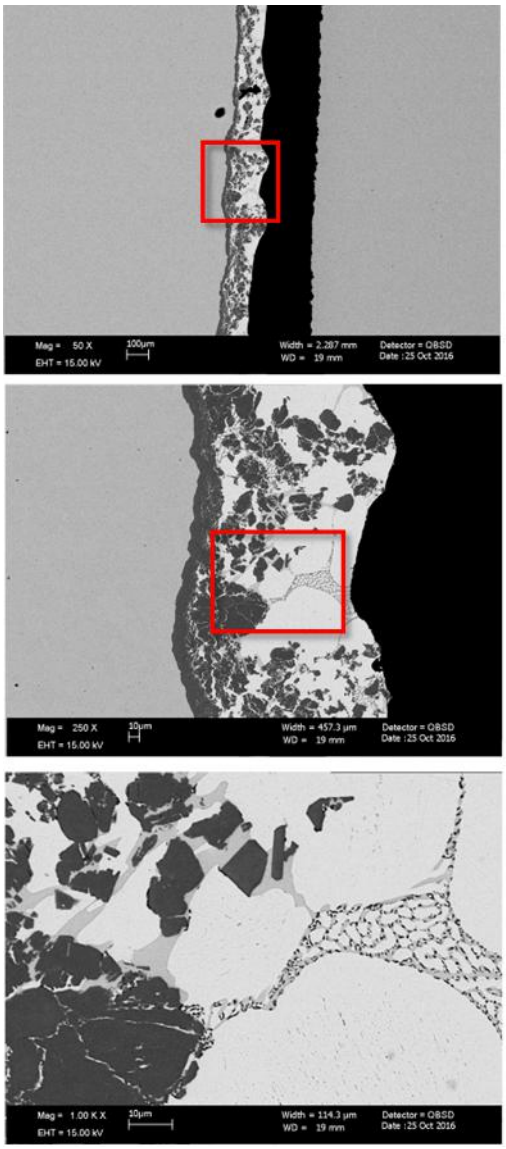

Figure 3-8: Cross section of build-up on right surface of the block a.) 50x magnification, b.) 250x magnification, c.) 1.000x magnification

In the top surface the Zn-elements are surrounded by binary $MgZn_2/Mg_2Zn_{11}$ and ternary Zn-Mg-Al (Figure 3-13).

Discussion

The hypothesis is that the delamination of the intermetallic particles on the substrate are the result of the transition from GI to MZ bath. This delamination is already shown in the build-up structure, visible in the outbursts of Fe_2Al_5 particles (shown in Figure 3-7 and 3-8). Remark is that the build-up structure of only the GI-campaign is unknown. From other SEM-analyses done at Tata Steel a typical build-up structure in only GI can be found. In such a typical structure the Fe_2Al_5 particles seem larger and more compact, hardly any delamination

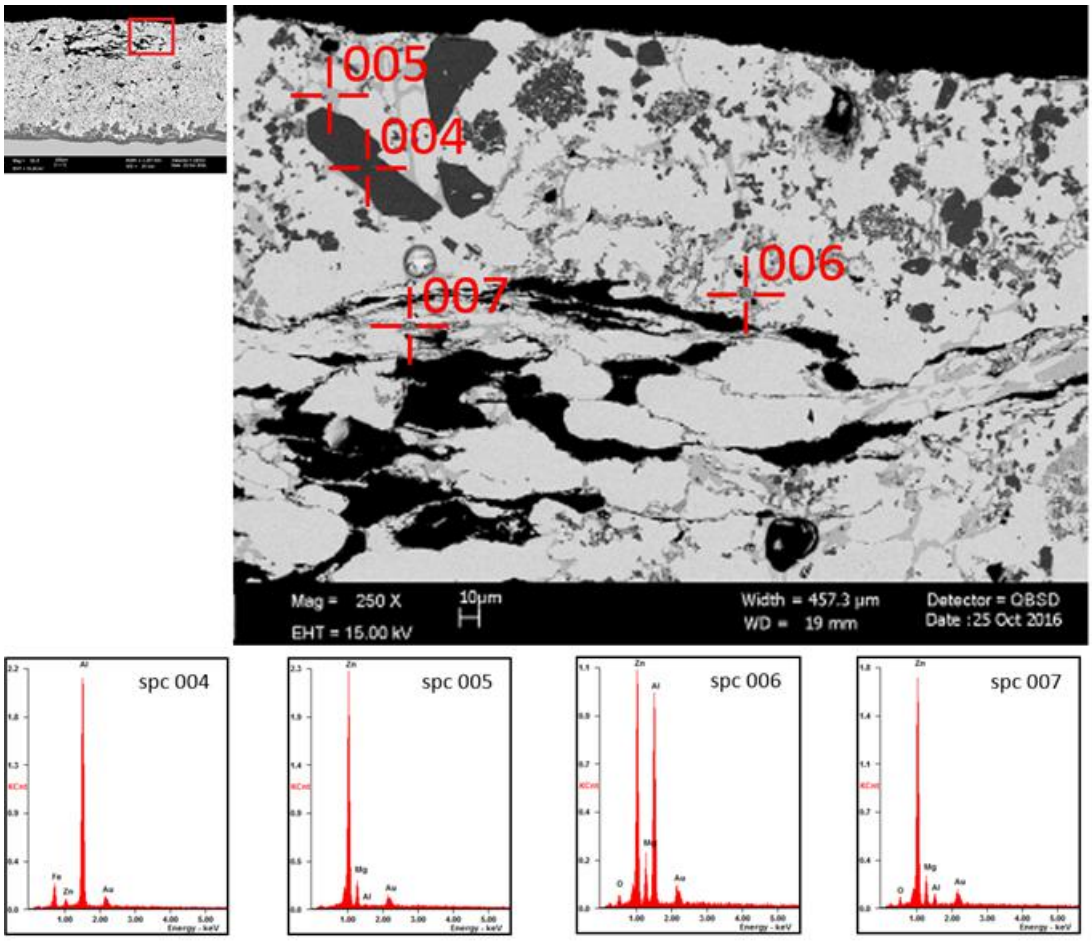

Figure 3-9: EDX analysis top surface (magnification of Figure 3-6)

of the Fe_2Al_5 particles is seen in GI build-up. In what manner or how quickly the build-up is diminishing in a MZ-campaign is unknown and needs to be studied in further research.

There are differences in dross build-up between the top surface and side surfaces. The top surface has a larger thickness than the side surfaces. This is mainly the result of skimming attached on the dross build-up on the substrate when transitioning baths. Furthermore the average size of Fe_2Al_5 particles in top surface is larger than that of the Fe_2Al_5 particles in de side surfaces. Another difference between surfaces is that in the side surfaces the Fe_2Al_5 particles are distributed over the whole thickness with about the same size. In the top surface the bigger particles are concentrated near the substrate and some at the outer surface of the build-up layer.

What the exact effect is of the magnesium and higher Al% is hard to say. The structure of the build-up right after the GI-bath is unknown, and therefore it is not possible to explain what the influence of the Al% is. An example that can be thought of is how and in what rate the Fe_2Al_5 particles are diminishing under the influence of the high Al% (1,6%) and Mg% (1,6%).

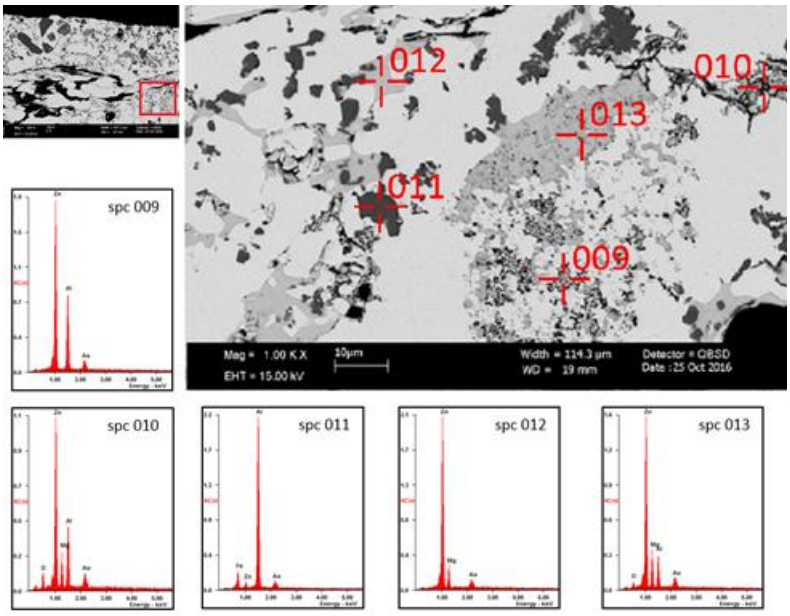

Figure 3-10: EDX analysis top surface (magnification of Figure 3-9)

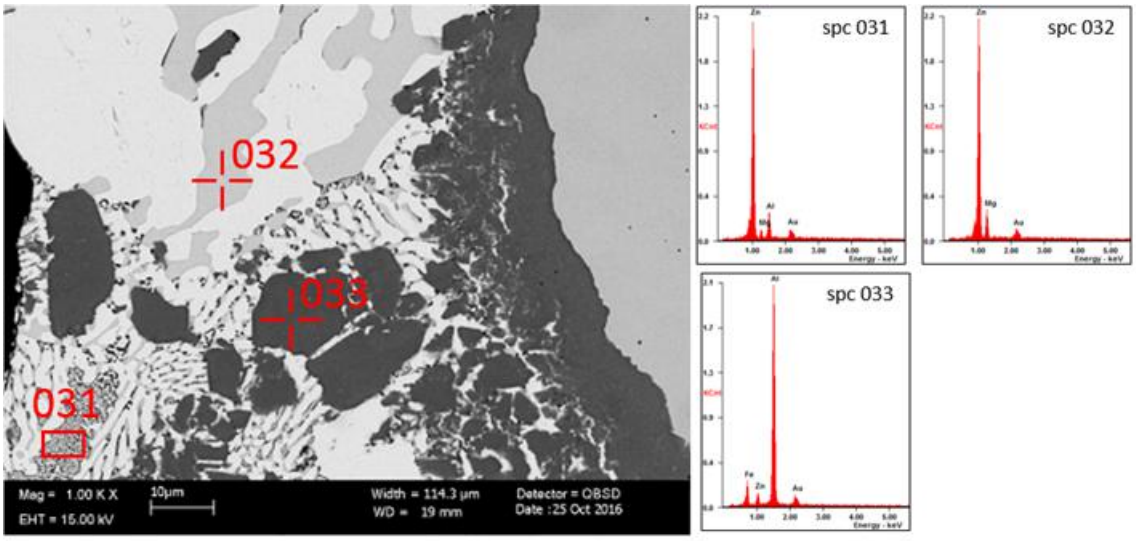

Figure 3-11: EDX analysis left side surface (same as Figure 3-7.c)

Future Testing

In the next phase of testing the dross build-up after each bath change will be investigated independently. Four samples (cylinder shaped, 316L SS) will hang partly submerged in the zinc bath of DVL2. The samples will be inserted at the start of the GI campaign. Before the bath is switched to the MZ-bath, one of the samples is taken out. This sample will have only dross build-up of GI. Before the bath is switched back to GI, another sample is taken out. It is expected that this second sample will have a similar dross build-up as the build-up on the block in this report. When the bath is switched for the third time (GI to MZ), the third

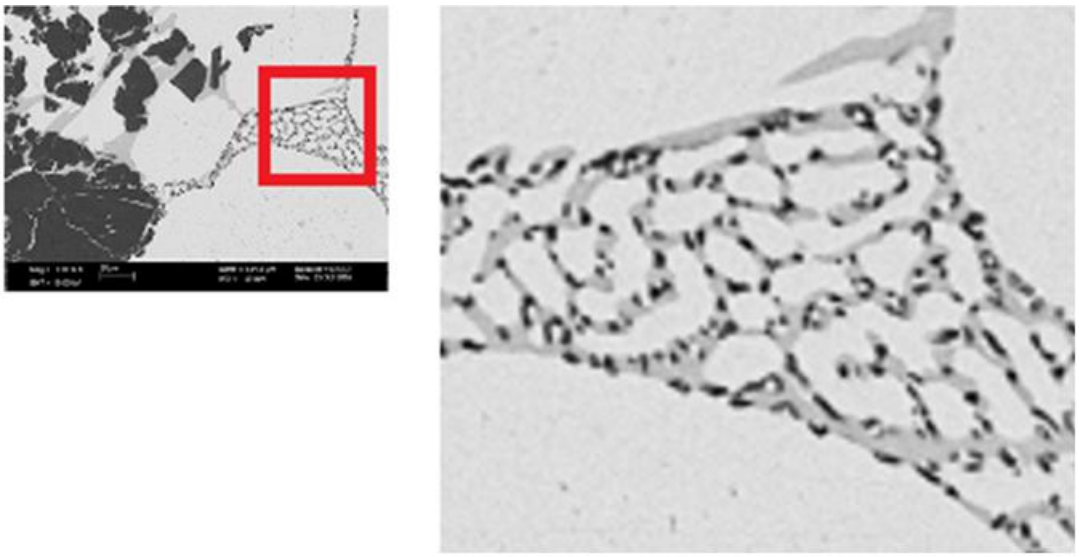

Figure 3-12: Typical MagiZinc structure in the right side surface (magnification of Figure 3-8.c)

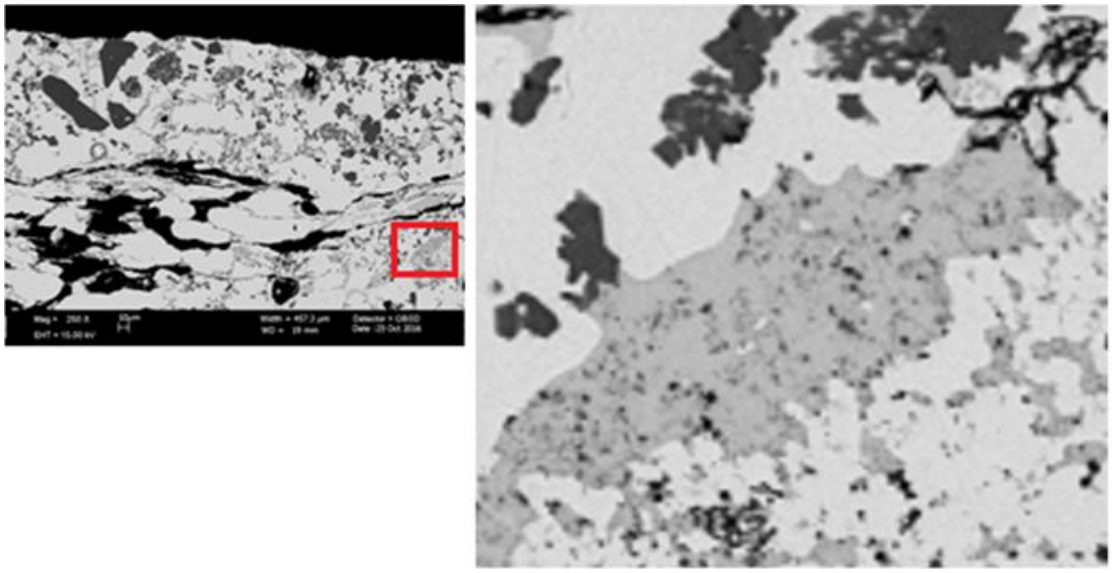

Figure 3-13: Ternary Zn-Mg-Al structure in the top surface (magnification of Figure 3-4)

sample is taken out. On this sample the dross build-up is visible when submerged twice in GI and one time in MZ. Also this sample could give more insight on what the influence will be of the high aluminium content and magnesium already in the dross build-up when switching baths. The last sample gives more insight on what sort of dross build-up is forming after four campaigns (1st: GI - 2nd: MZ - 3rd: GI - 4th: MZ). These samples should represent nearly the full hardware campaign for the rolls of DVL2.

The SEM-images of the samples together with the process- and composition data will give a possible explanation about the growth and diminishing of the build-up layer when there is a transition in baths.

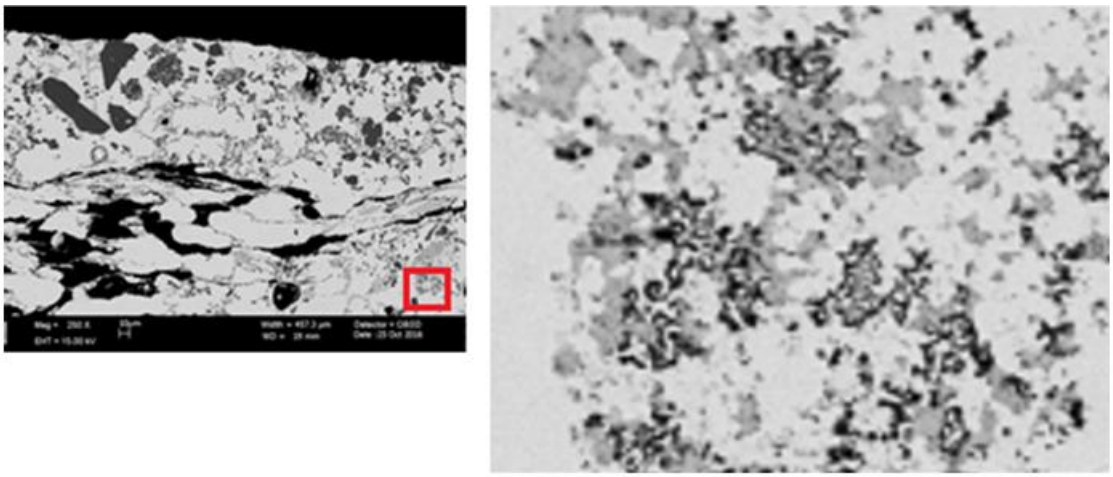

Figure 3-14: Zn-Al structure surrounded by Zn in top surface (magnification of Figure 3-4)

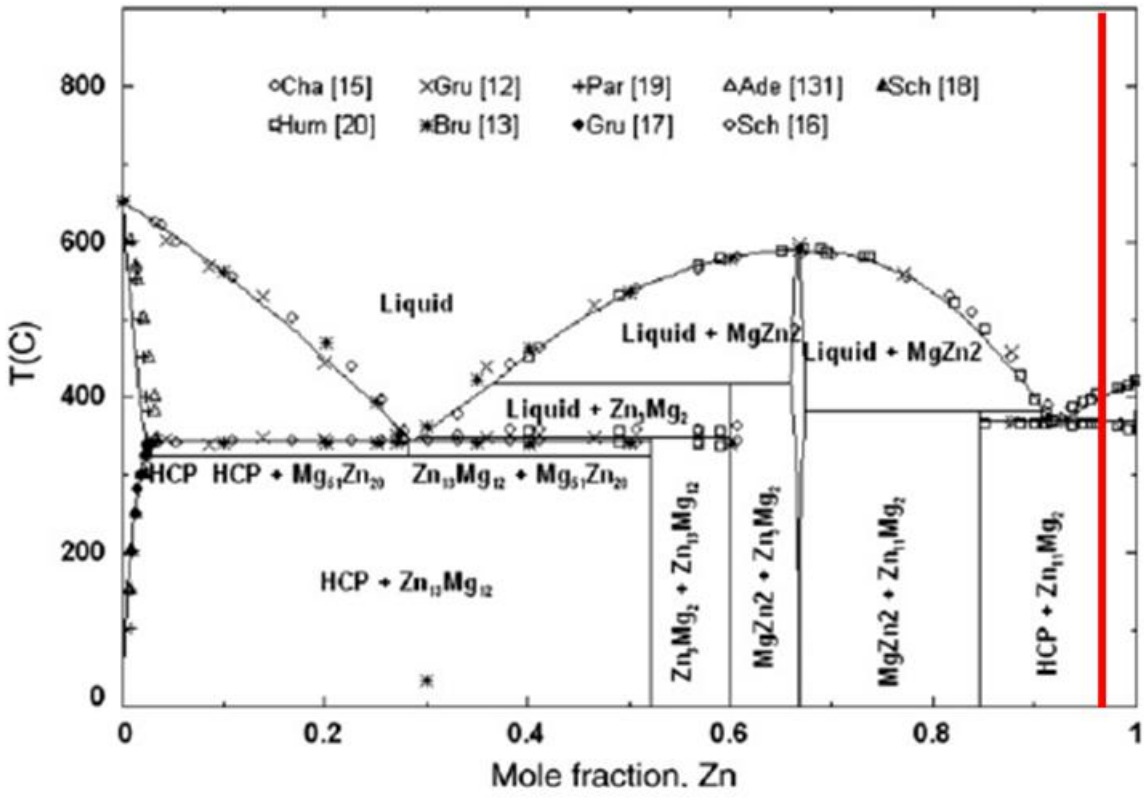

Figure 3-15: Phase diagram of MgZn. For a 1,6%Al, 1;6%Mg and thus 96,8%Zn the structure is probably Mg_2Zn_{11} [53]

Subsequently, a new trial with four samples will be started to get a better insight on what the rate will be for diminishing of the build-up in the MZ-bath. These samples will be taken out on different times within the same campaign of MZ after a GI to MZ bath change. With these samples, the dross build-up transformation on a typical set of DVL2 pot hardware should be represented.

Conclusions

A sample block from the DVL3 pot hardware was analysed to give a better understanding about the dross build-up characteristics during a typical hardware campaign after transitioning from GI to MZ. It appears that the dense Fe_2Al_5 dross build-up layer created during GI is starting to delaminate in the MZ-bath. However, complete breakdown of the Fe_2Al_5 dross build-up did not occur after 32 hours in MZ.

In addition to regions of pure zinc, typical intermetallic particles for both GI and MZ were found in the surface layers: Fe_2Al_5, $MgZn_2$, Mg_2Zn_{11} and ternary phases of Mg-Zn-Al.

A large difference in thickness of the build-up on the top surface and side surfaces was observed but this variation may be attributable to dross skimming that became attached on the upper surface whenever the hardware was removed from the zinc bath. However, the Fe_2Al_5 dross build-up particles on the side surfaces were significantly smaller than the particles on the top surface of the sample. Further testing is planned in order to understand the incremental differences on dross build-up when transitioning from GI to MZ.

Chapter 4

Experimental procedure

In Chapter 2 (the theoretical background) the dross build-up structure and the most important parameters that influence the growth behaviour of the dross build-up structure were described. In this chapter an overview of the experimental procedure is given.
In Section 4-1 the specific goals of this study are discussed in more detail. Subsequently the experimental set up and a concise description of the methods used to characterize the dross build-up structure are presented.

4-1 Research goal

As explained in Section 1-4, the research goal of this project is to identify the delamination behaviour in MZ of the dross build-up that is formed in GI on submerged bath hardware. In order to obtain the research goal, two experiments were carried out. The experiments were divided into two parts.

The first part of the investigations focused on the dross build-up behaviour in a full hardware campaign for the hardware. A full hardware campaign is the total time the hardware is placed in production before it is taken out for cleaning. During a full hardware campaign the baths get switched multiple times between GI and MZ. The exact amount of bath changes depends on the production schedule and therefore differs each hardware campaign. To investigate this first part experiment 1 is carried out.
The second part of the investigations was carried out in order to gain better insights in the diminishing rate of dross build-up in MZ-bath. The dross build-up that was created in a GI-bath is diminishing in the MZ-bath. Experiment 2 is carried out in order to investigate this second part.

The experiments were carried out with 316L stainless steel rods that were partly submerged in the zinc baths in production as shown in Figure 4-1. The reason why the experiments were conducted in production (in DVL 2) instead of in the laboratory is that the contributing parameters to the dynamic dross build-up, in particular the bath composition, are not possible to recreate in laboratory conditions.

Figure 4-1: Photos of where the sample rods are positioned in the Zn-bath in DVL 2. A schematic representation is shown in Figure 4-3

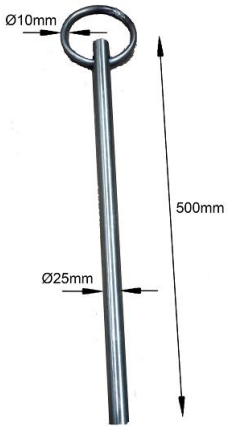

Figure 4-2: The dimensions of the sample rods used in the experiments are given in this Figure. Each sample in both experiments has the same dimensions

Simulating the bath composition (Fe and Al concentrations) in a laboratory condition that is similar to the production condition is not possible. As explained in Section 2-1-1 the dissolution of Fe depends on several parameters and these parameters cannot be exactly reproduced within a laboratory. Performing the experiments in the production line is therefore necessary in order to pursue the investigations.

4-2 Materials

The samples in the as-received condition were rods of 500 mm, with a diameter of 25 mm, shown in Figure 4-2. The rods were made of 316L stainless steel.
316L SS is a stainless steel, besides Fe mainly consisting of 16-18,5 wt% Cr and 10-14 wt% Ni. The steel also contains fractions of C, Mn, Mo, P, S and Si. The composition of 316L SS is presented in Table 4-1.

The GI and MZ baths were used in the experiments. Both baths contain 250 kT of Zn-alloy.

Element	% Present
Fe	Balance
C	<0,03%
Cr	16-18,5%
Ni	10-14%
Mn	<2,0%
Mo	2-3%
Si	<1%
P	<0,045%
S	<0,03%

Table 4-1: General composition of 316L SS, which is the material used for the sample rods[6]

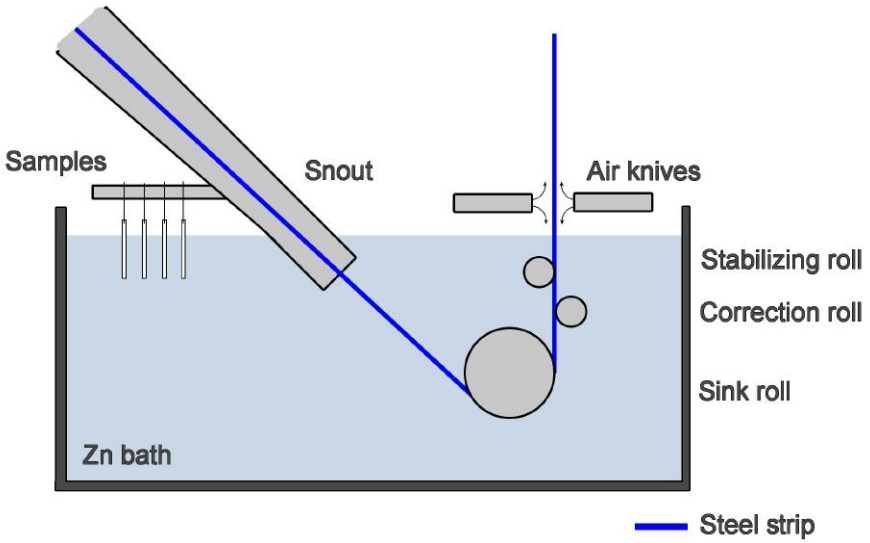

Figure 4-3: A schematic representation of the set-up for the experiments. A bar is welded on the snout at 20 cm above the Zn-bath surface. The sample rods are hanged on this bar, and partly submerged in the Zn-bath.

The composition of both baths fluctuated due to several parameters such as temperature or speed of the steel strip as explained in Section 1-1-3. The average composition of GI is 0,20wt% Al. As explained in section 2-1 the average composition of MZ is 1,6 wt% Al and 1,6 wt% Mg. Both baths also contain about 0,01 wt% Fe due to the continuous dissolution from the steel strip.

4-3 Experiments

To investigate the two parts as explained in Section 4-1, two experiments were carried out. In each experiment four rods were in the DVL 2, partly submerged in the zinc baths. The set-up is the same for both experiments. A schematic representation of the set-up is shown in Figure 4-3. In Figure 4-1 photos of the rods in the DVL2 are displayed.

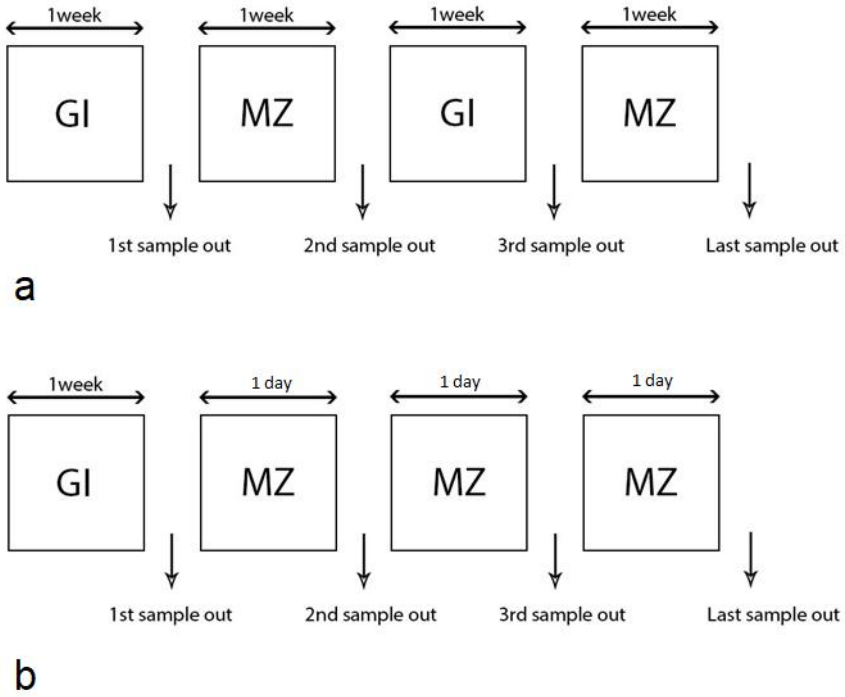

Figure 4-4: In a.) the schedule of experiment 1 is presented. In b.) the schedule of experiment 2 is presented. Each sample rod is taken out at a different time.

The schedules of both experiments are presented in Figure 4-4. The duration of the experiments differs for each experiment.
In Figure 4-4.a the schedule of experiment 1 is seen. This experiment represents nearly the full hardware campaign for the rolls of DVL2 and took 24 days. The goal for the first experiment is to identify the dross build-up behaviour in a full hardware campaign for the rolls. The sample rods are submerged 4 times in the baths: two times in GI, two times in MZ. At every switch one sample rod is taken out. The sample taken out represents the dross build-up structure of the baths was in.
In Figure 4-4.b the schedule of the second experiment is shown. This trial took less time than experiment 1, 7 days. Experiment 2 gives more insight on the diminishing rate in MZ of the dross build-up that is created in the GI-bath. The goal of this second experiment was to see the evolution of the dross build-up on the rolls. All samples start in GI. When the hardware is switched from GI to MZ, one sample rod is taken out. Once submerged in MZ every day another sample rod is taken out.

4-4 Sample preparation

After taking out the sample rods, the sample rods were air cooled to room temperature. The dross build-up structure on the sample rods is shown in Figure 4-5. Subsequently, the cylinders were cut to smaller dimensions, from various heights of the cylinder. Three samples were cut from each cylinder at heights 50 mm, 150 mm and 250 mm, seen from the bottom of the cylinder.

Figure 4-5: Pictures of the sample rods taken out the bath. Left rod is sample 1.3 (GI+MZ+GI), the right rod is sample 1.1 (GI only)

Once cut, all samples were embedded in resin and polished using sandpaper with ISO designations with the following particle sizes: P80 (201 µm), P180 (82 µm), P320 (46.2 µm), P800 (21.8 µm), P1200 (15.3 µm),P2000 (10.3 µm). During polishing, the samples were rinsed with ethanol to flush away dirt that could be embedded in the resin.
After polishing, the samples were placed in an ultrasonic bath to remove traces of contamination. After the ultrasonic bath the samples were final polished using diamond compound with particle sizes 3 µm and 1 µm. After final polishing the samples were rinsed with ethanol.

4-5 Instruments used for characterisation

The cross sections of the dross build-up structures were examined by Scanning Electron Microscopy (SEM) in order to characterize the microstructure. Energy dispersive X-Ray spectroscopy (EDX) was used to determine the chemical composition of the different phases in the dross build-up structure.
Before scanning the samples were slightly rinsed with ethanol to remove any contamination and roughness effects.

First, the prepared samples were investigated using a Leica MZ7.5 microscope for a preliminary optical inspection.
Scanning electron microscopy (SEM) analyses were performed in an Zeiss Ultra Plus equipped with an energy dispersive X-ray (EDX) micro-analyser. The morphology in the samples is studied in the secondary electron (SE) mode. The chemical compositions of various phases in the samples is studied in the backscattered electron (BSE) mode. The operating voltage for the SEM was 15 kV, unless indicated otherwise.

4-5-1 Optical Microscopy

Light microscopy techniques are widely used inspection tools in many applications in engineering and are present in almost any research laboratory. The first optical microscope that

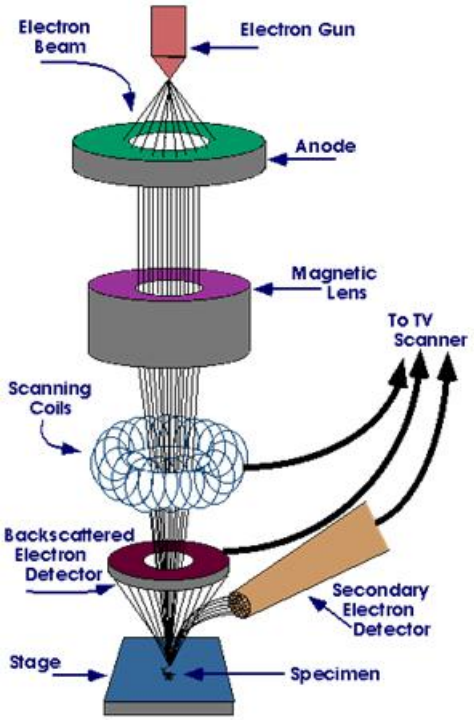

Figure 4-6: A schematic representation of a SEM. A beam of electrons is produced at the top of the microscope by heating of a metallic filament. The electron beam follows a vertical path through the column of the microscope. The electron beam makes its way through electromagnetic lenses which focus and direct the beam down towards the sample. Once it hits the sample, other electrons are ejected from the sample[56]

achieved a magnification in the order of 250 times is attributed to Antonie van Leeuwenhoek in the 17th century [54]. It was this particular development that revealed the existence microstructures that were unknown until then.
Optical microscopy of cross sections of specimens has been used to look at grain sizes and to the occurrence of exceptions in the dross build-up structure [55].

4-5-2 Scanning Electron Microscopy (SEM)

Scanning electron microscopy (SEM), together with energy dispersive spectroscopy (EDS), is a frequently used technique for investigations of materials. With these two techniques one can study the surface morphology and determine the composition of the surface locally on a microscale. Electron microscopy was first developed in the 1930's to overcome the limitations of optical microscopy [57]. The difference between optical microscopy and electron microscopy is that the SEM uses electrons instead of light. The basic idea is that the wavelength associated with electrons is much smaller than that of light. By extracting electrons from a source and focusing them using electromagnetic fields a much higher resolution can be obtained [58] [57].

In Figure 4-6 an overview of a SEM is displayed. A SEM consists of an electron gun that produces electrons, an anode that accelerates the electrons, a system of electromagnetic lenses that focuses the electron beam, scanning coils that enable scanning the electron beam over

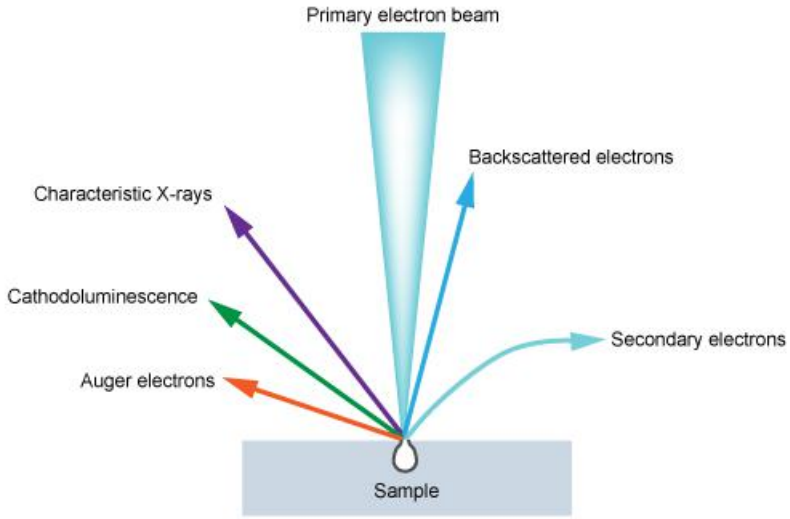

Figure 4-7: When the electron beam in the SEM hits the sample, the beam interacts with the atoms within that sample. In this Figure the outcomes of this interaction are shown [59]

the surface of the sample and a detector that measures the signals that are generated during the interaction of the electrons with the sample [58].
With SEM an image of the surface is formed by the use of moving electron beams. These beams of high-energy electrons generate a variety of signals at the surface, as seen in Figure 4-7. The accelerated electrons in this primary electron beam carry sufficient kinetic energy and interact with the atoms of the specimen. These interactions will generate electrons due to elastic and inelastic collisions[57].
The electrons that are emitted again from the surface are then detected as secondary electrons, backscattered electrons and diffracted backscattered electrons[58].

Backscattered electrons

The contrast for backscattered electron microscopy is generated by the difference in density, where a higher density generates a higher brightness. An area with a higher density contains more nuclei, generating more backscattered electrons than in areas with lower density. Therefore, the Zn rich phases appear brighter than Fe rich phases, since in heavier elements the electrons scatter more easily than lighter elements do [58].

Secondary electrons

Unlike the backscattered electrons, the secondary electrons are moving very slowly when the electrons leave the sample. Because of this low speed, the negative charged secondary electrons are attracted to the positive charged secondary electron detector. This attraction between the electrons and detector makes it possible to pull electrons from a large area, even from around corners. This ability to attract electrons from a large area creates a topographic image [57][58].

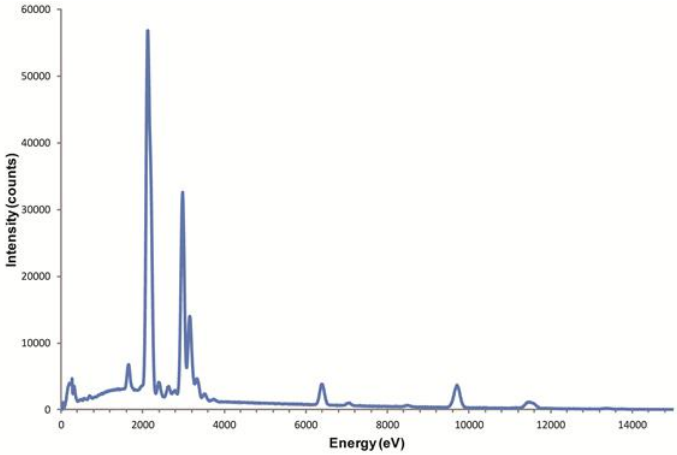

Figure 4-8: An example of an EDX-spectrum [61].

4-5-3 Energy-Dispersive X-ray Spectroscopy (EDX)

Energy-dispersive X-ray spectroscopy (EDX) is a technique to identify which elements a sample contains, determined by the specific X-ray peaks emitted by every element. By focusing the electron beam of the SEM on a single spot on the sample, atoms on that spot in the sample are excited and will emit X-ray radiation [58] [60][61]. The wavelength of these X-rays will depend on corresponding excited states, which are different for every element. EDX analysis is used mostly for higher elements (atom number higher than 3), since the lower elements have less excited states to distinguish. Because the beam has to be focused in one spot, EDX is limited to spot analysis [60] [61].
The EDX-technique can either qualitatively determine the elements that should be measured by displaying them in a spectrum, or it can semi-quantitatively identify the phase, by determining the approximate weight fraction [60].
An example of a spectrum is shown in Figure 4-8. On the Y-axis shows the number of counts. The higher the counts of a particular element, the higher will be its presence at that point of interest. The X-axis shows the energy level of those counts.

Chapter 5

Results

In this Chapter the results of the two experiments will be discussed. In Section 5-1 the results of experiment 1 are discussed. In this experiment the dross build-up behaviour of a full hardware campaign is investigated. In Section 5-2 the results of experiment 2 are discussed. In this experiment the diminishing rate of the dross build-up when submerged in MZ is investigated.

5-1 Results Experiment 1: Dross Build-up Behaviour in a Full Hardware Campaign

In this experiment four 316L SS rods were submerged in the GI and MZ baths. Each sample rod was taken out at a different time. The schedule of the four rods in experiment 1 is shown in Table 5-1. The dross build-up of each sample rod are presented in the next sections.

5-1-1 Results Sample 1.1 (GI Only)

In Figure 5-1 the layer of only GI can be seen respectively with a magnification of 50x, 200x, 800x and 1.500x.
Figure 5-1.a gives an overview of the dross build-up structure at 50x magnification. In this

Sample rod	Days submerged	Baths
Sample 1.1	8 days GI	GI
Sample 1.2	8 days GI + 5 days MZ	GI+MZ
Sample 1.3	8 days GI + 6 days MZ + 4 days GI	GI+MZ+GI
Sample 1.4	8 days GI + 6 days MZ + 4 days GI + 4 days MZ	GI+MZ+GI+MZ

Table 5-1: Schedule of the samples of experiment 1.

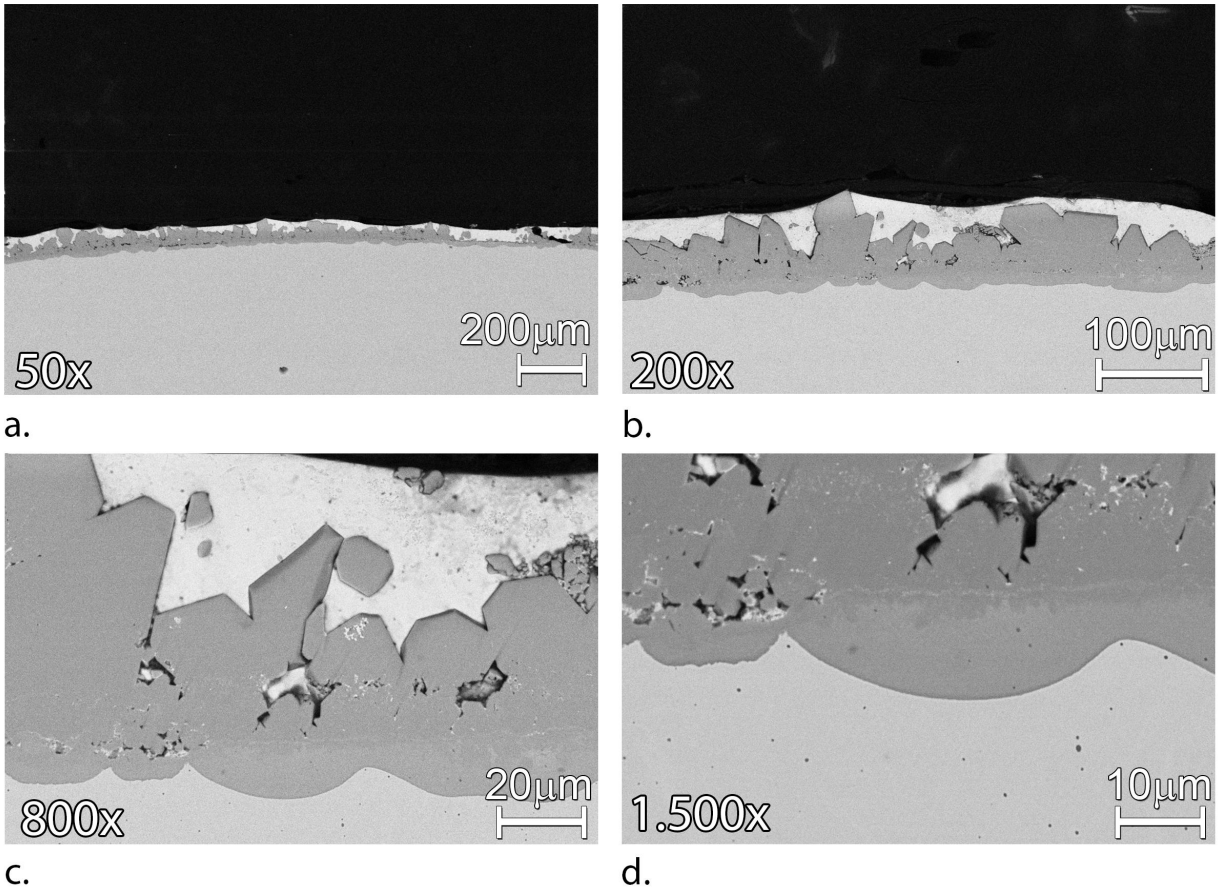

Figure 5-1: Cross section of the sample 1.1, that is only submerged in GI. a.) Cross section with a magnification of 50x, b.) Cross section with a magnification of 200x, c.) Cross section with a magnification of 800x and d.) Cross section with a magnification of 1.500x. The Zn-phase appears in white, the build-up structure has a grey colour. The light-grey area at the bottom is the stainless steel.

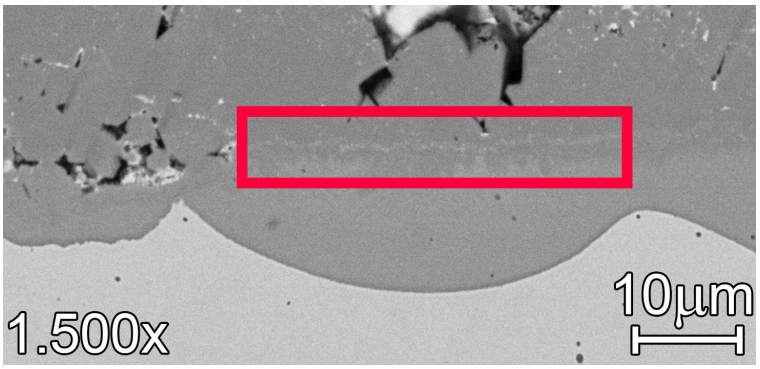

Figure 5-2: A clarification of the possible original surface is shown in the red square. In this square a line is visible, having the same colour as the diffusion layer.

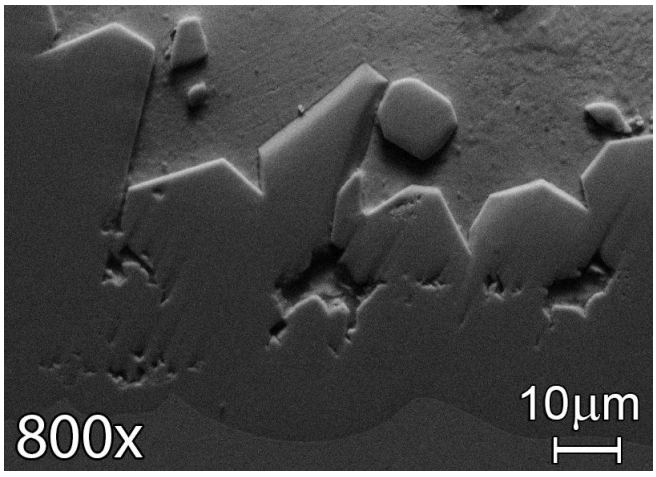

Figure 5-3: The topographic image of Figure 5-1.c at a magnification of 800x. The intermetallic dross particles protrude out of the solidified Zn. A distinction of the diffusion layer is not seen in this secondary electron mode.

figure it is visible that the layer of intermetallic dross particles formed over the whole surface. The dross build-up layer is about 90 µm thick (average) and mainly consists of intermetallic dross particles, covered with some pure Zn.
Figure 5-1.b shows a good distinction between the dross particles and the Zn: the intermetallic dross particles have a faceted shape. Furthermore, the particles are all attached to the diffusion layer that is formed onto the steel substrate. The particles do not 'float' in the solidified Zn.
Figure 5-1.d is zoomed in on the diffusion layer of sample 1.1. The grey colour of the diffusion layer is a shade lighter compared to the intermetallic dross particles. Moreover, above the diffusion layer the original surface of the stainless steel may be visible, which is clarified in Figure 5-2. In the red square in this Figure an enriched Zn-line in the intermetallic dross particles is shown.

In Figure 5-3 a topographic image of Figure 5-1.c is displayed. Here can be seen that the intermetallic dross particles protrude out of the Zn. The possible original surface that is shown in Figure 5-2 is not seen in the topographic image.

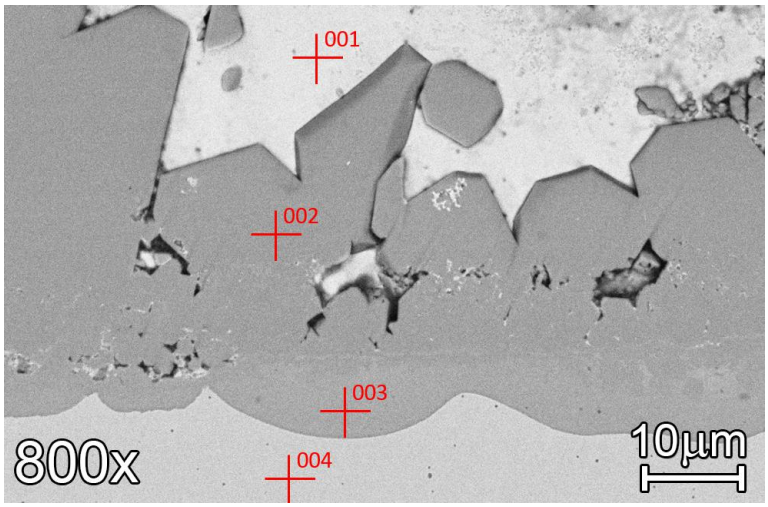

Figure 5-4: EDX-analysis on sample 1.1. Four analyses have been carried out on the build-up to determine the elements.

Process Data

All four samples are inserted in the GI bath at the same time. Sample 1.1 came out at the end of the GI-campaign, just before changing the bath to MZ. The sample is immersed of a total time of 7 days and 23 hours. In this time period, the temperature was stable. The temperature has an average of 465,0°C (maximum is 470,8°C, minimum is 452,0°C).
The Al-concentration varies between 0,182 wt% and 0,246%, with an average of 0,212 wt%. The concentration of Fe is on average 0,014 wt%. These values are in the acceptable range for production, which is between 0,2 and 0,3 wt% as can be read in Section 1-1-5.

Chemical Composition

An EDX-analysis was carried out in order to determine the different elements in the build-up structure. In Figure 5-4 the four points are shown that have been analysed in sample 1.1 (GI only). The EDX-spectra of this analysis are displayed in Appendix A. The measured compositions of the four points are shown in Table 5-2.

Another EDX-analysis is carried out to get a better insight on the diffusion line and the possible original surface which is shown in Figure 5-2. The points taken in this area are shown in Figure 5-5. Three points are selected, to get a better insight on the chemical compositions of that point, to determine the diffusion of elements in these regions. The quantitative results of the points taken are shown in Table 5-2. The EDX-spectra of the analysis is displayed in Appendix A.

5-1-2 Results Sample 1.2 (GI+MZ)

In Figure 5-6 the layer of GI followed by MZ can be seen, respectively with a magnification of 50x, 200x and 800x.
In Figure 5-6.a it can be seen that the intermetallic dross particles are not only attached

Points taken	Fe (wt%)	Al (wt%)	Zn (wt%)	Mo (wt%)	Other elements (wt%)	Possible Structure
EDX 001	0,31	0,51	98,97	-	-	Zn-phase
EDX 002	40,01	39,78	16,95	0,15	0,39 (Cr), 0,23 (Si)	Fe_2Al_5
EDX 003	36,90	40,11	20,29	1,48	0,48 (Cr), 0,20 (Si)	Fe_2Al_5
EDX 004	70,36	0,06	0,76	2,87	17,07 (Cr), 10,34 (Ni), 0,20 (Si)	316L SS
EDX 005	38,56	40,01	19,21	0,79	0,53 (Cr), 0,12 (Si)	Fe_2Al_5
EDX 006	39,71	41,43	17,10	0,18	0,41 (Cr), 0,29 (Si)	Fe_2Al_5
EDX 007	37,00	39,88	20,88	1,60	0,45 (Cr), 0,20 (Si)	Fe_2Al_5

Table 5-2: The quantification results are shown of the EDX-analysis that is carried out on sample 1.1

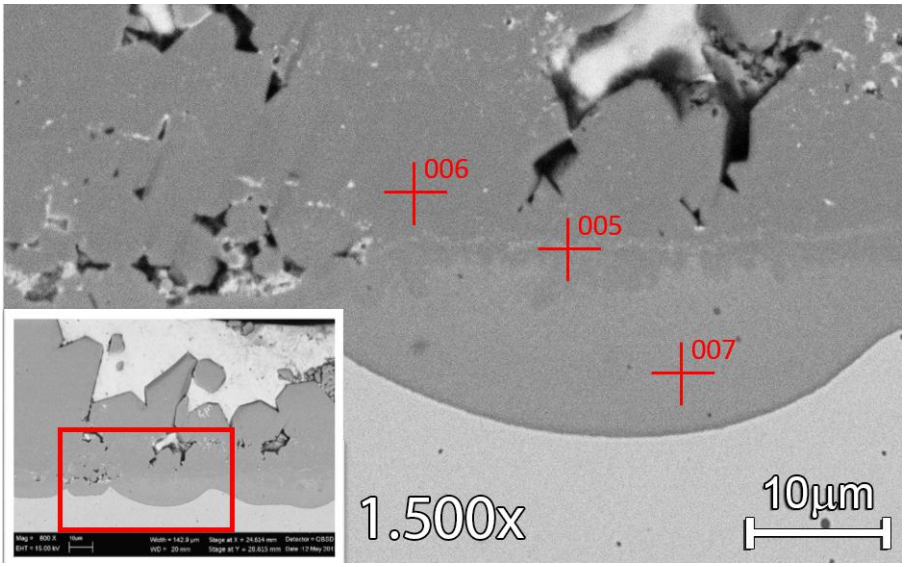

Figure 5-5: A second EDX-analysis on sample 1.1. Three analyses have been carried out on the build-up to determine the differences in composition between the intermetallic dross particles, diffusion layer and the enriched Zn-line that is indicated in Figure 5-2.

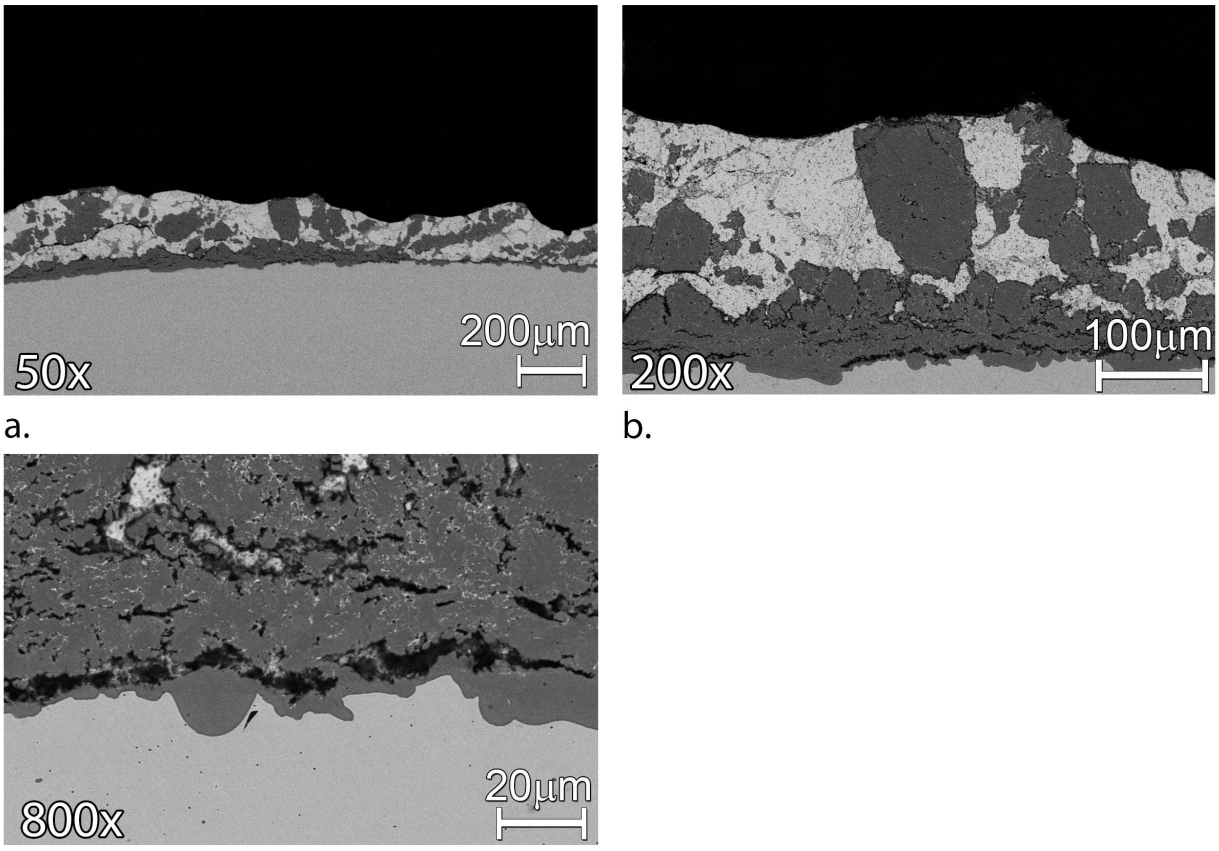

Figure 5-6: Cross section of sample 1.2, that is submerged in GI followed by MZ. a.) Cross section with a magnification of 50x, b.) Cross section with a magnification of 200x and c.) Cross section with a magnification of 800x. The Zn-phase appears as white and the dross build-up structure as dark grey. The stainless steel has a light grey colour in the backscattered mode.

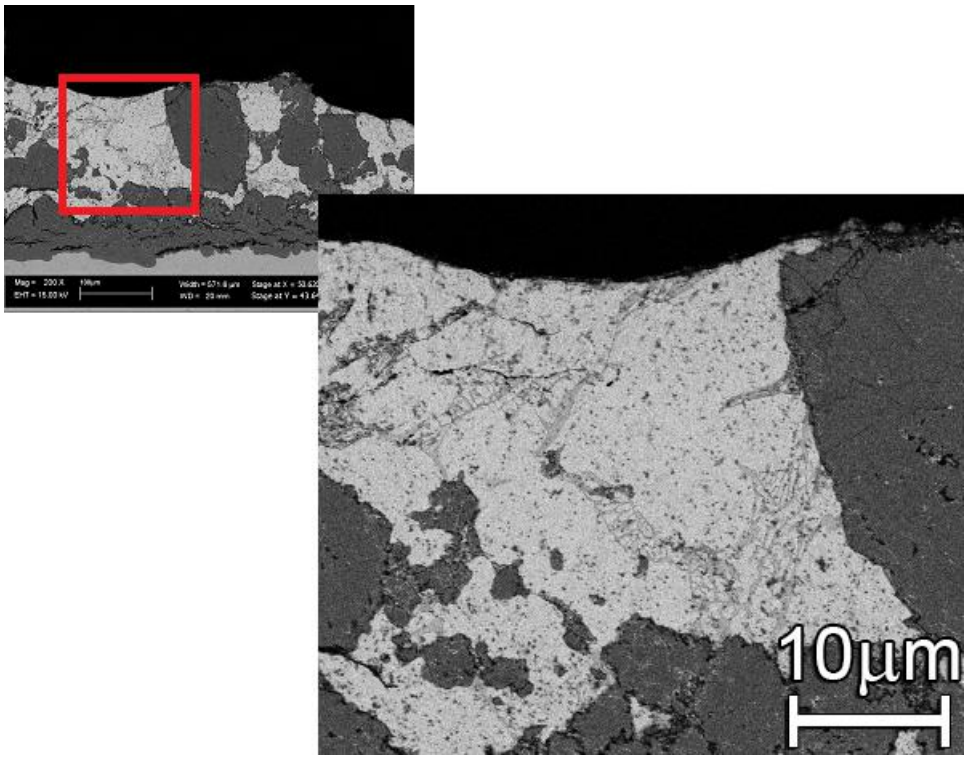

Figure 5-7: A magnification of Figure 5-6.b. The uniform Zn-phase as seen in sample 1, consists in this sample 1.2 of multiple phases.

onto the diffusion layer, but most 'float' through the solidified Zn. The total thickness of the dross build-up structure is 200 µm(on average). In Figure 5-6.b a typical morphology of the dross build-up layer when submerged in GI followed by MZ is seen. The intermetallic dross particles do not have the faceted structure anymore that is visible in the dross build-up structure of sample 1.1 in Figure 5-1.b. The shape is curved with jagged sides. In Figure 5-6.c it can be seen that in the intermetallic dross particles itself small white 'ribbons' are starting to appear.
Figure 5-7 shows that the Zn area is not uniform, but consists of more phases. In the white Zn-phase some light grey lines are visible, though dificiult to see. These lines are binary $MgZn_2$-phase. The typical MagiZinc structure with a ternary structure is not detected.

Furthermore, at the diffusion layer/intermetallic dross particles interface large cracks are visible. A topographical image is made, shown in Figure 5-8. A topographical image is an image made in the SEM-microscope mainly to identify the height differences. Here the cracks are visible: At every black spot shown in Figure 5-6.c a significant height difference appears in the topographic image, as shown in Figure 5-8. Another surprising result is that the cracks formed at the interface, close to the stainless steel. The thickness of the diffusion layer differs over the whole substrate. On the right in Figure 5-6.a it can be seen that the diffusion layer is very thin, at the left in the same Figure appears the diffusion layer thicker.

Figure 5-9 shows the delamination of the dross particles from the dross build-up structure. The intermetallic dross particles detach from the build-up/diffusion layer interface, since onto the stainless steel a small diffusion layer is still visible. The diffusion layer remains at the

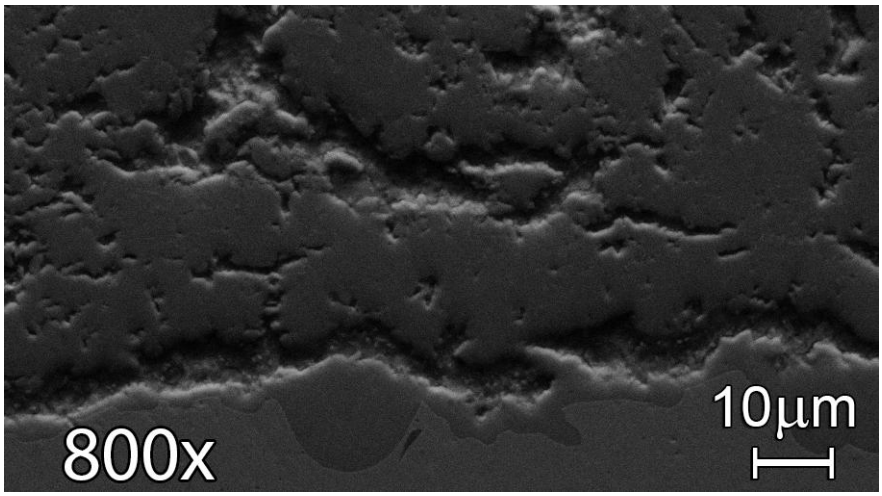

Figure 5-8: A topographical image is made from Figure 5-6.c, to identify cracks.

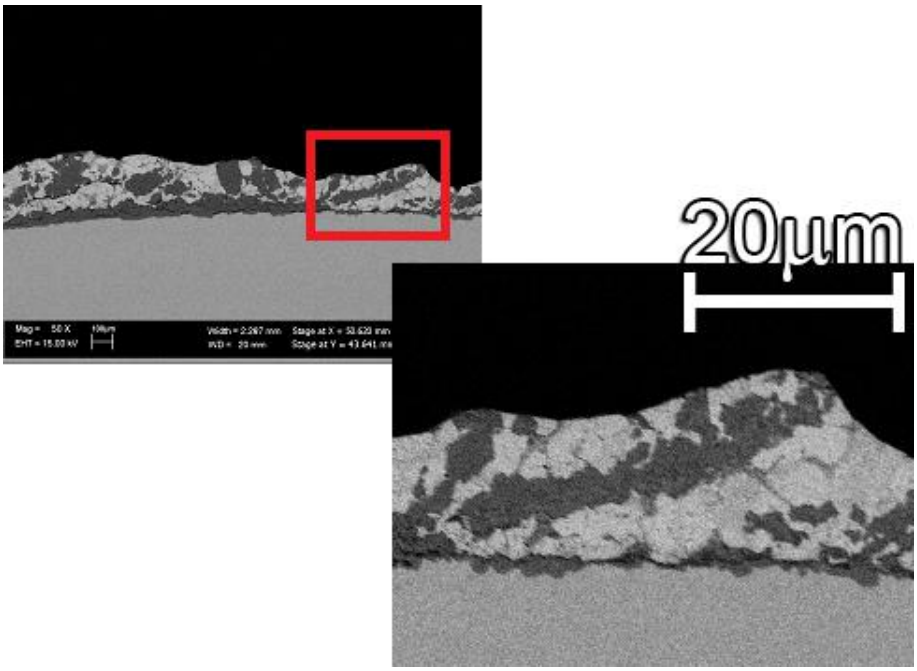

Figure 5-9: A magnification of Figure 5-6.a. The intermetallic dross particles (dark grey) are not attached to the diffusion layer, but they are surrounded by the Zn-phase (white) and some $MgZn_2$ (light grey lines). The intermetallic dross particles detach not particle by particle, but clustered with multiple particles. Furthermore, the diffusion layer (dark grey) is very thin or almost disappeared in some places at the substrate/build-up interface.

Points taken	Fe (wt%)	Al (wt%)	Zn (wt%)	Mo (wt%)	Other elements (wt%)	Possible Structure
EDX 001	38,16	45,31	16,53	-	-	Fe_2Al_5
EDX 002	41,11	41,83	17,06	-	-	Fe_2Al_5
EDX 003	1,98	2,04	94,38	0,06	1,49 (O)	Zn
EDX 004	37,44	41,42	17,02	3,04	0,18 (Cr), 0,08 (Si)	Fe_2Al_5
EDX 005	66,86	0,10	-	2,20	17,61 (Cr), 11,10 (Ni), 0,45 (Si)	316L SS

Table 5-3: The quantification results are shown of the EDX-analysis that is carried out on sample 1.2. The Fe_2Al_5 are all enriched with Zn.

stainless steel. Multiple dross particles detach at the same time clustered in a ribbon shape. The particles do not delaminate particle by particle.

Process Data

All four samples are inserted in the GI bath at the same time. Sample 1.2 was partly submerged in GI for 7 days and 23 hours followed by 4 days and 22,5 hours MZ. In this time period, the temperature was stable in both baths. The temperature in GI is the same as in sample 1.1 (see Section 5-1-1). The temperature in the MZ-bath has an average of 451,0°C (maximum is 458,2°C, minimum is 447,1°C). The concentration of Al in MZ varies between 1,61 wt% and 1,72 wt%, with an average of 1,67 wt%. The Mg-concentration has an average of 1,751 wt%, ranging between 1,71 wt% and 1,77 wt%.

Chemical Composition

An EDX-analysis is carried out on sample 2.2. The point taken are shown in Figure 5-10. To observe the chemical composition in sample 1.2, five points are selected for EDX-analysis. This analysis provides information of the chemical composition in this area. Furthermore the EDX-analysis gives information on what the influence of the cracks is on the chemical composition in the dross build-up structure. The quantitative results of these points are shown in Table 5-3. The EDX-spectra of the points in this analysis is shown in Appendix A.

5-1-3 Results Sample 1.3 (GI+MZ+GI)

In Figure 5-11 the build-up stucture of GI followed by MZ and again GI can be seen, respectively with a magnification of 50x, 200x, 1.000x and 2.500x.
As can be seen in Figure 5-11.a and 5-11.b the dross build-up layer consists of a diffusion layer, together with intermetallic particles attached to the layer and as well 'floating' in the solidified Zn. The colour of the diffusion layer is uniform in the backscattered electron mode. The intermetallic dross particles are dark grey. The total thickness of the dross build-up layer is 125 µm (on average). The amount of solidified Zn is significantly larger than was observed in the other samples of experiment 1.

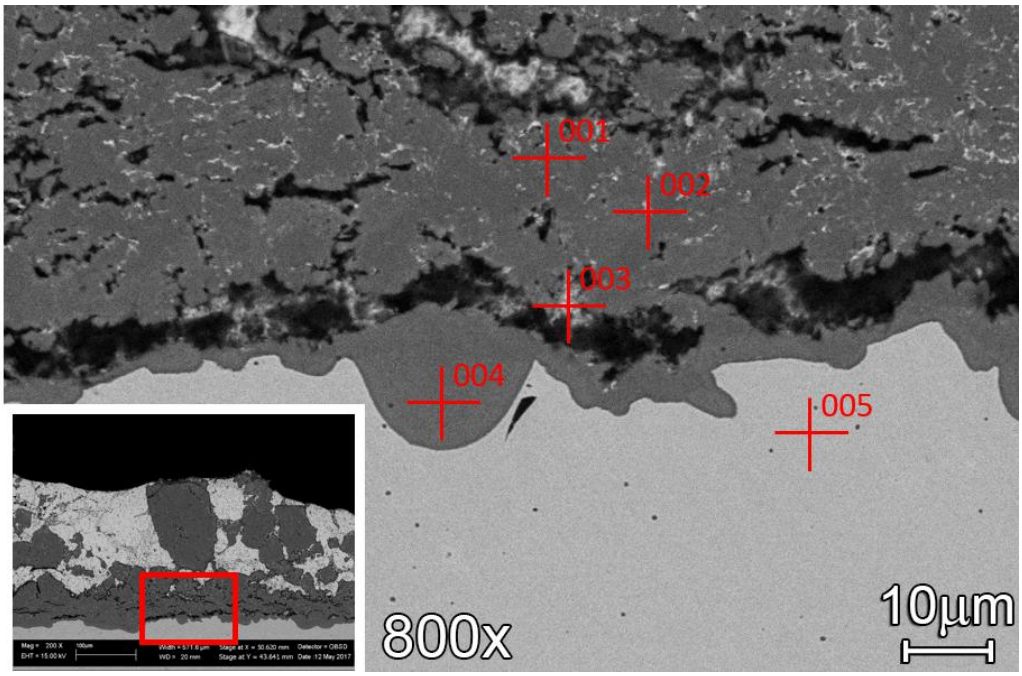

Figure 5-10: Points taken for EDX-analysis in sample 1.2 (submerged in GI, followed by MZ and GI again)

In the build-up structure two types of intermetallic dross particles are distinguished: Faceted shaped interface and curved shaped interface. This distinction is made clear in Figure 5-12. Most particles with the faceted interface are surrounded by the solidified Zn and partly attached to other intermetallic dross particles or the diffusion layer. The curved shaped are mostly attached to the diffusion layer.

The large cracks that are visible in the sample 1.2 (GI+MZ) are not detected in this sample 1.3 (GI+MZ+GI). Instead, multiple black spots are visible, together with numerous small white 'ribbons' in the intermetallic dross particles. These white 'ribbons' are found in all the intermetallic dross particles. The 'ribbons' appear to follow the grain boundaries within the intermetallic dross particles.
To distinguish what these black spots exactly are, a topographic image is made of sample 1.3 as can be seen in Figure 5-13. In this image the black spots are visible as holes, suggesting a difference in heights. The white 'ribbons' that are visible in Figure 5-11 are less visible in the topographic image, though it can be seen that the surface of the intermetallic dross particles is uneven where the white 'ribbons' locate, not as smooth as the surface of the diffusion layer. The diffusion layer does have a smooth surface, showing no irregularities in height. Furthermore, Figure 5-13 shows a difference in heights between the intermetallic dross particles and the solidified Zn.

The diffusion of Al and Zn into the stainless steel (or where the steel substrate originally was) is easily visible, as shown in Figure 5-11.c. The Figure shows an even distribution of these elements by showing a uniform light grey colour over the whole area of the diffusion layer without having a lot of gradient in the grey. A clear separation line is visible between the diffusion layer and the intermetallic dross particles. The diffusion layer shows a uniform

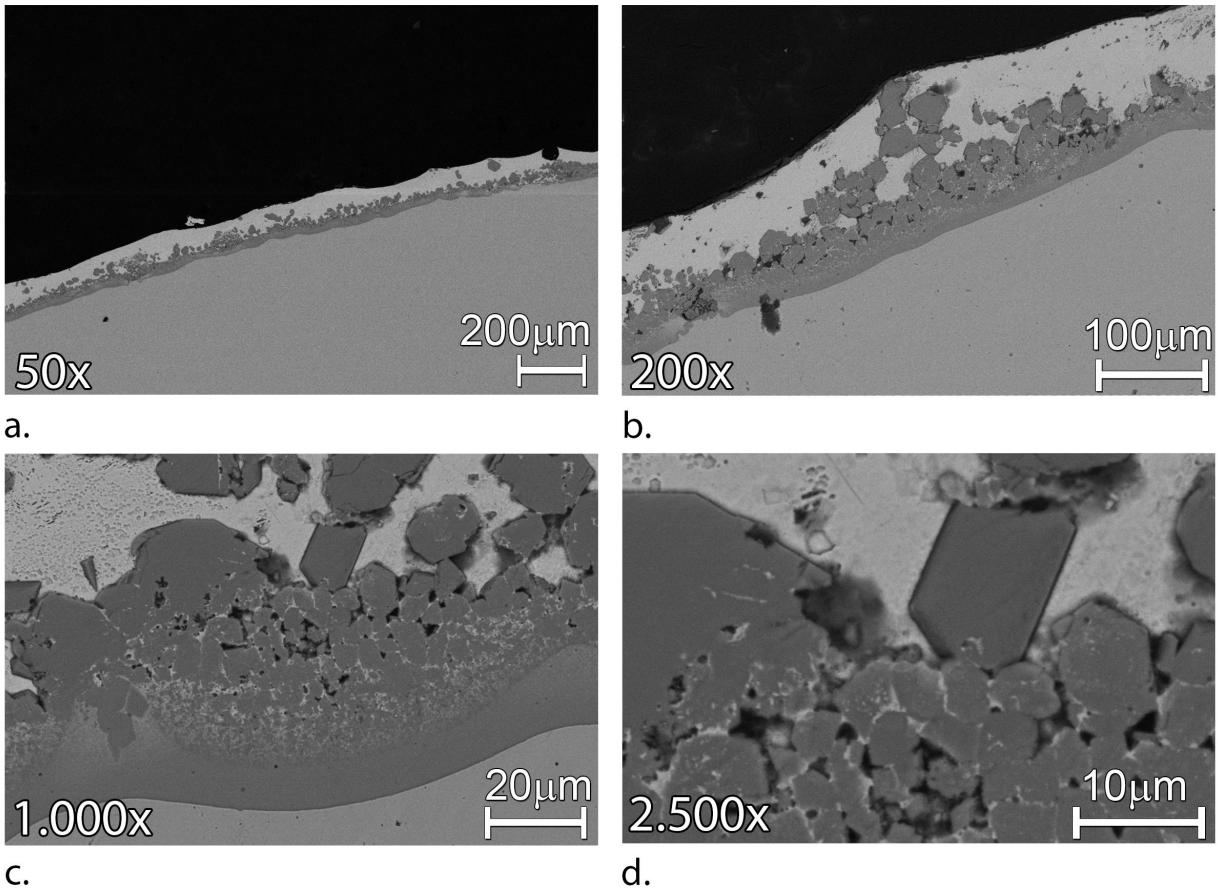

Figure 5-11: Cross section of the build-up structure of sample 1.3 that is submerged in GI, MZ, followed by GI again. The cross section with a magnification of a.) 50x, b.) 200x, c.) 1.000x and d.) 2.500x. The Zn-phase appears in white. The build-up structure has a grey colour. The light-grey area at the bottom is the steel subtrate.

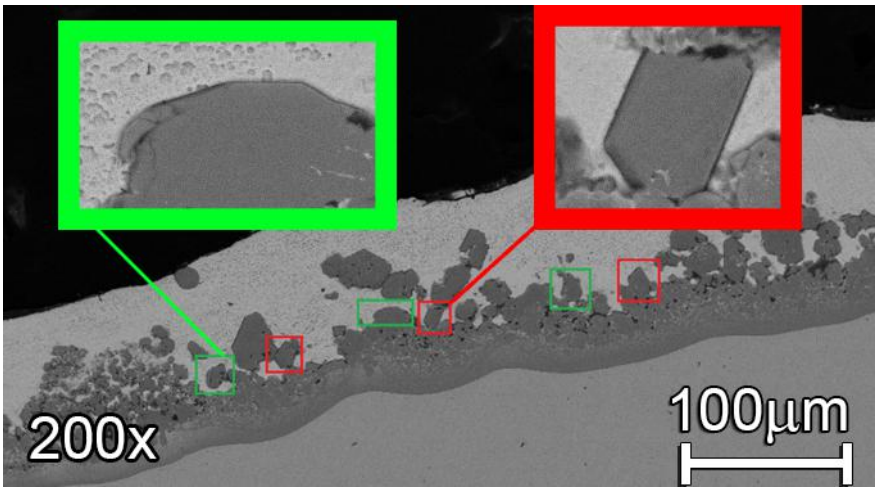

Figure 5-12: Intermetallic dross particles with Faceted (marked red) and curved (marked green) interfaces are visible in the dross build-up structure.

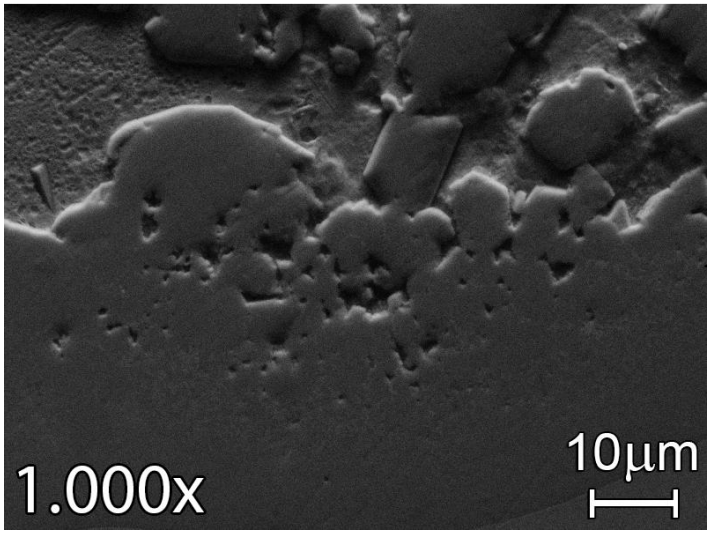

Figure 5-13: topographic image of Figure 6-14. Differences in height are made clear. It can be seen that the black spots are indeed holes. Where the white cracks are visible in Figure 5-11.c, the surface is uneven, though not very clear definable

colour. The intermetallic dross particles contains white ribbons and black spots. The black spots are visible as holes in the topographic figure (Figure 5-13), the white ribbons cannot be distinguished in this figure.

Process data

All four samples are inserted in the GI bath at the same time. Sample 1.3 was partly submerged in GI for 7 days and 23 hours followed by 4 days and 22,5 hours MZ and 4 days in GI. In this time period, the temperature was stable in the three baths. The temperature in the first GI-bath and in MZ is the same as in sample 1.2 (see 5-1-2).
The temperature in the second GI-bath has an average of 465,36°C (maximum is 460,4°C, minimum is 471,5°C). The concentration of Al varies between 0,172 wt% and ,238 wt%, with an average of 0,208 wt%. The Fe-concentration is stable with an average of 0,016 wt%.

Chemical Composition

Figure 5-14 shows the points where an EDX-analysis was carried out on sample 1.3. These points taken show similar results as in samples 1.1 (GI) and 1.2(GI+MZ). The quantitative results of the points are displayed in Table 5-4. The spectra are displayed in Appendix A.

In addition to the EDX-analysis an element mapping is carried out on sample 1.3 (GI+MZ+GI) as shown in Figure 5-15. The elements analysed were Al, C, Cr, Fe, Mg, Mo, O and Zn. For each element the following are observed:

- Al is found in the whole build-up structure. In the diffusion layer Al is evenly distributed. In the white ribbons Al is not found, or the Al is in low concentration in that place.

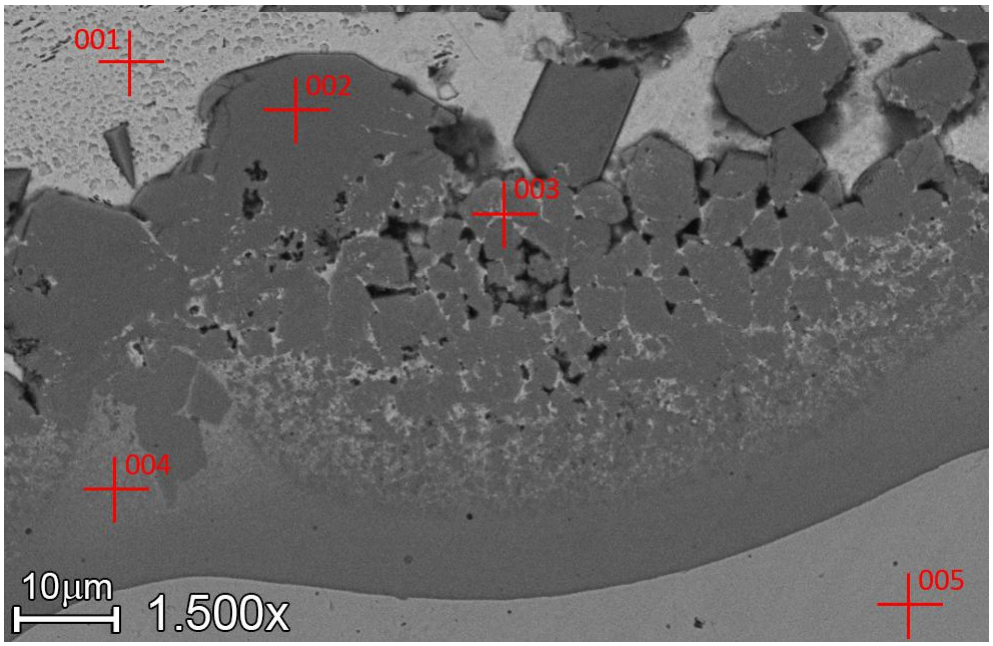

Figure 5-14: The points taken for EDX-analysis in sample 1.3. 001 is taken to measure the composition of the Zn-phase, 002 for the intermetallic dross particles, 003 measures the composition of the white 'ribbons', 004 the composition of the diffusion layer and point 005 measures the chemical composition of the stainless steel.

Points taken	**Fe (wt%)**	**Al (wt%)**	**Zn (wt%)**	**Mo (wt%)**	**Other elements (wt%)**	**Possible Structure**
EDX 001	0,21	0,17	98,56	-	-	Zn
EDX 002	42,18	47,85	9,85	-	-	Fe_2Al_5
EDX 003	2,03	1,18	96,76	-	-	Zn in white ribbons, Fe + Al detected from surrounding phases
EDX 004	32,93	46,20	19,04	1,83	0,15 (Cr), 0,06 (Si)	Fe_2Al_5
EDX 005	69,12	0,08	-	2,13	16,21 (Cr), 11,99 (Ni), 0,65 (Si)	316L SS

Table 5-4: The quantification results are shown of the EDX-analysis that was carried out on sample 1.3. The points correspond to the points taken in Figure 5-14.

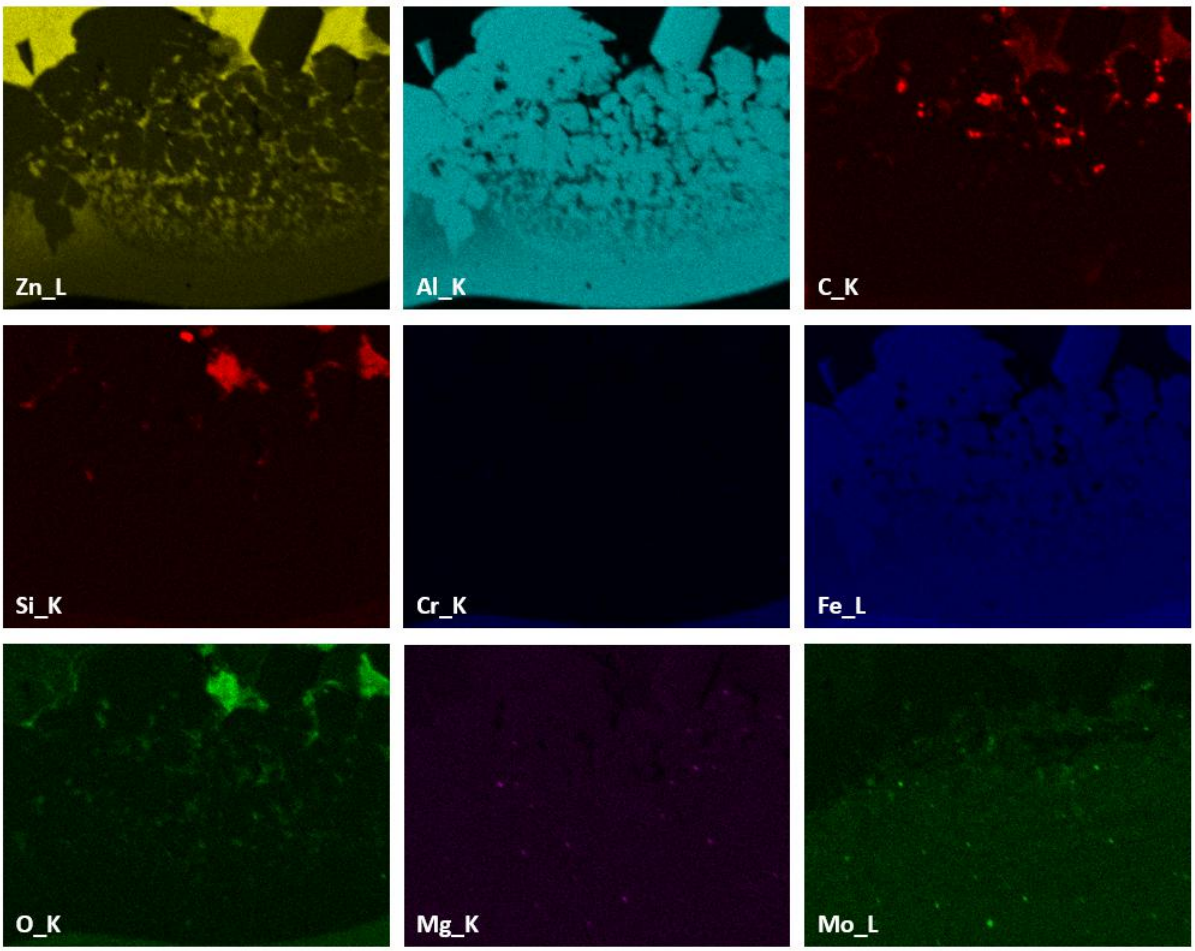

Figure 5-15: Element mapping of sample 1.3

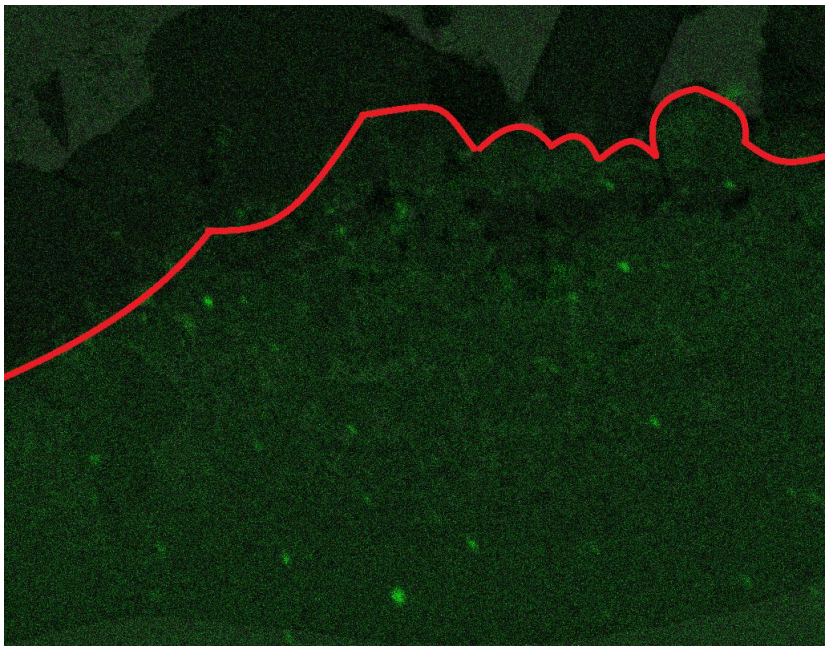

Figure 5-16: Diffusion of Mo in sample 1.3. Mo diffused not only in the diffusion layer, but also Mo is distinguished in the intermetallic dross particles.

- C is only found in the black spots (that can be distinguished as holes in the topographic image in Figure 5-13) between the intermetallic dross particles, not in the build-up structure itself.
- Cr is only found in the stainless steel. Cr is not found in the dross build-up structure or in the Zn-phase.
- Fe is found in the whole build-up structure. A higher concentration of Fe can be found in the 316L SS substrate. In the white ribbons no Fe is found.
- Mg is not found in the build-up structure. Only in a few spots a very high concentration is found.
- For Mo a clear diffusion line is visible. The diffusion line is identified in Figure 5-16. A very high concentration of Mo is visible in the exact same spots as Mg is found.
- O is only found in the black spots(holes in the topographic image).
- The solidified Zn layer that covers the build-up structure shows a very high concentration of Zn. No other element is found in this phase. Also Zn is found in the diffusion layer. In the small white ribbons a high concentration of Zn is found. No Zn or a very low concentration of it is found in the intermetallic dross particles.

Nevertheless the concentration of Zn in the dross particles cannot be determined properly with the element mapping. In the chemical composition of the EDX-analysis performed on this sample 1.3 it is seen that the intermetallic dross particles do contain some Zn. The EDX-spectra are shown in Appendix A.

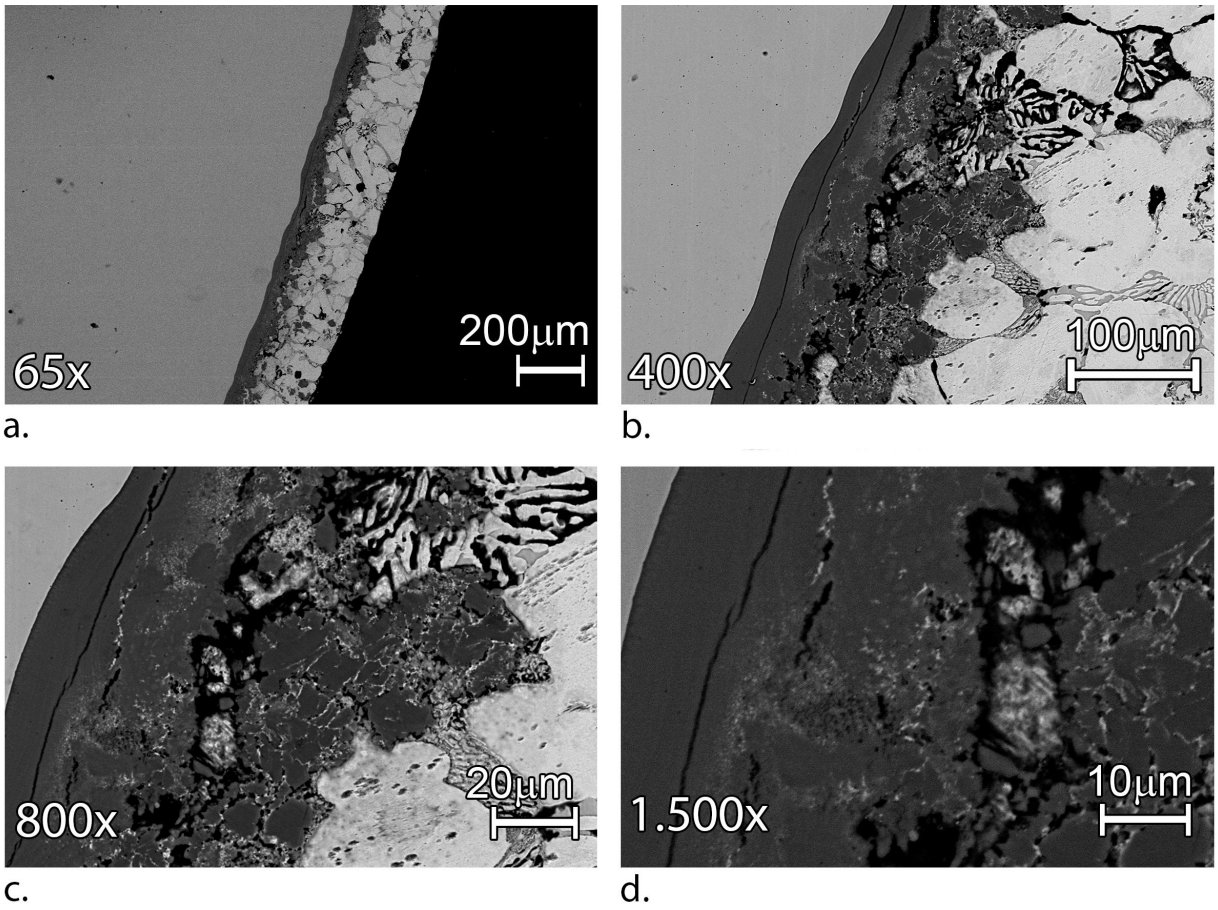

Figure 5-17: Cross section of the sample 1.4, that is only submerged GI, followed by MZ, GI and MZ. The cross section are shown with a magnification of a.) 65x, b.) 400x, c.) 800x and d.) 1.500x. The steel substrate appears as light grey and is shown on the left, the build-up structure has a dark-grey colour. The MZ-structure shows the different phases of MZ, including the ternary structure. Pure Zn appears as white.

5-1-4 Results Sample 1.4 GI+MZ+GI+MZ)

In Figure 5-17 the dross build-up structure of sample 1.4 is shown, respectively with a magnification of 65x, 400x, 800x and 1.500x. This sample has been twice in GI and twice in MZ. Figure 5-17.a shows an overview of the build-up structure on the sample at a magnification of 65x. A thick layer of the MagiZinc structure is shown: the binary and ternary structure is visible.

A similar build-up structure as in sample 1.2 (GI+MZ) is visible. All intermetallic dross particles have a curved shape with jagged sides. No faceted shaped particles are seen in the build-up structure. In the intermetallic dross particles itself small white ribbons are starting to appear.

Visible in Figure 5-17.c a narrow crack can be distinguished approximately 10 µm from the build-up/stainless steel interface. Comparable cracks are visible in the whole structure at a distance of approximately 10 µm from the build-up/stainless steel interface.

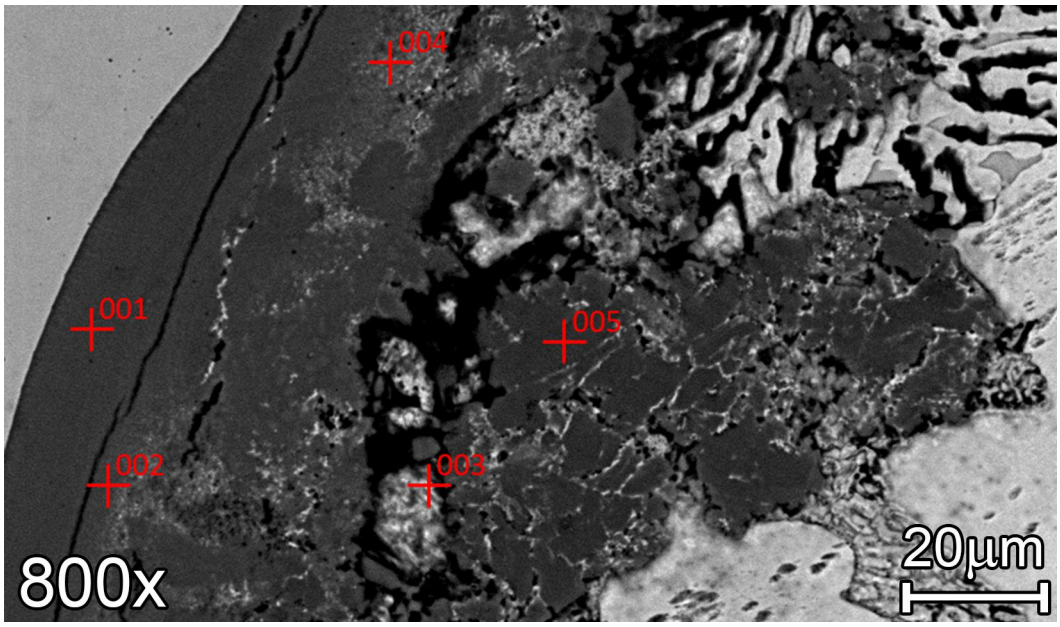

Figure 5-18: The points taken for EDX-analysis in sample 1.4. The image is tilted compared to the other samples. The stainless steel is located on the left.

Delamination of the structure is shown in Figure 5-17.c. At some places the intermetallic dross particles start to detach from the diffusion layer or are already delaminated and 'float' in the solidified MZ-structure. At other places there is no delamination of the intermetallic dross particles visible. Similar to sample 1.2 (GI+MZ) multiple dross particles detach at the same time, clustered in a ribbon shape. The particles do not delaminate particle by particle.

Process Data

All four samples are inserted in the GI bath at the same time. Sample 1.4 was partly submerged in GI for 7 days and 23 hours followed by 5 days and 20 hours MZ, 4 days in GI and 6 days and 4,5 hours in MZ. In this time period, the temperature was stable in both baths. The temperatures in the both GI and the first MZ-baths are the same as in sample 1.3 (see 5-1-3).
The temperature in the second MZ-bath has an average of 451,0°C (maximum is 447,6°C, minimum is 460,6°C). The concentration of Al in MZ varied between 1,60 wt% and 1,67 wt%, with an average of 1,64 wt%. The Mg-concentration has an average of 1,731 wt%, ranging between 1,70 wt% and 1,75 wt%.

Chemical Composition

To analyse the chemical composition in sample 1.4, an EDX-analysis is carried out. In Figure 5-18 the points taken for EDX-analysis on sample 1.4 are shown.
In Figure 5-17.d a crack between the presumed diffusion layer and intermetallic dross particles can be seen. Points 001 and 002 are taken to distinguish a difference in composition left or right of this crack. Point 003 is taken to quantify the composition of the white 'ribbons'

Points taken	Fe (wt%)	Al (wt%)	Zn (wt%)	Mo (wt%)	Other elements (wt%)	Possible Structure
EDX 001	40,52	49,16	6,57	4,83	-	Fe_2Al_5
EDX 002	41,11	41,83	17,06	-	-	Fe_2Al_5
EDX 003	1,36	3,04	57,88	0,10	24,45 (C), 0,13 (Mg), 11,71 (O)	Zn + dirt from polishing
EDX 004	37,44	41,42	17,02	4,04	0,18 (Cr), 0,08 (Si)	Fe_2Al_5
EDX 005	33,41	48,18	16,65	0,11	0,11 (Mg), 1,83 (O)	Fe_2Al_5

Table 5-5: The quantification results are shown of the EDX-analysis that was carried out on sample 1.4. The points corresponds to the points taken in Figure 5-18.

present in the intermetallic dross particles. Point 004 is taken to see if there is a difference in composition compared to point 002. Point 004 is taken in the light grey colour that is visible in the build-up structure. Point 005 is taken to see what the composition is in the intermetallic dross particles that are located further from the steel substrate. The quantitative results of the EDX-analysis are shown in Table 5-5.

5-1-5 Summary of Results Experiment 1

Experiment 1 is aimed to investigate the influence of bath changes (GI to MZ and vice versa) on the dross build-up structure on the bath hardware.
From the EDX-analyses and element mapping carried out on the four samples it can be seen that the diffusion layer consists mainly of Fe (35-40 wt%), Al (40-45 wt%), Zn (15-20 wt%) and Mo (1-3 wt%). Furthermore, some traces of Cr and Si can be found. The intermetallic dross particles consist of Fe, Al and Zn, the difference with the diffusion layer is that there is no Mo detected.

The diffusion layer does not have a straight diffusion layer/steel interface. This interface has a wavy profile. As seen in Figure 5-19 the average thickness of the diffusion layer is similar for all the samples. The thickness varies between 3 µm and 20 µm, with an average of 10 µm.

In sample 1.1 (GI) the intermetallic dross particles do have a faceted structure. The samples 1.2 (GI+MZ), 1.3 (GI+MZ+GI) and 1.4 (GI+MZ+GI+MZ) mainly show curved intermetallic dross particles with jagged sides. Sample 1.2 and 1.4 only show this curved shape, whereas sample 1.3 shows a combination of the faceted shape and the curved shape. Whereas the intermetallic dross particles are closely attached to the diffusion layer in sample 1.1, the particles get loosened from the diffusion layer in sample 1.2 (GI+MZ). This phenomenon is shown in Figure 5-9. The large particles are detached from the diffusion layer in a ribbon shape.
In sample 1.3 (GI+MZ+GI) approximately 80% of the intermetallic dross particles are attached to the diffusion layer. There are dross particles 'floating' in the solidified Zn-phase, located near the build-up structure. There are no dross particles visible in the solidified Zn-phase near the embedded resin. In sample 1.2 dross particles are observed near the embedded resin. The shape of the particles that 'float' near the build-up structure in sample 1.3 (GI+MZ+GI) have a faceted shape.
Sample 1.4 shows a similar structure as that of sample 1.2. The shape of the particles is for all

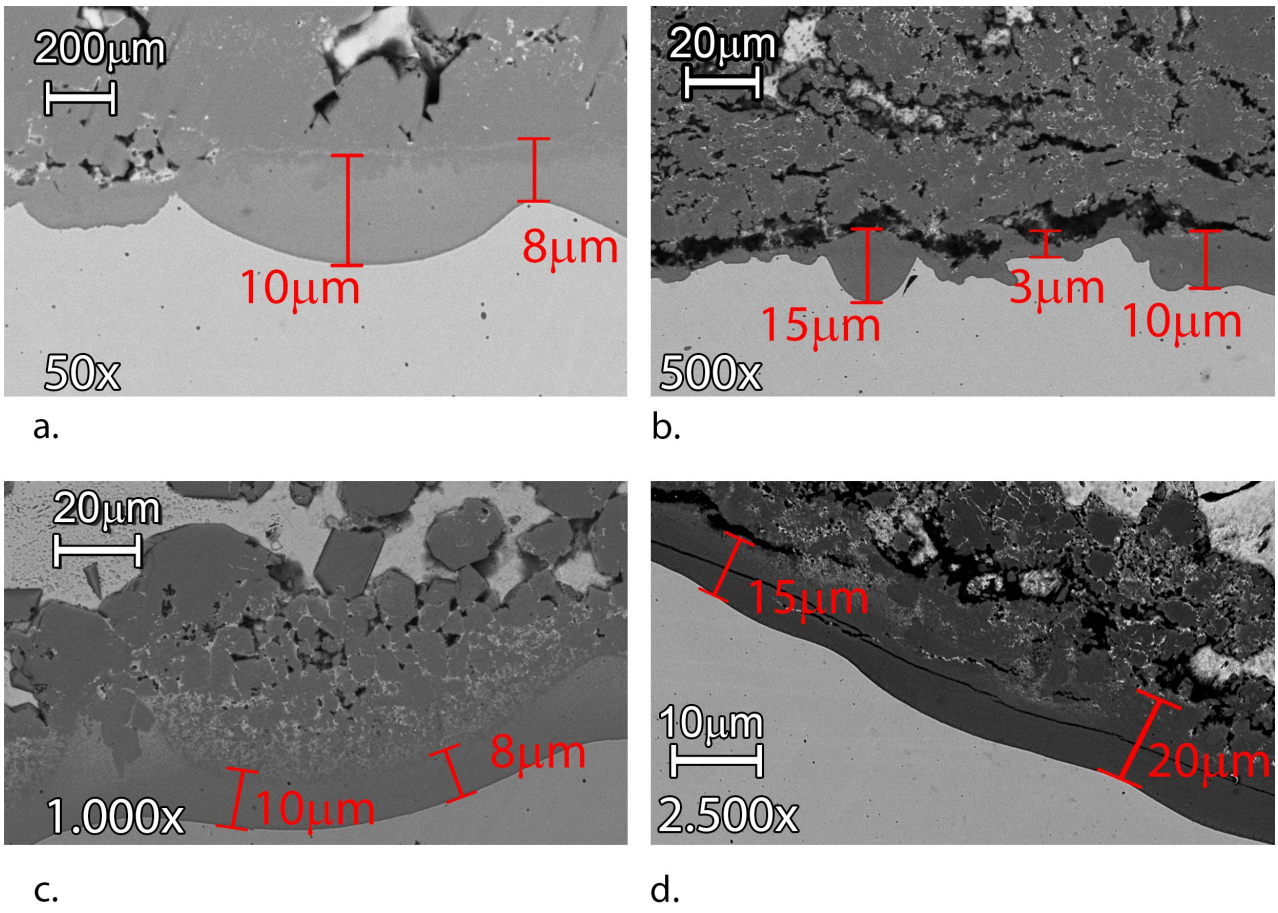

Figure 5-19: The thickness of the diffusion layers are displayed. Figure a.) shows the thickness in sample 1.1, b.) shows the thickness in sample 1.2 , c.) shows the thickness in sample 1.3 and d.) shows the thickness in sample 1.4. In all samples the average estimated thickness of the diffusion layer is around $10\,\mu\mathrm{m}$. The thickness varies between $3\,\mu\mathrm{m}$ and $20\,\mu\mathrm{m}$.

Sample	Days submerged	Baths
Sample 2.1	93 hours GI	GI
Sample 2.2	93 hours GI + 32,5 hours MZ	GI+MZ
Sample 2.3	93 hours GI + 55,5 hours MZ	GI+MZ
Sample 2.4	93 hours GI + 70,5 hours MZ	GI+MZ

Table 5-6: Schedule of the samples of experiment 2

particles curved with jagged sides. The difference between these two samples is the position of the intermetallic dross particles in the build-up. In sample 1.2 (GI+MZ) the intermetallic dross particles are scattered throughout the whole solidified Zn-phase, whereas approximately 95% of the loosened intermetallic dross particles 'float' near the dross build-up structure in sample 1.4 (GI+MZ+GI+MZ).

Samples 1.2 (GI+MZ), 1.3 (GI+MZ+GI) and 1.4 (GI+MZ+GI+MZ) have besides curved shaped intermetallic dross particles also small white ribbon shapes within the intermetallic dross particles. Sample 1.3 contains more white 'ribbons' as sample 1.2. Sample 1.4 contains more 'ribbons' than sample 1.3.

5-2 Results Experiment 2: Diminishing Rate of Dross Build-up in MZ

In experiment 2 four 316L SS rods were all submerged in the GI. Sample 2.1 was taken out after 93h in GI. The samples 2.2, 2.3 and 2.4 are after 93h GI submerged in MZ for 32,5 hours, 55,5 hours and 70,5 hours, respectively. The schedule of the four rods in experiment 2 is shown in Table 5-6. The dross build-up of each rod are presented in the next sections.

5-2-1 Sample 2.1 (93h GI only)

In Figure 5-20 the layer of only GI can be seen, respectively with a magnification of 50x, 200x, 800x and 1.500x. At a 50x magnification Figure 5-20.a gives an overview of the dross build-up layer on the 316L SS sample. In this figure it is visible that the layer of intermetallic dross particles formed over the whole surface, similar to that of the sample 1.1 of experiment 1, as seen in Figure 5-1.
In Figure 5-20.c large faceted particles are shown. These particles are 'floating' in the solidified Zn, or partly attached on the diffusion layer. The thickness of the floating particles varies between the 10 µm and 120 µm. The intermetallic dross particles attached varies between the 10 µm and 50 µm.

In build-up layer cracks are shown, which are visible in Figures 5-20.c and 5-20.d. These cracks are between the diffusion layer and the intermetallic dross particles, at a distance of about 10-15 µm from the build-up/steel interface.

Additionally, in Figure 5-20.a and 5-20.b in the pure Zn an accumulation of multiple 'floating' dross particles are seen. These particles have faceted as well as curved shapes. The curved

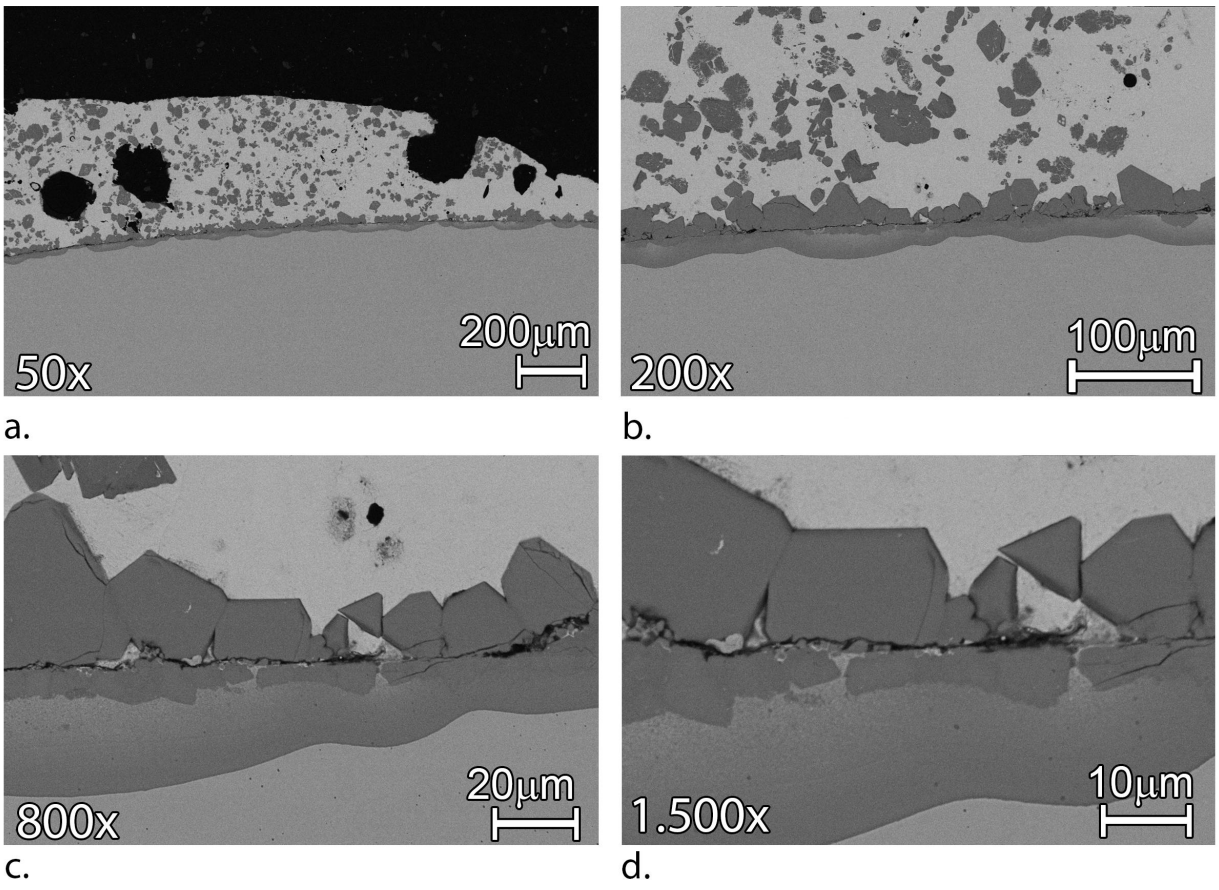

Figure 5-20: Cross section of sample 2.1 that is submerged only in GI for 93 hours. The magnifications of the cross sections are a.) 50x, b.) 200x, c.)800x and d.) 1.500x

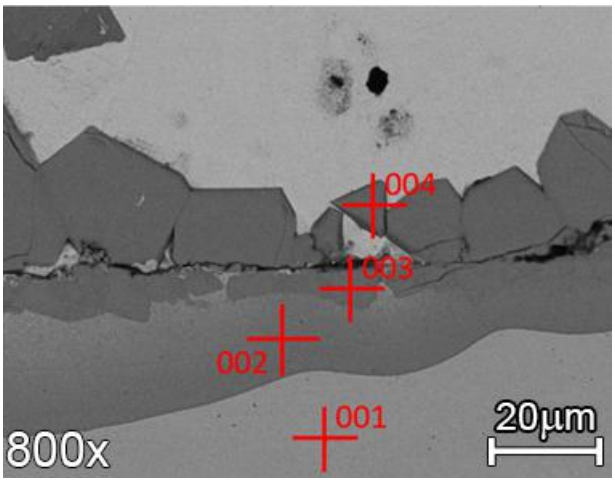

Figure 5-21: Four points are taken in an EDX-analysis of sample 2.1. The four points are taken in different areas of the sample.

shaped particles are located near the mount. The faceted particles are located near the steel/build-up interface.

As seen in Figure 5-20.d the diffusion layer shows two different shades of grey. Near the intermetallic dross particles, the diffusion layer appears in the same colour as the intermetallic dross particles. Towards the steel substrate there is a gradient visible in the grey-colour of the diffusion layer: the closer towards the stainless steel the diffusion layer appears darker.

Process Data

All four samples are inserted in the GI bath at the same time. Sample 2.1 came out a few hours before the bath changed to MZ. The sample is immersed of a total time of 73 hours and 18 minutes. In this time period, the temperature was stable. The temperature had an average of 465,3°C (maximum is 471,4°C, minimum is 457,1°C).
The Al-concentration varied between 0,178 wt% and 0,239 wt%, with an average of 0,208 wt%. The concentration of Fe was on average 0,017 wt%. These values were in the acceptable range for production, which is between 0,2 and 0,3 wt% as can be read in Section 1-1-5.

Chemical Composition

As seen in Figure 5-20.c and 5-20.d in the diffusion layer various gradients of grey are observable. An EDX-analysis was carried out in order to determine the different elements. In Figure 5-21 the four points are shown that have been analysed in sample 2.1. The EDX-spectra are shown in Appendix B.
Point 001 gives the chemical composition of the stainless steel. Point 002 and 003 are taken to distinguish the difference in composition of the dark-grey and light-grey colour that are visible in the diffusion layer that is clearly visible in Figure 5-20. Point 004 is taken to distinguish if there is a difference in composition between the diffusion layer and intermetallic dross particles.

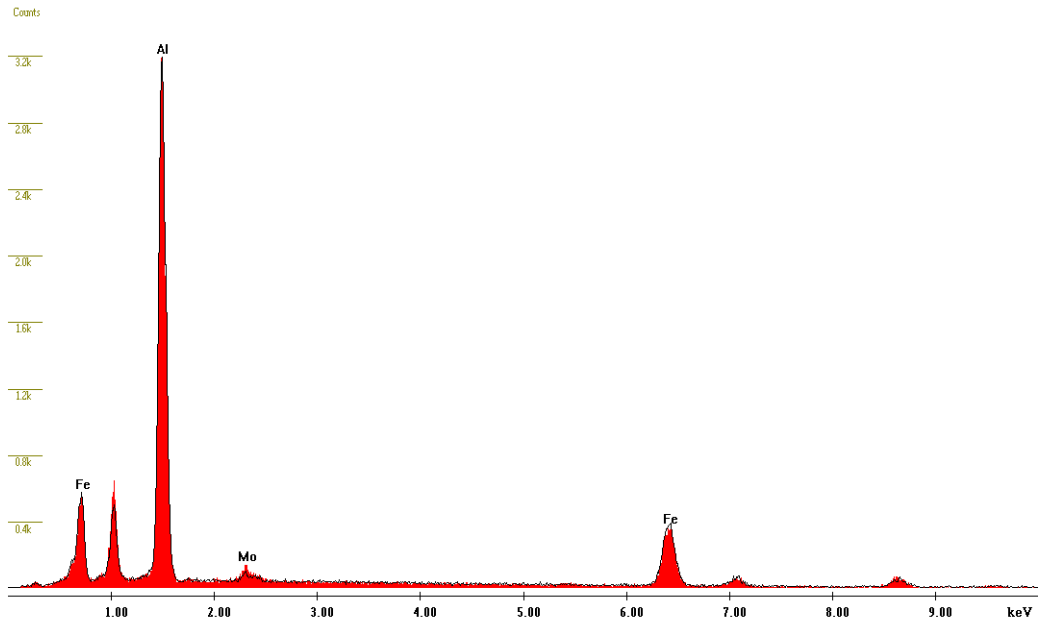

Figure 5-22: An overlay of the spectra of point 002 (red) and point 003 (black) is created. Between the spectra very little difference is observed.

Points taken	Fe (wt%)	Al (wt%)	Zn (wt%)	Mo (wt%)	Other elements (wt%)	Possible Structure
EDX 001	69,27	-	-	2,05	16,35 (Cr), 10,13 (Ni), 0,5 (Si), 1,64 (Mn)	316L SS
EDX 002	38,16	45,21	16,63	2,03	-	Fe_2Al_5
EDX 003	37,44	41,42	17,10	1,84	-	Fe_2Al_5
EDX 004	40,19	41,72	18,09	-	-	Fe_2Al_5

Table 5-7: The quantification results are shown of the EDX-analysis that is carried out on sample 2.1. The points correspond to the points taken in Figure 5-21.

Points 002 and 003 in Figure 5-21 are taken in different shades of grey in the diffusion layer. As seen in Appendix B the spectra show very similar peaks. In order to distinguish if there is a difference in composition between the points of interest, an overlay of the spectra of the point 002 and point 003 is made.
The overlay is shown in Figure 5-22. Only very small differences in composition between the two areas are observed. Both points have similar composition of Fe and Al, point 002 shows a little less fraction of Zn and Mo. In Figure 5-23 an overlay of the spectra of point 002 and spectrum 004 is shown. In point 002 Mo is observed, whereas point 004 does not contain Mo. The other elements Fe, Al and Zn show similar compositions in both points.
The quantitative results of the EDX-analysis are displayed in Table 5-7. The points 002, 003 and 004 do not differ much in composition. Only in point 004 no Mo is detected.

An element mapping of this sample was produced, as shown in Figure 5-24. This element mapping showed the spatial distribution of elements in the sample. The elements analysed

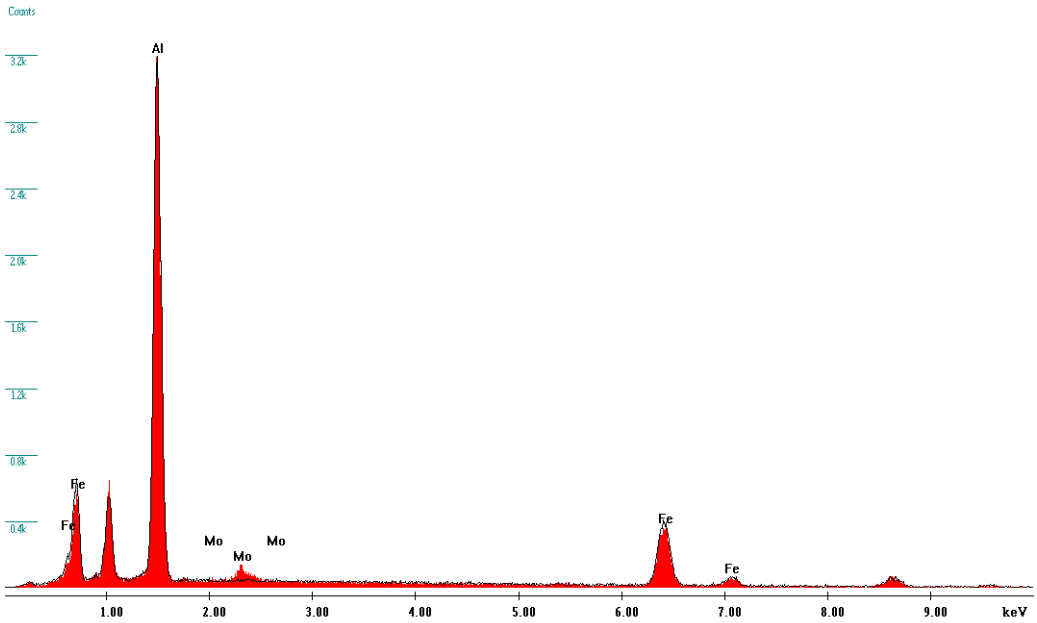

Figure 5-23: An overlay of the spectra of point 002 (red) and point 004 (black) is created. Between the spectra very little difference is observed. There is a significant difference in Mo. No Mo is detected in point 004.

were Al, C, Cr, Fe, Mo, Ni, O and Zn. For each element the following are observed:

- A high concentration of Al is shown in the intermetallic dross particles, as well as the dark grey area in the diffusion layer. A lower concentration of Al is seen in the rest of the diffusion layer. In the lightgrey area of the diffusion layer (where point 002 is taken in Figure 5-21) a gradient in the concentration of Al towards the stainless steel is seen.
- C is seen in the holes around and between the intermetallic dross particles, as well as O.
- Cr is found in the stainless steel. Also a spot with a high concentration of Cr is seen in a hole between the intermetallic dross particles and in the diffusion layer.
- Fe is similar to Al. A high concentration of Fe is shown in the intermetallic dross particles, as well as the dark grey area in the diffusion layer. A lower concentration of Fe is seen in the rest of the diffusion layer. In the light grey area of the diffusion layer Fe is equally distributed.
- A concentration of Mo is seen in the diffusion layer, below the crack. Furthermore some spots of a very high concentration Mo are seen in the diffusion layer. In the spots with a high concentration of Mo, no Al or Fe is distinguished. Mo is not observed in the intermetallic dross particles.
- Ni is only found in the 316L stainless steel substrate.
- Zn is found in the solidified Zn layer. A low concentration of Zn is shown in the light grey area of the diffusion layer.

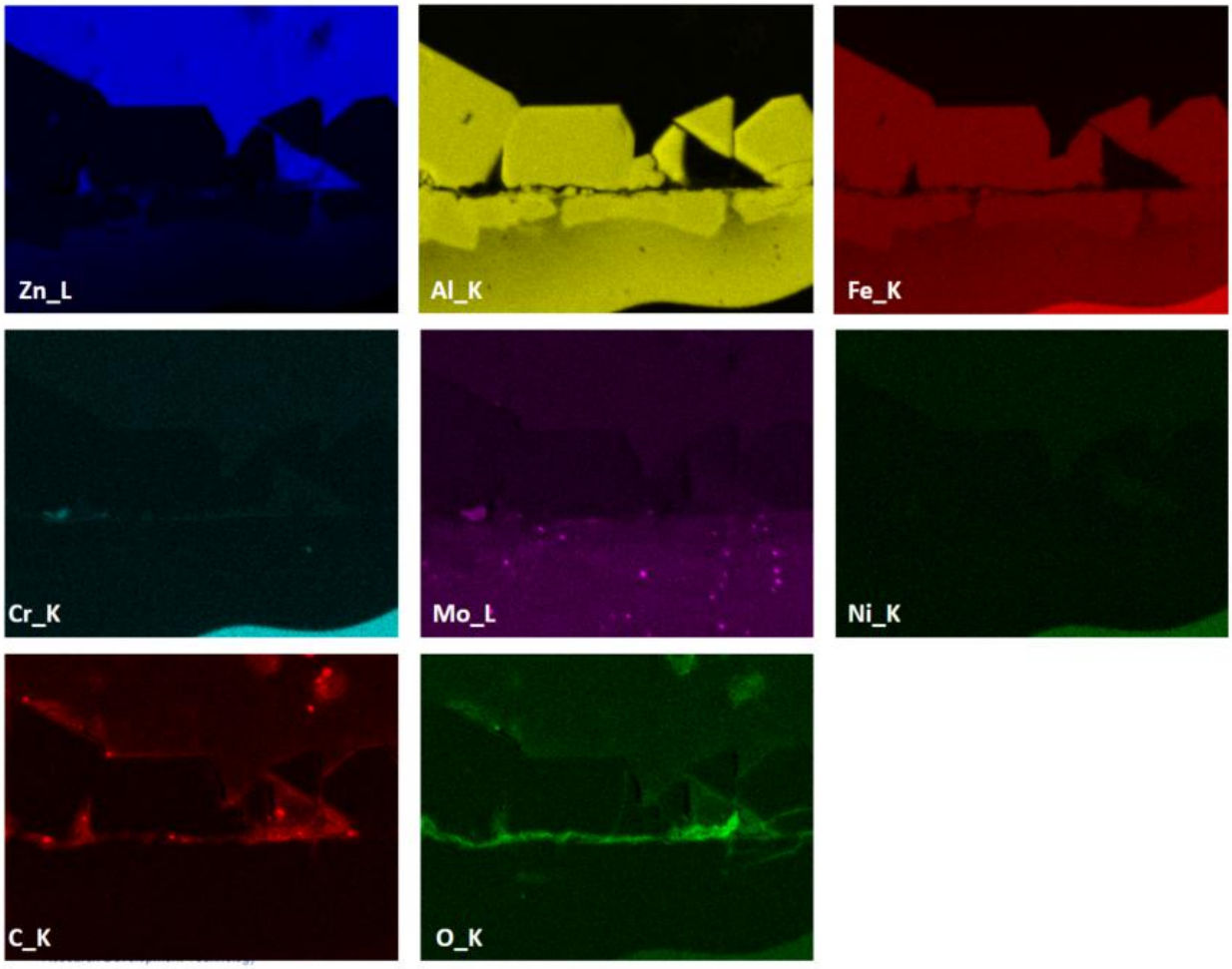

Figure 5-24: The results of the element mapping of sample 2.1 are displayed.

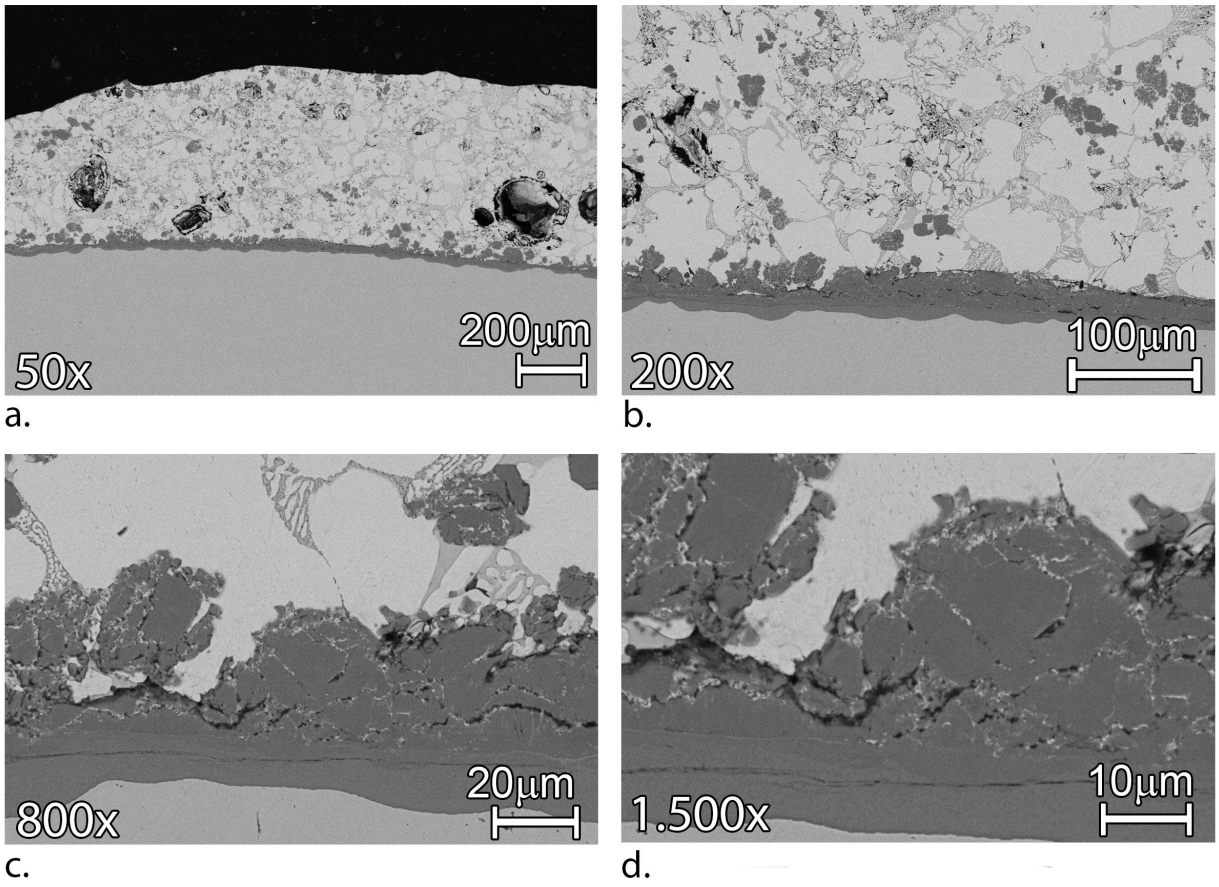

Figure 5-25: Cross section of sample 2.2, that is submerged in GI for 6 days and 32,2hours in MZ. The magnifications of the cross sections are a.) 50x, b.) 200x, c.)800x and d.) 1.500x

5-2-2 Sample 2.2 (93h GI+32,5h MZ)

In Figure 5-25.a to 5-25.d the layer of GI followed by 32,2 hours in MZ can be seen with a magnification of 50x, 200x, 800x and 1.500x, respectively. The total thickness of the dross build-up layer is 500 µm (on average), including the solidified MagiZinc. Without the solidified MagiZinc the dross build-up structure has an average thickness of 30 µm.

In Figure 5-25.a again the typical morphology of the dross build-up layer when submerged in GI and MZ is seen. Far less 'floating' dross particles are seen in the MZ-structure. On the left and right side of the image it is seen that the intermetallic dross particles are loosening from the diffusion layer. Some particles are already 'floating' in the MZ-structure close to the diffusion layer, while other particles are still attached on the diffusion layer. In the middle of the image it is seen that there are no particles 'floating' above the diffusion layer. In this area it seems that the process of delamination of the particles is not yet started. A magnification of the area where delamination has started is shown in Figure 5-25.b.
In Figure 5-25.b it can be seen that part of the layer starts to delaminate, whereas the other part only shows a few cracks in the build-up layer. The particles that are loosening from the diffusion layer are not fully surrounded by Zn. The cracks are in line of each other at a distance of about 30 µm parallel to the build-up/stainless steel interface.

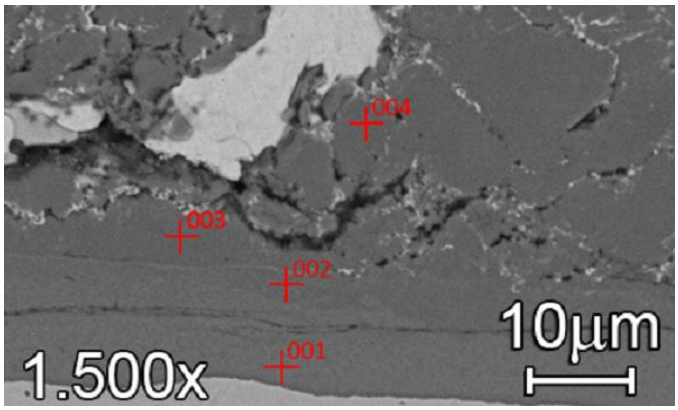

Figure 5-26: Points taken for an EDX-analysis in sample 2.2. The points are taken in order to determine the difference in composition in the diffusion layer and in intermetallic dross particles.

Figure 5-25.c and Figure 5-25.d were focused on the dross particles, at a magnification of 800x and 1.500x respectively. The intermetallic dross particles do not have the faceted structure anymore. The shape of the particles is curved with jagged sides. The particles contain white ribbons as seen in Figure 5-25.d. The size of these dross particles have similar size to the particles in sample 2.1, namely 10 µm to 50 µm.

Process Data

In this experiment, all four samples are inserted in the GI bath at the same time. Sample 2.2 remained in the set-up at when the bath changed from GI to MZ and came out after it was 32,5 hours submerged in MZ. The sample was immersed 73 hours and 18 minutes in GI and 32,5 hours in MZ. The temperature in GI was the same as in sample 2.1 (see 5-2-1). The temperature in the MZ-bath had an average of 450,7°C (maximum is 453,4°C, minimum is 444,8°C). The Al-concentration in the MZ-bath varied between 1,53 wt% and 1,63 wt%, with an average of 1,57 wt%. The concentration of Mg was on average 1,66 wt%.

Chemical Composition

In Figure 5-26 the points of where the EDX-analysis were carried out on sample 2.2 are shown. In Appendix B the spectra of the points are presented. The quantitative result of the EDX-analysis is shown in Table 5-8.

Point 001 gives the chemical composition of the diffusion layer below the crack that is visible in the diffusion layer. Point 002 and 003 are taken to distinguish the difference in composition of the dark-grey and light-grey colour that are visible in the diffusion layer above the crack. Point 004 is taken to distinguish if there is a difference in composition between the diffusion layer and intermetallic dross particles.

5-2-3 Sample 2.3 (93h GI+55,5h MZ)

In Figure 5-27.a to 5-27.d the layer formed in GI and followed by 55,5 hours of immersion in MZ can be seen, respectively with a magnification of 50x, 200x, 800x and 1.500x.

Points taken	Fe (wt%)	Al (wt%)	Zn (wt%)	Mo (wt%)	Other elements (wt%)	Possible Structure
EDX 001	38,96	49,86	6,83	3,21	-	Fe_2Al_5
EDX 002	39,08	49,79	6,88	1,87	0,83 (Cr)	Fe_2Al_5
EDX 003	37,18	51,52	9,09	1,71	0,34 (Cr)	Fe_2Al_5
EDX 004	38,52	53,87	7,42	-	0,12 (Si)	Fe_2Al_5

Table 5-8: The quantification results are shown of the EDX-analysis that is carried out on sample 2.2. The points correspond to the points taken in Figure 5-26.

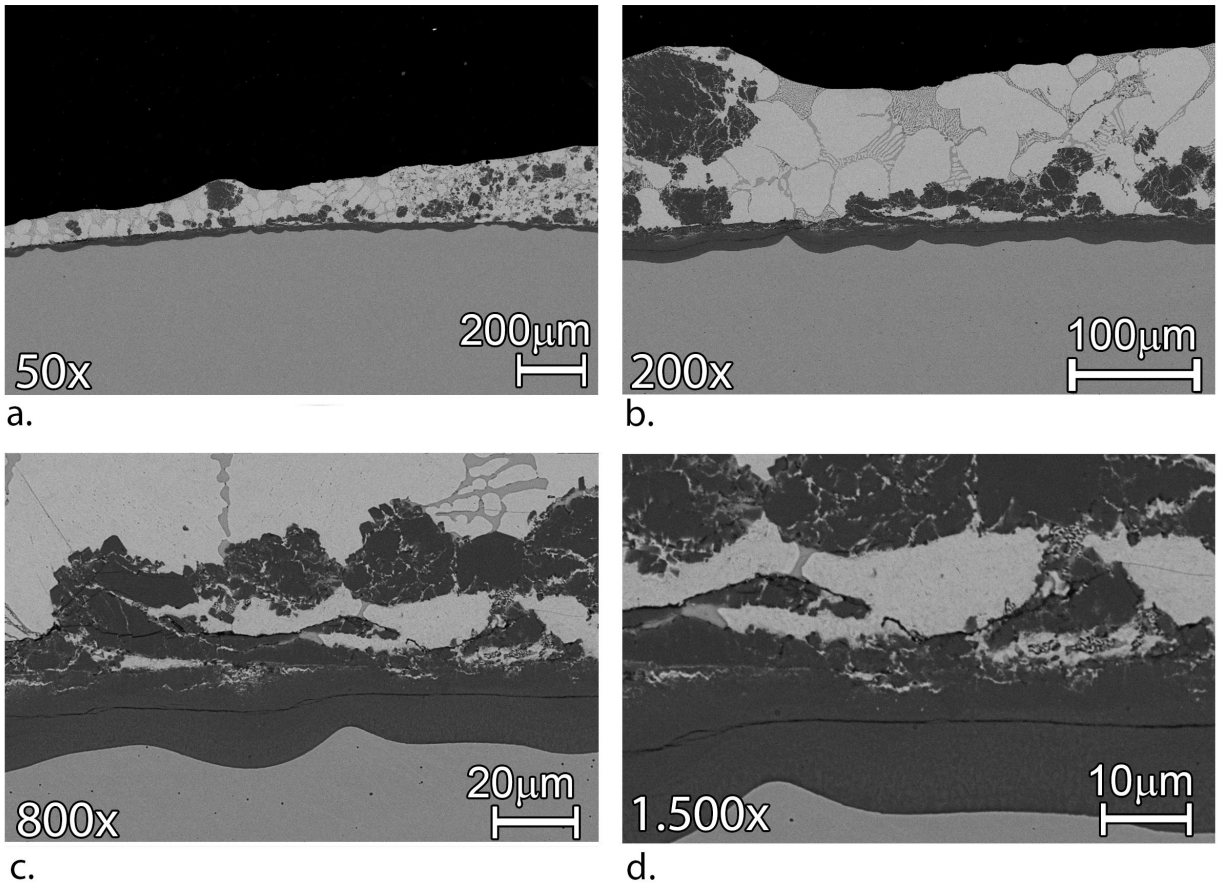

Figure 5-27: Cross section of sample 2.3 that is submerged for 140h in GI and 55,5hours in MZ. The magnifications of the cross sections are a.) 50x, b.) 200x, c.)800x and d.) 1.500x

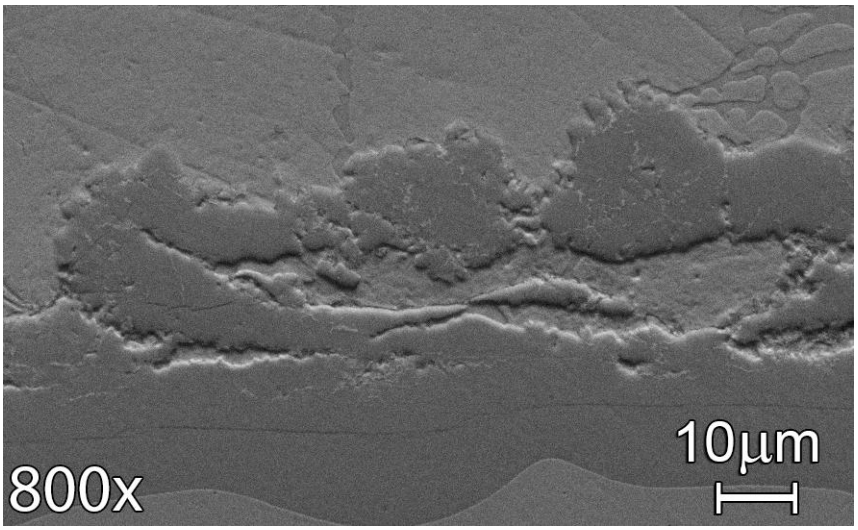

Figure 5-28: An image in the topographical mode of Figure 5-27.c.

In Figure 5-27.c the diffusion layer is visible. Above the diffusion layer towards the mount, the intermetallic dross particles are 'floating' in the MZ-structure; the particles are surrounded by the MZ-structure. The distance between the floating particles and the diffusion layer is about 2 µm to 10 µm. Most of the intermetallic dross particles are located near the diffusion layer. Only a few large intermetallic dross particles are visible 'floating' in the solidified Zn, as shown in Figure 5-27.a.

Figure 5-27.c shows a magnification of a collection of floating intermetallic dross particles. Small white ribbons appear in the 'floating' particles. The white ribbons are in a higher concentration than the white ribbons in the sample 2.2 (93h GI+32,5h MZ). The thickness of the dross particles are between 10 µm to 40 µm, on average20 µm. This particle size is similar to the size of the particles in samples 2.1 and 2.2. Between the floating particles and diffusion layer only pure Zn is seen. Only a small phase of binary $MgZn_2$ is shown between the particle and diffusion layer. This phase is best visible in Figure 5-27.d. In the diffusion layer a crack is visible, parallel to the diffusion layer/stainless steel interface. This crack is visible throughout the whole build-up layer. A topographical image of Figure 5-27.c is displayed in Figure 5-28. The crack is still visible, however very superficial.

Process Data

Sample 2.3 was partly submerged in GI for 73 hours and 18 minutes followed by 55,5 hours in MZ. In this time period, the temperature was stable in both baths. The temperature in GI was the same as in sample 2.1 (see 5-2-1). The temperature in the MZ-bath had an average of 451,1°C (maximum is 464,2°C, minimum is 444,8°C). The concentration of Al in MZ varied between 1,53% and 1,63 wt%, with an average of 1,58 wt%. The Mg-concentration had an average of 1,66 wt%, ranging between 1,60 wt% and 1,69 wt%.

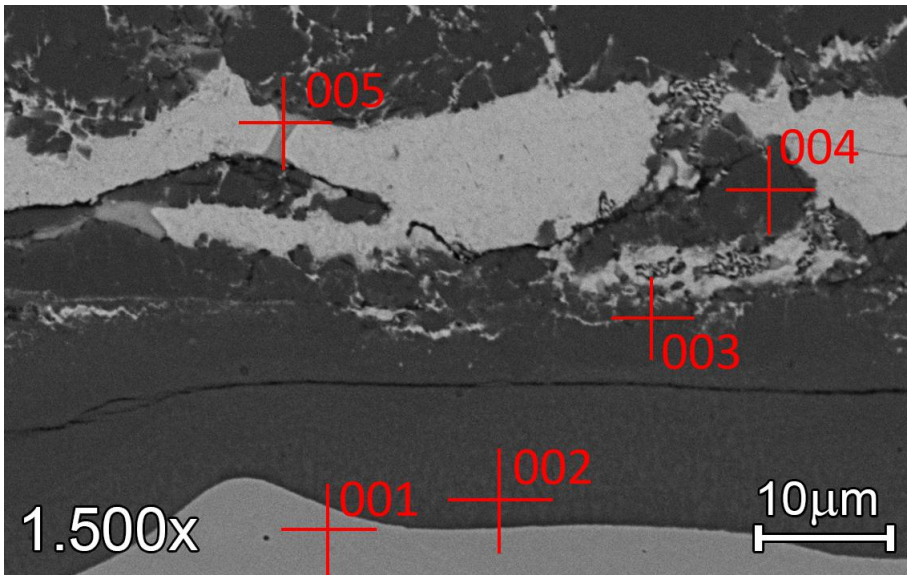

Figure 5-29: The points that are taken for EDX-analysis of sample 2.3 are denoted. Point 001 is taken in the stainless steel. Point 002 is taken near the stainless steel/diffusion layer interface. Point 003 is taken to distinguish if there is a difference in chemical composition above the crack. Point 004 is taken to see if there is a difference in composition in the 'floating' intermetallic dross particles and 005 is taken to determine the chemical composition of the binary structure of MZ.

Chemical Composition

Again, an EDX-analysis was carried out in order to determine the different elements in the dross build-up layer. In Figure 5-29 the five points are shown that have been analysed in sample 2.3. The quantitative data of the points is displayed in Table 5-9.

Point 001 gives the chemical composition of the stainless steel. Point 002 is taken to distinguish the chemical composition of the diffusion layer. Point 003 is taken in the diffusion layer above the crack. This point is taken to show if there is any influence of Mg in the possible delamination of the intermetallic dross particles from the diffusion layer. Point 004 is taken to distinguish if there is a difference in composition between the diffusion layer and

Points taken	**Fe (wt%)**	**Al (wt%)**	**Zn (wt%)**	**Mo (wt%)**	**Other elements (wt%)**	**Possible Structure**
EDX 001	69,02	-	-	2,11	16,48 (Cr), 1,67 (Mn), 10,16 (Ni), 0,56 (Si)	316L SS
EDX 002	37,04	50,01	7,44	4,21	0,94 (Cr), 0,30 (Ni)	Fe_2Al_5
EDX 003	36,78	50,93	6,94	3,06	0,30 (Cr)	Fe_2Al_5
EDX 004	38,69	54,66	6,64	-	-	Fe_2Al_5
EDX 005	-	-	85,12	-	14,86 (Mg)	$MgZn_2$

Table 5-9: The quantification results are shown of the EDX-analysis that is carried out on sample 2.3. The points corresponds to the points taken in Figure 5-29.

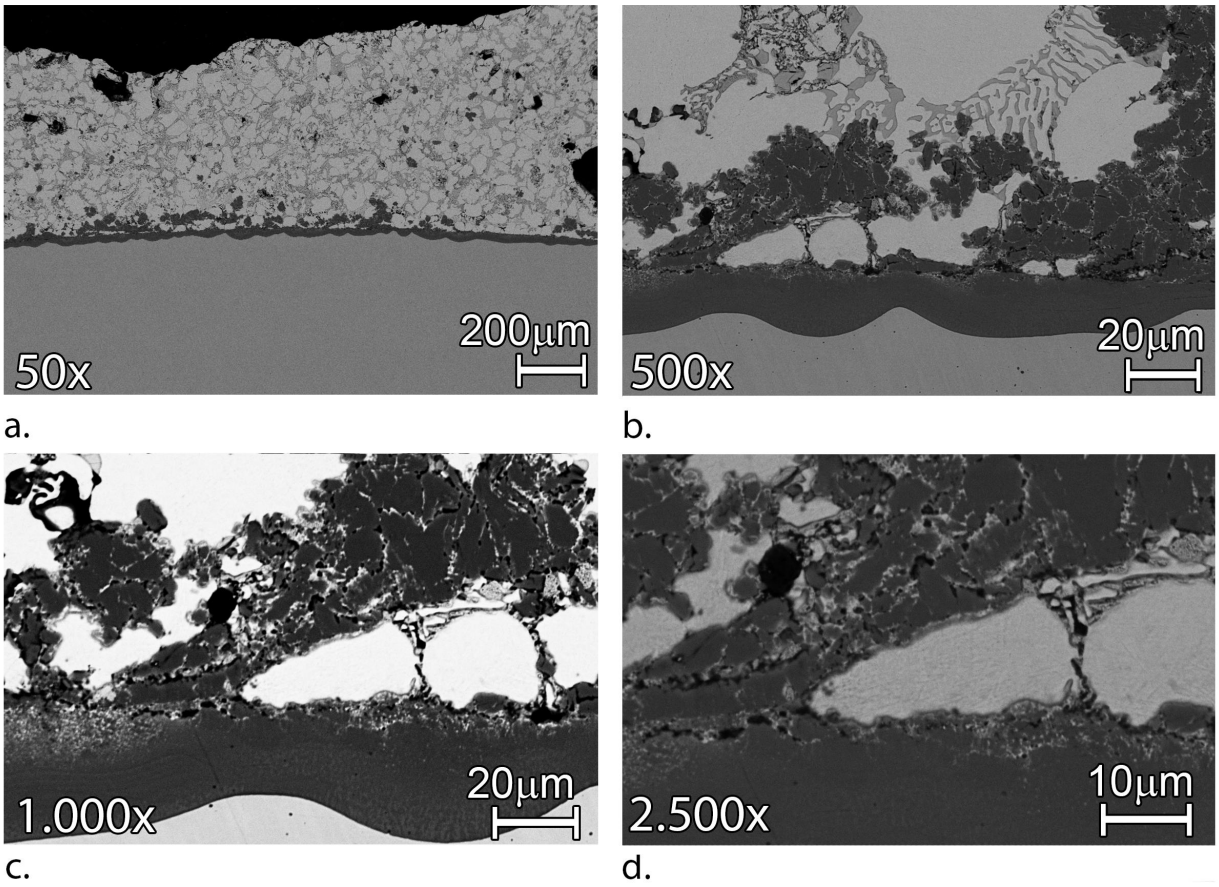

Figure 5-30: Cross section of sample 2.4 that is submerged in GI and 70,5 hours in MZ. The magnifications of the cross sections are a.) 50x, b.) 500x, c.)1.000x and d.) 1.500x

intermetallic dross particles. Point 005 is taken to identify the light grey phase that is visible in the solidified MZ-structure.

5-2-4 Sample 2.4 (93h GI+70,5h MZ)

In Figure 5-30 the dross build-up structure submerged in GI and followed by 70,5 hours in MZ is displayed with a magnification of 50x, 500x, 1.000x and 1.500x, respectively.
At a 50x magnification Figure 5-30.a gives an overview of the dross build-up layer. In this Figure it is seen that there is a diffusion layer over the whole surface of the stainless steel. On top of this layer large particles are seen. The particles are covered with a layer that has the MZ structure: pure Zn (white), binary structure and ternary structure are visible. The thickness of the intermetallic dross particles are between 5 µm to 40 µm, on average 15 µm.
At a magnification of 500x Figure 5-30.b shows the intermetallic dross particles loosening from the diffusion layer. Between the loosened particles pure Zn can be seen, as well as ternary structure of MZ.
In Figure 5-30.c a magnification of Figure 5-30.b is shown. The particles floating in the MZ-structure contains more white ribbons, in a higher concentration than in seen in sample 2.2 (93h GI+32,5h MZ) and 2.3 (93h GI+55,5h MZ).

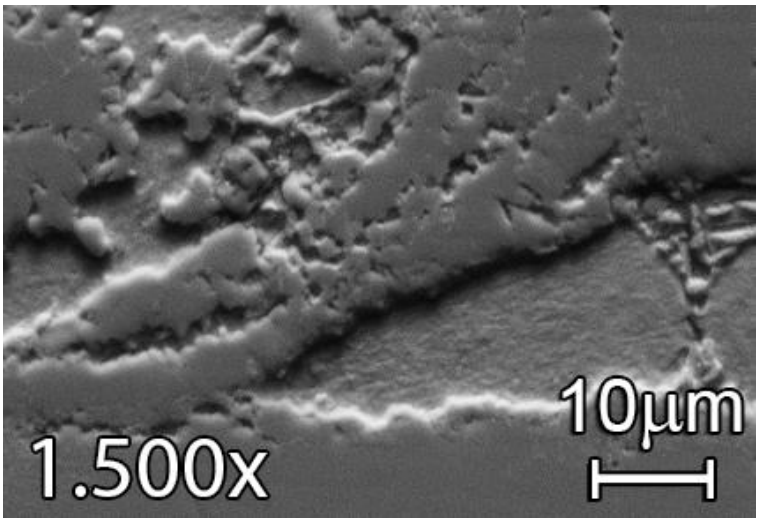

Figure 5-31: An image in the topographical mode of sample 2.4. The white ribbons appear in this figure as dimples or small cracks/holes.

Points taken	Fe (wt%)	Al (wt%)	Zn (wt%)	Mo (wt%)	Other elements (wt%)	Possible Structure
EDX 001	42,01	48,75	8,58	-	-	Fe_2Al_5
EDX 002	1,83	2,66	73,56	-	0,54 (Mg), 22,94 (O)	Zn + oxides from polishing
EDX 003	0,56	0,62	98,62	-	-	Zn

Table 5-10: The quantitative results are shown of the EDX-analysis that is carried out on sample 2.4. The points corresponds to the points taken in Figure 5-32.

Moreover, the white ribbons look wider and deeper penetrated into the dross particles. In the topographic image in Figure 5-31 it can be seen that some white ribbons are already visible, indicating a height difference. Other white ribbons look superficial. The average thickness of the diffusion layer is about 15 µm.

Process Data

Sample 2.4 was partly submerged for 140 hours in GI followed by 70,5 hours in MZ. In this time period, the temperature was stable in both baths. The temperature in GI was the same as in sample 2.1 (see 5-2-1). The temperature in the MZ-bath has an average of 451,0°C (maximum is 464,1°C, minimum is 444,8°C). The concentration of Al in MZ varied between 1,61 wt% and 1,72 wt%, with an average of 1,67 wt%. The Mg-concentration had an average of 1,667 wt%, ranging between 1,60 wt% and 1,69 wt%.

Chemical Composition

An EDX-analysis was carried out to get a better insight on the different elements in the build-up structure in sample 2.4. In Figure 5-32 the three points are shown that have been

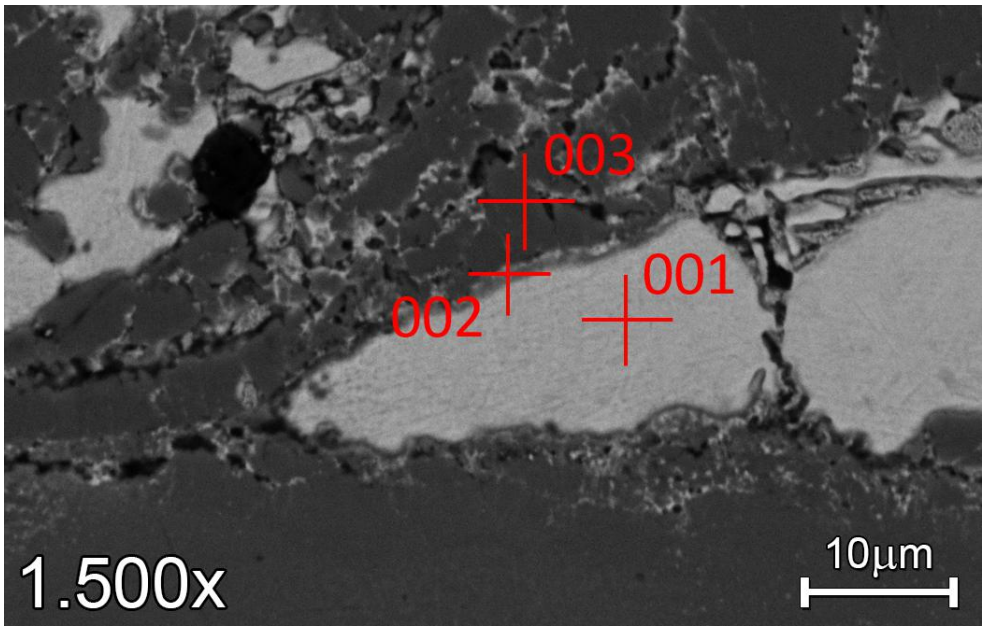

Figure 5-32: The points taken for EDX-analysis in sample 2.4 are displayed. Point 001 is taken in the Zn-phase. 002 is taken in the transition area to the intermetallic dross particles and point 003 is taken in the intermetallic dross particle.

analysed. The quantitative results of the chemical composition is displayed in Table 5-10. The corresponding spectra are shown in Appendix B.
Point 001 is taken in the white Zn-phase. Point 002 is taken to investigate whether there is a transition zone when the intermetallic dross particles start to detach from the diffusion layer.

An element mapping was carried out on sample 2.4. The element mapping is produced from Figure 5-30.d, as shown in Figure 5-33. The elements analysed were Al, C, Cr, Fe, Mg, Mo, O, Si and Zn.

5-2-5 EPMA Line Scans Performed in Sample 2

To determine the composition of the different elements present in the steel, the diffusion layer and the intermetallic dross particles and why Mo is detected in the diffusion layer and not other elements from the 316L SS e.g. Cr or Ni, EPMA line scans were carried out on four different 316L SS samples: A sample rod without Zn, that was heated, but not immersed in the liquid Zn, sample 2.1 (GI only), sample 2.2 (93h GI+32,5h MZ) and sample 2.4 (93h GI+70,5h MZ). The results of the performed line scans are displayed in Figure 5-34. These results give more insight in behaviour of elements in the different areas. The same elements to be analysed are the same in all the four line scans in order to make a good comparison between the different measurements.

In the sample rod without Zn the composition is similar over the area measured. The percentages are similar to the composition of 316L SS. In the other three samples the measurement in the steel show approximately the same composition. The measurements in the diffusion layer give similar percentages. In all three samples Ni is not detected and Cr is only detected

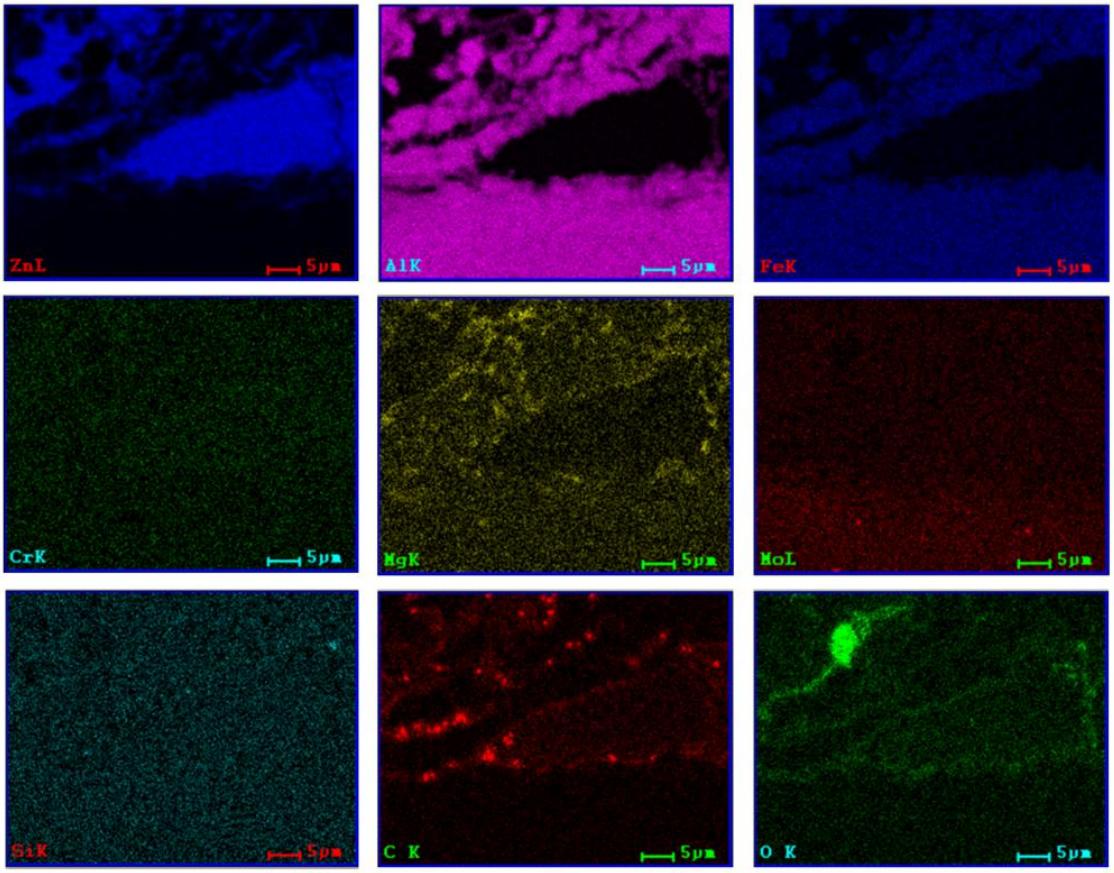

Figure 5-33: The results of the element mapping of sample 2.4 are displayed.

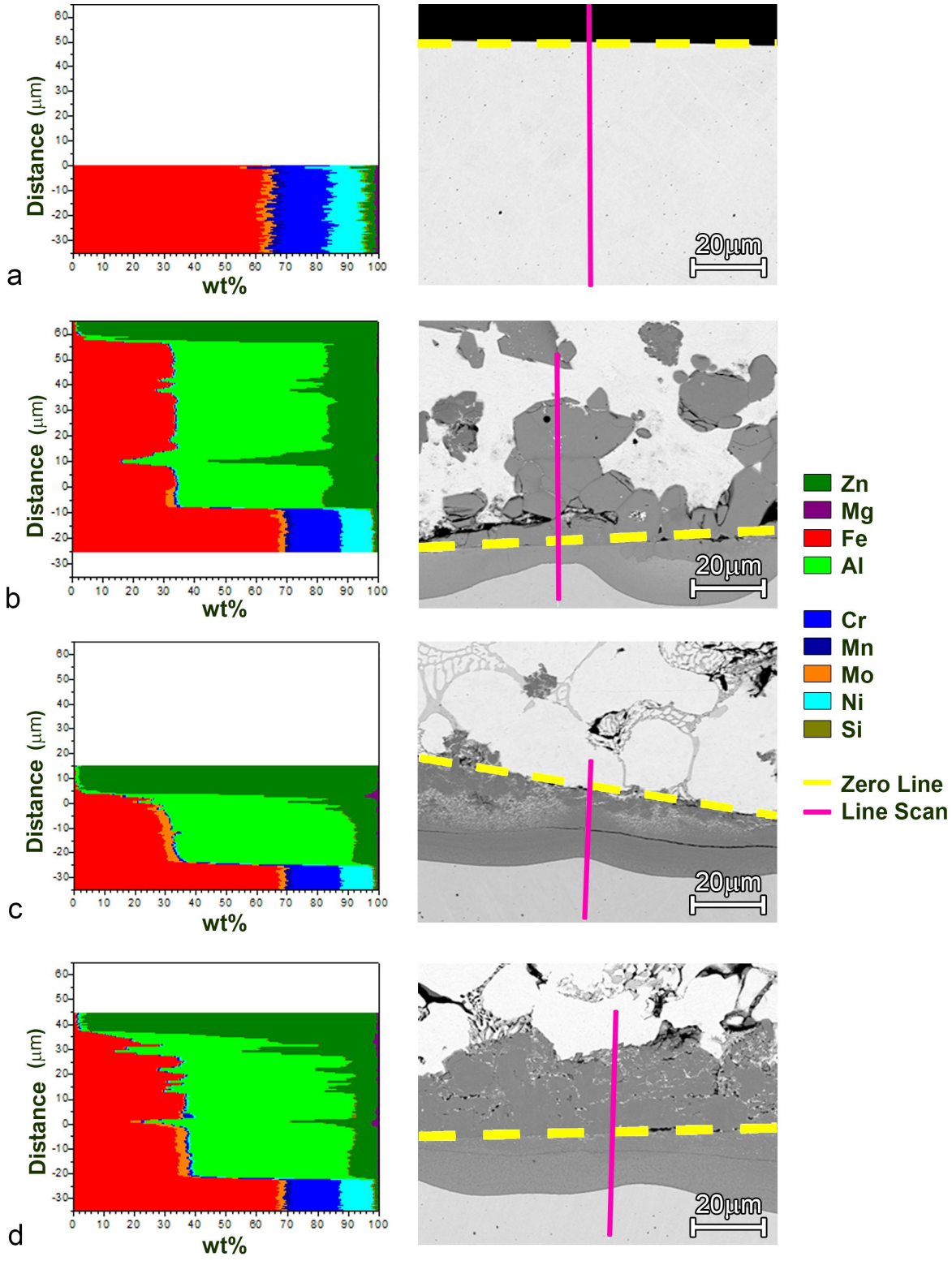

Figure 5-34: EPMA Line scans were performed on four different samples: a.) a sample that is not submerged in the liquid Zn, b.) Sample 2.1 (GI only), c.) sample 2.2 (93h GI+32,5h MZ) and d.) sample 2.4 (93h GI+70,5h MZ). In the results on the left the steel, the diffusion layer, intermetallic dross particles and solidified Zn-phase significantly differ in composition. The zero line is set on where the original surface of the steel was.

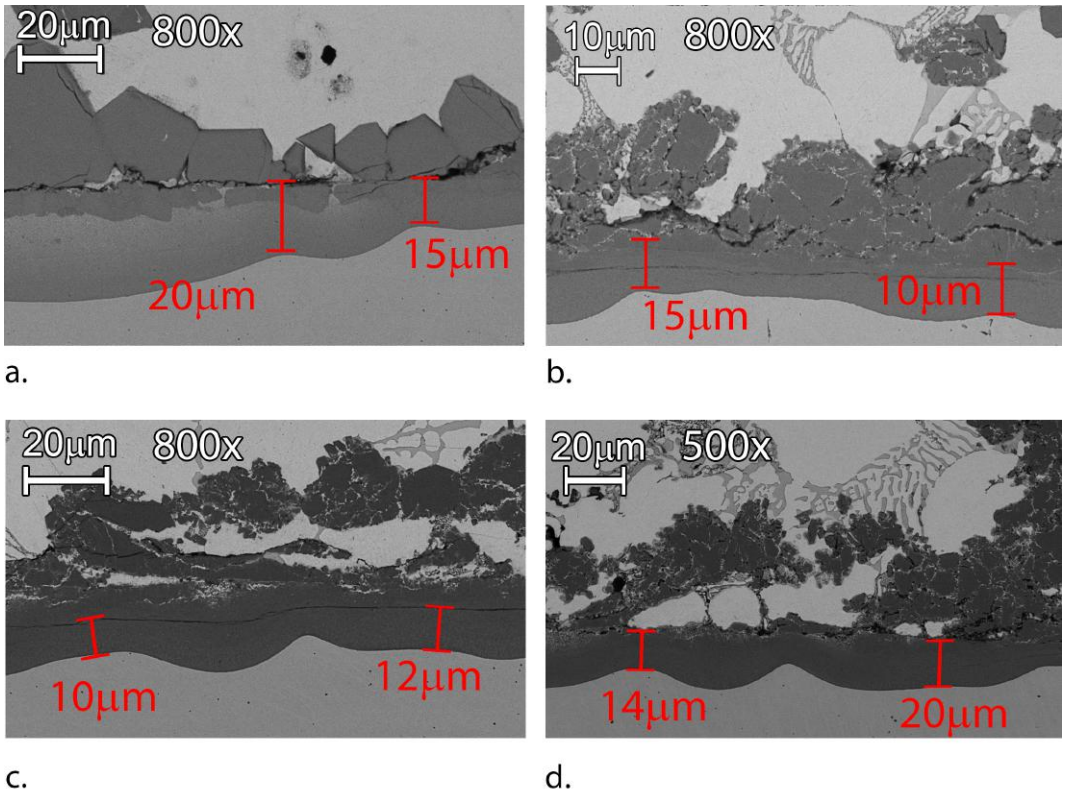

Figure 5-35: The sizes of the diffusion layers of the samples of experiment 2. Figure a.)shows sample 2.1 (93h GI only), b.) shows sample 2.2 (93h GI+32,5h MZ), c.) shows sample 2.3 (93h GI+55,5h MZ) and d.) shows sample 2.4 (93h GI+70,5h MZ).

in very low concentrations (∼1 wt%). Mo has a similar composition in the diffusion layer as in the steel. For the sample without Zn the zero line is set at the surface, for sample 2.1, 2.2 and 2.4 the zero line is set between the diffusion layer and the intermetallic dross particles.

5-2-6 Summary of Results Experiment 2

Experiment 2 is aimed to get insight on what the rate of delamination of the build-up structure is, when submerged in MZ-bath after a GI-campaign. Throughout the samples an evolution in delamination of the dross build-up structure between the samples 2.1 (93h GI only), 2.2 (93h GI+32,5h MZ), 2.3 (93h GI+55,5h MZ) and 2.4 (93h GI+70,5h MZ) can be seen.

The diffusion layer is of similar thickness in all the samples of experiment 2, as shown in Figure 5-35. The thickness is between 10 µm and 20 µm, on average 15 µm. All four samples have similar shape of the diffusion layer/steel interface. This interface has a wavy profile.

The composition of the diffusion layer will stay to some extent the same, namely Fe (35-45 wt%), Al (40-50 wt%), Zn (5-10 wt%) and Mo (1-4 wt%). In the backscattered images a colour gradient can be seen in the diffusion layer of sample 2.1, as seen Figure 5-20.c. This difference in colour is also visible in sample 2.2 (Figure 5-25.c) and sample 2.3 (Figure 5-27.c). Sample 2.4 hardly any difference in grey-scale in the diffusion layer is shown.

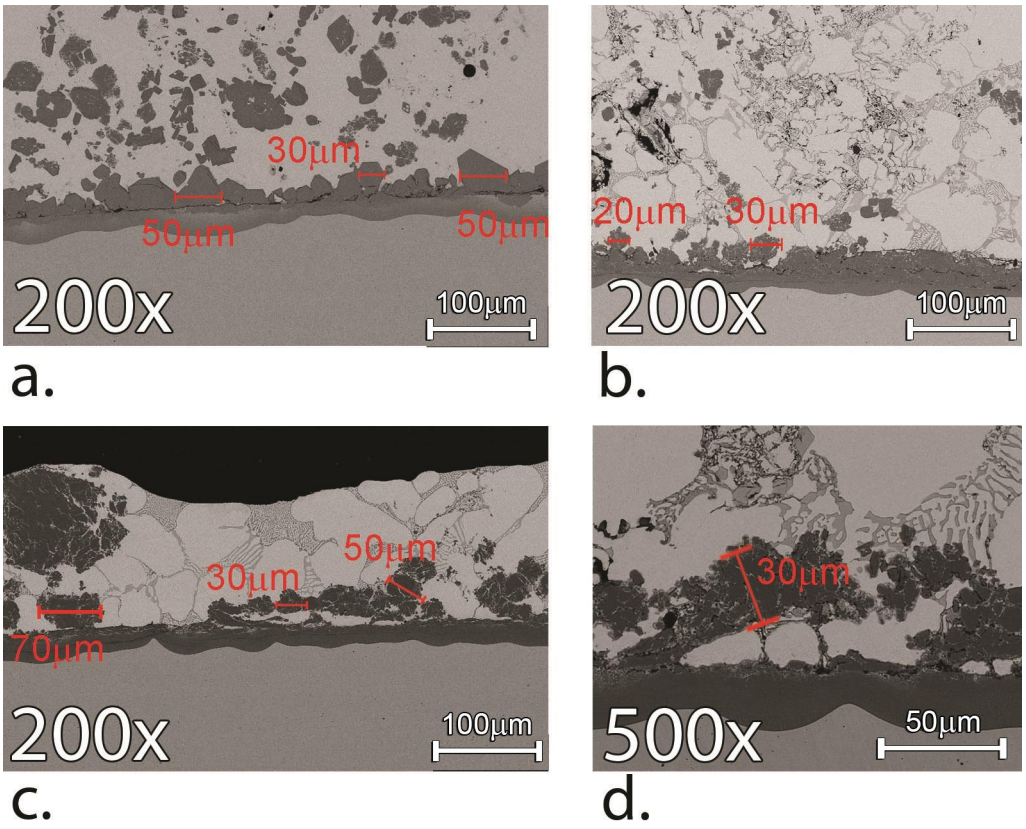

Figure 5-36: The sizes of the intermetallic dross particles are indicated in the samples.Figure a.)displays sample 2.1, b.)displays sample 2.2, c.)displays sample 2.3 and d.)displays sample 2.4

The intermetallic dross particles differ not much in size among the four samples of experiment 2. As seen in Figure 5-36.a, the average size of the particles in sample 2.1 40 µm. The average thickness of sample 2.2, sample 2.3 and sample 2.4 are shown in Figure 5-36.b, 5-36.c and 5-36.d respectively.
The average size of sample 2.2, sample 2.3 and sample 2.4 are 25 µm, 50 µm and 30 µm, respectively. However, these particles do not have the faceted structure that the intermetallic dross particles have in sample 2.1. The particles have a curved shape in the sample 2.2, sample 2.3 and sample 2.4.

Together with the curved shape, the intermetallic dross particles in the sample 2.2 (93h GI+32,5h MZ), sample 2.3 (93h GI+55,5h MZ) and sample 2.4 (93h GI+70,5h MZ) also show white 'ribbons' in the intermetallic dross particles. The size of the pieces these white 'ribbons' form become smaller the longer the samples are immersed in the MZ-bath. The difference in frequency of the white cracks in the intermetallic dross particles in sample 2.2, sample 2.3 and sample 2.4 is shown in Figure 5-37. In this Figure 5-37 it can be seen that the average distance between the white cracks in the intermetallic dross particles is 15 µm, 10 µm and 4 µm, respectively.

Sample 2.2 in Figure 5-25 shows the start of delamination; some dross particles start to detach from the diffusion layer. In this sample the majority (approximately 85%)of the intermetallic dross particles stick to the diffusion layer. In sample 2.3 in Figure 5-27 the majority of the

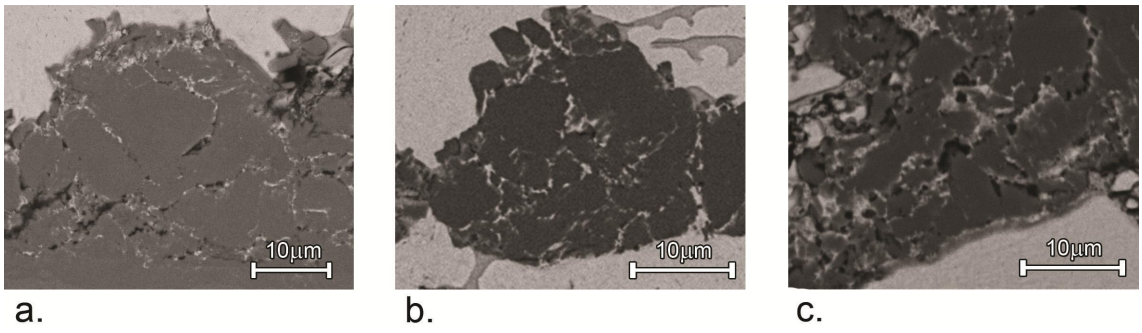

Figure 5-37: The differences in thickness of the white ribbons in the intemetallic dross particles is displayed. In Figure a.)Sample 2.2 is displayed, in b.) sample 2.3 and in c.) sample 2.4

dross start to detach or are already detached from the diffusion layer. The dross particles loosen clustered in a ribbon shape. This shape is also seen in sample 2.4, shown in Figure 5-30.

The behaviour of the phases of MZ is different in each of the three samples. In sample 2.2 the dross build-up structure is mostly surrounded by the pure Zn-phase, in a few places the binary $MgZn_2$ phase is at the dross build-up structure. In sample 2.3 the binary and ternary structure MZ are visible, especially between the loosened particles and diffusion layer. In sample 2.4 the distance between the diffusion layer and loosened particles is larger than in sample 2.3, on average 20 µm compared to 10 µm, respectively.

Chapter 6

Discussion and Recommendations

In this chapter the discussion and recommendations are presented. In Section 6-1 a discussion reflects on the experiments and results of this thesis. Furthermore, some phenomena of the experiments that are not understood completely at this time are given with corresponding hypothesis that could explain them. In Section 6-2 some recommendations are given that can help further research to better understand these unknown phenomena, as well as overall recommendations for future experiments on the dross build-up behaviour in Zn baths.

6-1 Discussion

From the results in Chapter 5 two characteristics can be determined that contribute to the delamination of the dross build-up structure. The first characteristic is the formation of cracks that are visible in the dross build-up structure. The other characteristic is the formation of small white ribbons in the intermetallic dross particles that have a curved interface. The two phenomena seem to be in relation with each other. The ribbons do not form in the intermetallic dross particles with a faceted interface. The relation between these two mechanisms is discussed.
Section 6-1-1 focuses on the cracks formed in the intermetallic dross particles and in the diffusion layer. Section 6-1-2 discusses the smoothening and curvature transition of the boundaries of the intermetallic dross particles. As a result of this faceted to curved interface transition the small white ribbons were formed in the intermetallic dross particles when submerged in MZ. These white ribbons are discussed in Section 6-1-3.
Furthermore, the presence of Mo and the absence of Cr and Ni in the diffusion layer are discussed in Section 6-1-4. Although the wavy pattern and chemical composition of the diffusion layer does not seems to have an effect on the delamination of the dross build-up structure, the observation concerning the composition of Cr, Mo and Ni is an interesting side-effect. This section ends with Section 6-1-6 where a mechanistic sequence of events of the explained phenomena.

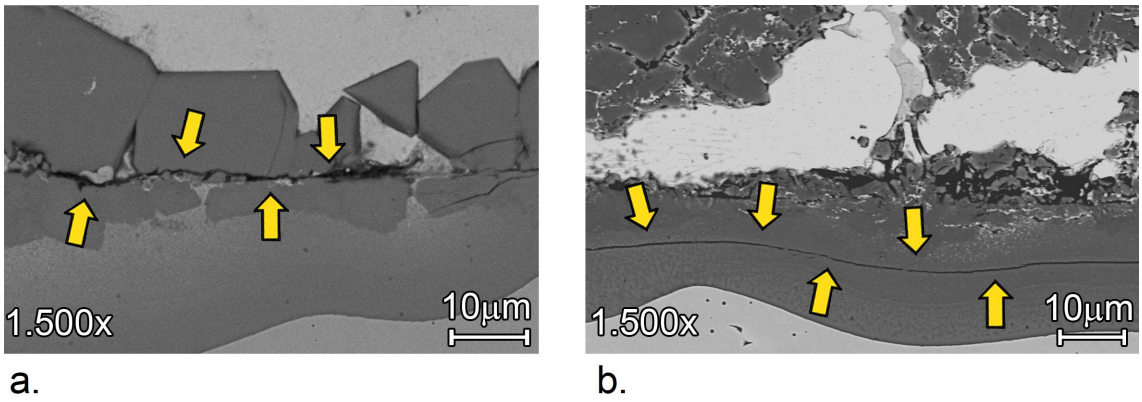

Figure 6-1: Two different types of cracks can be distinguished in all the samples of the experiments. In a.) a crack in the intermetallic dross particle-layer as a result of thermal stress cracking in sample 2.1 is displayed. In b.) a small crack in the diffusion layer in sample 2.2 is displayed.

6-1-1 Crack Formation

From the micrographs of the samples displayed in Chapter 5 two types of cracks can be distinguished. The two type of cracks are the cracks in the intermetallic dross particle-layer and in the diffusion layer, displayed in Figure 6-1.
Type 1 (Figure 6-1.a) is located mostly at or near the intermetallic dross particle/diffusion layer interface whereas type 2 (Figure 6-1.b) is located within the diffusion layer. Type 2 has a smooth line while type 1 has a more uneven shape. Furthermore type 1 appears black on the SEM-micrographs , type 2 is displayed more dark-grey and not black. This difference in colour indicates a difference in thickness of the crack.

Crack Type 1: Thermal Stress Cracking

At changing the baths the samples are air cooled. Subsequently the liquid Zn solidifies and a solid dross build-up layer is formed. At solidification strains are generated by this temperature change because of the difference in thermal expansion coefficients between the stainless steel and the dross build-up structure which causes thermal expansion mismatch. This mismatch generates strains within the sample. If the strain is large enough cracking will occur.

An example of this type of cracking is shown in Figure 6-1.a. The cracks shown in this figure are visible in all the samples of the two experiments are located in the intermetallic dross particles or between the intermetallic dross particles and diffusion layer.
This observation indicates that the thermal expansion coefficient in the intermetallic dross particles is lower than in the diffusion layer, causing strain in the intermetallic dross particles. However, as seen in the several EDX-analyses the composition of the diffusion layer is similar to the composition of the intermetallic dross particles. Both layers do have the composition of $Fe_2Al_5Zn_x$-phase. The explanation above about the difference in thermal expansion in the dross build-up structure needs to be explained in more detail.

The observation that only in the intermetallic dross particles large cracks are visible can be explained by that the diffusion layer has a better adhesion to the roll surface compared with

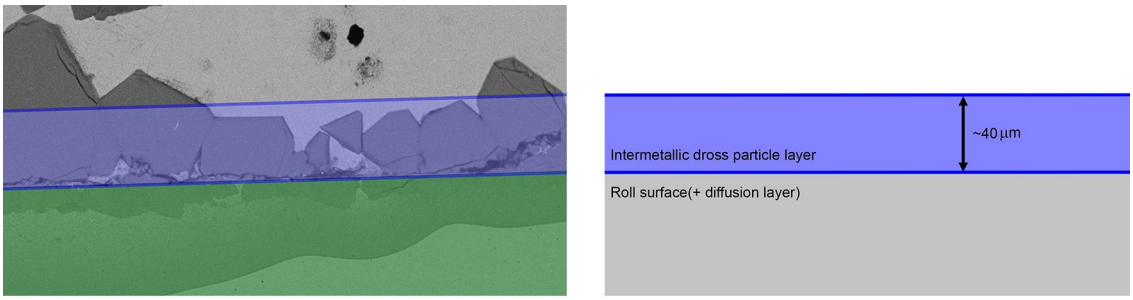

Figure 6-2: The simplification for determining the cracks formed due to cooling. In a.) the sample 2.1 (GI only) is used as a reference to make the simplification more clear. In b.) a schematic representation of this simplification is displayed.

the adhesion of the intermetallic dross particles to the diffusion layer. This better adhesion of the diffusion layer can be explained by that the diffusion layer is formed as a result of the diffusion of Al into the roll surface.

Part of Fe diffuses in the Zn-bath and a part of Fe remains in the diffusion layer and presumably does not change in orientation. Therefore the diffusion layer has similar orientation structure as of the 316L stainless steel. The diffusion layer can be characterized in terms of crystallography, topography or chemistry. Each of those factors is closely related to the constitution of the adhesive properties.

Because of this better adhesion the assumption is made that the intermetallic dross particles can be simplified as a coating layer formed on top of the roll surface, where the diffusion layer is merged in the roll surface. A schematic representation of this simplification is shown in Figure 6-2. With this simplification, a first indication can be made at what temperature change the cracks in the intermetallic dross particles will form.

The roll surface is much thicker than the intermetallic dross particle-layer; 40 µm compared with 12.5×10^3 µm, respectively. The thermal stresses within the dross build-up structure can be simplified as shown as in Figure 6-2. As the temperature dropped when the samples were taken out of the bath the dross build-up structure tends to shorten, but cannot as it is restrained along the 316L SS. This causes the build-up structure to be stressed, and eventually crack. Since the 316L SS roll surface has a factor two higher thermal expansion coefficient as the intermetallic dross particle-layer, $18.2 \times 10^{-6}\,\mathrm{K}^{-1}$ compared with $9.9 \times 10^{-6}\,\mathrm{K}^{-1}$, respectively, the intermetallic dross particle-layer shrinks more than the 316L SS roll surface [62]. The intermetallic dross particle-layer needs to be strained in order to stick on the more massive roll surface. This strain can be calculated by the following equation:

$$\epsilon = \Delta T(\alpha_1 - \alpha_2) \tag{6-1}$$

where α is the thermal expansion coefficients of the intermetallic dross particle-layer (α_1) and the roll surface (α_2) and ΔT the difference in temperature at cooling.

On cooling the roll surface and intermetallic dross particle-layer contract by different amounts because their expansion coefficients differ. This difference puts the intermetallic dross particle-

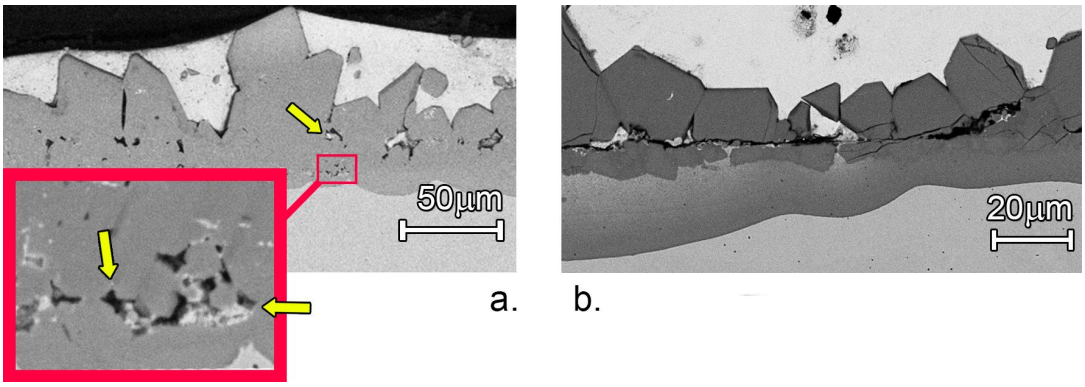

Figure 6-3: Sample 1.1 (a.) and 2.1 (b.) are displayed. Both samples contain only the faceted structure. In b.) a crack due to thermal shock is shown. This type of crack is absent in sample 1.1. With the yellow arrows closed volumes are indicated that can be the initiation for crack formation.

layer under stress. This residual stress can be calculated with the following equation [63]:

$$\sigma = \frac{E}{1-v}(\alpha_1 - \alpha_2)\Delta T \tag{6-2}$$

where σ is the stress in the intermetallic dross particle-layer, E the Young's modulus and v the Poisson's ratio. In equation 6-2 the Poisson's ratio is added due to the biaxial stress state in the intermetallic dross particle-layer.

As stated before, the $Fe_2Al_5Zn_x$-structure in the intermetallic dross particles has a different thermal expansion coefficient in comparison with the 316L stainless steel surface, $9.9 \times 10^{-6}\,K^{-1}$ compared with $18.2 \times 10^{-6}\,K^{-1}$, respectively [62]. The Young's Modulus of Fe_2Al_5 is 284 GPa [64], the Poisson's ratio is assumed to be 0,3 [64].
Filling in equation 6-2 gives:

$$\begin{aligned}\sigma &= \frac{284 * 10^9}{1-0,3}(9,9 * 10^{-6} - 18,2 * 10^{-6}) * (465 - 20) \\ &= 1,5 * 10^9 Pa \\ &= 1,5 GPa\end{aligned} \tag{6-3}$$

This calculated stress is higher than the stress of the intermetallic dross particle layer: 1,5 GPa compared to 715 MPa [64]. Therefore, the large cracks are the result of cooling the sample by changing the bath.

The cracks formed by the temperature change when the samples are taken out of the bath (Type 1) also influenced the dross build-up structure when submerged again in the liquid Zn-alloy.
The samples 1.1 and 2.1 are the only two samples that were submerged in only one bath (GI). These two samples show similar dross build-up structures: The intermetallic dross particles have a facet structure and mostly (95%) attached to the diffusion layer or to other intermetallic dross particles. The crack formation of these two samples are shown in Figure 6-3. The cracks formed by thermal shock in these samples do not cause delamination of the intermetallic dross particles, since these cracks are formed at cooling. After cooling these

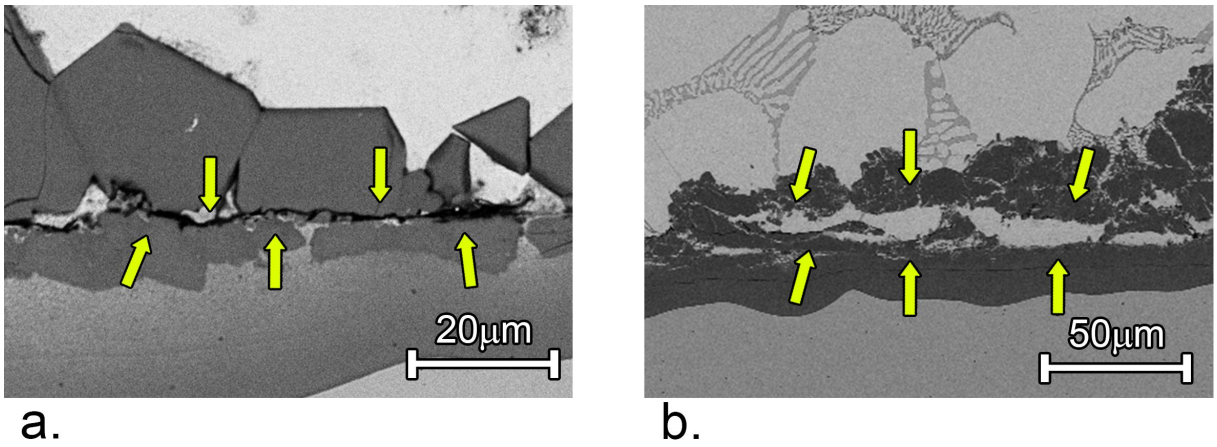

Figure 6-4: Two examples of cracks that are the result of thermal shock. In a.) Sample 2.1 is displayed. This figure is a duplicate of Figure 6-1.a. With the yellow arrows the crack is indicated. In the crack no Zn is diffused into. In b.) sample 2.3 is visible, where Zn is already penetrated into the crack. Both cracks are possibly formed at the same bath change, since sample 2.3 was immersed afterwards Zn could penetrate into the formed crack.

samples were not submerged again in the Zn-bath. When the samples would be submerged into the bath again after formation of these cracks, these cracks would cause delamination of the intermetallic dross particles, since Zn (GI or MZ) can diffuse into this crack. An initiation for the crack formation could be the closed volumes that formed at growth (see Figure 2-13). However this observation is not proven.

If inside the crack no Zn is detected, which is the case in sample 1.1 and 2.1 it can be concluded that this crack is formed by thermal shock since Zn is already solidified when crack formation due to cooling occurs. Zn cannot flow inside the crack any more when the Zn-phase is solidified. Subsequently no Zn can be found within the crack caused by thermal shock. In Figure 6-4.a Sample 2.1 is displayed. In this crack no Zn is detected.
The other samples (Sample 1.2, 1.3, 1.4, 2.2, 2.3 and 2.4) were submerged again in other baths. These samples differ from sample 1.1 and 2.1. Besides the curved structure the particles are not fully attached to other intermetallic dross particles or the diffusion layer, but 50-70% intermetallic dross particles are significantly more surrounded by solidified Zn-phase. The exact percentage differs on each sample. The cracks formed by thermal shock do have an influence on the intermetallic dross particles being surrounded by Zn.

In Figure 6-5 sample 1.2 is used as an example to indicate how the particles are surrounded by Zn. The particles are attached in a ribbon-shape to each other, surrounded by Zn. This 'ribbon' of intermetallic dross particles seems to fit within the remaining dross build-up structure that is attached to the stainless steel. The hypothesis is that a crack was formed close to the transition between the diffusion layer and intermetallic dross particles. Due to the better adhesion of the diffusion layer to the 316L SS roll surface compared with the adhesion of intmertallic dros particles onto the diffusion layer, a crack was formed within is intermetallic dross particle-layer. A closed volume of Zn that was created at the formation and growth of the intermetallic dross particles could be a precursor for crack formation due to thermal shock. Examples of closed volumes are indicated in Figure 6-3.
Once these samples were submerged again, Zn penetrated into this crack, pushing the inter-

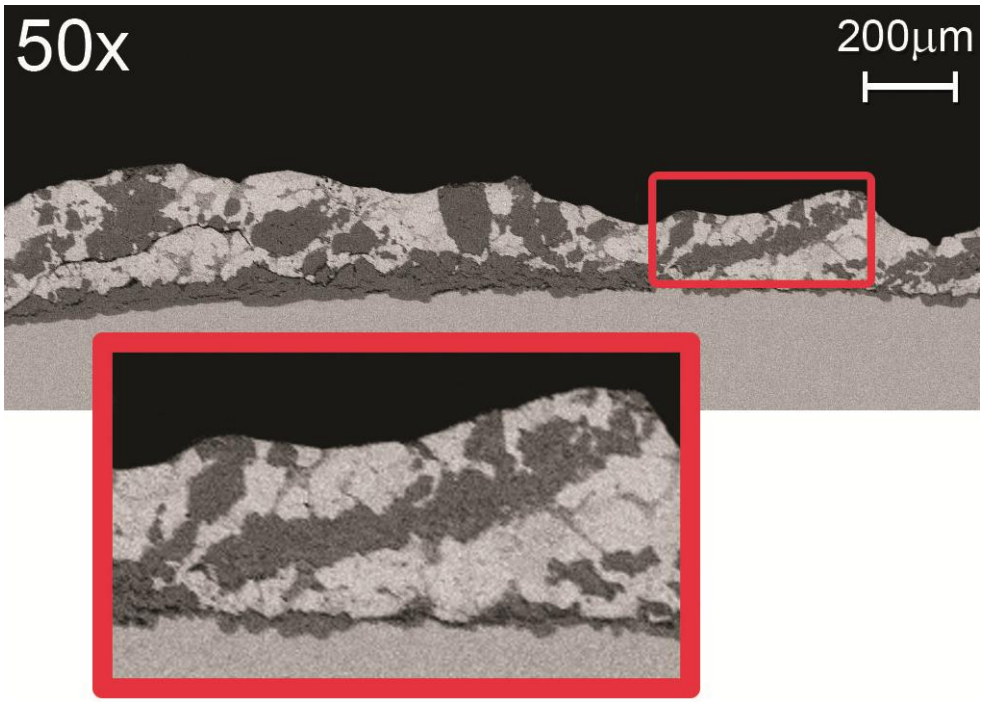

Figure 6-5: A ribbon-shaped cluster of particles is shown in sample 1.2. Due to thermal shock a crack is formed. Zn is penetrated into this crack and pushes probably the cluster particles towards the liquid Zn.

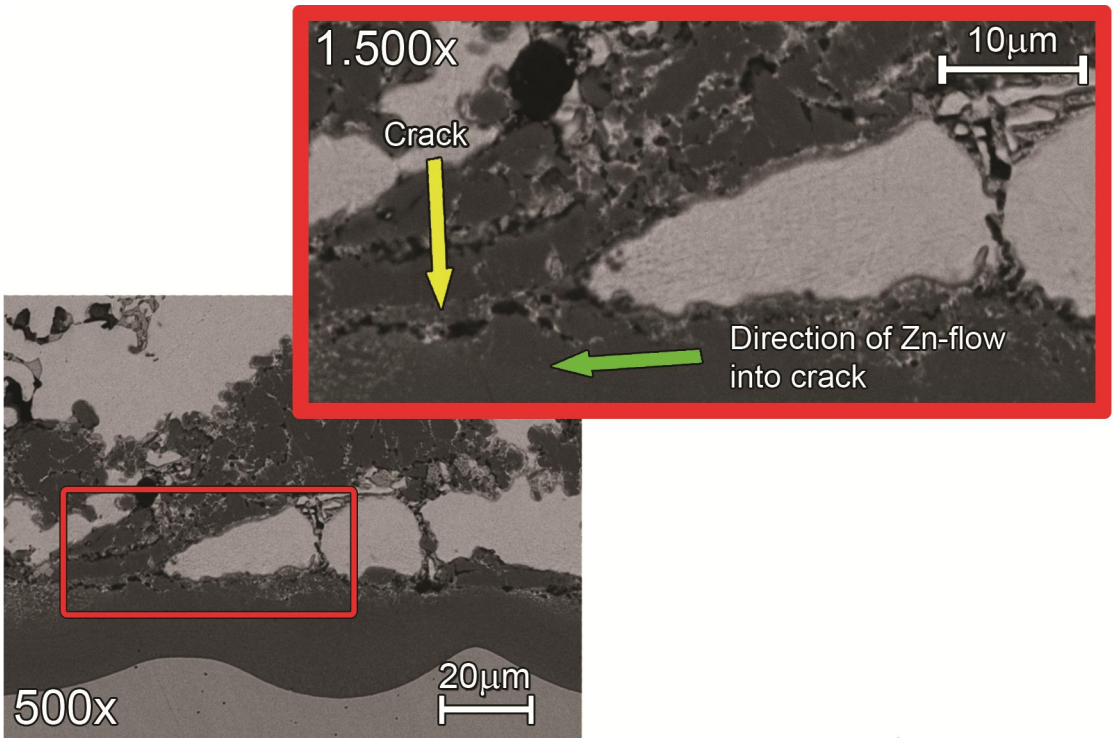

Figure 6-6: A crack that is formed near the diffusion layer is pushed away because Zn tries to penetrate the crack. Denoted with the yellow arrow, Zn is not yet penetrated into the crack.

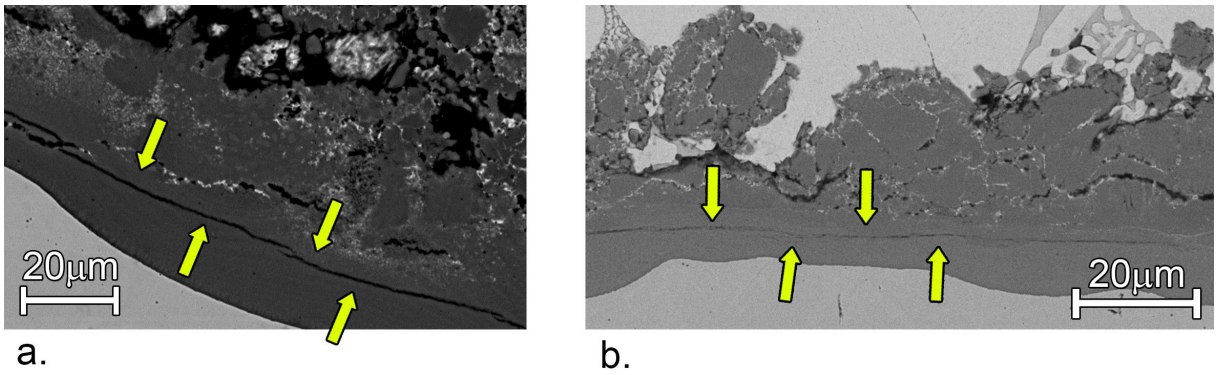

Figure 6-7: Small, fine cracks are visible within the diffusion layer, denoted by the yellow arrows. The cracks do not contain Zn. In a.) sample 1.4 is displayed and in b.) sample 2.2 is shown. The crack of sample 2.2 looks more superficial than the crack of sample 1.4.

metallic dross particles away from the diffusion layer towards the liquid Zn-bulk. In Figure 6-6 sample 2.4 (93h GI+70,5h MZ) is displayed. In this figure a part of a crack where no Zn was penetrated yet is displayed together with a part where the Zn-phase pushing the intermetallic dross particles towards the bulk Zn. If this sample was immersed longer, Zn would probably penetrate into the crack, further detaching the intermetallic dross particles from the diffusion layer. However, more experiments needs to be performed in order to prove this assumption. In Figure 6-4.b Sample 2.3 (93h GI+ 55,5h MZ) is displayed. This figure shows that Zn is penetrated into the crack as a result of thermal shock.

Crack Type 2: Small Crack in Diffusion Layer

Besides the relatively large cracks (Type 1), whether Zn is penetrated into the crack or not, another type of crack can be distinguished in the dross build-up structure. In the diffusion layer of three samples a fine, smooth crack is visible. The estimated thickness is hundreds of nanometres. This type of crack is displayed again in Figure 6-7.
Different from the intermetallic dross particle-layer with the diffusion layer is the presence of Mo in the diffusion layer. This difference is distinguished in the results of the experiments in Section 5-2-5. The line scan images do also show a significant increase in Mo concentration near the area where the crack is located compared with the rest of the diffusion layer. This observation is made clear in the case of sample 2.2 (93h GI+32,5h MZ) in Figure 6-8.

A possible explanation for the formation of these type of cracks is that the Mo-precipitates in the diffusion layer act as stress concentrators at cooling and thereby becoming the source for the cracks. When the samples were cooled to room temperature a stress is generated within the dross build-up structure. Because of this stress a small crack tended to first initiate around the Mo-precipitates within the diffusion layer and then propagate towards other Mo-precipitates in the surrounding. Since there is locally a higher concentration of Mo the crack can more easily propagate. Further propagation results in failure (the visible cracks). Therefore the most probable cause of these fine cracks is due to the presence of Mo-rich composition gradient in the diffusion layer. Further research is needed to determine the exact influence of Mo on this type of crack.

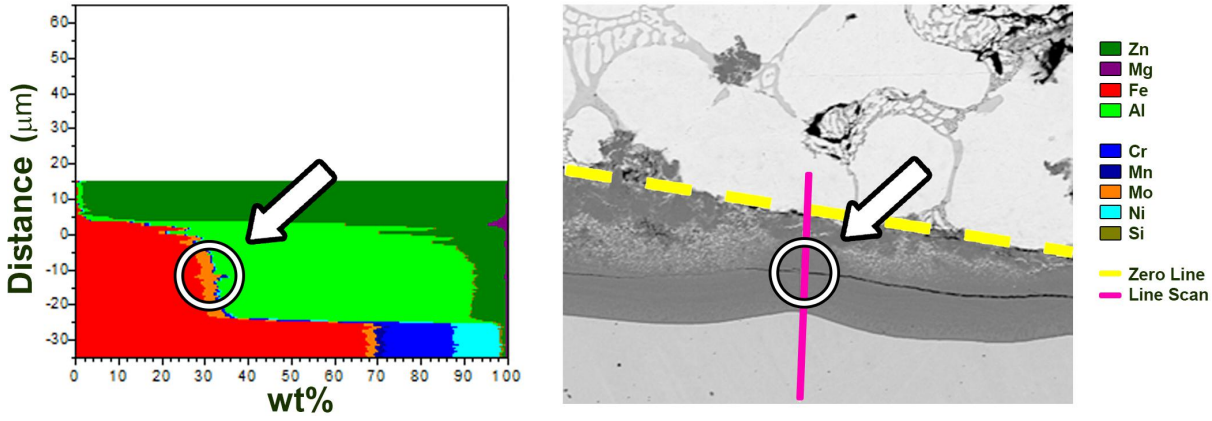

Figure 6-8: In the EPMA line scan performed on sample 2.2(93h GI+32,5h MZ) a significant increase in Mo is visible. This indicates that the crack formation is possibly due to the higher concentration of Mo compared with the rest of the diffusion layer. The exact difference in concentration is unknown.

If there is an influence on the dross build-up structure when the temperature fluctuates during production (not when changing the baths) is not to say with certainty. The temperature throughout the experiments is stable. Only in experiment 2 a temperature increase of 6°C which lasted 2 hours is detected. The reason why this temperature increase occurs is unknown. Nevertheless, this temperature change seems to have no effect on the dross build-up structure that is formed. After this increase in temperature occurred sample 2.3 came out. The structure of this sample is similar to that of sample 2.2 and sample 1.2 that were also immersed in MZ but without the temperature peak.

6-1-2 Faceted to Curved Interface Intermetallic Dross Particles

In Section 5-1-5 it is observed that the structure of the intermetallic dross particles has changed from a faceted to a curved structure. This change in structure is observed in all the samples that were submerged in MZ, the samples that were only submerged in GI (sample 1.1 and 1.2) do not have this curved interface. This observation gives the indication that this change occurred through the influence of MZ.

Only in sample 1.3 (GI+MZ+GI) both types of structures are visible in the dross build-up structure. The fact that sample 1.3 also shows the faceted shaped particles can be explained by the last bath this sample was in. As stated earlier in this section the faceted shape is a characteristic feature of intermetallic dross particles in GI. The intermetallic dross particles that have the curved interface are particles that were already formed in the first bath (GI) and already attacked in the second bath (MZ).

When immersed in MZ the particles undergo the transition in shape of the interface. Figures 2-8 and 2-9 display the solubility curves of 1,5 wt% Al Zn-alloy and 1,5 wt% Mg + 1,5 wt% Al Zn-alloy. However, the difference between these two figures is hard to distinguish. Therefore, in Figure 6-9 the Figure 2-9 is laid over Figure 2-8. This Figure 6-9 shows that the liquid becomes thermodynamically more stable when 1,5 wt% is added.

When liquid becomes more thermodynamically stable the solubility is higher. As explained

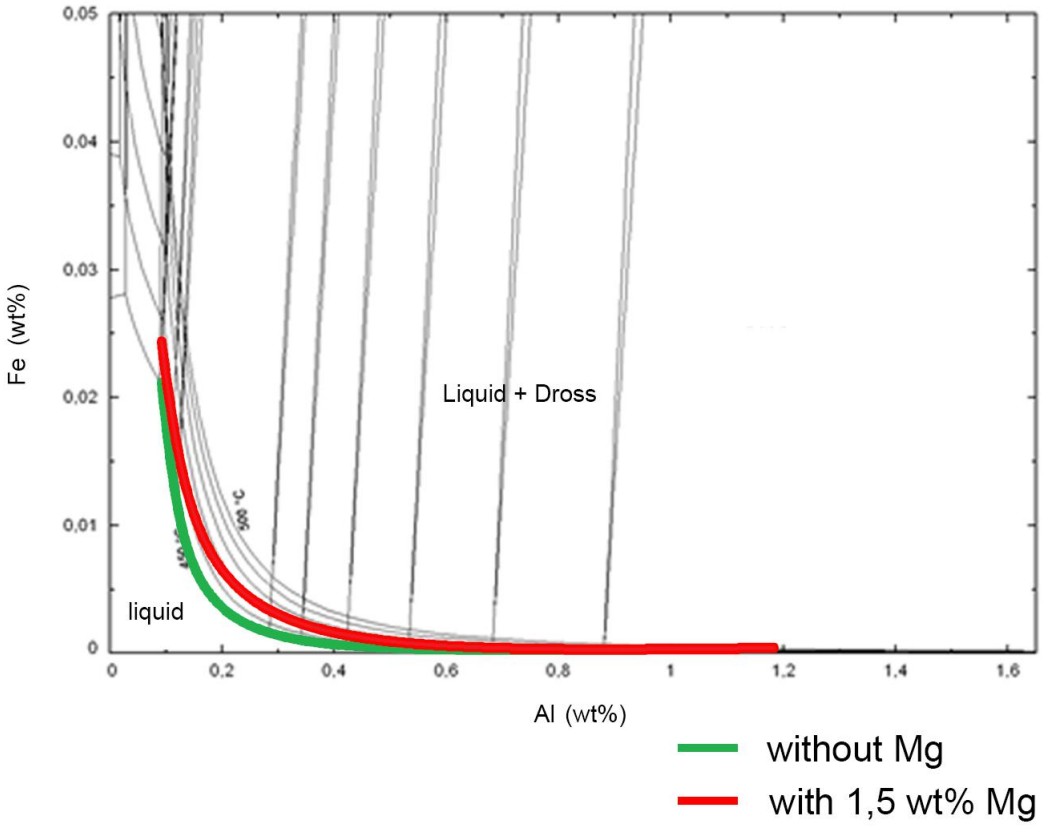

Figure 6-9: The solubility curves from Figure 2-8(no Mg) and 2-9 (with 1,5 wt% Mg) at a temperature of 450°C are laid over each other. The addition of Mg shows that the liquid is more stable than without the addition of Mg. A higher thermodynamic stability of the liquid results in the dissolution of intermetallic dross particles [27].

in Section 2-2-1 when the solubility is increased more $Fe_2Al_5Zn_x$-phase is able to dissolve in the liquid MZ. The increase in solubility that is distinguished in Figure 6-9 is the result of the decrease in Gibbs free energy (ΔG). The Gibbs free energy becomes more negative by the disturbance of the balance in free energy between the liquid Zn (MZ) and solid $Fe_2Al_5Zn_x$-phase (intermetallic dross particles).

From the experimental results it cannot be concluded that the described mechanism is the exact and only mechanism that causes the change in structure. The thermodynamic properties such as surface tension and free energy are not known in GI, in the bath direct after changing to MZ and after a significant immersion time in MZ. Further research in this area is needed, especially in thermodynamics at the change in structure of the interface. A recommendation of what can be done to further investigate this observation can be found in Section 6-2.

The average size of the intermetallic dross particles does not significantly differ between all the samples. This observation indicates that equilibrium is reached between the liquid Zn and intermetallic dross particles in very little time in the first bath the samples are submerged in. The particles do not grow further when submerged in another bath. That the particles do not grow further agrees well with the growth mechanism explained in the theoretical background (Section 2-1-3).

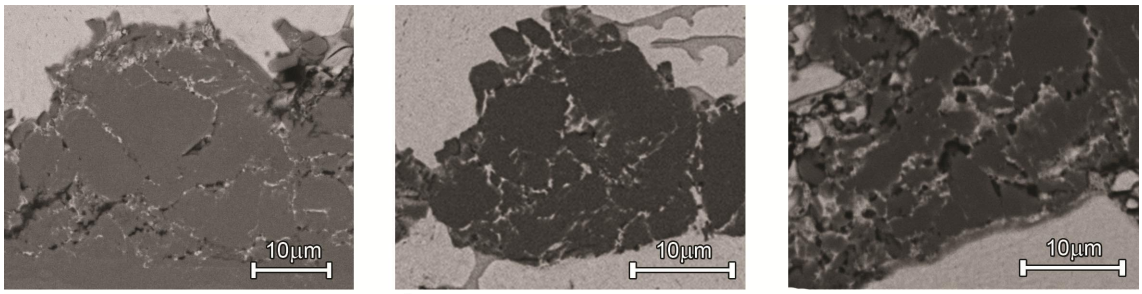

Figure 6-10: In a.) Sample 2.2, b.) Sample 2.3 and c.) Sample 2.4 are displayed. The figures show that with longer immersion time more Zn is diffused in the grain boundaries. In sample 2.4 (Figure c) contains small cracks or voids in the intermetallic dross particle (the black spots in the backscattered mode). This is probably the result of cooling.

6-1-3 Intergranular Diffusion of Zn

Together with the curved structure the intermetallic dross particles in the samples that were immersed in MZ after GI (Sample 1.2 (GI+MZ), 1.3 (GI+MZ+GI), 1.4 (GI+MZ+GI+MZ), 2.2 (93h GI+32,5h MZ), 2.3 (93h GI+55,5h MZ) and 2.4 (93h GI+70,5h MZ)) also contain white ribbons within the intermetallic dross particles. At longer immersion time in MZ the white ribbons become more frequent within the intermetallic dross particles as shown in Figure 6-10.
The cross sections in Figure 6-10 indicate that the brittleness is caused by intergranular diffusion of Zn into the intermetallic dross particles. These figures show cracks penetrating the intermetallic dross particles, following an intergranular path in the intermetallic dross particles. The presence of Zn is determined by the EDX-analyses as well as the performed line scans in Section 5-2-5.

The intergranular diffusion of Zn in the intermetallic dross particles explains the break up into smaller pieces of the intermetallic dross particles. The diffused Zn lowers the grain boundary strength remarkably. By this mechanism the intermetallic dross particles are eventually broken into smaller pieces.
The time it takes to split into the smaller pieces should be longer than the immersion time in MZ in the experiments performed. Sample 1.4 had the longest consecutive immersion time in MZ (140h) and in this sample Zn is penetrated throughout the grain boundaries, displayed in Figure 6-12. However the intermetallic dross particles are still attached to each other. The start of the delamination into smaller pieces can be seen in this sample 1.4, where the width of the grain boundaries where Zn diffused is significantly larger compared with other areas where the thickness is relatively thin. This observation is also seen in the comparison of samples of experiment 2, displayed in Figure 6-10.

The exact time it takes for Zn to diffuse into all grain boundaries is hard to distinguish since multiple factors are involved such as bath temperature, line speed and exact composition of the Zn-bath. An estimation has been made by measure the amount of white in the figures from Figure 6-10. These amount of whites are compared with each other by plotting this amount over immersion time. The plot is displayed in Figure 6-11. An exact description of the method including the code used to measure the white in the images can be found in

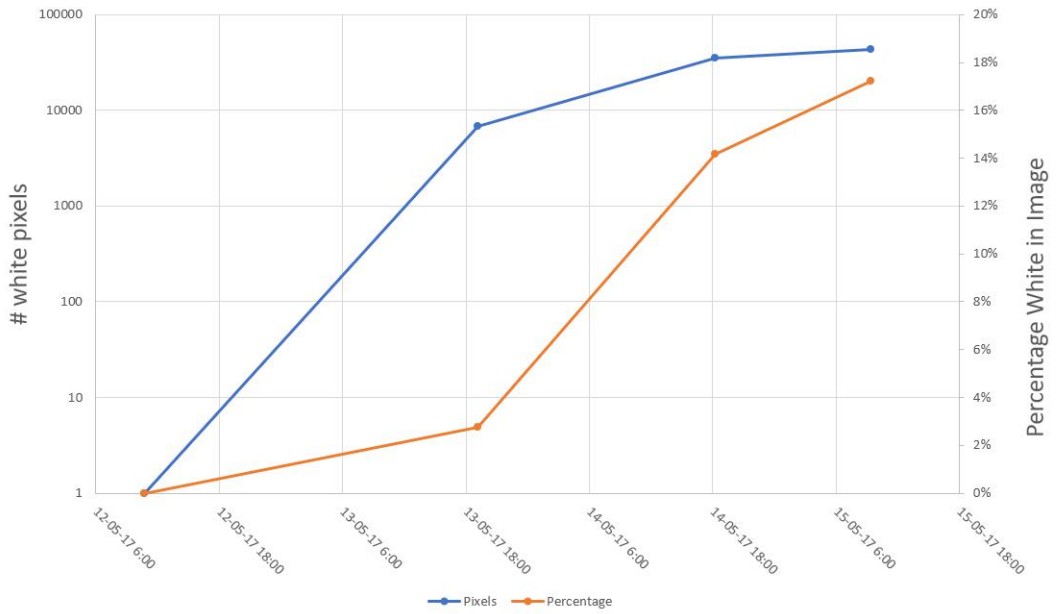

Figure 6-11: The percentage (orange) and the amount of white pixels (blue) are plotted over the immersion time. The amount of white pixels of each sample that is displayed in Figure 6-10 is measured by a code, explained in Appendix D.

Appendix D.
Figure 6-11 shows a parabolic relation between the amount of white in the image with immersion time.

Next to the intergranular diffusion of Zn in the intermetallic dross particles, Zn also diffuses into cracks formed due to cooling at changing the baths. This observation is briefly explained in Section 6-1-1.
A wide area of Zn between intermetallic dross particles or between the diffusion layer and intermetallic dross particles could be the result of cooling when changing the baths, since no Zn throughout the whole length is distinguished. An example is displayed in Figure 6-12, emphasized with yellow. This crack was probably formed at changing the baths when a previous sample (sample 1.1, sample 1.2 or sample 1.3) was taken out of the bath since Zn is detected within this crack.
Similar behaviour is also visible in sample 2.4 (70,5h MZ) where in the backscattered image black cracks can be distinguished together with white Zn at the edges of the crack. The cracks in sample 2.4 are emphasized in Figure 6-6.

In general, when enough Zn is diffused into the grain boundaries of the intermetallic dross particles, the intermetallic dross particle will eventually break up into smaller pieces. Breaking into smaller pieces is the result of cracking in the grain boundaries that became the weakest spot because of the intergranular diffusion of Zn. This crack formation in the grain boundaries occurs when there is a temperature gradient, e.g., at cooling towards room temperature.

The exact rate of intergranular diffusion and the crack formation in the grain boundaries cannot be determined with the experimental data of this thesis project. A larger data set is needed in order to determine the rate. Furthermore the diffusion rate depends on too many factors that have an influence in the diffusion of Zn, such as the exact composition of the

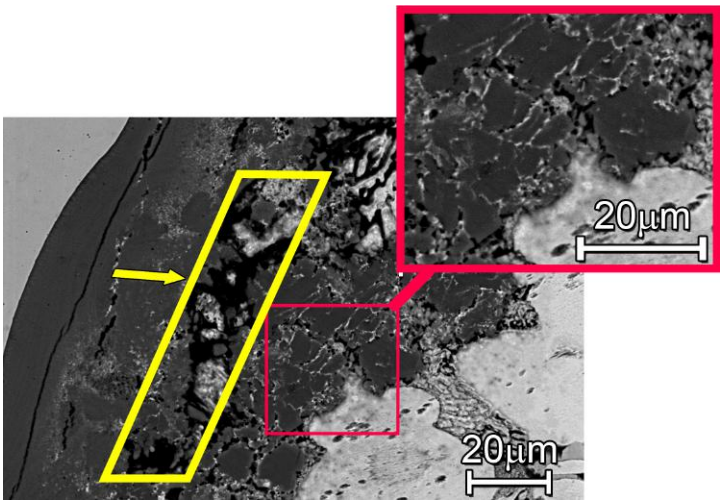

Figure 6-12: Intergranular Zn-diffusion in sample 1.4 is displayed. Furthermore, in yellow, in a crack that was formed when changing the baths Zn is now penetrated in. The figure is tilted compared with the other figures, where the stainless steel is located left.

intermetallic dross particles and the bath temperature.

Access for Zn to Grain Boundaries

In the results in Chapter 5 the intergranular Zn diffusion into the grain boundaries is only visible in samples that were immersed in MZ.
With the immersion in MZ the interface between the intermetallic dross particles and liquid Zn changed from a faceted to a curved interface, as explained in Section 6-1-2. This change in structure contributes to the intergranular diffusion of Zn.

In Figure 6-13 a schematic representation of the faceted to curved transition is shown. Because of this change in structure the contact angle is lowered from 180° to around the 37°, as explained in Section 2-2-3. As a result of this lowering, the grain boundaries in between the Fe_2Al_5-Fe_2Al_5 intermetallic dross particles experiences grain boundary wetting. The contact angle is not 37° since no complete grain boundary wetting is visible.
Further research needs to be performed to precisely obtain the contact angle and diffusion rate. Some recommendations are given in Section 6-2.

6-1-4 Wavy Pattern of Interface Diffusion Layer - Roll Surface

The interface between the diffusion layer and roll surface has a wavy pattern. In all the samples of the two experiments this wavy pattern at the diffused interface (diffusion layer/steel interface) is visible. Four examples of this wavy pattern are displayed in Figure 6-14. Previous research extensively studied the reaction of 316L SS with Zn-Al alloy baths [7, 31, 34, 37, 65]. However none of these studies explained the wavy interface.
This wavy pattern does not seem to have an influence on the delamination of the intermetallic dross particles discussed in this report since no crack formation nor delamination is visible at this interface. However, this interface is considered an interesting side effect worth mentioning

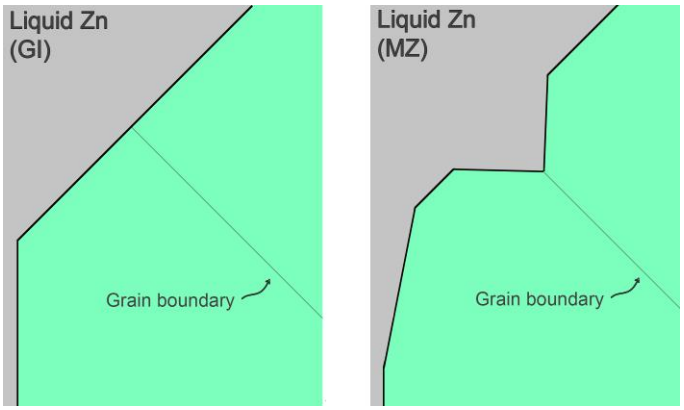

Figure 6-13: A schematic representation of the transition from faceted (left) to curved interface (right). Because the interface of the intermetallic dross particles with the liquid Zn gets curved when submerged in MZ, the grain boundaries in the intermetallic dross particles gets more easily accessible for the Zn.

since a relatively straight interface with only a few micrometers difference in 'height' between the diffusion layer and roll surface is expected.

The quantitative results of the EDX-analyses show that the diffusion layer consist of $Fe_2Al_5Zn_x$ (40-50 wt% Al, 35-45 wt% Fe and 10-15 wt% Zn) with a concentration of Mo (∼3 wt%) and some traces of Cr and Si. The concentration of Mo depends on the location in the interface. The further away from the roll surface in the diffusion layer, the less Mo is found.

Mo is known for its low diffusion coefficient [66][67]. Therefore an interesting result is that Mo has been found in the diffusion layer by the performed EDX-analyses, whereas the other elements (Cr and Ni) are not found or at very low concentrations.

To determine whether indeed Mo has a lower diffusion coefficient than Cr and Ni at a specific temperature can be calculated with the following equation [39]:

$$D = D_0 * \exp(\frac{-Q_D}{RT}) \tag{6-4}$$

where D_0 the exponential factor, Q_D the activation energy for diffusion, R the gas constant (8,314 J/K/mol) and T the temperature. The pre-exponential factor (D_0) and the activation energy for diffusion (Q_D) are material properties.

Lattice Diffusion

With the values for pre-exponential factor and activation energy for lattice diffusion known equation 6-4 can be filled in for the elements Cr, Mo and Ni.
For Cr the diffusion coefficient for lattice diffusion at 465°C is:

$$\begin{aligned} D &= D_0 * \exp(\frac{-Q_D}{RT}) \\ &= 8,52 * 10^{-4} * \exp(\frac{-250,8 * 10^3}{8,314 * 738}) \\ &= 1,51 * 10^{-18} m^2/s \end{aligned} \tag{6-5}$$

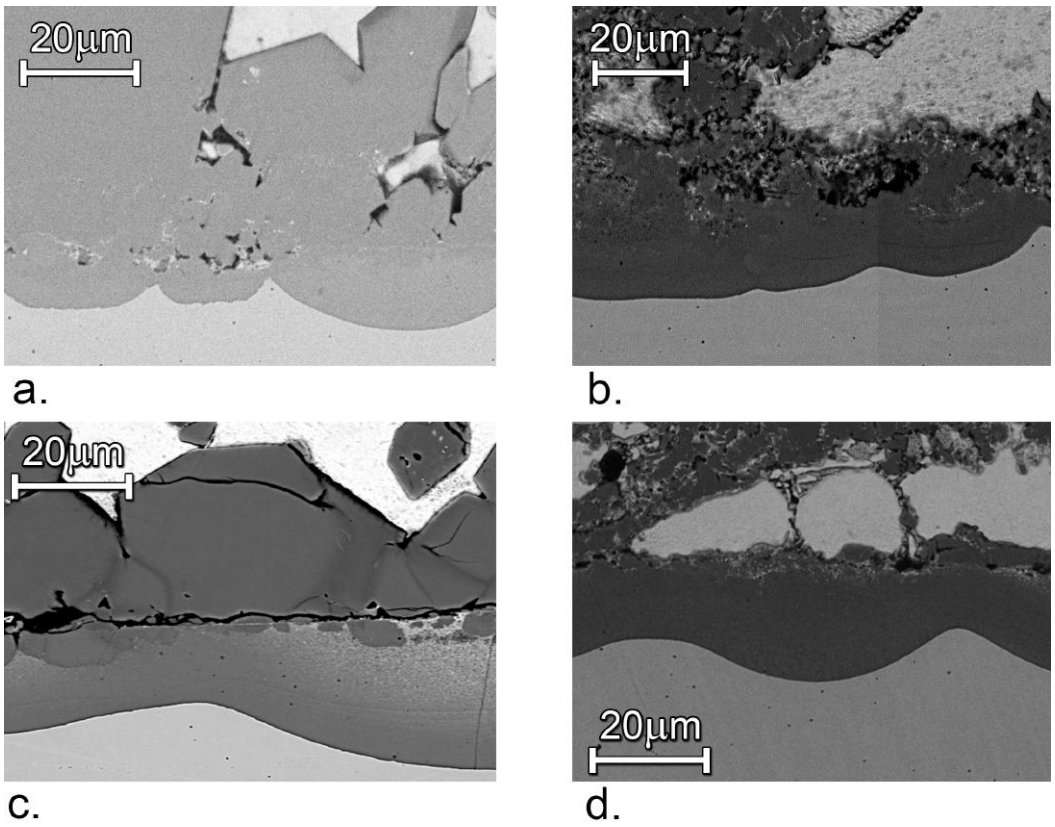

Figure 6-14: The wavy pattern is visible in all the samples. Four samples are displayed as an example: In a.) sample 1.1 is displayed, in b.) sample 1.4, in c.) sample 2.1 and in d.) sample 1.4.

Chemical Element	**Pre-exponential Factor D_0 (cm^2/s)**	**Activation Energy Q_D (kJ/mol)**
Cr	$8{,}52^{-4}$	250,8
Fe	$1{,}78^{-4}$	326,5
Mo	$3{,}60^{-6}$	239,8
Ni	$1{,}30^{-4}$	234,5

Table 6-1: Pre-exponential factors and the activation energies for lattice diffusion of the elements present in or near the dross build-up structure. The values for D_0 and Q_D are taken from reference [68].

For Mo the diffusion coefficient for lattice diffusion at 465°C is:

$$\begin{aligned} D &= D_0 * \exp(\frac{-Q_D}{RT}) \\ &= 3,6 * 10^{-6} * \exp(\frac{-239,8 * 10^3}{8,314 * 738}) \\ &= 3,83 * 10^{-23} m^2/s \end{aligned} \tag{6-6}$$

For Ni the diffusion coefficient for lattice diffusion at 465°C is:

$$\begin{aligned} D &= D_0 * \exp(\frac{-Q_D}{RT}) \\ &= 1,3 * 10^{-4} * \exp(\frac{-234,5 * 10^3}{8,314 * 738}) \\ &= 3,82 * 10^{-21} m^2/s \end{aligned} \tag{6-7}$$

From the equations 6-5, 6-6 and 6-7 it can be seen that Cr has the highest diffusion coefficient. Mo has a 50.000 times lower value for the diffusion coefficient compared to Cr. Ni is 100 times faster than Mo.

The average thickness of the diffusion layer is 10 µm, as stated in the results (Chapter 5). The time it takes for Cr to completely dissolve from the diffusion layer is:

$$\begin{aligned} t &= \frac{x^2}{D} \\ &= \frac{(10^{-5})^2}{1,51 * 10^{-18}} \\ &= 66,23 * 10^6 s \\ &= 2,09 year \end{aligned} \tag{6-8}$$

For Mo it takes:

$$\begin{aligned} t &= \frac{x^2}{D} \\ &= \frac{(10^{-5})^2}{3,83 * 10^{-23}} \\ &= 2,61 * 10^{12} s \\ &= 82793 year \end{aligned} \tag{6-9}$$

For Ni it takes:

$$\begin{aligned} t &= \frac{x^2}{D} \\ &= \frac{(10^{-5})^2}{3,82 * 10^{-21}} \\ &= 2,62 * 10^{10} s \\ &= 830,1 year \end{aligned} \tag{6-10}$$

The low diffusion coefficients with the corresponding extremely long diffusion times for lattice diffusion do not match the thickness of the diffusion layer. The diffusion is thicker than what the atoms can diffuses by lattice diffusion. Therefore, the formation of the wavy pattern by lattice diffusion is unlikely.

The activation energy (Q_D) for grain boundary diffusion is lower than for lattice diffusion. For FCC metals such as 316L SS it is generally found that the activation energy for grain boundary diffusion is about half the activation energy for lattice diffusion: $Q_{GB\ D} \sim {}^1\!/_2\ Q_{Lattice\ D}$ [39].

Grain Boundary Diffusion

For Cr the diffusion coefficient for grain boundary diffusion at 465°C is:

$$\begin{aligned} D &= D_0 * \exp(\frac{-Q_D}{RT}) \\ &= 8,52 * 10^{-4} * \exp(\frac{-(0,5 * 250,8 * 10^3)}{8,314 * 738}) \\ &= 1,13 * 10^{-12} m^2/s \end{aligned} \tag{6-11}$$

For Mo the diffusion coefficient for grain boundary diffusion at 465°C is:

$$\begin{aligned} D &= D_0 * \exp(\frac{-Q_D}{RT}) \\ &= 3,6 * 10^{-6} * \exp(\frac{-(0,5 * 239,8 * 10^3)}{8,314 * 738}) \\ &= 1,17 * 10^{-14} m^2/s \end{aligned} \tag{6-12}$$

For Ni the diffusion coefficient for grain boundary diffusion at 465°C is:

$$\begin{aligned} D &= D_0 * \exp(\frac{-Q_D}{RT}) \\ &= 1,3 * 10^{-4} * \exp(\frac{-(0,5 * 234,5 * 10^3)}{8,314 * 738}) \\ &= 6,52 * 10^{-13} m^2/s \end{aligned} \tag{6-13}$$

As stated in the results (Chapter 5)the average thickness of the diffusion layer is 10 µm. Therefore, the time it takes for Cr to completely dissolve from the diffusion layer by grain boundary diffusion is:

$$\begin{aligned} t &= \frac{x^2}{D} \\ &= \frac{(10^{-5})^2}{1,13 * 10^{-12}} \\ &= 88,5s \end{aligned} \tag{6-14}$$

For Mo it takes:

$$\begin{aligned} t &= \frac{x^2}{D} \\ &= \frac{(10^{-5})^2}{1,17 * 10^{-14}} \\ &= 8547s \\ &= 2,37h \end{aligned} \tag{6-15}$$

For Ni it takes:

$$\begin{aligned} t &= \frac{x^2}{D} \\ &= \frac{(10^{-5})^2}{6,52 * 10^{-13}} \\ &= 153,4s \end{aligned} \tag{6-16}$$

Ni takes two times more time to diffuse out completely from the diffusion layer than Cr. Ni diffuses about 55 times faster than Mo.

This calculated time is longer than the time that is found in literature (see also Section 2-1-3). In the literature it is stated that the diffusion layer is formed in the steel surface within seconds. From equation 6-14 and 6-16 the diffusion of Cr and Ni and thereby the formation of the diffusion layer in the hardware steel is 1-3 minutes. However, the thickness of the diffusion layer in the literature is a few micrometres whereas the average thickness in the results (Chapter 5) is 10 µm. This difference in thickness could explain the longer diffusion time in this study.
Nevertheless, this study is the first study that makes a comparison with the diffusion of Cr and Ni and the formation of the diffusion layer. Taking into account the diffusion of Cr and Ni from the diffusion layer could take longer than (1-3minutes) than the diffusion of Al into the diffusion layer (few seconds). Further research is needed to determine the influence of the diffusion of Cr and Ni on the formation of the diffusion layer.

From the experiments the composition of the steel sample consists of 16,5-17,5 wt% Cr and 10-11,5 wt% Ni, in the diffusion layer less than 0,5 wt% Cr and no Ni is found. The concentration of Mo in the 316L SS is 2-3 wt%. In the diffusion layer the Mo-concentration is similar.
From the calculations in 6-14 to 6-16 it is shown that Cr is the fastest to completely diffuse out the diffusion layer, followed by Ni. However, from the experiments still 0,5 wt% Cr is found in the diffusion layer.

The composition of Mo is similar for the 316L SS as for the diffusion layer. Equation 6-15 shows that Mo needs 2,3h to completely diffuse out of the diffusion layer. The most probable explanation is that the grain boundary diffusion time for Mo is too long and therefore did not diffuse out the diffusion layer.
Once submerged in the liquid Zn, Al diffused into the 316L SS surface. Al has a preference to react with Fe, forming the diffusion layer. Since Al has a high diffusion coefficient and low activation energy in stainless steels, thereby diffusing fast into the steel, forming the diffusion layer.

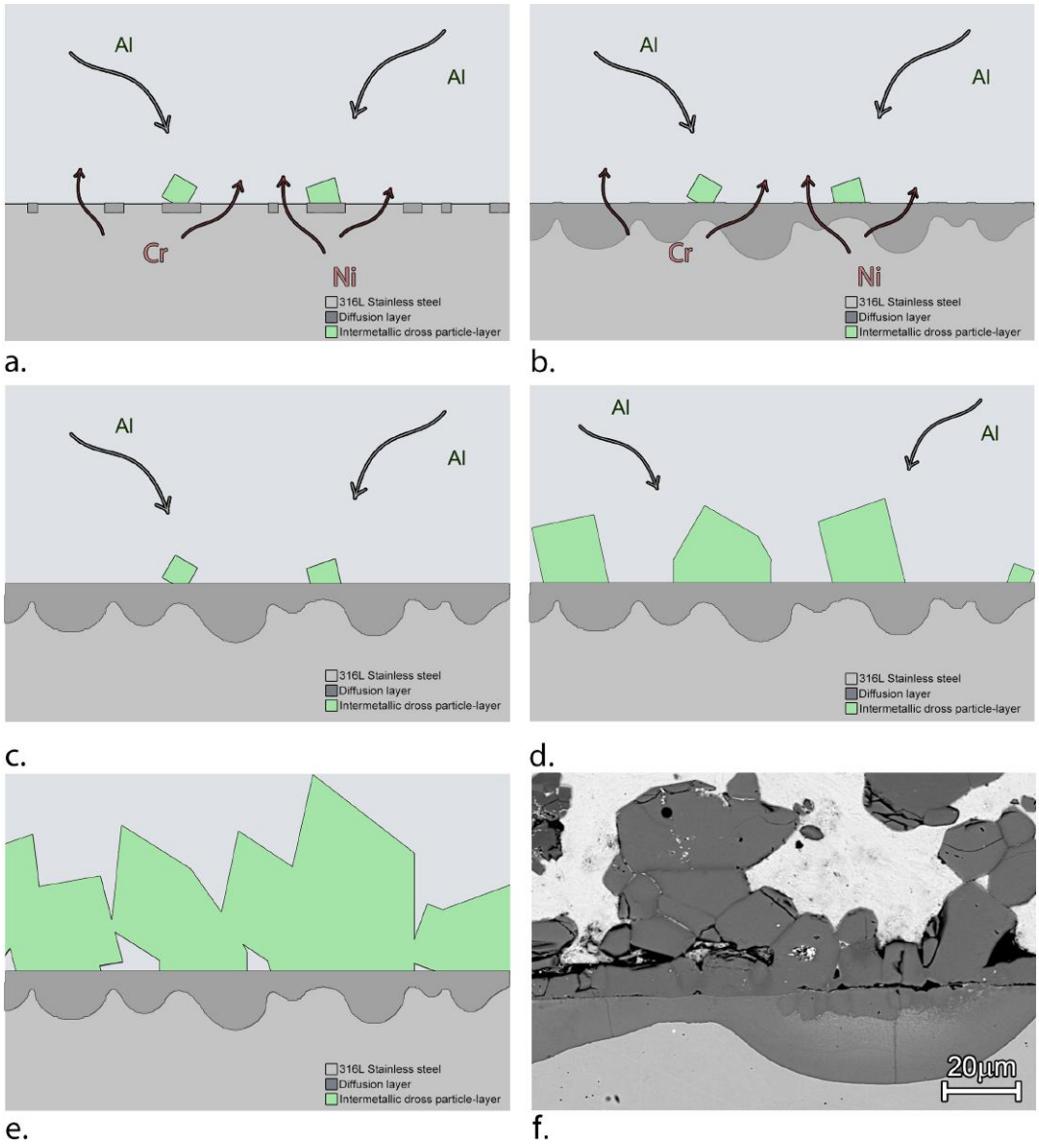

Figure 6-15: A schematic representation of the hypothesis that the formation of the wavy pattern is a result of the diffusion of Cr and Ni in the liquid Zn. The blue and dark-grey area together visualize the diffusion layer. In Figure a.) the first intermetallic dross particles are formed. Cr and Ni diffuse along these particles into the liquid Zn. In b.) is seen that where no particles are formed yet, the diffusion of Cr and Ni is larger. In c.) the diffusion of Cr and Ni is stopped since a barrier layer is formed as a reaction of Fe and Al (see Section 2-1-3). in d.) and e.) the particles grow, leaving the wavy pattern in the steel visible. In f.) sample 2.1 is displayed as an example what is found in the observations.

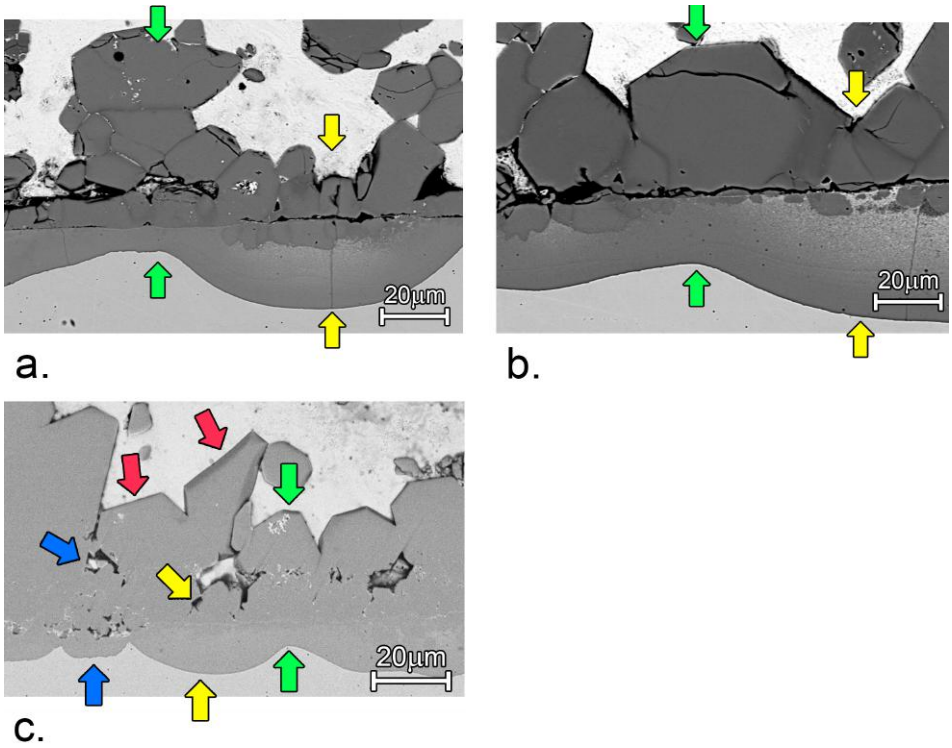

Figure 6-16: In spots where large intermetallic dross particles are attached to the diffusion layer, a smaller diffusion layer is shown. In spots where small intermetallic dross particles are attached a large diffusion layer can be seen. In Figure a.) Sample 2.1 is displayed. With the green arrows a large intermetallic dross particles is attached to where the diffusion layer is the thinnest. Where the diffusion layer has the highest thickness very small intermetallic dross particles (compared to other the other particles in this sample) are attached to the diffusion layer, denoted with the yellow arrows. In b.) similar observations can be made in Sample 2.1. The green arrows show large intermetallic dross particles with thin diffusion layer, the yellow arrows show where the diffusion layer has the highest thickness with the smallest intermetallic dross particles. In c.) Sample 1.1 is shown in where the thickness of the diffusion layer can be related to the size of the intermetallic dross particles, however this is harder to distinguish. The green arrows show where the diffusion layer is the thinnest with large intermetallic dross particles. The yellow arrows show where the thick diffusion layer has small intermetallic dross particles. Hereby it is assumed that the intermetallic dross particle is attached and grown in a later stage in where the diffusion layer is formed. A similar observation is made with the blue arrows: a relatively thick diffusion layer is seen with small intermetallic dross particles, when the size is counted from the diffusion layer to the void. That sample 1.1 is different than sample 2.1 can be related to the difference in immersion time (190 hours compared to 93 hours respectively).

The hypothesis is that the original roll surface can be found between the diffusion layer and the intermetallic dross particles by looking at the composition of Al and Mo.
The hypothesis for the significant less concentration of Cr and Ni in the diffusion layer as a result from these line scans and results in Chapter 5 is that Cr and Ni started to diffuse into the liquid Zn as soon as the steel was submerged in the Zn because Cr and Ni are thermodynamically more stable in the liquid Zn. This phenomenon is illustrated in Figure 6-15. The dissolution of Cr and Ni continues at areas where no intermetallic dross particle is attached and grown on the steel surface. Once the intermetallic dross particles completely

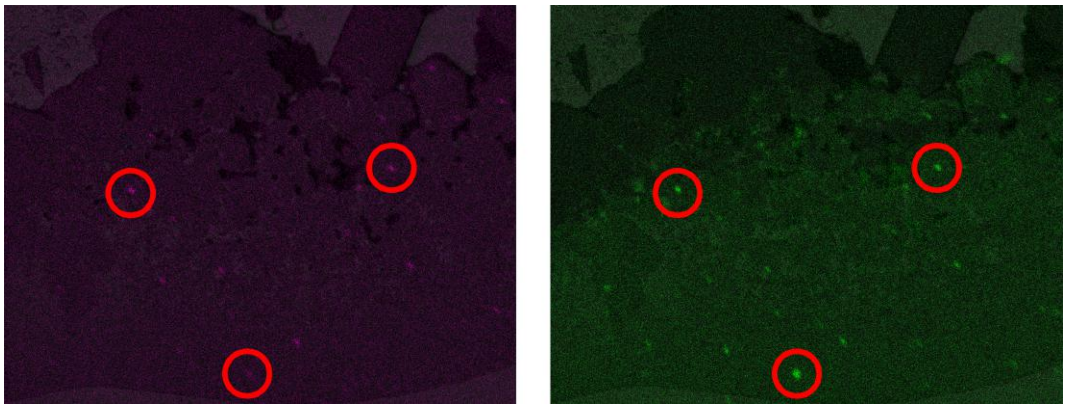

Figure 6-17: The element mappings of Mg (left) and Mo (right) in Sample 1.3 (GI+MZ+GI) are shown. A few bright spots are marked with red. As can be seen that these bright spots are in the same place for both element mappings. As further research turned out these bright spots do not contain Mg or Mo, but are MnS inclusions.

cover the diffusion layer the diffusion of Ni and Cr into the liquid Zn slows down significantly, since Cr and Ni now have to cross the intermetallic dross particles first in order to reach the liquid Zn.

This observation is clarified in Figure 6-16 where sample 1.1 and sample 2.1 are taken as example. In this figure it can be seen that in places where a small diffusion layer is visible, a relatively large intermetallic dross particle is seen. In spots where a relatively large diffusion layer is seen relatively small intermetallic dross particles are attached.
Further research is needed to confirm this observation. The immersion times for the samples 1.1 and 1.2 are long, 190 hours and 93 hours respectively. In these immersion times the intermetallic dross particles can grow more in the direction where originally was no intermetallic dross particle attached. This is best visible in sample 1.1 (Figure 6-16.a).

The elements Cr and Ni rather do not react with Zn at 465°C. From this observation the assumption is that Cr and Ni are diffusing into pure liquid Zn and the other elements in the liquid Zn are neglected. However the liquid Zn is not pure Zn and consists of more elements such as Al and Fe. Though, Fe and Al prefer to react with each other and therefore the assumption is made Cr and Ni will diffuse instead of precipitate.

The diffused concentration Cr and Ni is so low as compared to the 250 T liquid Zn-bath in which Cr and Ni are dissolved that the amount of Cr and Ni cannot be distinguished when the bath composition is measured.

6-1-5 Analysis of the Performed Element Mappings

In the element mappings performed on sample 1.3 (GI+MZ+GI), sample 2.1 (93h GI only) and sample 2.4 (93h GI+70,5h MZ) C and O are distinguished. The most logical assumption that C and O are found in the element mapping is that C and O are dirt and are accumulated in the corners and holes when the samples are prepared and polished. The high concentrations measured with the element mapping of C do not match the concentration C available in the 316L SS.

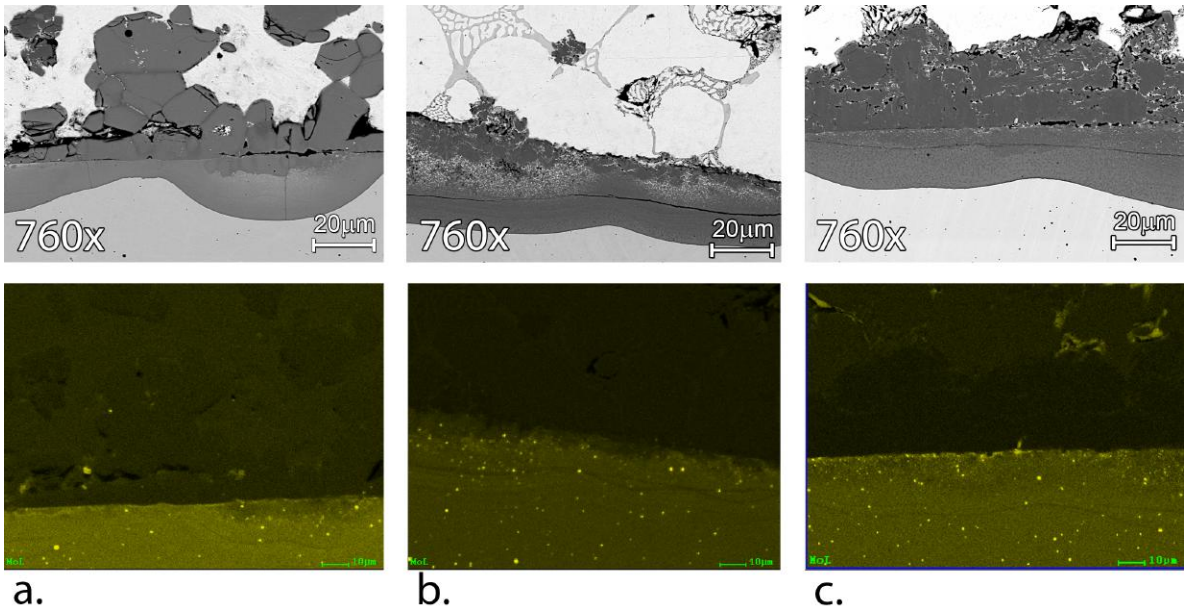

Figure 6-18: Three element mappings are carried out of sample a.) 2.1(GI only), b.) 2.2 (93h GI+32,5h MZ) and c.) 2.3(93h GI+55,5h MZ). The upper images are secondary electron images of the same place on the sample as a reference. In the element mapping (left) it can be seen that Mo including the bright spots is located only in the steel substrate and the diffusion layer. This applies to all the samples. As further research turned out these bright spots are MnS inclusions.

Mg is not as bright as other elements in the element mapping in sample 1.3 (GI+MZ+GI) as can be seen in Figure 6-17. However, there are some bright spots visible in the Mg-element mapping, indicating that in these spots must be Mg present. Another observation is that the mapping of Mo has the same bright spots. This observation raises the question: Why do Mg and Mo cluster together in small spots?

An extra element mapping is carried out to obtain more knowledge about the bright spots. This element mapping is carried out on samples 2.1(GI only, see Section 5-2-1), 2.2 (93h GI+32,5h MZ, see section 5-2-2) and 2.3 (93h GI+55,5h MZ, see 5-2-2). In Figure 6-18 the bright Mo spots are only found in the diffusion layer and roll surface. This figure gives the indication that Mo is only located where the original surface of the sample was. This observation is in agreement with the observation in Section 6-1-4.

It is unrealistic that Mg and Mo are react with each other, as can be seen in Figure 6-19 [69]. The bright spots are probably other elements that have peaks that overlap with the peaks of Mg and Mo in the EDX elemental analysis.

The material of the sample rods, 316L SS, is a type of stainless steel. 300 series stainless steels are known for the addition of manganese (Mn) to retain an austenitic structure at elevated temperatures. A side effect of the addition of Mn is that Mn is likely to react with Sulphur(S) forming MnS inclusions. In uncoated steels these MnS inclusions act as initiation sites of pitting corrosion in stainless steels [70]. In 300 series stainless steels it is known that these MnS inclusions are randomly distributed throughout the steel.
To verify that these bright spots are indeed MnS inclusions another element mapping is performed on the three samples (2.1, 2.2 and 2.3). The result of the element mapping is

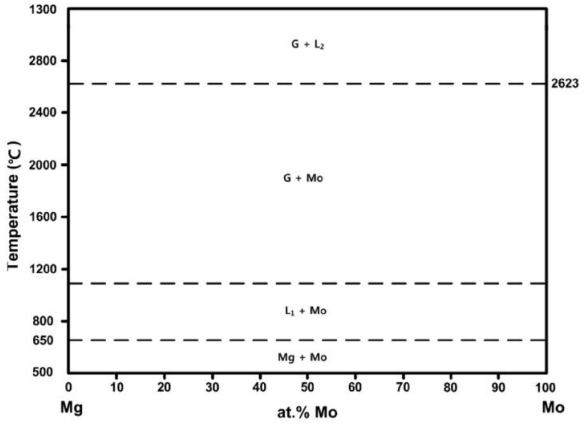

Figure 6-19: The phase diagram of Mo and Mg. As can be seen the two elements do not react with each other [69].

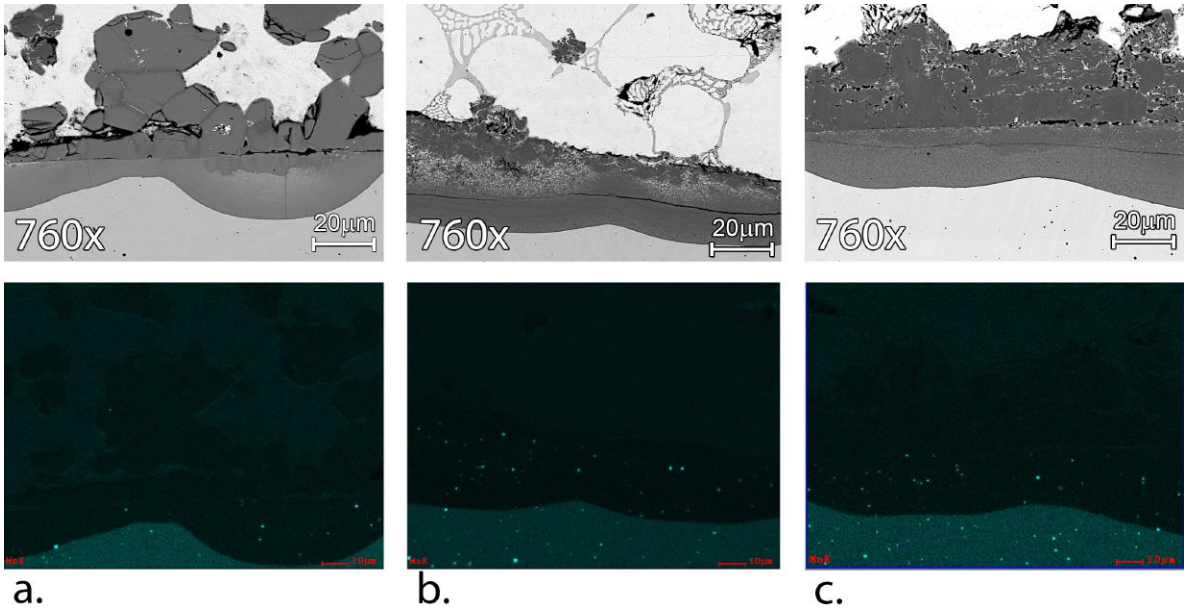

Figure 6-20: Three element mappings of element Mn are carried out of sample a.) 2.1(93h GI only), b.) 2.2 (93h GI+32,5h MZ) and c.) 2.3(93h GI+55,5h MZ). The upper images are secondary electron images of the same place on the sample as a reference. In the element mapping (left) it can be seen that Mn is located only in the steel substrate, the inclusions (bright spots) are also shown in the diffusion layer and steel substrate. This applies to all the samples.

shown in Figure 6-20.

The Mn-element mapping shows that the bright spots also appear with Mn. These bright spots are randomly distributed over the steel substrate and diffusion layer. With the line scan measurements in this same sections it was concluded that the intermetallic dross particle/diffusion layer interface was the original surface of the steel. As seen in Figure 6-20 the bright spots do not cross this intermetallic dross particle/diffusion layer interface and are not found in the intermetallic dross particles. Furthermore the bright spots also appear in the Mn-element mapping.

With the appearance of the bright spots in the element mapping and the fact that the bright spots are only found in where the original steel substrate was, it can be concluded that the bright spots are presumably MnS inclusions that originate in the steel substrate.

Though the MnS inclusions do have a negative effect in uncoated steel as they are an initiation for pitting, these inclusions do not seem to have any influence on the delamination of the intermetallic dross particles when submerged in MZ. The location of the cracks formed in the diffusion layer (discussed in Section 6-1-1) do not match the locations of the MnS inclusions.

In the SEM-micrographs of several samples show a difference in colour in the diffusion layer. Four examples are given in Figure 6-21. Although the SEM-images do show difference in colour, the results of the EDX-analyses, the figures of the element mappings and in the results of the EPMA line scans show a homogeneous composition in the same area.
This heterogenity does not seem to influence the delamination of the dross build-up structure. Therefore this observation is not further investigated. A first estimate is that this heterogenity is due a difference in crystallography or topography. Whether this estimate is indeed the case can be further investigated by for example XRD-analysis.

6-1-6 Mechanistic Sequence of Events

As described in the sections above the mechanisms that cause the delamination process are crack formation (6-1-1, curved structure (6-1-2) and intergranular diffusion of Zn into the grain boundaries (6-1-3). In this subsection the mechanistic sequence of events are explained.

Figure 6-22 graphically shows the sequence of events. This figure shows the formation of dross build-up (Figure 6-22a-d). Figure 6-22-e shows the crack formation due to thermal shock since the hardware is not submerged in one of the baths. Once the hardware is submerged in MZ (Figure 6-22.f) the faceted geometry is changed in a curved structure, therefore Zn is able to diffuse into the grain boundaries. Furthermore Zn is able to diffuse into the cracks due to thermal stress cracking, trying to push away the intermetallic dross particle layer from the diffusion layer. The latter is shown in Figure 6-22g and i. These two figures show that the crack (due thermal shock) will become larger. Figures h and j show that when submerged again in a bath (independent if the bath is GI or MZ) the intergranular diffusion continues.

Although in Figure 6-22 seems that the crack becomes larger when the hardware is taken out of the bath, this widening occurs before taken out of bath when the hardware is still submerged since then Zn is able to diffuse in the already formed crack. If there are cracks visible without Zn within the crack, these cracks are formed the last time the hardware is taken out the bath. Zn cannot diffuse into the crack since Zn is already solidified when the crack is formed due to thermal shock.

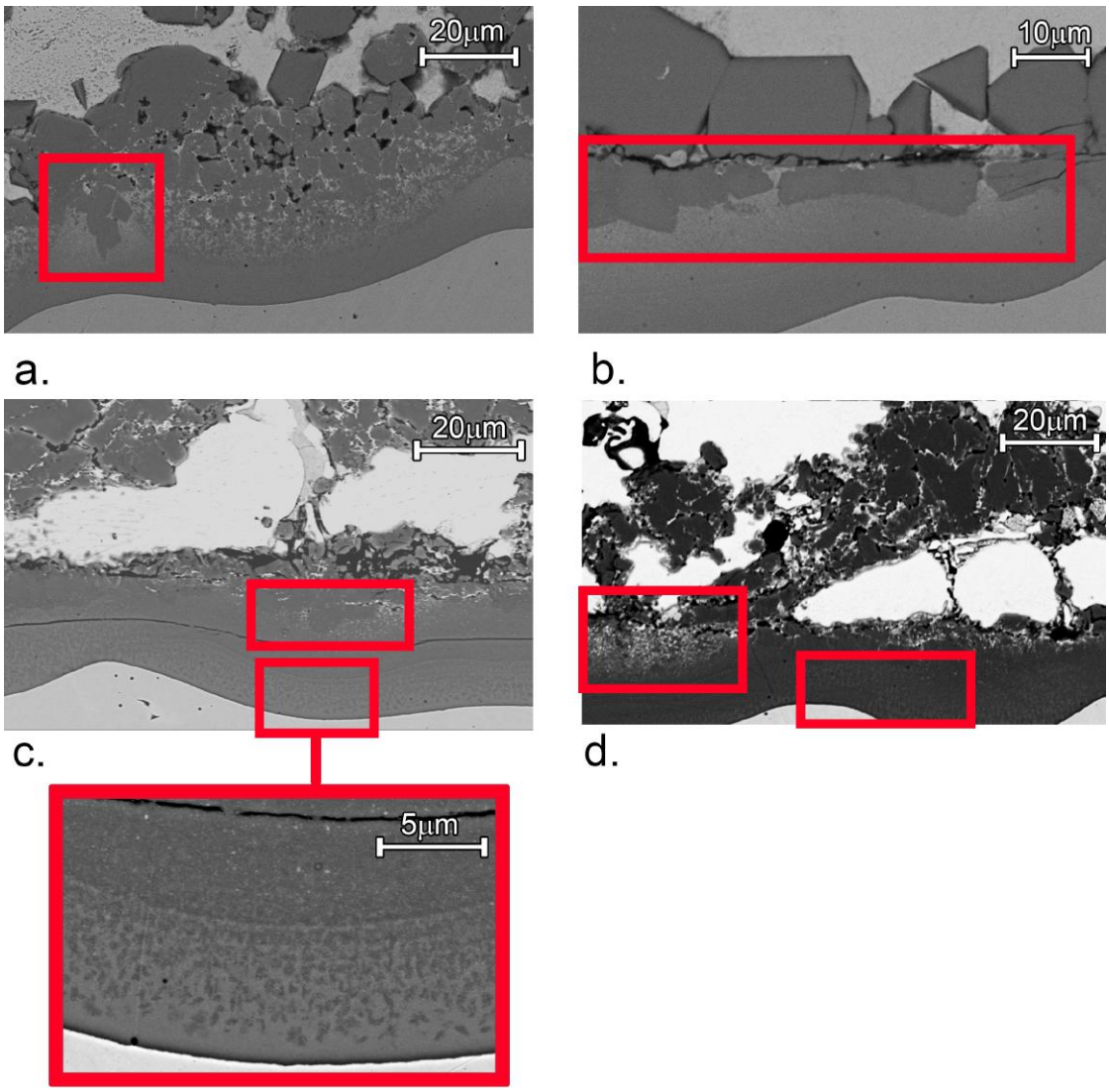

Figure 6-21: a.) In Sample 1.3 particles are shown in dark grey in the diffusion layer. In b.) Sample 2.1 is displayed in where grey particles are seen in the diffusion layer near the interface with the intermetallic dross particles, the rest of the diffusion layer has a colour gradient from dark-grey at the steel-diffusion layer interface and light-grey at the particles visible in the diffusion layer. In c.) similar particles are shown in Sample 2.2, furthermore very small needle-shaped particles (with an average length of 50nm) are visible in the diffusion layer. In d.) Sample 2.4 is displayed in where white spots are visible near the interface with the intermetallic dross particles, in the diffusion layer near the steel-interface the needle-shaped particles can be dinstinguished.

The small cracks in the diffusion layer are not taken into account in Figure 6-22. These cracks presumably form the first time the hardware is submerged into the bath. However, if this assumption is indeed right needs to be researched since this crack is not visible in every sample taken for this thesis. Further research is needed to determine formation of this crack and the exact influence of Mo with this formation of this crack.

6-2 Recommendations

There are several recommendations for future research resulting from this thesis project. First, further research is needed to completely understand the morphology of the dross build-up structure since there are many different phases and orientations present indicated from the SEM micrographs. No research was done to determine these phases and orientations in the build-up structure. Therefore it is unknown what the exact behaviour of these phases is in both baths. Characterisation techniques such as electron backscatter diffraction (EBSD) and transmission electron microscopy (TEM) could give more insight in a precise determination and quantification of the phases present.

To conclude from the performed SEM micrographs, EDX-analyses, element mappings and line scan analysis the most probable cause for the intermetallic dross particles breaking into smaller pieces is by the intergranular diffusion of Zn that over time eventually lead to breaking of the intermetallic dross particles into smaller pieces. The exact mechanism is in the grain boundaries on atomic level is still unknown. TEM-characterisation technique could give more understanding into this matter. This understanding could lead to determining a diffusion rate of Zn into the grain boundaries and delamination rate of the intermetallic dross particles.

Although the experiments in this thesis cannot completely explain the faceted to roughened structure change, it is most likely that this is caused by the decrease in surface tension. However the exact reason why this change occurs is not clear and needs to be further investigated. The roughening rate from faceted to curved structure of the intermetallic dross particles can be researched with for example molecular dynamic computer simulations.

The current results are observed on a sample rod, with a diameter far less than the rolls used in the Zn-bath: 25 mm compared with 800 mm respectively. The geometry is also different between the samples used for the experiments and the sink roll. The sink roll is hollow with a wall thickness of 35 mm. The differences in the specimen's thickness are presumably not big enough to observe large differences in the thermal shock resistance of the stainless steel components and therefore not in the dross build-up structure. However the geometry of the roll could play a role in the dross build-up because of a different flow around it. New experiments with similar geometry (in different proportions) could give more information about the dross build-up structure with respect to the geometry of the sample.
The flow in the bath is different near where the samples were placed and where the hardware is positioned in the bath. When comparing the dross build-up structure of the experiments (Chapter 4) to the dross build-up structure on the sides of the block of the paper (Chapter 3), the dross build-up structure is similar to each other. Since the block of the paper was attached on the bearings the dross build-up structure on these bearings is perhaps similar. Because of the rotation of the rolls the flow near the rolls is different to the flow near the

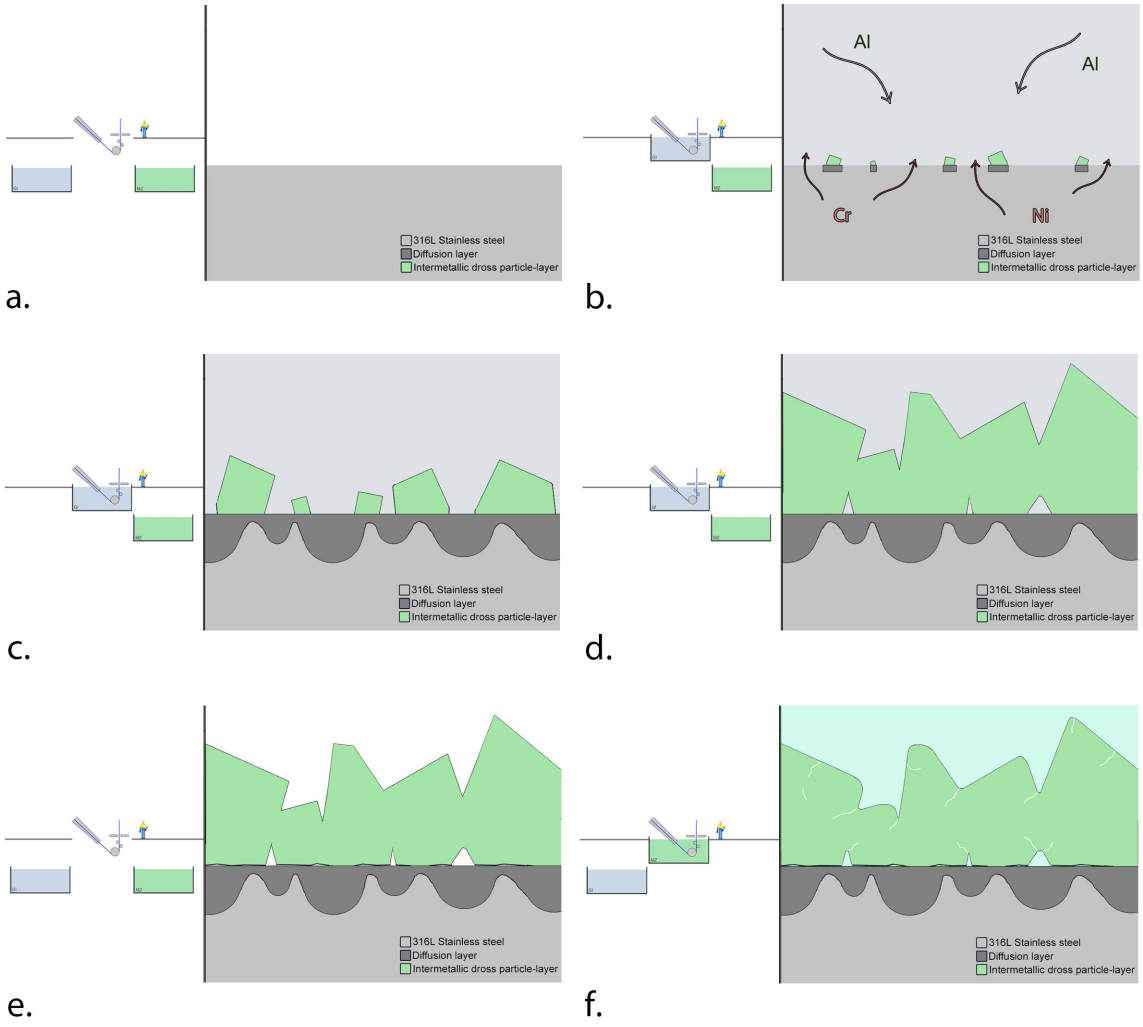

Figure 6-22: The mechanistic seguence of events is graphically explained. Figures a to j consists of two parts. On the left the position of the baths to the hardware is shown, on the right a cross section of a steel substrate of the hardware is seen. From a to j the sequence of events is graphically displayed.
a.) The steel substrate is not submerged in one of the baths and therefor no dross build-up structure is formed. b.) The hardware is submerges in GI, Cr and Ni dissolve into the Zn bath, Al will react with Fe from the steel to form a barrier layer on the steel substrate. In c.) the diffusion of Cr and Ni is stopped, the intermetallic dross particles still grow until the metastable equilibrium is reached (d.)). In e.) the bath is changed to MZ, causing the hardware to cool down. Cracks due to thermal shock will occur in between the diffusion layer and intermetallic dross particles. in F the hardware is submerged in MZ, causing the geometry changing from faceted to a curved structure. Because of this curved structure Zn is able to diffuse into the grain boundaries of the intermetallic dross particles.

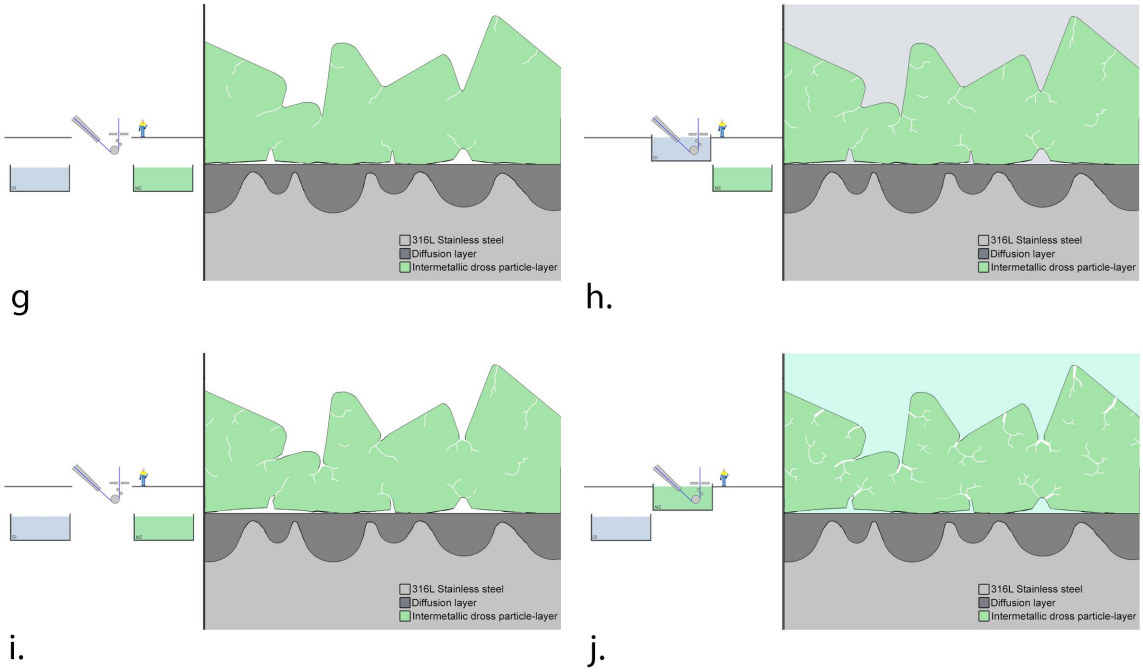

Figure 6-22 (Continued): The mechanistic seguence of events is graphically explained. Figures a to j consists of two parts. On the left the position of the baths to the hardware is shown, on the right a cross section of a steel substrate of the hardware is seen. From a to j the sequence of events is graphically displayed.
g.) The bath is changed again. Zn is penetrated into the crack, 'pushing' the intermetallic dross particle layer away from the steel substrate. In h.) the hardware is submerged again, Zn is diffusing further along the grain boundaries of the intermetallic dross particles. Since Zn is still 'pushing' the intermetallic dross particle layer away from the steel substrate the crack appears to be larger in thickness (i.)). The longer the hardware is submerged in a bath, the more Zn is diffused along the grain boundaries and cracks that formed due to thermal shock, as seen in h.).

sample rods. The dross build-up structure on the rolls could have more ribbon-shaped clusters of intermetallic dross particles as a result of the faster flow near the rolls. Further research is needed to investigate if this is actually the case. An option how this issue can be researched is in a laboratory set-up with rotating samples instead of stationary samples in this study. The best option would be to perform the same experiments in the production line with rotating samples. Another option is to attach sample blocks onto rolls itself.

In Section 6-1-1 two types of cracks are described that were probably the result of the existence of Mo in the diffusion layer in combination with the temperature difference when switching the baths.
That the addition of Mo indeed strengthened the diffusion layer cannot be concluded with the data from this thesis project. The same applies for the crack formation due to the significantly higher concentration of Mo in the diffusion layer. Too few measurement have been carried out where only the addition of Mo is extensively researched. Further research with performing quench testing experiments, the thermal shock resistance can be determined. Hereby two types of stainless steels need to be used: 304L SS (without Mo) and 316L SS (with Mo).

What the influence is on the dross build-up structure when the temperature is increased or decreased for a longer period of time during production is unknown. Further research can give more insight into this topic. Experiments to research this question could be done with the similar set-up as for this study. However the experiments could be performed best in a laboratory condition so that the production is not influenced by changing the temperature. If performed in a laboratory condition it should be taken in mind that the Fe and Al concentration may not be exactly the same as in the production line.

Chapter 7

Conclusions

This thesis describes the characterisation of the delamination of the dross build-up behaviour of the hardware submerged in the GI followed by MZ baths. Moreover, the effect is studied of changing the bath from GI and MZ and vice-versa on the delamination of the dross build-up structure.

Based on the results from this study the following main conclusion can be drawn:

- The delamination process of the dross build-up structure is a combination of crack formation as a result of thermal shock and as a result of intergranular diffusion of Zn into the intermetallic dross particles.

The underlying mechanisms of the delamination process that support this main conclusion are:

- The intermetallic dross particle/liquid Zn interface changes from a faceted to a curved geometry due to the dissolution of Fe and Al atoms from the intermetallic dross particles into the liquid in the case the bath is changed from GI to MZ. This observation corresponds to the phase diagrams which show that the Fe_2Al_5 is less stable in the MZ-bath than in the GI-bath with respect to the liquid phase
- By the change in geometry from faceted to curved, Zn is able to diffuse into the grain boundaries of the intermetallic dross particles which is referred as the intergranular diffusion of Zn. This intergranular diffusion lowers the grain boundary cohesion, contributing to the delamination by eventually breaking the intermetallic dross particles into smaller pieces
- Intergranular diffusion of Zn in the intermetallic dross particles only happen when the interface changed from faceted to curved, thus when the bath is changed from GI to MZ.

- Changing the baths speeds up the delamination process because of crack formation in the intermetallic dross particle-layer due to the thermal shock as a result of the rapid cooling during switching the baths. This observed mechanism is independent from the type of Zn-bath the hardware is immersed in
- These cracks as a result of thermal shock do form in the intermetallic dross particle-layer, not in the diffusion layer. The diffusion layer remained largely unaffected because the intermetallic dross particle-layer has a lower thermal expansion coefficient compared to the diffusion layer
- The diffusion layer has a good chemical bonding to the steel substrate, thereby less prone to thermal cracking
- In the diffusion layer small cracks are formed. In the vicinity of these cracks an increase of Mo is measured. Nevertheless, these small cracks do not seem to have an influence on the delamination process of the dross build-up structure.
- The interface between the diffusion layer and stainless steel substrate has a wavy pattern. This pattern is due to the dissolution of Cr and Ni from the 316L stainless steel into the liquid Zn at time of immersion. Cr and Ni dissolve into the liquid Zn and do not seem to contribute to the delamination of the dross build-up structure.
- The area where no intermetallic dross particle is deposited, more Cr and Ni might diffuse into the liquid Zn. This diffusion results in the wave-like interface between diffusion layer and stainless steel.

Appendix A

EDX-analyses of experiment 1

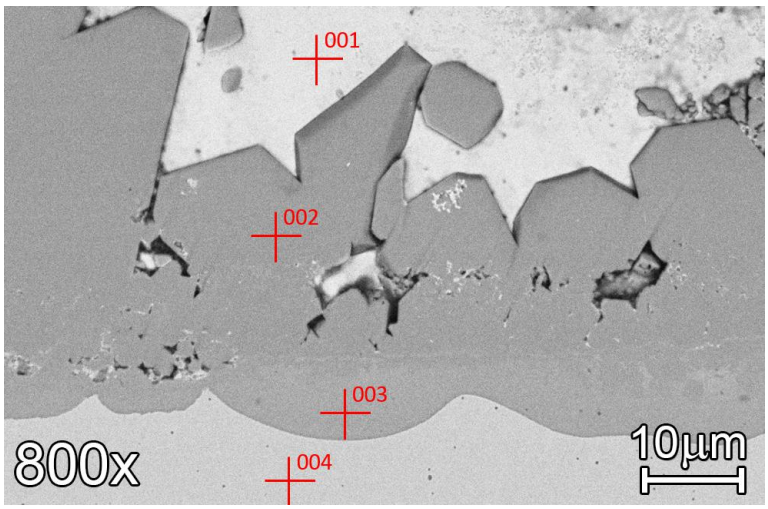

Figure A-1: EDX-analysis on sample 1.1 (GI only). Four analyses have been carried out on the build-up to determine the elements.

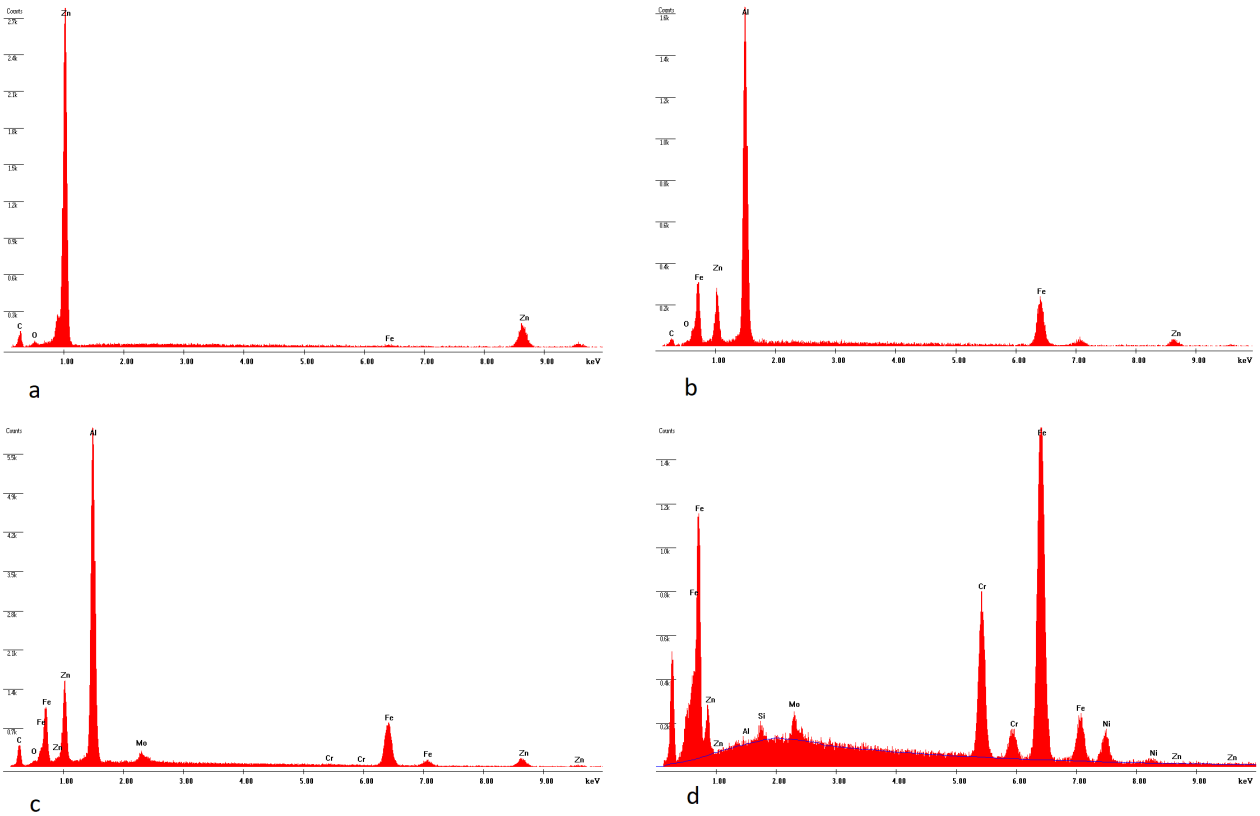

Figure A-2: Spectra of the points seen in Figure A-1 in sample 1.1 (GI only). a.)point 001, b.)point 002, c.) point 003, d.) point 004

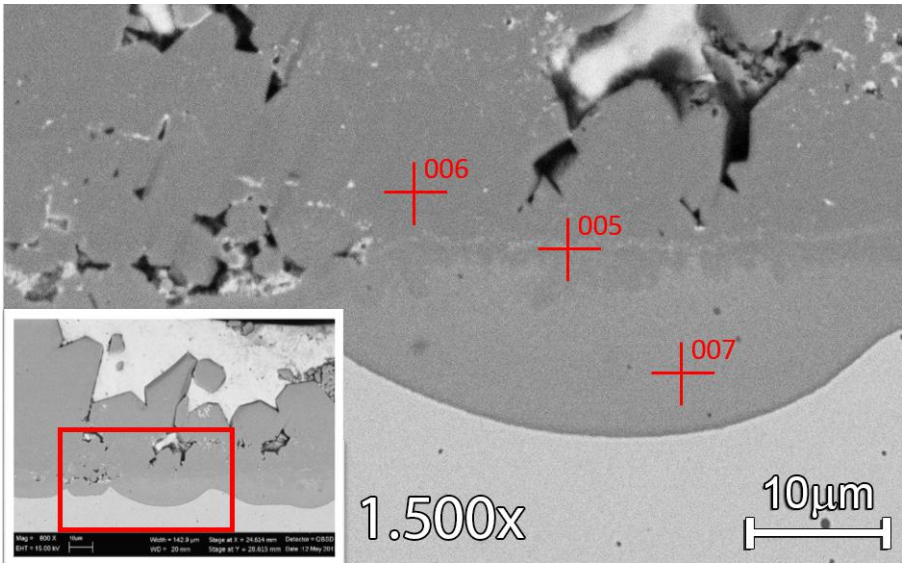

Figure A-3: A second EDX-analysis on sample 1.1 (GI only). Three analyses have been carried out on the build-up to determine the differences in composition between the intermetallic dross particles, diffusion layer and the enriched Zn-line that is indicated in Figure 5-2.

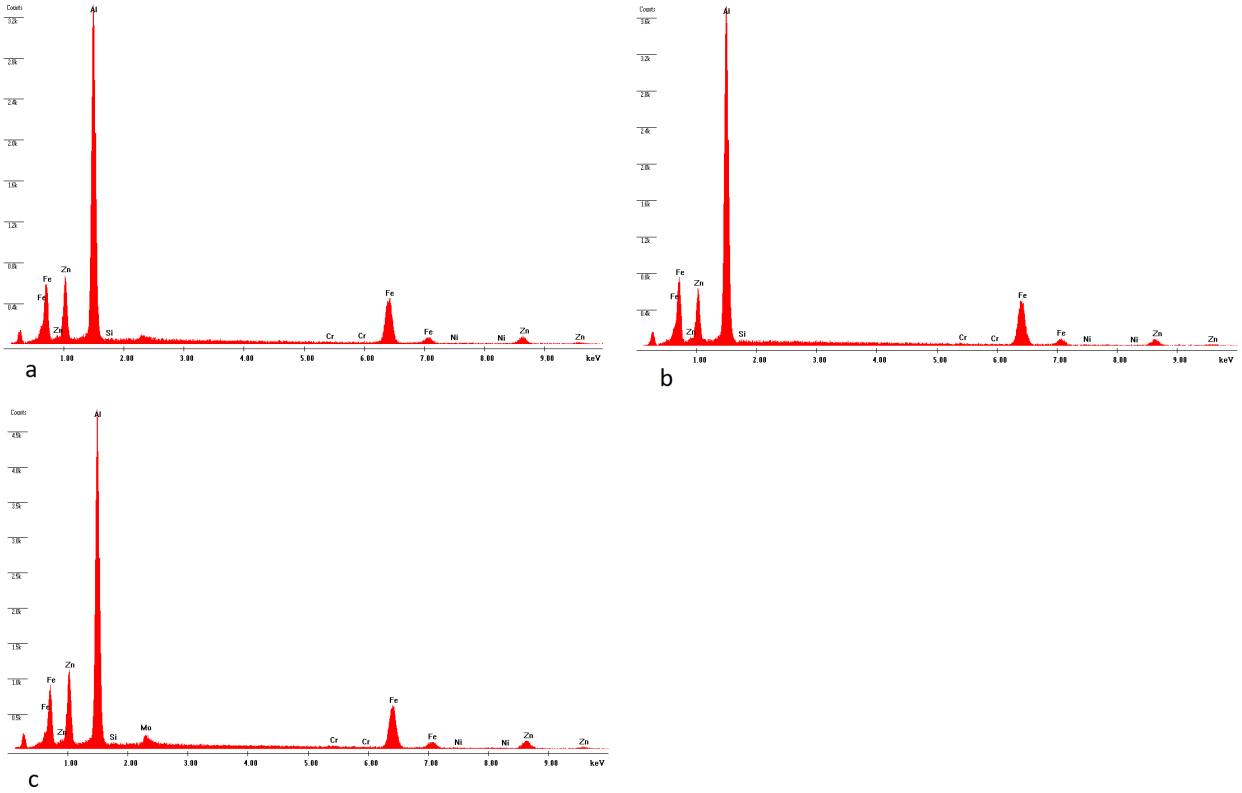

Figure A-4: Spectra of the points seen in Figure A-3. a.)point 005, b.)point 006, c.) point 007

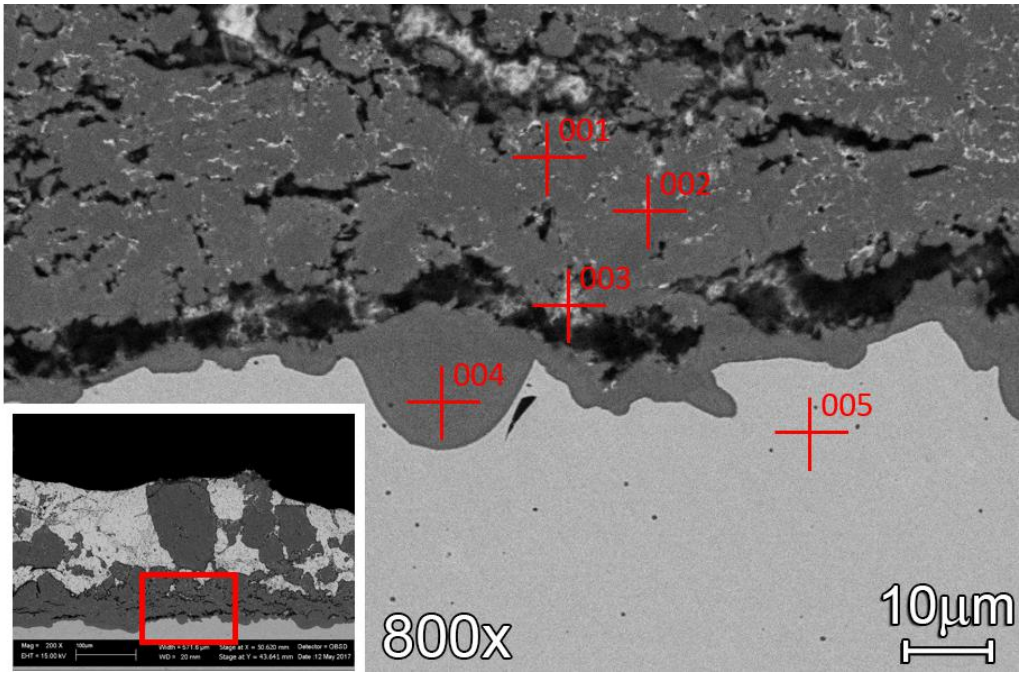

Figure A-5: Points taken in sample 1.2 (GI+MZ). Point 001 is taken in the intermetallic dross particles above the visible crack. Point 002 is taken in the small white spots visible in the intermetallic dross particles. Point 003 is taken in the large white spots in the intermetallic dross particles. Point 004 is taken in the diffusion layer. Point 005 is taken in the roll surface as a reference.

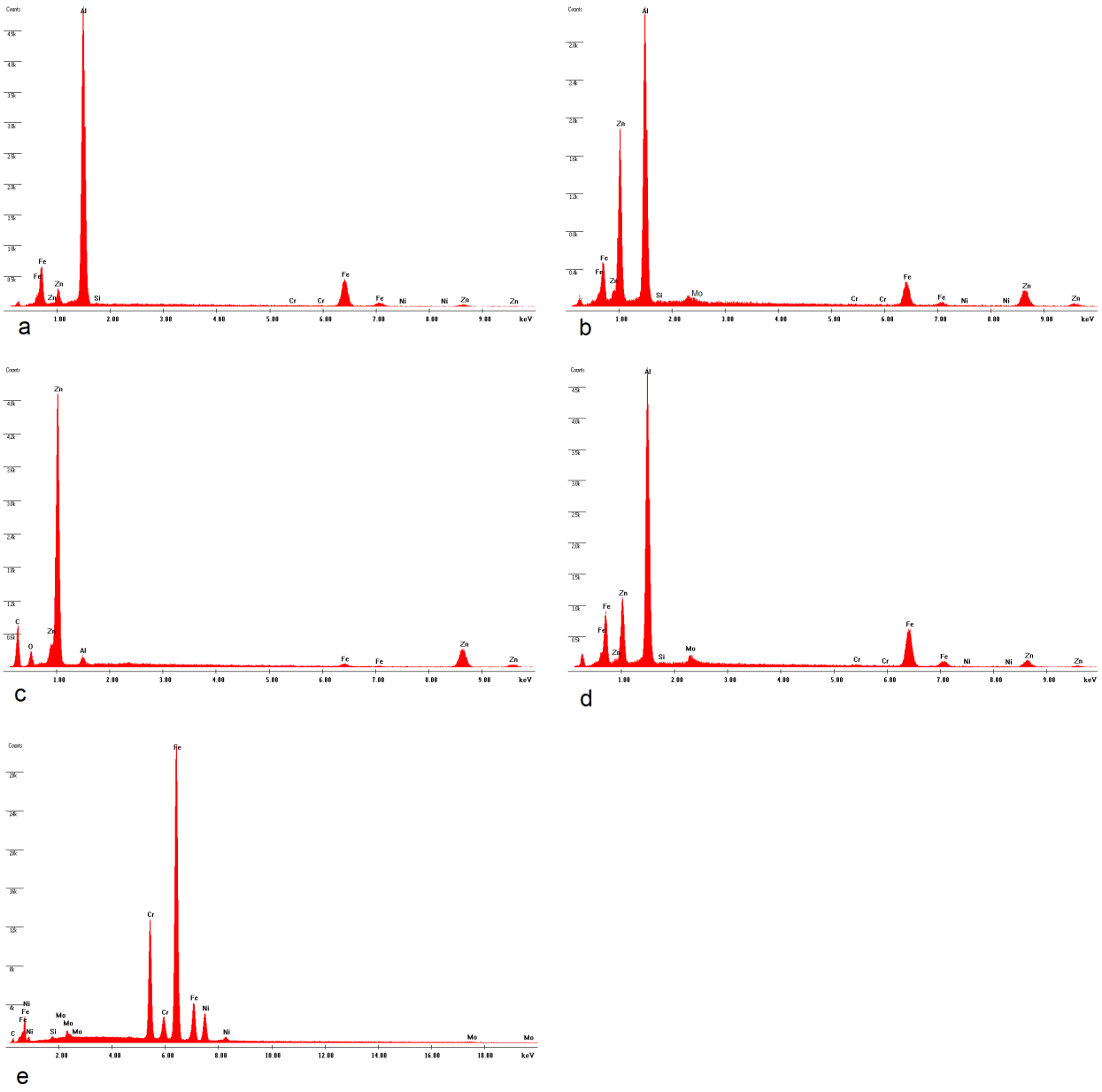

Figure A-6: EDX-spectra of points taken in Figure A-5 in sample 1.2 (GI+MZ). a.) point 001, b.) point 002, c.) point 003, d.) point 004, e.) point 005
Spectrum 001 mainly detects Al, Zn and Fe, no other elements are detected. Spectrum 002 shows a similar composition as that of spectrum 001. Spectrum 003 is carried out on a white spot in the intermetallic dross particles. As seen in c.) these white spots consists of mainly Zn, with a little Al.
Spectrum 005 (e.)) shows the 316L stainless steel composition, shown in Figure A-6. This composition is similar to spectrum 004 of sample 1.1 (Figure A-2.d). In this point Al, Zn and Fe is mainly detected. Furthermore a small peak of Mo is visible.

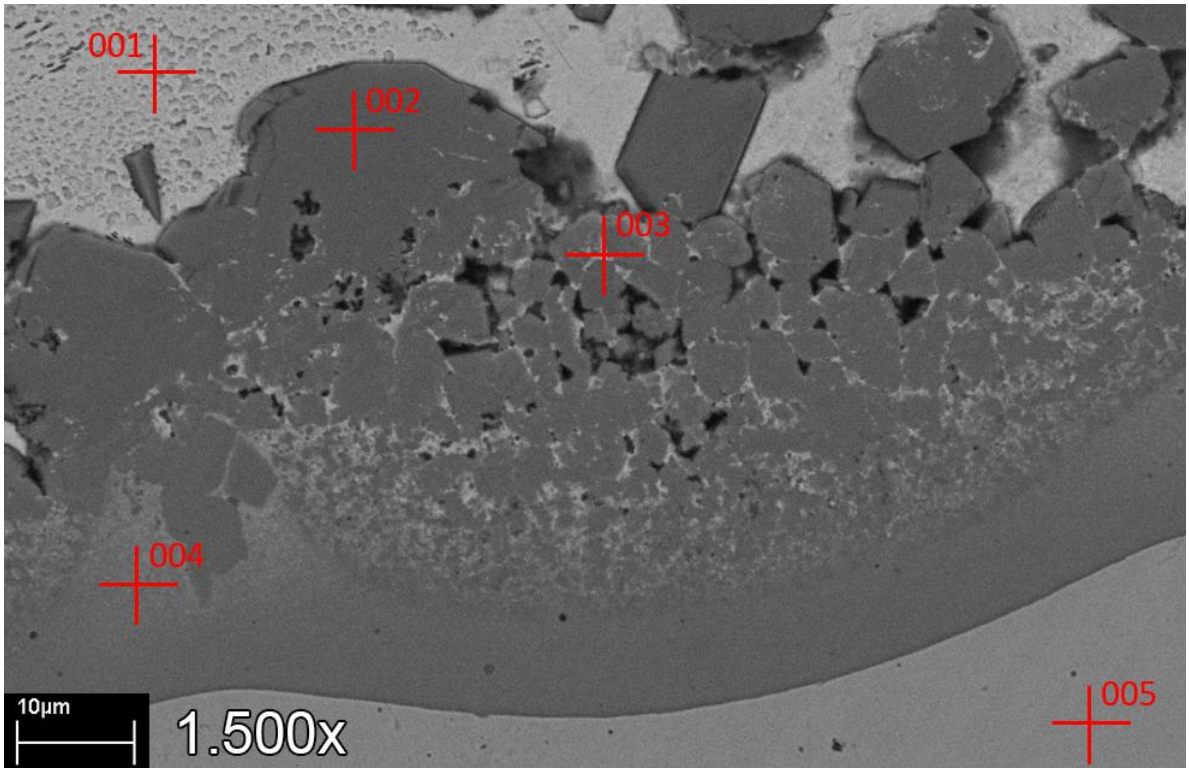

Figure A-7: The points taken for EDX-analysis in sample 1.3 (GI+MZ+GI). Point 001 is taken in the solidified Zn. Point 02 is taken in the intermetallic dross particles near the solidified Zn. Point 003 is taken in the white ribbons. Point 004 is taken in the diffusion layer. Point 005 is taken in the roll surface as a reference.

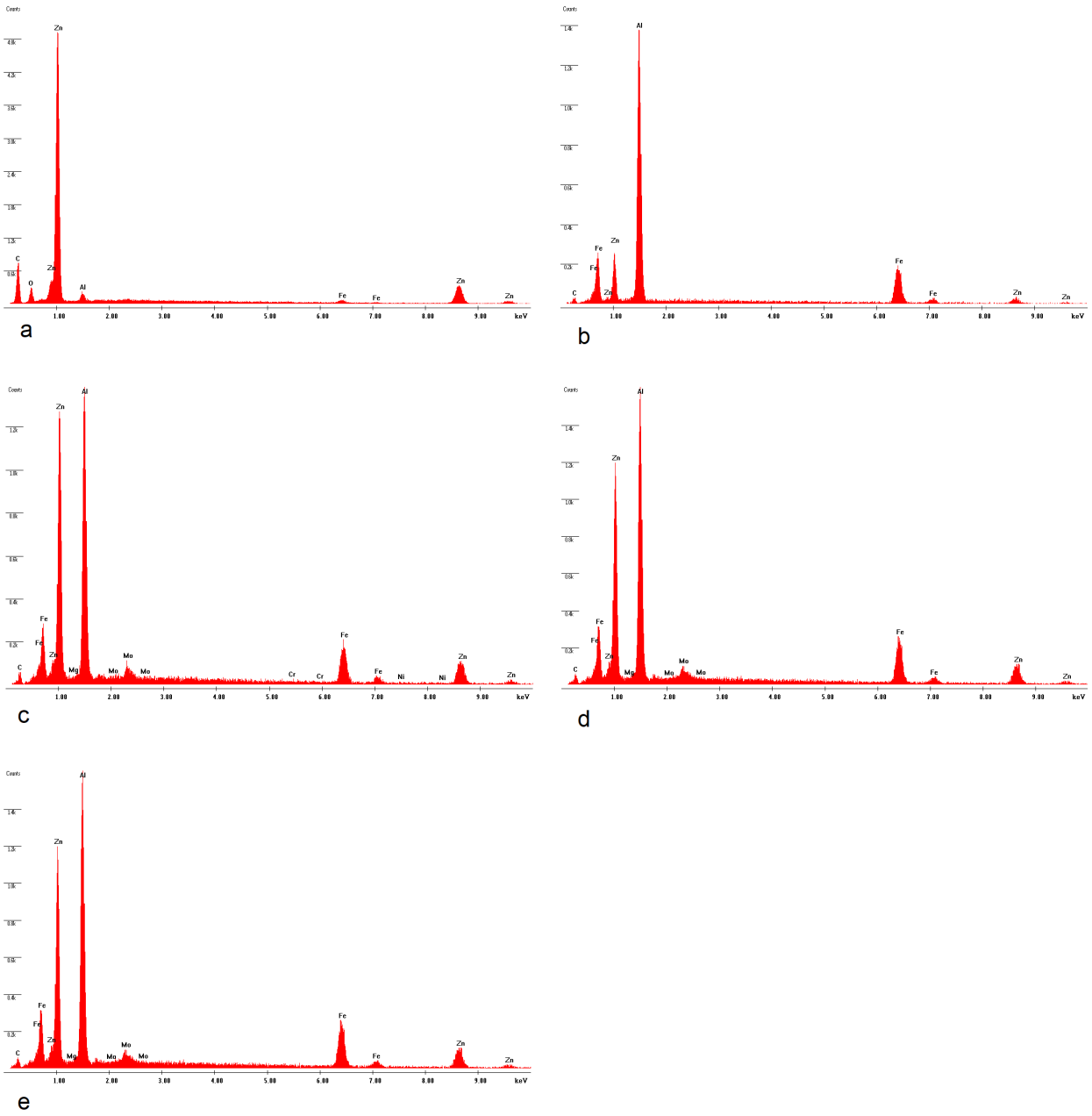

Figure A-8: The spectra of the EDX-analysis from Figure A-7in sample 1.3 (GI+MZ+GI)

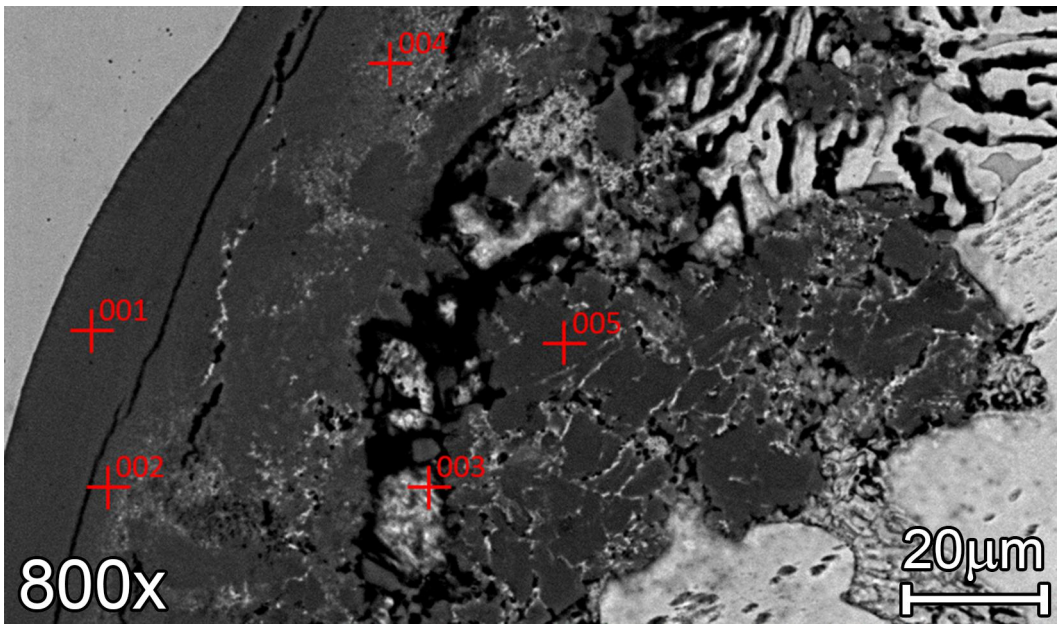

Figure A-9: The points taken for EDX-analysis in sample 1.4 (GI+MZ+GI+MZ). This image is tilted, in the upper left corner the steel substrate is visible.
Point 001 is taken in the diffusion layer under the visible crack. Point 002 is taken just above the crack. Point 003 is taken in the white area between the intermetallic dross particles. Point 004 is taken in the white dots visible in the dross build-up structure. Point 005 is taken in the intermetallic dross particles above the large crack visible.
Points 001 and 002 show similar chemical compositions, as seen in the spectra in Figure A-10. The elements found are Fe, Al and Zn, with comparable amounts. Also some Mo is found in these spectra.

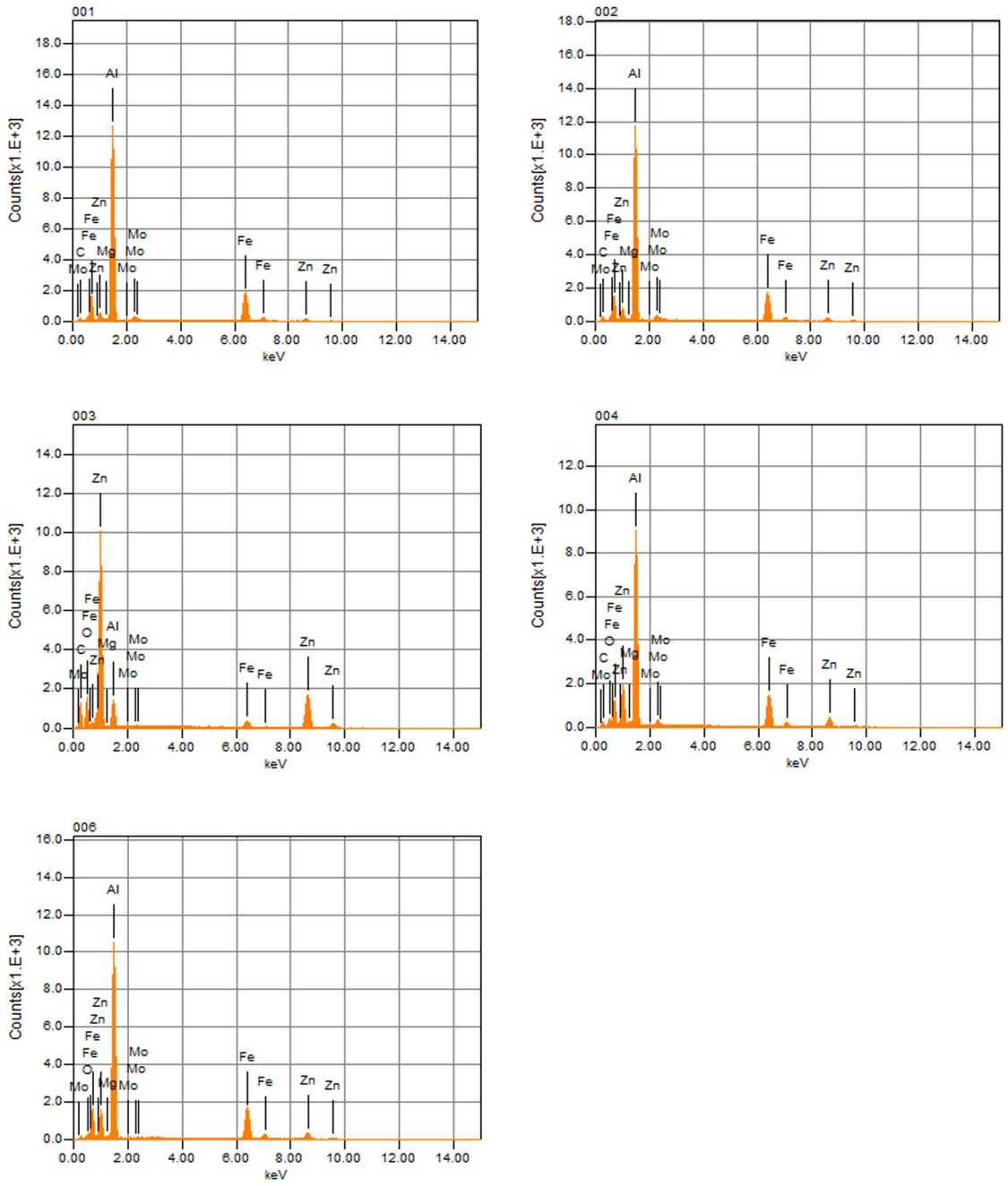

Figure A-10: The EDX-spectra of the points taken for EDX-analysis in sample 1.4 (GI+MZ+GI+MZ), as seen in Figure A-9.
Spectrum 003 (c.)) is carried out in the white spots. This point mainly consists of Zn, also a lot of C and O is detected. Small amounts of Fe and Al are also found. Mo is not detected. The spectrum of point 004 in d.) shows also a composition of Fe, Al and Zn, however this spectrum has a higher percentage in Zn. Similar amount of Mo is found. Spectrum 005 (e.)) has an almost identical composition as spectrum 004, however only less Zn is detected.

Appendix B

EDX-analyses of experiment 2

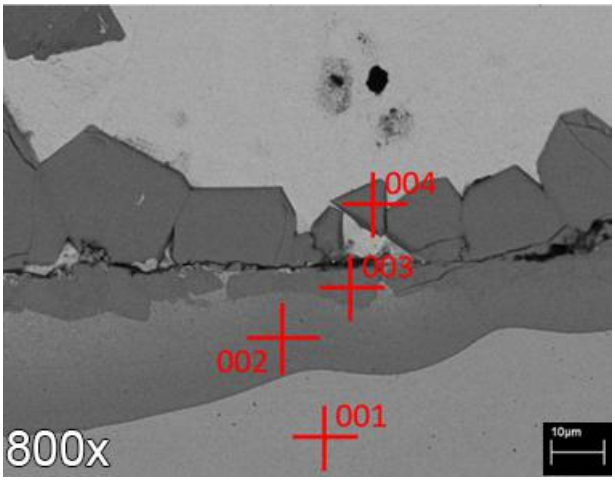

Figure B-1: Point taken for EDX-analysis in sample 2.1(93h GI only). Point 001 is taken in the roll surface in the 316L stainless steel. Point 002 is taken in the diffusion layer, in the light grey area. Point 003 is taken in the diffusion layer in the darker grey area, just below the visible crack. Point 004 is taken in the intermetallic dross particle.

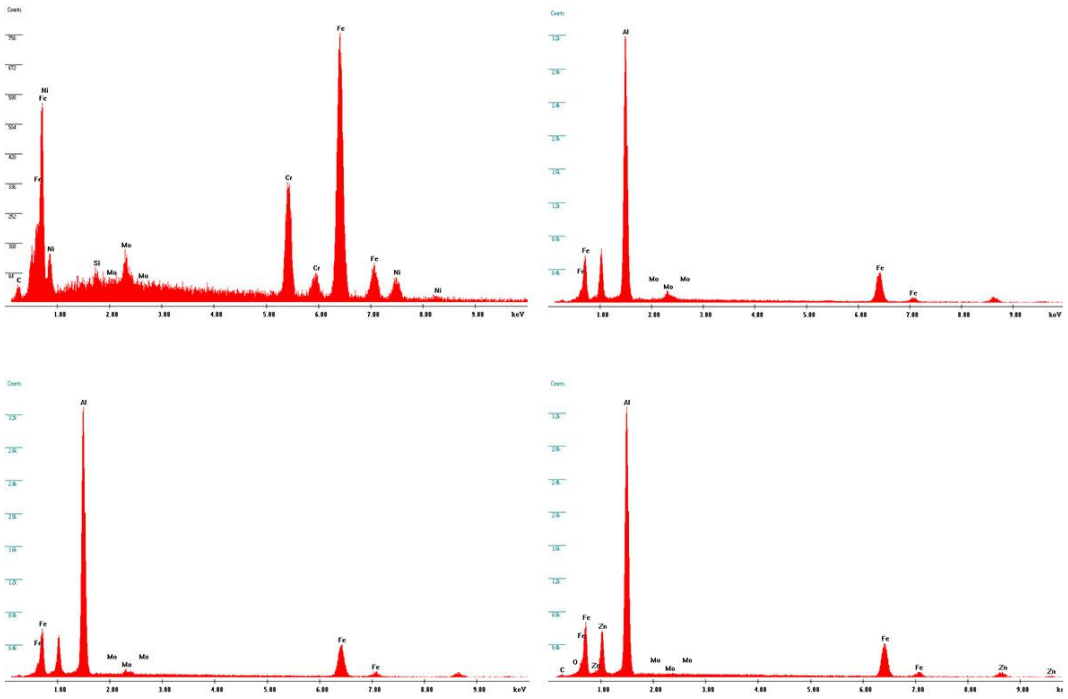

Figure B-2: The spectra of the EDX-analysis of sample 2.1 (93h GI only), as shown in Figure B-1. Spectrum 001 shows the composition of 316L SS as expected: peaks of the elements Fe, Ni, Cr, Mo and Si are clearly visible. Elements found in point 002 are Al, Fe, Zn and some Mo, as seen in b.). The spectrum of point 003 shows a very similar composition as spectrum 002, as seen in c.). d.) shows the composition of the intermetallic dross particles above the cracks (point 004 in Figure B-1). These particles contain consist of Fe, Al and Zn. The element Mo is not detected.

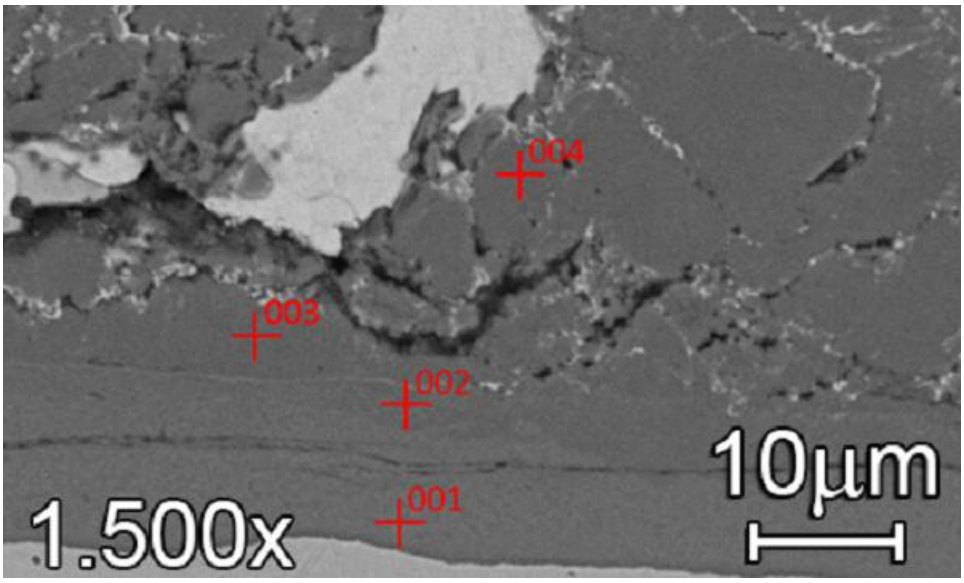

Figure B-3: Points taken for an EDX-analysis in sample 2.2 (93h GI+32,5h MZ). Point 001 is taken in the diffusion layer, near the steel. Point 002 is taken above teh visible crack. Point 003 is to determine whether it is the diffusion layer or intermetallic dross particles. Point 004 is taken in the intermetallic dross particles

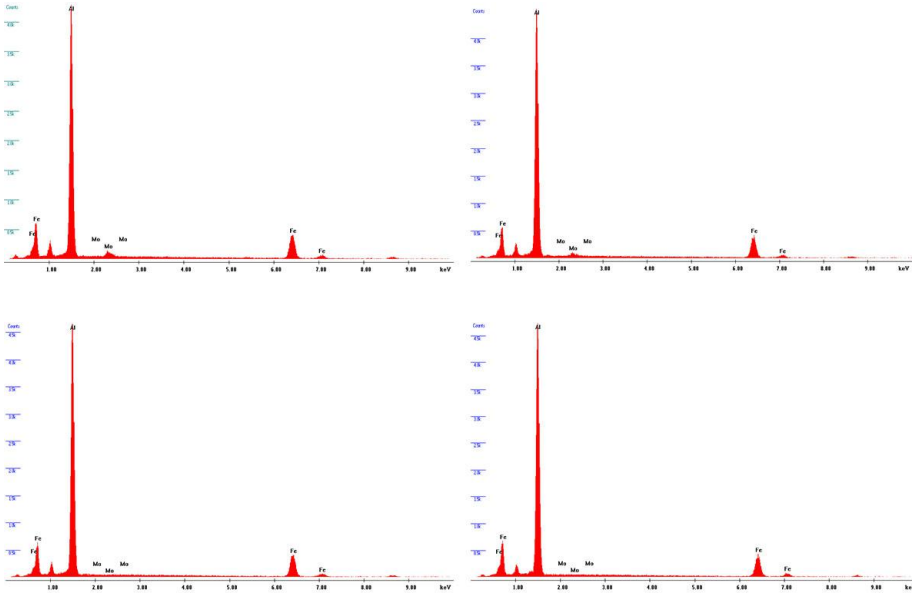

Figure B-4: The spectra of the EDX-analysis of sample 2.2 (93h GI+32,5h MZ), as shown in Figure B-3
point 001 (a.)) contains Al, Fe and Zn, with a trace of Mo. Spectrum 002 (b.)) shows a lower concentration of Zn and Fe compared to spectrum 001, with a higher peak of Al. The peak of Mo is less than in the spectrum of point 001, however Mo is still detected. Point 003 (c.)) shows similar composition of point 002, though no Mo is detected in point 003.
The spectrum of point 004 (d.)) is similar to that of point 003, only a fraction smaller concentration of Fe is seen.

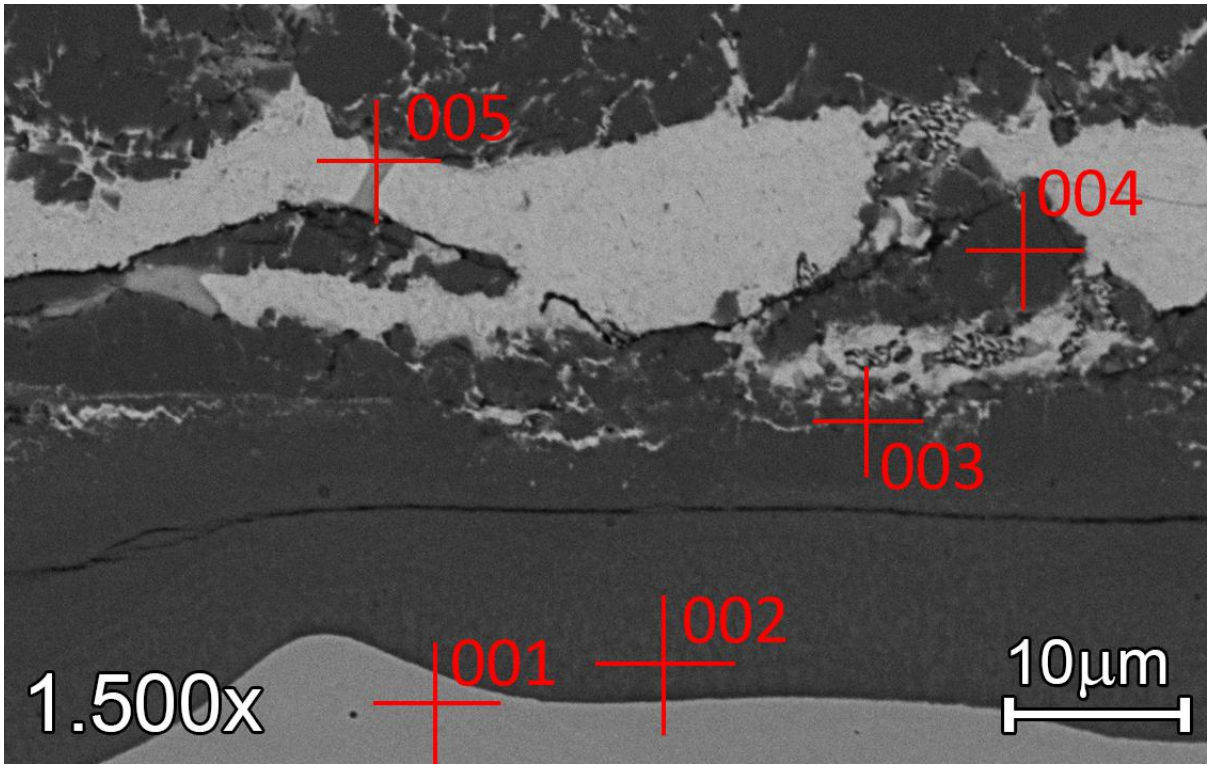

Figure B-5: EDX-analysis of sample 2.3 (93h GI+55,5h MZ). Point 001 is taken in the stainless steel substrate. Point 002 is taken in the difussion layer near the steel. Point 003 is taken net the white Zn, above the visible crack. Point 004 is taken in the 'floating' intermetallic dross particle. Point 005 is taken in the light grey area.

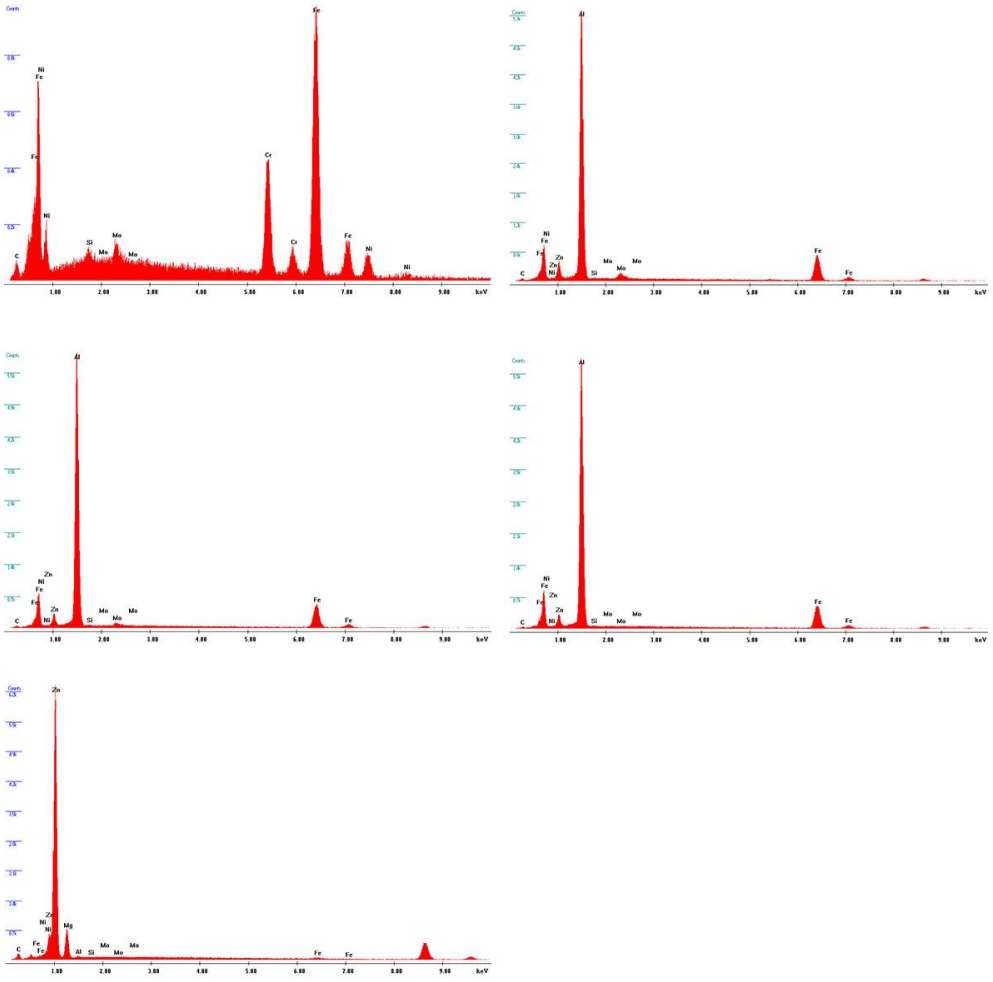

Figure B-6: The spectra of the EDX-analysis of sample 2.3 (93h GI+55,5h MZ), as shown in Figure B-5.a.) shows the composition of 316L SS (point 001 in B-5). In b.) the spectrum of point 002 is seen that this point contains the expected Fe, Al and Zn, with some traces of Mo. Other elements of the 316L SS are not detected. The corresponding spectrum of point 003 is shown in c.) shows the same concentration of point 002. An overlay of spectrum 002 and 003 is made, as can be seen in Figure 5-22. In this Figure it can be seen that point 003 contains less Zn, Fe and Al peaks are the same in both spectra. Mo is only detected in point 002, and not detected in point 003.
The spectrum of point 004 (d.)) shows the same spectrum as the spectrum of point 003. The spectrum of point 005 shows a Mg-Zn structure, seen in e.).

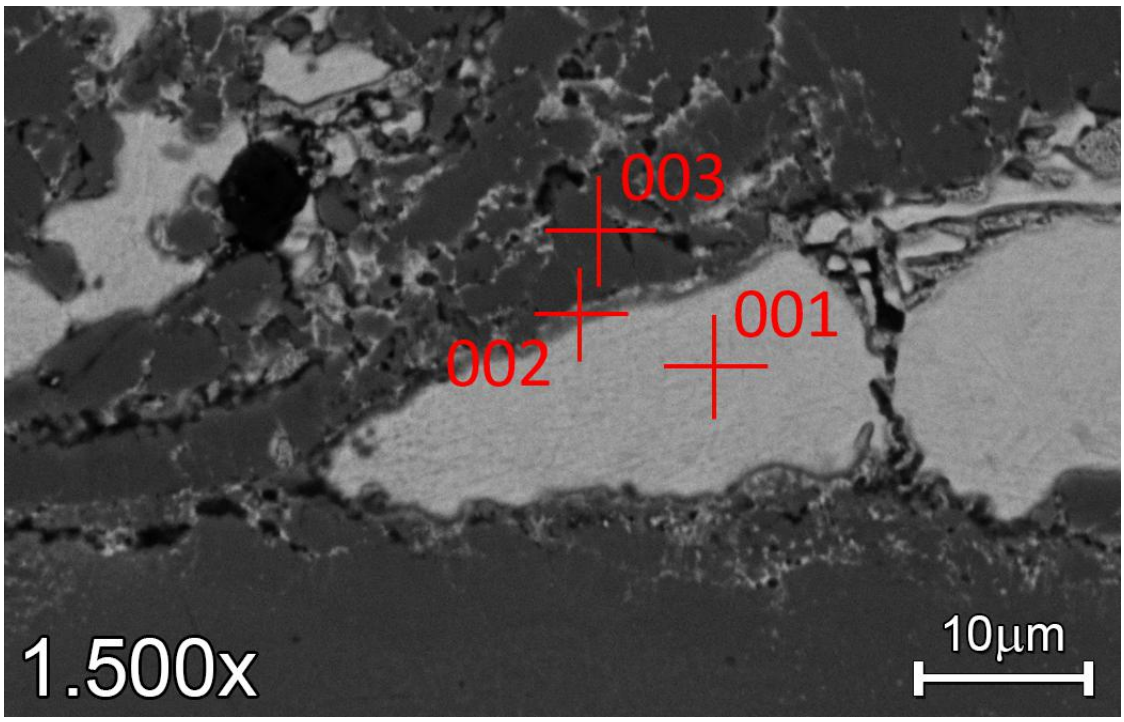

Figure B-7: Points taken for EDX-analysis in sample 2.4 (93h GI+70,5h MZ). Point 001 is taken in the white area. Point 002 is taken in the light grey area, between the Zn-phase and intermteallic dross particles. Point 003 is taken in the intermetallic dross particles.

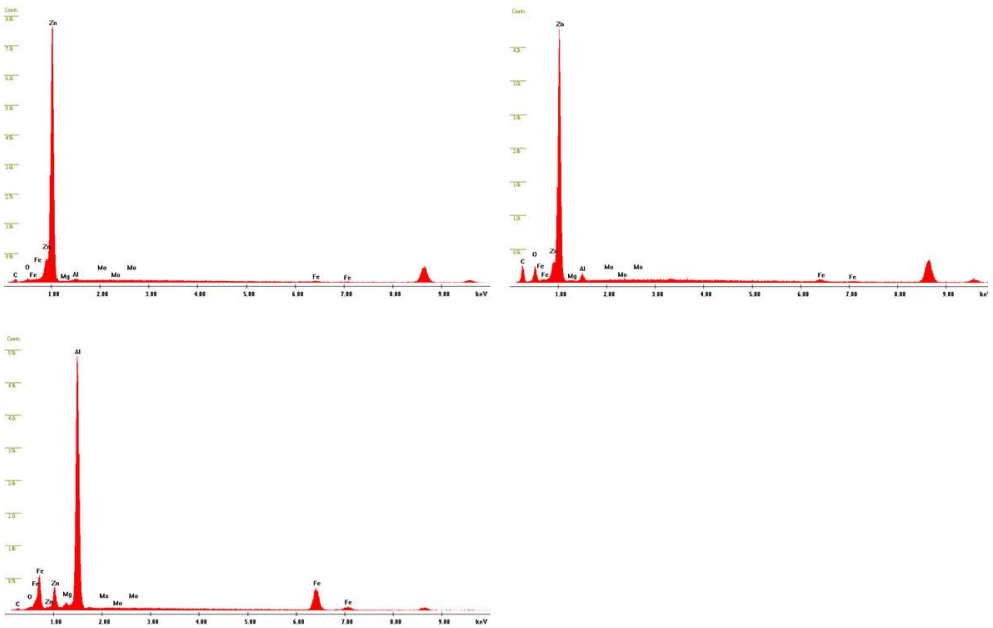

Figure B-8: EDX-spectra of points taken in sample 2.4 (93h GI+70,5h MZ) as seen in Figure B-7. Seen in the spectrum in a.) point 002 mainly consists of Zn and C and O. Spectrum 003 shows the same composition as the intermetallic dross particles in the sample 2.2 and 2.3: Al with lower concentration of Fe and Zn. No other elements are detected.

Appendix C

Process data of all samples

In this Appendix graphs of the relevant process data is presented for each sample. The process data is created with data points that are taken every 20 seconds in production line.
Since the chemical composition , it is not possible to measure the chemical composition of the bath every 20 seconds, since the composition is not equal in the whole bath, furthermore there is no equipment available that is able to measure the composition in this short time frame. To measure the chemical composition, every 4-6 hours a sample is taken from the Zn-bath. From these samples the composition is measured. Though the chemical composition is not as accurate as the other process data is, the data gives an indication of the change in composition over time.

C-1 Process Data of Experiment 1

In Figure C-1 the temperature in GI and MZ and the concentration of Al and Mg are displayed when experiment 1 was executed.

C-2 Process Data of Experiment 2

In Figure C-2 the temperature in GI and MZ and the concentration of Al and Mg are displayed.

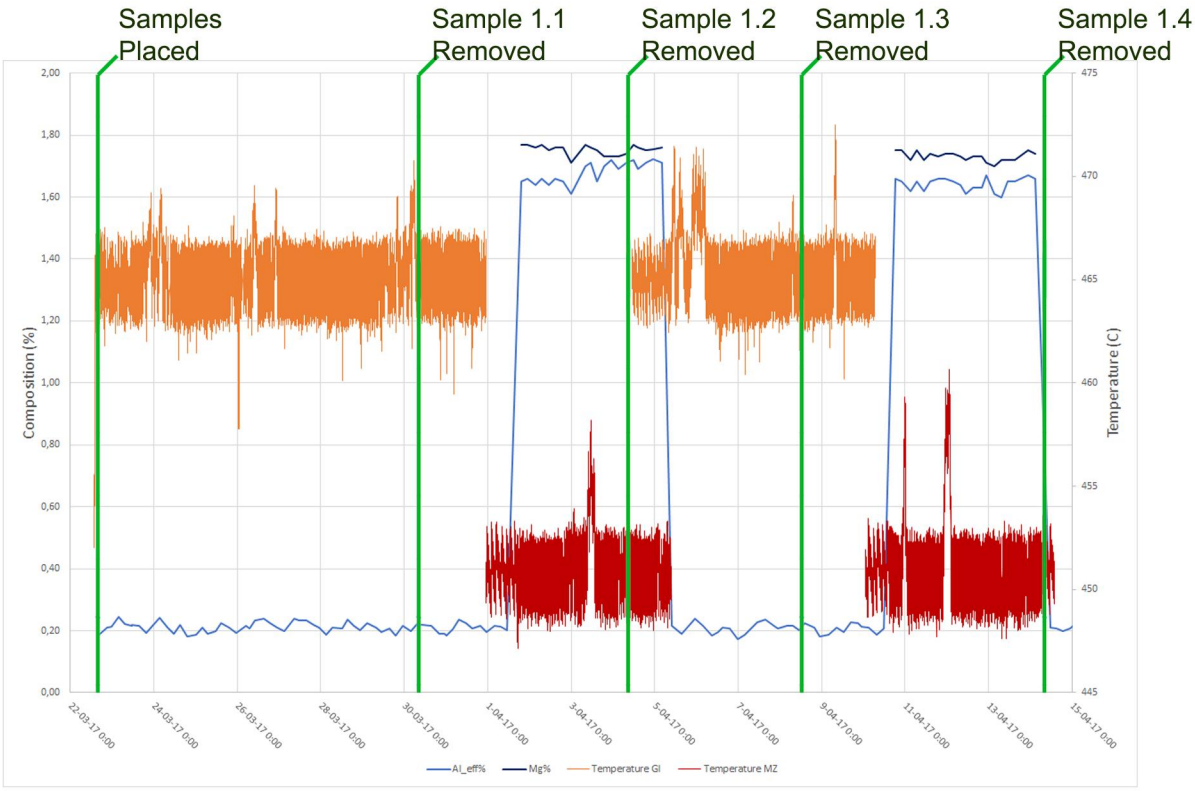

Figure C-1: The process data of the whole period experiment 1 took place. The graphs shows the temperature and composition of Al and Mg.

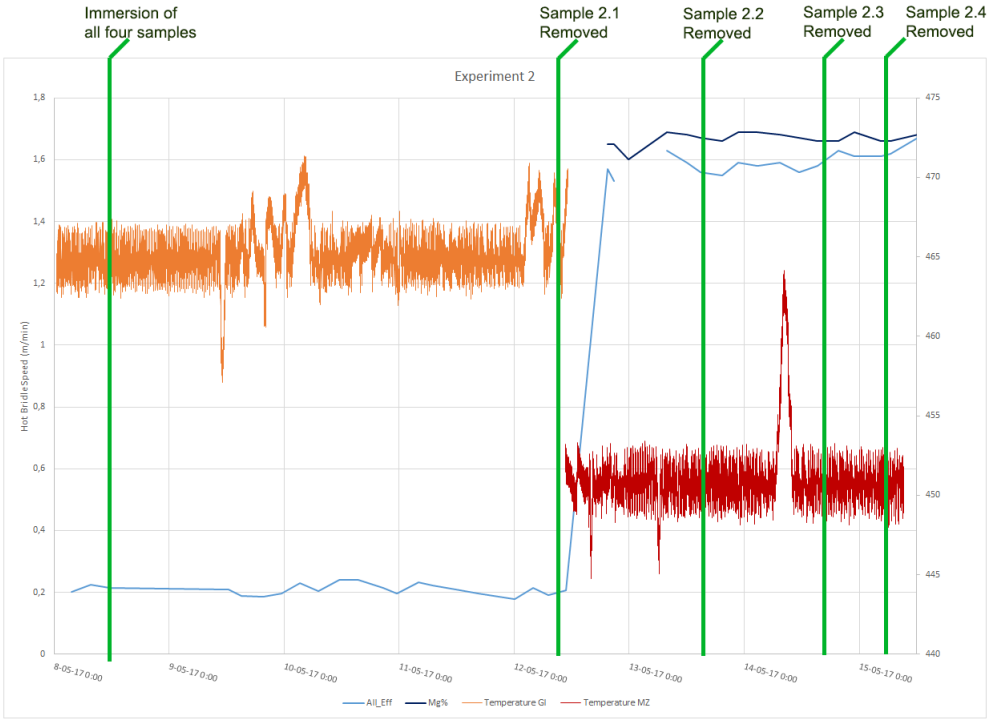

Figure C-2: The process data of the whole period experiment 2 took place. The graphs shows the temperature and composition of Al and Mg. Fe is not measured in MZ.

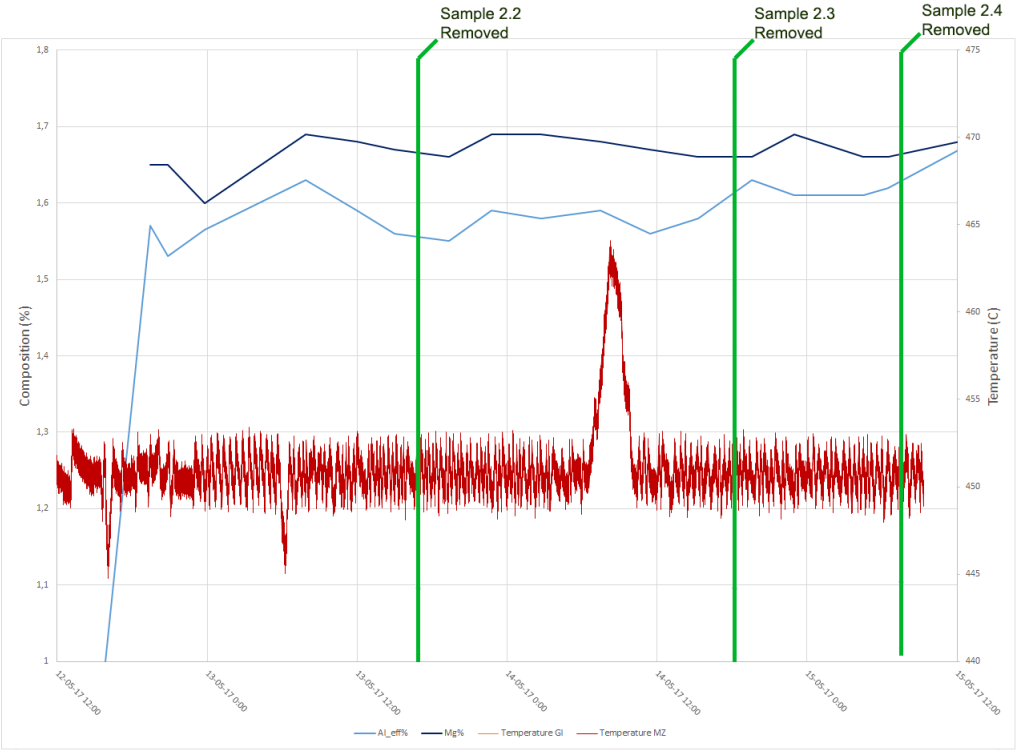

Figure C-3: The process data of experiment 2 of the period when the samples were submerged in MZ. The graphs shows the temperature and composition of Al and Mg in MZ. Fe is not measured in MZ.

Appendix D

Code R-package for Intergranular Diffusion

In this Appendix the results are presented of the intergranular diffusion of Zn in the intermetallic dross particles. The algorithm shown below is written in the program 'R'.
By this code the amount of white and grey pixels are counted. As expected the figures show that with longer immersion time more Zn is diffused in the grain boundaries, thus more white pixels are counted with time.

D-1 Images

The figures are cropped to the same size in order to compare the three figures. All figures are now 500x500 pixels. Via the code the white pixels are counted.
There is a difference in grey-scale between the images. To avoid misinterpretation a range of colours is inserted the code. The code converts the images to white and grey. Every grey-tone that has a colour code very close to white is converted to white. The grey-tones that do have a colour code above the treshold are converted to grey. These grey-tones above the treshold is the same for every image. The results of the conversion to white for each sample is displayed in Figure D-2, D-3 and D-4
Hereafter the amount of white pixels are counted, since white is the same colour in all the images and hereby the same code in the RGB-colour model.

D-2 Code 'R'-package

```
1 # PNG analysis
2 rm(list=ls())
3 library(png)
4 library(grid)
5 library(gridExtra)
```

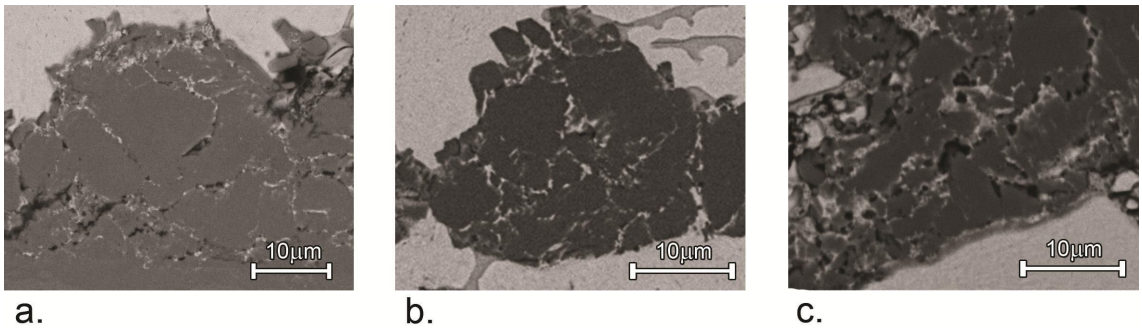

Figure D-1: The original image (A duplicate of Figure 6-10). In a.) Sample 2.2, b.) Sample 2.3 and c.) Sample 2.4 are displayed. The figures show that with longer immersion time more Zn is diffused in the grain boundaries. In sample 2.4 (Figure c) contains small cracks or voids in the intermetallic dross particle (the black spots in the backscattered mode).

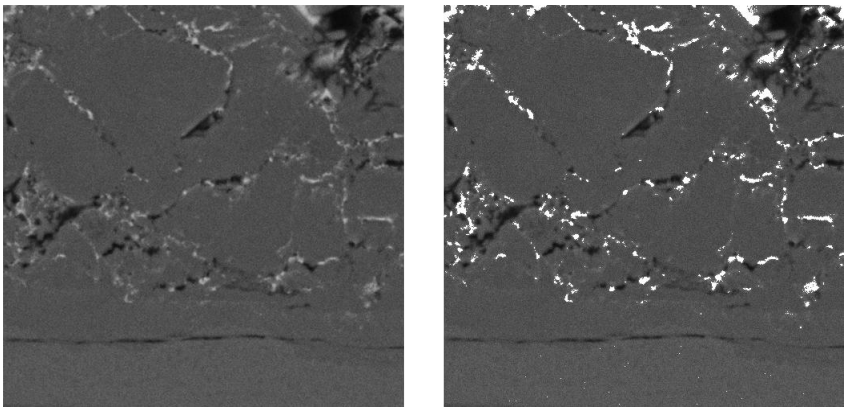

Figure D-2: On the left the original image Sample of 2.2 is displayed, the same as in Figure D-1.a. On the right the converted image is shown.

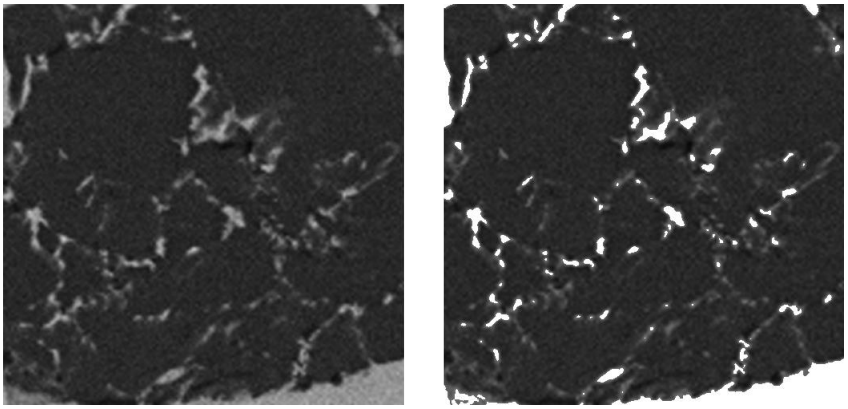

Figure D-3: On the left the original image Sample of 2.3 is displayed, the same as in Figure D-1.b. On the right the converted image is shown.

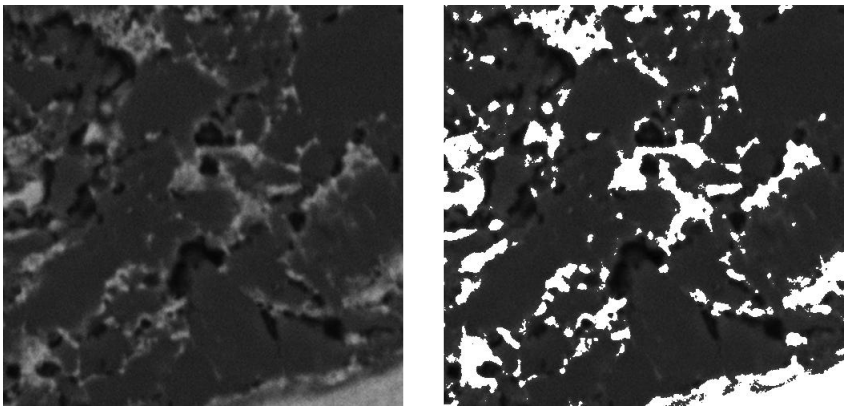

Figure D-4: On the left the original image Sample of 2.4 is displayed, the same as in Figure D-1.c. On the right the converted image is shown.

```
6
7  setwd("/Users/Marianne/Documents/pixel")
8
9  # reshape image into a data frame
10 figure = readPNG("22_1500.png")
11
12 figureR = (matrix(figure[,,1], ncol=1))
13 figureG = (matrix(figure[,,2], ncol=1))
14 figureB = (matrix(figure[,,3], ncol=1))
15
16 #c = mean(figureB)
17 ## 22 = 130/255 - no = 6852
18 ## 23 = 80/255 - no = 35414
19 ## 24 = 80/255 - no = 43057
20 c = 130/255
21 figureR[figureR>c] <- 1
22 figureG[figureG>c] <- 1
23 figureB[figureB>c] <- 1
24
25 figure_nieuw = array(dim=dim(figure))
26 figure_nieuw[,,1] = figureR
27 figure_nieuw[,,2] = figureG
28 figure_nieuw[,,3] = figureB
29
30 grid.raster(figure_nieuw)
31 length(figureB[figureB>c])
32 ##
33
34 figure = readPNG("23_1500.png")
35 figureR = (matrix(figure[,,1], ncol=1))
36 length(figureR[figureR>0.5])
37
38 matrix_pixel = cbind(figureR,figureG,figureB)
39
40 ##
41
```

```
## 22_5000 = 0.387
## 23_5000 = 0.255
## 24_5000 = 0.241
```

D-3 Graphs

Graphs show the amount of white pixels over immersion time in MZ. Furthermore the corresponding percentage is displayed.

Sample	Date/Time Immersion	# Pixels	Percentage White
	May 12, 2017 10:41	0	0
2.2	May 13 , 2017 19:07	6852	2,75
2.3	May 14, 2017 18:17	35414	14,17
2.4	May 15 2017 9:20	43057	17,22

Table D-1: The time when the sample is taken out of MZ is displayed together with the corresponding amount of pixels. May 12, 2017 is the time the samples were submerged in MZ after GI.

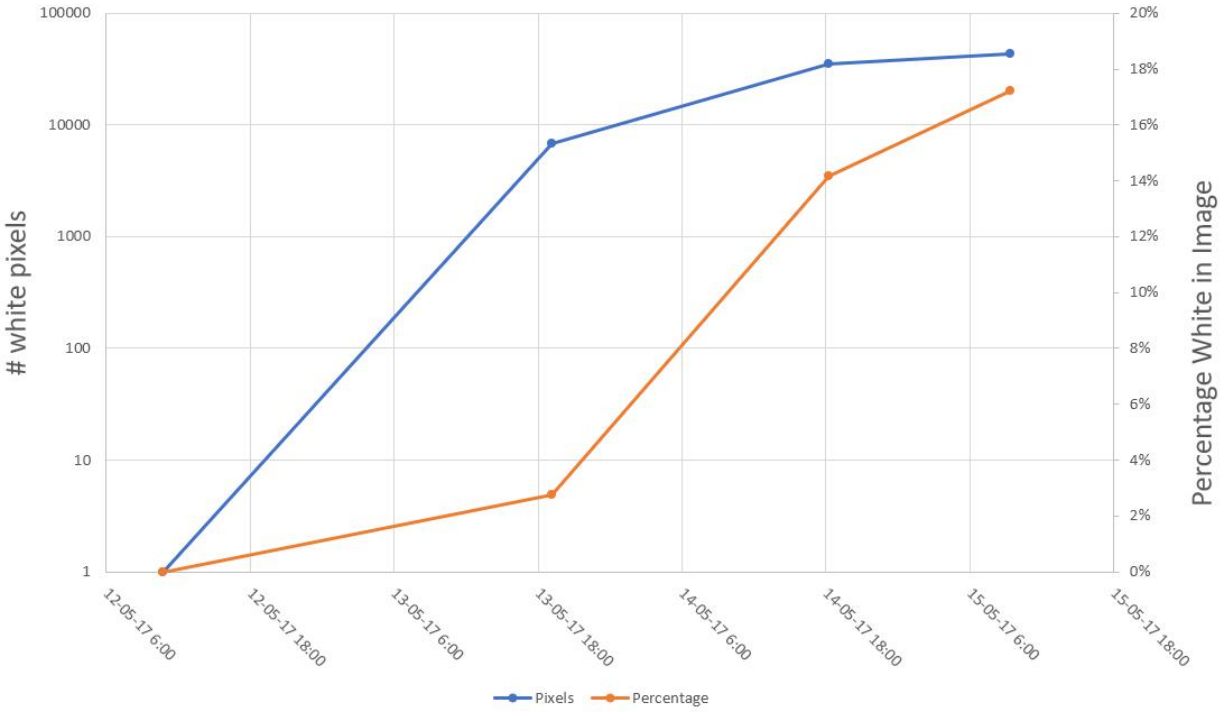

Figure D-5: The amount of white pixels is plotted over the immersion time as well as the percentage of white in the image. The amount of white pixels shows a parabolic function.

Bibliography

[1] website. http://www.lenntech.com/periodic/elements/fe.htm. Lenntech, 06 2017.

[2] website. http://www.tatasteel.com. Company website Tata Steel Europe, 2017.

[3] A.R. Marder. The metallurgy of zinc-coated steel. *Progress in Materials Science*, (45):191–271, 2000.

[4] Laurens Witjens. Inwerkliteratuur hot dip galvanising. *Internal paper Tata Steel*, 2015.

[5] A. Kargar. *Improving Galvanizing Bath Hardware*. PhD thesis, The University of Western Ontario, 2015.

[6] website. https://www.alurvs.nl/roestvast-staal/artikellijst/4720/. AluRVS - Soorten roestvast staal en hun eigenschappen, 05 2017.

[7] M.S. Brunnock, R.D. Jones, G.A. Jenkins, and D.T. Llewellyn. Supermeniscus interactions between molten zinc and bath hardware materials in galvanising. *Ironmaking and Steelmaking*, 1997.

[8] website. Aalco: Alloying elements in stainless steel. http://www.aalco.co.uk/datasheets/Stainless-Steel-Alloying-Elements-in-Stainless-Steel-98.ashx, 2017.

[9] GalvInfo. *Zinc Bath Management on Continuous Hot-Dip Galvanizing Lines - GalvInfoNote 2.4.1.* International Zinc Association, 2009.

[10] M. Vlot and C.J. Kooij. Dross thermodynamics: Technical report 2000. Technical report, Corus Research Development &Technology, 2001.

[11] N.Y. Tang, G.R. Adams, and P.S. Kolesnyk. On determining effective aluminium in continuous galvanizing baths. Technical report, Cominco Ltd., 1995.

[12] S. Chang and J.C. Shin. Effect of the zinc bath composition on hot dip galvanized and galvannealed steel sheet. In *Galvatech 1995 Conference Proceedings*, 1995.

[13] E.W. Fossen, J.P. Landriault, and M.G. Lamb. Aluminum control on stelcos z-line. In *Galvatech 1995 Conference Proceedings*, 1995.

[14] K. Otsuka, M. Arai, and S. Kasai. Developments of dross control methods in a continuous galvanizing pot by numerical bath flow analyses. In *Proceedings of the 4th international conference on zinc and zinc alloy coated steel sheet - Galvatech*, 1998.

[15] GalvInfo. *The Role of Aluminum in Continuous Hot-Dip Galvanizing - GalvInfoNote 2.4*. International Zinc Association, 2009.

[16] J.R. McDermid, M.H. Kaye, and W.T. Thompson. Fe solubility in the zn-rich corner of the zn-al-fe system for use in continuous galvanizing and galvannealing. *The Minerals, Metals & Materials Society and ASM International*, 2007.

[17] M. Bright. Effect of aluminum concentration on the dissolution of 316l stainless steel in molten zinc. In *Galvatech 2007 Conference Proceedings*. West Virginia University, 2007.

[18] W. D. Callister. *Materials Science and Engineering: an introduction*. John Wiley & Sons, 2007.

[19] P. Biele. Determination of the active al and fe contents in the zn bath and their influence on alloy layer formation in hdg process. In P. Biele, editor, *Determination of the active Al and Fe contents in the Zn bath and their influence on alloy layer formation in HDG process*. Krupps Hoesch Stahl AG, Galvatech, 1995.

[20] M. van Schaijk, C. Dane, and B. Berkhout. Magizinc - the new high performance coating for steel in the biw and closures. *SAE International*, 2016.

[21] H.K. Sohn, J.W. Lee, Y. Yoo, J. Min, and M. Oh. Corrosion behaviors of almgzn2 eutectic structure in znalmg coatings. In *International Lead Zinc Research Organization 2009 Conference Proceedings*, Korea, 2009. POMIA.

[22] M. Vlot and M. Zuiderwijk. Sample characterisation of magizinc and other zinc coating. Technical report, Tata Steel internal paper, 2006.

[23] M. Vlot, N. Jones, and H. Leeuwenstein. Solidification of magizinc. Technical report, Tata Steel internal paper, 2009.

[24] J.K. Chang and C.S. Lin. Microstructural evolution of 11al-3mg-zn ternary alloy-coated steels during austenitization heat treatment. *Metallurgical and Materials Transactions A*, 48(8):3734–3744, Aug 2017.

[25] H. Wang, Y. Liu, H. Gao, and Z. Gao. Effects of aging on microstructure evolution and mechanical properties of high-temperature zn-4al-3mg solder. *Soldering and Surface Mount Technology*, 26(4):203–213, 2014.

[26] J. Schulz, F. Vennemann, and G. Nothacker. Zn-mg-al hot-dip galvanized coatings for exposed parts in the automotive industry. In *Galvatech 2015 Conference Proceedings*, 2015.

[27] D. Ruvalcaba. Determining fe solubility in magizinc. internal document Tata Steel, 05 2017.

[28] C. Kato, H. Koumura, K. Mochizuki, and N. Morito. Dross formation and flow phenomena in molten zinc bath. In *Galvatech 1995 Conference Proceedings*, 1996.

[29] P. Perrot, G. Reumont, J.C. Tissier, and J.Foct. Dross formation by reaction between the tank surface and zn-al bath. *Galvatech 1995 Conference Proceedings*, 1995.

[30] R. Thiounn, R. Zanfack, H. Saint-Raymond, and P. Durighello. Understanding hot-dip galvanizing skimmings. In *Galvanizers Association 100th Annual Meeting*, 2008.

[31] N.Y. Tang and K. Zhang. On-line testing of 316l stainless steel. Technical report, Teck Cominco Metals Ltd., 2006.

[32] N.Y. Tang, M. Dubois, and F.E. Goodwin. Progress in development of galvanizing bath management tools. *International Lead Zinc Research Organization 2009 Conference Proceedings*, 2009.

[33] R. Thiounn, M. Simonnet, L. Pineau, and C. Dulcy. Improvement of line productivity and of immersed hot-dip galvanizing roll lifetime by dross build-up control. Technical report, European COmmision - Research Fund for Coal and Steel, 2010.

[34] N.Y. Tang and D. Liu. Improving performance of galvanizing bath hardware. In *Dross Build-up on Submerged Hardware - Influences of Materials and Line Operating Conditions*. ILZRO, 2007.

[35] N.Y. Tang, D.Liu, and K. Zhang. Performance of submerged hardware in continuous galvanizing. In *Galvatech 2009 Conference Proceedings*, 2009.

[36] S. Alibeigi. *Short-term formation kinetics of the continuous galvanizing interfacial layer on mn-containing steels*. PhD thesis, Mc.Master University - Materials Science and Engineering, 2014.

[37] K. Zhang, N.Y. Tang, and F.E. Goodwin. On the reaction of 316l stainless steel with galvanizing baths. In *Galvatech 2007 Conference Proceedings*, 2007.

[38] J.R. McDermid, L. Chen, and R. Fourmentin. Morphology and kinetics of interfacial layer formation during continuous hot-dip galvanizing and galvannealing. *The Minerals, Metals & Materials Society and ASM International*, 2008.

[39] D.A. Porter and K.E. Easterling. *Phase transformations in metals and alloys*. CRC Press, 3rd edition edition, 2009.

[40] B. B. Straumal and O. A. Kogtenkova. Grain boundary faceting-roughening phenomena. *Journal of Materials Science*, 2015.

[41] S. Schonecker, X. Li, B. Johansson, S. Kwon, and L. Vitos. Thermal surface free energy and stress of iron. *Nature*, 5:14860, 10 2015.

[42] P. Lejcek. *Grain Boundary Segregation in Metals*. Springer, 2010.

[43] J.D. Verhoeven. *Fundamentals of Physical Metallurgy*. Wiley, 1975.

[44] M. Herbig, D. Raabe, Y.âĂŁLJ. Li, P. Choi, S. Zaefferer, and S. Goto. Atomic-scale quantification of grain boundary segregation in nanocrystalline material. *Physical Review Letters*, 112, 03 2014.

[45] P. Lejcek, M. Sob, and V. Paidar. Interfacial segregation and grain boundary embrittlement an overview and critical assessment of experimental data and calculated results. *Progress in Materials Science*, 87, 11 2017.

[46] G. Kaptay. Modelling equilibrium grain boundary segregation, grain boundary energy and grain boundary segregation transition by the extended butler equation. *Journal of Materials Science*, 51(4):1738–1755, 2 2016.

[47] S. Mandal, K.G. Pradeep, S. Zaefferer, and D. Raabe. Novel approach to measure grain boundary segregation in bulk polycrystalline materials in dependence of the boundaries five rotational degrees of freedom. *Scripta Materialia*, 2014.

[48] Helmut Mehrer. *Diffusion in Solids*. Springer, 2007.

[49] B. S. Matisoff. *Handbook of Electronics Manufacturing Engineering*. Springer Science & Business Media, 2012.

[50] B. Straumal and B. Baretzky. Grain boundary phase transitions and their influence on properties of polycrystals. *Interfacial Science*, 12(2-3):147–155, 04 2004.

[51] S. Hu, J. Nozawa, S. Guo, H. Koizumi, K. Fujiwara, and S. Uda. Effect of solid-liquid interface morphology on grain boundary segregation during colloidal polycrystallization. *Crystal Growth and Design*, 16(5):2765–2770, 4 2016.

[52] M.E. Kuperus. Effect of transition from gi to mz on dross build-up. *Internal paper Tata Steel*, 2017.

[53] P. Ghosh. Critical assessment and thermodynamic modeling of mg-zn, mg-sn, sn-zn and mg-sn-zn systems. *Elsevier Calphad*, 36:28–43, 2012.

[54] website. http://www.visioneng.com/resources/history-of-the-microscope. Vision Engineering - History of the Microscope, 2017.

[55] M. W. Davidson and M. Abramowitz. *Optical Microscopy*. Olympus Optical Microscopy Resource Center, 2002.

[56] website. https://www.mse.iastate.edu/research/laboratories/sem/microscopy/how-does-the-sem-work/. Iowa State University - How does the SEM work, 2017.

[57] P. W. Hawkes. *The Beginnings of Electron Microscopy*. Academic Press, 2013.

[58] I.C. Kwakernaak and I.W.G. Sloof. *Introduction in the use and application of Scanning Electron Microscopy and Energy Dispersive X-ray Spectroscopy in materials*. TU Delft, course me1301 edition, 2014.

[59] website. http://www.ammrf.org.au/myscope/sem/background/concepts/interactions.php. MyScope - Electron-matter interactions, 2017.

[60] B. Hafner. *Energy Dispersive Spectroscopy on the SEM: A Primer*. Characterization Facility, University of Minnesota, 2011.

[61] website. http://www.ammrf.org.au/myscope/analysis/eds/. MyScope - What is energy dispersive X-ray spectroscopy?, 2017.

[62] website. http://www.engineeringtoolbox.com/linear-expansion-coefficients-d-95.html. Coefficients of Linear Thermal Expansion - Engineering Toolbox, 06 2017.

[63] M.F. Ashby. *Materials Engineering, Science, Processing and Design*. Elsevier Science and Technology, 2009.

[64] P. Matysik, S. Jozwiak, and T. Czujko. Characterization of low-symmetry structures from phase equilibrium of fe-al system - microstructures and mechanical properties. *Materials*, 8:914–931, 03 2015.

[65] N.Y. Tang, D.Y.H. Liu, and F.N. Coady. Corrosion of 316l stainless steel in molten zn-al alloys. In *Galvanizers Association 101st Annual Meeting*, 2009.

[66] J. Askill and D. H. Tomlin. Self-diffusion in molybdenum. *Philosophical Magazine*, 8(90):997–1001, 1963.

[67] O Sbaizero and G Pezzotti. Influence of molybdenum particles on thermal shock resistance of alumina matrix ceramics. *Materials Science and Engineering: A*, 343(1):273 – 281, 2003.

[68] J. Kucera and K. Stransky. Diffusion in iron, iron solid solutions and steels. *Materials Science and Engineering*, 52(1):1 – 38, 1982.

[69] Kunshan Huang, H Heinrich, Dennis Keiser, and Yongho Sohn. Fuel-matrix chemical interaction between u-7wt.333:199–206, 02 2013.

[70] A. Chiba, I. Muto, Y. Sugawara, and Nobuyoshi Hara. Effect of inclusion size on pit initiation at mns in stainless steel. *High Resolution Characterization of Corrosion Processes II*, 2014-02(14):801, 02 2014.